frontiers | Research Topics

Advances of radiomics and artificial intelligence in the management of patients with central nervous system tumors

Edited by
Xuejun Li, Harrison Bai and Paul J. Zhang

Published in
Frontiers in Oncology
Frontiers in Neurology

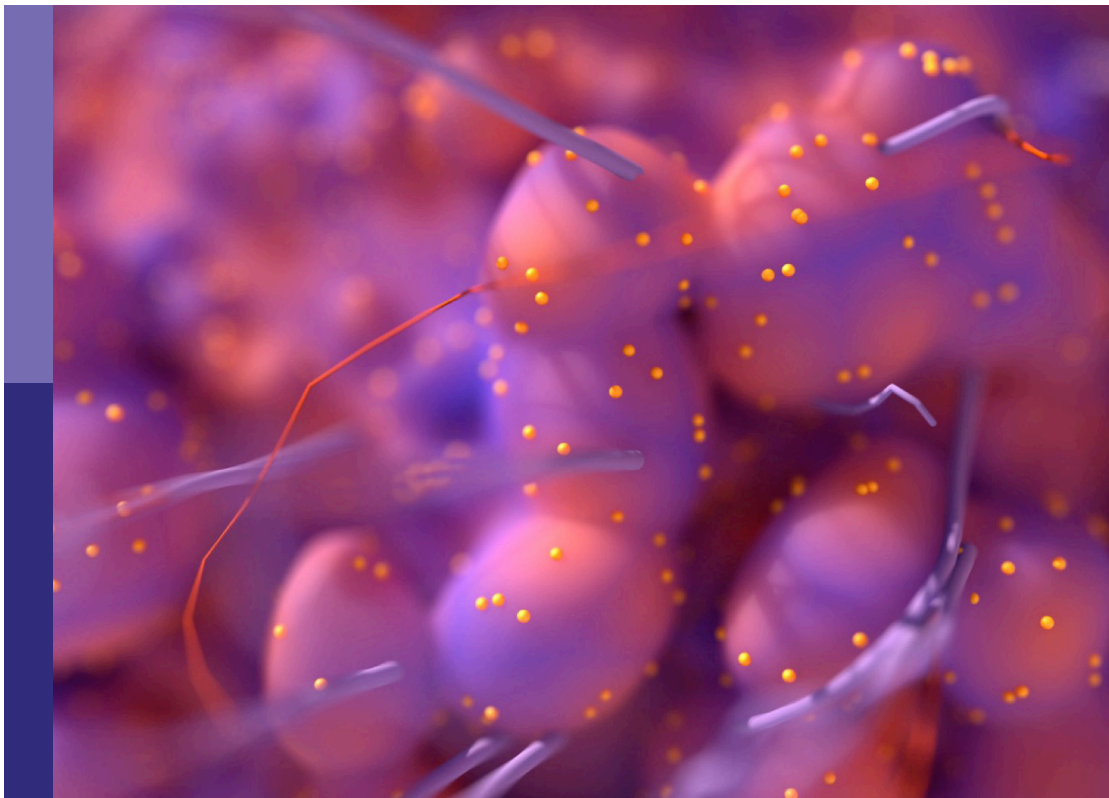

ISSN 1664-8714
ISBN 978-2-83251-551-8
DOI 10.3389/978-2-83251-551-8

About Frontiers

Frontiers is more than just an open access publisher of scholarly articles: it is a pioneering approach to the world of academia, radically improving the way scholarly research is managed. The grand vision of Frontiers is a world where all people have an equal opportunity to seek, share and generate knowledge. Frontiers provides immediate and permanent online open access to all its publications, but this alone is not enough to realize our grand goals.

Frontiers journal series

The Frontiers journal series is a multi-tier and interdisciplinary set of open-access, online journals, promising a paradigm shift from the current review, selection and dissemination processes in academic publishing. All Frontiers journals are driven by researchers for researchers; therefore, they constitute a service to the scholarly community. At the same time, the *Frontiers journal series* operates on a revolutionary invention, the tiered publishing system, initially addressing specific communities of scholars, and gradually climbing up to broader public understanding, thus serving the interests of the lay society, too.

Dedication to quality

Each Frontiers article is a landmark of the highest quality, thanks to genuinely collaborative interactions between authors and review editors, who include some of the world's best academicians. Research must be certified by peers before entering a stream of knowledge that may eventually reach the public - and shape society; therefore, Frontiers only applies the most rigorous and unbiased reviews. Frontiers revolutionizes research publishing by freely delivering the most outstanding research, evaluated with no bias from both the academic and social point of view. By applying the most advanced information technologies, Frontiers is catapulting scholarly publishing into a new generation.

What are Frontiers Research Topics?

Frontiers Research Topics are very popular trademarks of the *Frontiers journals series*: they are collections of at least ten articles, all centered on a particular subject. With their unique mix of varied contributions from Original Research to Review Articles, Frontiers Research Topics unify the most influential researchers, the latest key findings and historical advances in a hot research area.

Find out more on how to host your own Frontiers Research Topic or contribute to one as an author by contacting the Frontiers editorial office: frontiersin.org/about/contact

Advances of radiomics and artificial intelligence in the management of patients with central nervous system tumors

Topic editors

Xuejun Li — Central South University, China

Harrison Bai — Brown University, United States

Paul J. Zhang — University of Pennsylvania, United States

Citation

Li, X., Bai, H., Zhang, P. J., eds. (2023). *Advances of radiomics and artificial intelligence in the management of patients with central nervous system tumors*. Lausanne: Frontiers Media SA. doi: 10.3389/978-2-83251-551-8

Table of contents

frontiers | Frontiers in Oncology

TYPE Editorial
PUBLISHED 19 January 2023
DOI 10.3389/fonc.2023.1081301

OPEN ACCESS

EDITED AND REVIEWED BY
David D. Eisenstat,
Royal Children's Hospital, Australia

*CORRESPONDENCE
Xuejun Li
lxjneuro@csu.edu.cn

SPECIALTY SECTION
This article was submitted to Neuro-Oncology and Neurosurgical Oncology, a section of the journal Frontiers in Oncology

RECEIVED 27 October 2022
ACCEPTED 11 January 2023
PUBLISHED 19 January 2023

CITATION
Chen Z, Zhang H, Zhang PJZ, Bai HX and Li X (2023) Editorial: Advances of radiomics and artificial intelligence in the management of patients with central nervous system tumors.
Front. Oncol. 13:1081301.
doi: 10.3389/fonc.2023.1081301

Editorial: Advances of radiomics and artificial intelligence in the management of patients with central nervous system tumors

Ziyan Chen[1,2], Helen Zhang[3], Paul J. Z. Zhang[4], Harrison X. Bai[3,5] and Xuejun Li[1,2]*

[1]Department of Neurosurgery, Xinagya hospital, Central South University, Changsha, China, [2]Hunan International Scientific and Technological Cooperation Base of Brain Tumor Research, Xiangya Hospital, Central South University, Changsha, China, [3]Department of Diagnostic Imaging, Rhode Island Hospital and Alpert Medical School of Brown University, Providence, RI, United States, [4]Department of Pathology and Laboratory Medicine, Perelman School of Medicine at the University of Pennsylvania, Philadelphia, PA, United States, [5]Department of Radiology and Radiological Science, Johns Hopkins University School of Medicine, Baltimore, MD, United States

KEYWORDS

central nervous system, radiomics, artificial intelligence, imaging, management

Editorial on the Research Topic
Advances of radiomics and artificial intelligence in the management of patients with central nervous system tumors

Central nervous system (CNS) tumors can cause severe morbidity and mortality across all populations. The average annual age-adjusted incidence rate of all CNS tumors was 24.25 per 100,000 in the US from 2014-2018 and 5.57 per 100,000 in China in 2016 (1, 2). Although rare, CNS tumors are considered as a significant contributor to cancer mortality due to their high mortality rate (3). In the US, only one-third of patients diagnosed with a malignant CNS tumor survived at least 5 years past diagnosis (4). CNS tumors are extremely heterogeneous with over 100 histological subtypes, requiring individualized management strategies (5, 6). Nowadays, there is a plethora of imaging, biological, and clinical data that can inform identification and management of patients with CNS tumors. Recent approaches allow us to extract hidden information from this data to explore the deep nature of tumors.

Radiomics has shown the capability to extract quantitative information from medical images and demonstrated robust performance in clinical diagnosis and grading, prognosis prediction and molecular parameter recognition 7). Artificial intelligence (AI) has demonstrated the potential to increase the workflow and performance of radiomics models (8). In previous studies, we implemented deep learning models to determine IDH status of glioma patients (9) and automatically segment abnormal contrast enhancement of gliomas on post-treatment magnetic resonance imaging (MRI) (10). We also reported the use of deep learning models to differentiate between glioma and germinoma (11), and meningioma and hemangiopericytoma (12), providing valuable clinical information for surgery and other treatments.

This Research Topic was introduced to highlight the use of AI-based radiomics and radiogenomics methods to improve diagnostic approaches and therapeutic options for CNS tumor patients. The papers within this Research Topic cover various types of CNS tumors

including glioma, craniopharyngioma, meningioma, brain metastasis, pituitary macroadenoma etc. The research objectives are diverse and include tumor status evaluation, differential diagnosis, survival and recurrence assessment, and genomic features prediction.

Gliomas are the most common type of primary CNS tumor (13). Molecular biomarkers have been widely used in glioma tumor taxonomy and survival assessment (14). Fan et al. identified five valuable radiomics features with significant difference in WHO grade II glioma patients with different 1p/19q status using elastic net and support vector machine (SVM) algorithms. Similarly, Fang et al. established a radiomics-based machine-learning algorithm highlighting 12 radiomics features capable of predicting telomerase reverse transcriptase promoter (pTERT) mutations in patients with WHO grade II gliomas. Both studies obtained relatively high predictive performance with area under the curve (AUC) of 0.808 and 0.844, respectively. Thus, radiomics offers a promising approach to predict molecular biomarkers using radiological images, and has the potential to save patients from invasive biopsies. Qi et al. studied 223 glioma samples from The Cancer Imaging Archive (TCIA) and proposed a Voxel-based lesion-symptom mapping (VLSM) approach to detect glioblastoma (GBM) topography of proneural and mesenchymal subtypes. They found a difference in survival characteristics and proneural-mesenchymal transition (PMT) progression of samples in and outside of the VLSM-determined area. This study provides a valuable VLSM-determined area related to prognosis and PMT progression. To improve differential diagnosis, Zhang et al. trained a deep learning model to classify MRI lesions as GBM, primary central nervous system lymphoma (PCNSL), or tumefactive demyelinating lesion (TDL). The model achieved improved diagnostic performance over neuroradiologists. Imaging data aside, radiology reports remain the major point of reference for many diagnostic and treatment decisions. Cao et al. applied natural language processing to automatically interpret glioma pre-operative MRI reports and predict IDH mutation. They identified 30 glioma enhancement descriptions and established a high-performance model based on report features and age, achieving an AUC of 0.89 in predicting IDH mutation status. These varying approaches demonstrate the potential integration of a wide range of data into glioma assessment.

Meningiomas are thought to originate from arachnoid cells and account for over 30% of all primary brain tumors (15). Surgical resection is generally the preferred treatment for meningiomas. Malignant meningiomas, however, are more aggressive and have a higher risk of recurrence after surgery compared to benign meningiomas. Ko et al. applied pre-operative radiomic features evaluated by SVM to predict progression/recurrence in 128 meningioma patients. Using SVM scores, an AUC of 0.80 was achieved, with an optimal cutoff value of 0.224. Xiao et al. explored the use of 3D radiomics features extracted from multi-parameter MRI to evaluate postoperative cerebral edema exacerbation in patients with meningioma. A combined model was constructed from the established radiomics signature and clinical data. This combined model demonstrated a high prediction accuracy, with an AUC of 0.91 in the primary cohort and 0.83 in the validation cohort. This work demonstrates the potential contributions of AI-based radiomics to characterization and clinical management of meningiomas.

Brain metastases (BM) are a common manifestation of cancer that can worsen clinical outcomes (16). An estimated 20% of all patients with cancer will develop brain metastases, with most brain metastases occurring in those with lung cancer, especially non-small cell lung cancer (NSCLC) (17). Advances in neuroimaging and computer-assisted approaches have provided additional opportunities to accurately screen and precisely target intracranial lesions noninvasively. To predict survival of patients with BM from NSCLC, Chen et al. retrospectively identified 110 patients with BM from EGFR, ALK, and/or KRAS mutation-positive NSCLC and constructed a model using MRI radiomics and clinical features. The model yielded an AUC of 0.977, 0.905, and 0.947 for the EGFR, ALK, and KRAS mutation-positive groups, respectively. Zhang et al. implemented a CT-based radiomics nomogram model to predict prognosis of patients with BM from NSCLC treated with whole brain radiotherapy. Five radiomics features were selected through LASSO Cox regression and used to construct the nomogram. The resulting AUCs were 0.786 and 0.788 for short-term and long-term survival predictions, respectively. These studies demonstrate the applicability of radiomics and AI-based approaches to outcome prediction in patients with brain metastases.

Lastly, we considered studies that applied radiomics methods to biological status prediction of other tumors in CNS. Ma et al. reported the construction of a radiomics-clinical nomogram for individualized preoperative prediction of the invasiveness of adamantinomatous craniopharyngioma (ACP) before surgery. A total of 355 patients were enrolled in the study and 11 features associated with the invasiveness of ACPs were selected. A nomogram incorporating peritumoral edema and the radiomics signature reached an AUC of 0.735 in the validation cohort. This study described a potential and reliable tool for clinical decision making. Zhang et al. constructed a radiomics model based on routine MRI to predict progression/recurrence of non-functioning pituitary macroadenomas (NFPAs) after surgical resection. They used an SVM classifier to evaluate the importance of extracted parameters to build a prediction model. The model showed an accuracy of 82% and AUC of 0.78 in differentiating between progression/recurrence and non-progression/recurrence in NFPAs.

Conclusion and perspective

The 11 papers collected in this Research Topic produced promising results in their application of radiomics and AI to the management of patients with various CNS tumors. With the rapid advancement of AI and medical imaging techniques, radiomics is assuming a larger role in cancer diagnosis and treatment, as well as biological investigation. We are encouraged by the great support from the research community for this topic; a total of 99 authors contributed to the 11 selected papers, which have already generated significant attention within the field. Nevertheless, more work is needed to advance computational precision medicine. Models with

higher accuracy and robustness as well as clinical interpretability require further exploration. All studies within this Research Topic are retrospective and may be limited by smaller sample sizes. To facilitate clinical translation, additional studies may need to focus on image and data standardization between different institutions, data sharing, and prospective research. However, the present contributions of radiomics and AI-based approaches to tumor diagnosis and management indicate significant promise for the near future.

Author contributions

All authors listed have made a substantial, direct and intellectual contribution to the work, and approved it for publication.

Conflict of interest

The authors declare that the research was conducted in the absence of any commercial or financial relationships that could be construed as a potential conflict of interest.

Publisher's note

References

1. Ostrom QT, Cioffi G, Waite K, Kruchko C, Barnholtz-Sloan JS. CBTRUS statistical report: Primary brain and other central nervous system tumors diagnosed in the united states in 2014-2018. *Neuro Oncol* (2021) 23(12 Suppl 2):iii1–iii105. doi: 10.1093/neuonc/noab200

2. Zheng R, Zhang S, Zeng H, Wang S, Sun K, Chen R, et al. Cancer incidence and mortality in China 2016. *J Natl Cancer Center*. (2022) 2(1):1–95. doi: 10.1016/j.jncc.2022.02.002

3. Miller KD, Ostrom QT, Kruchko C, Patil N, Tihan T, Cioffi G, et al. Brain and other central nervous system tumor statistics 2021. *CA.: A. Cancer J Clin* (2021) 71(5):381–4065. doi: 10.3322/caac.21693

4. Siegel RL, Miller KD, Fuchs HE, Jemal A. Cancer statistics 2022. *CA Cancer J Clin* (2022) 72(1):7–33. doi: 10.3322/caac.21708

5. Louis DN, Perry A, Wesseling P, Brat DJ, Cree IA, Figarella-Branger D, et al. The 2021 WHO classification of tumors of the central nervous system: A summary. *Neuro-Oncology* (2021) 23(8):1231–12515. doi: 10.1093/neuonc/noab106

6. Nabors LB, Portnow J, Ahluwalia M, Baehring J, Brem H, Brem S, et al. Central nervous system cancers, version 3.2020, NCCN clinical practice guidelines in oncology. *J Natl Compr Cancer Network. J Natl Compr Canc. Netw* (2020) 18(11):1537–15705. doi: 10.6004/jnccn.2020.0052

7. Gillies RJ, Kinahan PE, Hricak H. Radiomics: Images are more than pictures, they are data. *Radiology* (2016) 278(2):563–77. doi: 10.1148/radiol.2015151169

8. Bi WL, Hosny A, Schabath MB, Giger ML, Birkbak NJ, Mehrtash A, et al. Artificial intelligence in cancer imaging: Clinical challenges and applications. *CA Cancer J Clin* (2019) 69(2):127–1575. doi: 10.3322/caac.21552

9. Chang K, Bai HX, Zhou H, Su C, Bi WL, Agbodza E, et al. Residual convolutional neural network for the determination of IDH status in low- and high-grade gliomas from MR imaging. *Clin Cancer Res* (2018) 24(5):1073–81. doi: 10.1158/1078-0432.CCR-17-2236

10. Chang K, Beers AL, Bai HX, Brown JM, Ly KI, Li X, et al. Automatic assessment of glioma burden: A deep learning algorithm for fully automated volumetric and bidimensional measurement. *Neuro Oncol* (2019) 21(11):1412–22. doi: 10.1093/neuonc/noz106

11. Ye N, Yang Q, Chen Z, Teng C, Liu P, Liu X, et al. Classification of gliomas and germinomas of the basal ganglia by transfer learning. *Front Oncol* (2022) 12:844197. doi: 10.3389/fonc.2022.844197

12. Chen Z, Ye N, Jiang N, Yang Q, Wanggou S, Li X. Deep learning model for intracranial hemangiopericytoma and meningioma classification. *Front Oncol* (2022) 12:839567. doi: 10.3389/fonc.2022.839567

13. Ostrom QT, Francis SS, Barnholtz-Sloan JS. Epidemiology of brain and other CNS tumors. *Curr Neurol Neurosci Rep* (2021) 21(12):68. doi: 10.1007/s11910-021-01152-9

14. Szopa W, Burley TA, Kramer-Marek G, Kaspera W. Diagnostic and therapeutic biomarkers in glioblastoma: Current status and future perspectives. *BioMed Res Int* (2017) 2017:8013575. doi: 10.1155/2017/8013575

15. Buerki RA, Horbinski CM, Kruser T, Horowitz PM, James CD, Lukas RV. An overview of meningiomas. *Future Oncol* (2018) 14(21):2161–77. doi: 10.2217/fon-2018-0006

16. Achrol AS, Rennert RC, Anders C, Soffietti R, Ahluwalia MS, Nayak L, et al. Brain metastases. *Nat Rev Dis Primers* (2019) 5(1):5. doi: 10.1038/s41572-018-0055-y

17. Suh JH, Kotecha R, Chao ST, Ahluwalia MS, Sahgal A, Chang EL. Current approaches to the management of brain metastases. *Nat Rev Clin Oncol* (2020) 17(5):279–99. doi: 10.1038/s41571-019-0320-3

frontiers in Oncology

ORIGINAL RESEARCH
published: 18 December 2020
doi: 10.3389/fonc.2020.590083

Radiomics Approach for Prediction of Recurrence in Non-Functioning Pituitary Macroadenomas

Yang Zhang[1†], Ching-Chung Ko[2,3†], Jeon-Hor Chen[1,4], Kai-Ting Chang[1], Tai-Yuan Chen[2,5], Sher-Wei Lim[6,7], Yu-Kun Tsui[2] and Min-Ying Su[1]*

[1] Department of Radiological Sciences, University of California, Irvine, Irvine, CA, United States, [2] Department of Medical Imaging, Chi-Mei Medical Center, Tainan, Taiwan, [3] Department of Health and Nutrition, Chia Nan University of Pharmacy and Science, Tainan, Taiwan, [4] Department of Radiology, E-DA Hospital, I-Shou University, Kaohsiung, Taiwan, [5] Graduate Institute of Medical Sciences, Chang Jung Christian University, Tainan, Taiwan, [6] Department of Neurosurgery, Chi-Mei Medical Center, Chiali, Tainan, Taiwan, [7] Department of Nursing, Min-Hwei College of Health Care Management, Tainan, Taiwan

OPEN ACCESS

Edited by:
Xuejun Li,
Central South University, China

Reviewed by:
José M. Roda,
University Hospital La Paz, Spain
Lorenzo Ugga,
Federico II University Hospital, Italy
Yazhuo Zhang,
Capital Medical University, China

***Correspondence:**
Ching-Chung Ko
kocc0729@gmail.com

†These authors have contributed equally to this work

Specialty section:
This article was submitted to Neuro-Oncology and Neurosurgical Oncology, a section of the journal Frontiers in Oncology

Received: *31 July 2020*
Accepted: *19 November 2020*
Published: *18 December 2020*

Citation:
Zhang Y, Ko C-C, Chen J-H, Chang K-T, Chen T-Y, Lim S-W, Tsui Y-K and Su M-Y (2020) Radiomics Approach for Prediction of Recurrence in Non-Functioning Pituitary Macroadenomas. Front. Oncol. 10:590083. doi: 10.3389/fonc.2020.590083

Objectives: A subset of non-functioning pituitary macroadenomas (NFPAs) may exhibit early progression/recurrence (P/R) after surgical resection. The purpose of this study was to apply radiomics in predicting P/R in NFPAs.

Methods: Only patients who had undergone preoperative MRI and postoperative MRI follow-ups for more than 1 year were included in this study. From September 2010 to December 2017, 50 eligible patients diagnosed with pathologically confirmed NFPAs were identified. Preoperative coronal T2WI and contrast-enhanced (CE) T1WI imaging were analyzed by computer algorithms. For each imaging sequence, 32 first-order features and 75 texture features were extracted. Support vector machine (SVM) classifier was utilized to evaluate the importance of extracted parameters, and the most significant three parameters were used to build the prediction model. The SVM score was calculated based on the three selected features.

Results: Twenty-eight patients exhibited P/R (28/50, 56%) after surgery. The median follow-up time was 38 months, and the median time to P/R was 20 months. Visual disturbance, hypopituitarism, extrasellar extension, compression of the third ventricle, large tumor height and volume, failed optic chiasmatic decompression, and high SVM score were more frequently encountered in the P/R group ($p < 0.05$). In multivariate Cox hazards analysis, symptoms of sex hormones, hypopituitarism, and SVM score were high risk factors for P/R ($p < 0.05$) with hazard ratios of 10.71, 2.68, and 6.88. The three selected radiomics features were T1 surface-to-volume radio, T1 GLCM-informational measure of correlation, and T2 NGTDM-coarseness. The radiomics predictive model shows 25 true positive, 16 true negative, 6 false positive, and 3 false negative cases, with an accuracy of 82% and AUC of 0.78 in differentiating P/R from non-P/R NFPAs. For SVM score, optimal cut-off value of 0.537 and AUC of 0.87 were obtained for differentiation of P/R. Higher SVM scores were associated with shorter progression-free survival ($p < 0.001$).

Conclusions: Our preliminary results showed that objective and quantitative MR radiomic features can be extracted from NFPAs. Pending more studies and evidence to support the

findings, radiomics analysis of preoperative MRI may have the potential to offer valuable information in treatment planning for NFPAs.

Keywords: radiomics, MRI, pituitary, macroadenoma, recurrence

INTRODUCTION

Pituitary adenomas constitute 10–15% of all intracranial tumors (1), the majority being non-functioning pituitary adenomas (2, 3). The most common presentation is the macroadenoma, which is defined as a tumor larger than 10 mm in size. Non-functioning pituitary macroadenomas (NFPAs) may cause bitemporal hemianopia resulting from optic chiasm compression due to mass effect. Hypopituitarism is observed in some patients due to tumor compression of normal pituitary glandular tissue. According to 2017 WHO classification system, pituitary tumors are formally classified as adenoma, carcinoma, or blastoma (4). Although more than 90% of NFPAs are diagnosed as benign tumors, 25–55% of these tumors may undergo early progression/recurrence (P/R) after surgical resection (5–8). Gross-total resection (GTR) *via* a transsphenoidal approach (TSA) is the optimal method of treatment for NFPAs in current clinical practice. However, complete resection is often difficult to achieve for large solid tumor with extrasellar extension (9). Although adjuvant radiotherapy (RT) is implemented in some institutions in attempts to minimize postoperative P/R in NFPAs, this approach may result in progressive pituitary insufficiency and other long-term complications (10).

Conventional MR imaging findings such as cavernous sinus invasion, tumor size, and absence of tumor apoplexy have been reported as important parameters related to P/R in NFPAs. However, the abovementioned parameters are subjective to significant inter-observer variation (11, 12). Radiomics analysis is recently emerging as a comprehensive quantitative method for the evaluation of various clinical diseases (13–15). The extracted imaging features have been shown to reveal visually imperceptible information extending beyond radiology to histopathology. Several studies even suggest that radiomics may be able to provide valuable predictors regarding diagnosis, prognosis, and thus aid in therapeutic planning in brain tumors (13, 16–18).

In regard to the application in NFPAs, radiomics has been used in the evaluation of tumor subtypes, consistency, ki-67 proliferation indices, and cavernous sinus invasion (18–22), but rarely for the prediction of clinical outcomes (23). The purpose of this study was to investigate the role of radiomics features extracted from segmented tumor sampling for the prediction of P/R in NFPAs.

MATERIALS AND METHODS

Ethics Statement

This study was approved by our Institutional Review Board (IRB no. 10902-009). Written consent was waived because the retrospective nature of this project does not influence the health-care of the included patients. All patients' medical records and imaging documentations were anonymized and de-identified prior to analysis.

Patient Selection

The inclusion criteria of this study were patients diagnosed with benign NFPAs by pathological confirmation, complete and good imaging quality of preoperative brain MRIs, and postoperative follow-up MRIs more than 1 year after treatment. Patients with clinical, biochemical, and histopathological evidence of hormone hypersecretion were excluded. According to studies by Brochier et al. (11) and Hong et al. (24), diagnosis of prolactinoma is considered unlikely if the prolactin levels were below 100 mg/L, a conclusion thereafter confirmed by immunocytochemical studies. Patients who received postoperative adjuvant RT before P/R were also excluded. From September 2010 to December 2017, 50 patients (29 men, 21 women, age 19–80 years; median age, 52 years) were identified for this study in accordance with the abovementioned inclusion and exclusion criteria. Forty-eight patients underwent surgery performed by TSA, and craniotomy was performed in two patients due to large tumor sizes. The median follow-up duration for all patients was 38 months (range from 12 to 115 months). In 28 patients with P/R, the median time to P/R was 20 months (range from 6 to 67 months). Clinical and biochemical data were also obtained from medical records.

Extent of Resection and Progression/Recurrence

The extent of surgical resection was determined by review of postoperative MRI by a neuroradiologist (C-CK) and a neurosurgeon (S-WL). According to published literature (25), GTR was defined as lesion resection with a residual tumor volume of less than 10% of its original size. In contrast, subtotal tumor resection (STR) was defined as the presence of residual lesion more than 10% of its original volume. For determining P/R in NFPAs, pretreatment and postoperative MR images were evaluated by two experienced neuroradiologists (C-CK with 6 years of experience and T-YC with 18 years of experience), both of whom were blinded to the clinical and imaging outcomes of the studied population. P/R was defined as tumor recurrence after GTR or enlargement of residual tumor after STR observed on postoperative contrast-enhanced (CE) T1WI. The threshold of P/R was defined as a more than 2-mm increase in size of residual tumor in at least one dimension when compared with postoperative MRI studies (11, 26). Inter-observer reliability in the determination of P/R was obtained *via* a Cohen k value of 0.9. In equivocal cases, judgment was made *via* consensus. On preoperative MR images, cavernous sinus invasion (Knosp classification) (27) and extrasellar

extension (Hardy's classification) (28) were determined on coronal T2WI and CE T1WI.

Imaging Acquisition

Preoperative brain MRI images were acquired with a 1.5-T (Siemens, MAGNETOM Avanto) (n = 19), 1.5-T (GE Healthcare, Signa HDxt) (n = 17), or a 3-T (GE Healthcare, Discovery MR750) (n = 14) MR scanner equipped with eight-channel head coils in each machine. Scanning protocols include axial and sagittal spin echo T1-weighted imaging (T1WI), axial and coronal fast spin echo T2- weighted imaging (T2WI), axial fluid attenuated inversion recovery (FLAIR), and axial T2*-weighted gradient-recalled echo (GRE). Dynamic contrast-enhanced (CE) coronal T1WI images with a small field of view through the pituitary gland as well as coronal and sagittal CE T1WI with fat saturation were performed after intravenous administration of 0.1 mmol/kg of body weight of gadobutrol or gadoterate meglumine. Detailed imaging parameters in the MR scanners were described in **Supplementary File 1**.

Tumor Segmentation

Because both T2WI and CE T1WI are associated with cavernous sinus invasion, histopathologic subtypes, tumor consistency, and therapeutic response in pituitary tumors (18, 19, 21, 29–31), they were analyzed in our study. **Figure 1** shows the flowchart in the process of analysis. Tumor segmentation was performed on coronal CE T1WI with MATLAB 2018b software (32). In image pre-processing, the slices were resampled to isotropic 3D rendering. Then the pixel intensities inside the 3D rendered ROIs were normalized to mean of 0 and standard deviation of 1. For each lesion, the operator places an initial rectangular region of interest (ROI) on the image to locate the tumor as well as select the beginning and ending slices containing the lesion. Subsequently, the fuzzy c-mean (FCM) clustering algorithm was applied to segment the lesion ROI on each image slice (33). In cases of under- or over-segmentation, manual correction was performed. After segmentation/correction was performed, the ROIs from all imaging slices containing the particular tumor were combined. The 3D connected-component labeling was then applied to remove scattered voxels not connected to the main lesion. The hole-filling algorithm was applied to include all voxels contained within the main ROI labeled as non-lesion. The segmented tumor mask was transferred onto corresponding coronal T2WI by using affine transformation with linear interpolation. This process was conducted by FMRIB's Linear Image Registration Tool (FLIRT) (34).

Texture Feature Extraction and Selection

Within segmented tumor on CE T1WI and T2WI, 107 imaging features, including 32 first order features and 75 textural features were extracted on each modality by Python 3.75 software (35) (**Figure 1**). Filters were not used in the feature extraction process. Because some small NFPAs may be inseparable from surrounding normal pituitary tissue, boundary pixels of tumor masks on each slice were removed by binary erosion to ensure only tumorous tissues were included in the ROI (32). Lengths of 0.25 and 0.5 cm were used to determine the outer shells of the boundary pixels to be removed. Therefore, three tumor ROIs were obtained: original masks, original mask with 0.25 cm erosion, and original mask with 0.5 cm erosion. For each of the abovementioned tumor ROIs, a total of 214 features were extracted from CE T1WI and T2WI.

To evaluate the importance of these features in the differentiation between patients with and without P/R, the sequential feature selection process was implemented *via* constructing multiple support vector machine (SVM) classifiers by MATLAB 2018b software (32). In this process, SVM with Gaussian kernel was used as the objective function to test the performance of models built with a subset of features (36, 37). In the beginning, an empty candidate set was presented, and features were sequentially added. The 10-fold cross validation method was applied to test the model performance (38). For each iteration, the training process was repeated 1,000 times to explore the robustness of each feature. At the conclusion of each iteration, the feature which results in the best performance

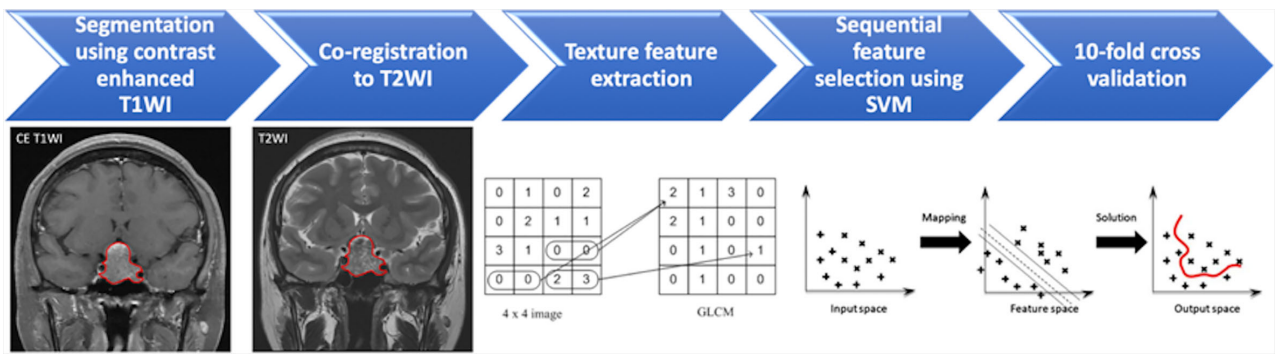

FIGURE 1 | Flowchart of the analytical process for prediction of progression/recurrence (P/R) in non-functioning pituitary macroadenomas (NFPAs). The NFPA (red outline) is segmented on coronal contrast-enhanced (CE) T1WI and then mapped to the coronal T2WI. On each set of images, a total of 107 imaging features, including 32 first order features and 75 textural features, are extracted. The most important three features are selected by sequential feature selection and support vector machine (SVM) classifiers to build the prediction model. A 10-fold cross validation method is applied to test the model performance.

was added into the candidate set. In this instance, we use 10^{-6} as the termination tolerance for the objective function value. Once the addition of features no longer meets the criterion, cessation of the selection process ensues.

Besides, the SVM score was calculated for each patient based on the selected features as described below.

$$f(x) = \sum_{n=1}^{N} w_n y_n G(x_n, x) + b$$

where x was the input features, N was the length of support vector. y_n and x_n were the entries of the supporting vector. Wn was the parameter and b was the bias. $G(x_n, x)$ was the Gaussian kernel function which indicated the dot product in the predictor space between x and the support vectors (33). Here,

$$G(x_n, x) = e^{-\|x_n - x\|^2}$$

Statistical Analysis

Statistical analyses were performed using SPSS for Windows (V.24.0, IBM, Chicago, IL, USA). For the evaluation of clinical parameters and conventional MR imaging, Chi-square (or Fisher exact test) and Mann-Whitney U tests were performed for categorical and continuous data, respectively. The true positive (TP), true negative (TN), false positive (FP), false negative (FN), accuracy, and area under the receiver operating characteristic curve (ROC) curve (AUC) in prediction models of different tumor masks were calculated. ROC analysis of SVM scores was performed to obtain the optimal cut-off value. Further, Kaplan-Meier analysis based on cut-off value of SVM score was used to evaluate the progression-free survival (PFS), and log-rank test was used to assess the significance. Cox proportional hazard model with univariate and multivariate analysis was performed to determine independent predictors of P/R. Variables with a $p < 0.05$ in univariate analysis were brought forward to the multivariate analysis. For multivariate analyses and all other statistical analyses, $p < 0.05$ were considered statistically significant.

RESULTS

Clinical Data and Conventional MRI Findings

The clinical data and conventional MRI findings were summarized in **Table 1**. P/R was diagnosed in twenty-eight (28/50, 56%) patients. No statistical difference was found between the extent of tumor resection and P/R ($p = 0.157$). Visual disturbance, hypopituitarism, extrasellar extension, compression of the 3rd ventricle, large tumor height and volume, and high SVM score were more frequently observed in the P/R group ($p < 0.05$) (**Figure 2**). In multivariate Cox proportional hazards analysis (**Table 2**), symptoms of sex hormones, hypopituitarism, and SVM score were high risk factors for P/R ($p < 0.05$) with hazard ratios of 10.71, 2.68, and 6.88.

TABLE 1 | The clinical data and conventional MR imaging of non-functioning pituitary macroadenomas (NFPAs) with and without progression/recurrence (P/R).

	P/R	Non-P/R	p
Number of patients	28	22	
Sex			0.111
Male	19 (67.9%)	10 (45.5%)	
Female	9 (32.1%)	12 (54.5%)	
Age (y)	53.5 (44, 63)	42 (23.5, 60.5)	0.089
Clinical symptoms			
Visual disturbance	26 (92.9%)	13 (59.1%)	0.006*
Headache	8 (28.6%)	11 (50%)	0.121
Symptoms of sex hormones (decreased libido, sexual dysfunction, and/or amenorrhea/ oligomenorrhea)	5 (17.9%)	1 (4.5%)	0.211
Incidental	2 (7.1%)	4 (18.2%)	0.385
Hypopituitarism			0.047*
No	12 (42.9%)	17 (77.3%)	
Single	8 (28.6%)	3 (13.6%)	
Multiple	8 (28.6%)	2 (9.1%)	
Hyperprolactinemia	10 (35.7%)	6 (27.3%)	0.525
Extent of surgical resection			0.157
Gross-total resection (GTR)	3 (10.7%)	6 (27.3%)	
Gross-total resection (STR)	25 (89.3%)	16 (72.7%)	
Successful chiasmatic decompression	9 (32.1%)	17 (77.3%)	0.002*
Cavernous sinus invasion (Knosp classification)			0.077
Grade 1–2	18 (64.3%)	19 (86.4%)	
Grade 3–4	10 (35.7%)	3 (13.6%)	
Extrasellar extension (Hardy's classification)			0.045*
Grade 1–2	17 (60.7%)	19 (86.4%)	
Grade 3–4	11 (39.3%)	3 (13.6%)	
Compression of optic chiasm	27 (96.4%)	17 (77.3%)	0.075
Compression of the third ventricle	21 (75%)	9 (40.9%)	0.015*
Hydrocephalus	2 (7.1%)	1 (4.5%)	1
Giant (>40 mm)	9 (32.1%)	2 (9.1%)	0.085
Maximum tumor height (mm)	35.5 (27.5, 43.5)	18 (10, 26)	<0.001*
Tumor volume (cm^3)	12.3 (4.4, 20.1)	2.7 (1.2, 8)	<0.001*
SVM score	0.999 (0.960, 1.040)	0.030 (–0.241, 0.301)	<0.001*

Continuous variables were presented as median and interquartile range (IQR).
**Statistical difference (p < 0.05).*

Radiomics Approach for Prediction of P/R

In radiomics analyses, the most important three parameters selected by the final SVM model for the prediction of P/R were: T1 surface-to-volume radio, T1 GLCM-informational measure of correlation, and T2 NGTDM-coarseness, and all show significant differences (Mann-Whitney U test) (**Figure 3**). The reproducibility of ROI-based radiomics feature was good between two readers, and the intra-class correlation coefficients

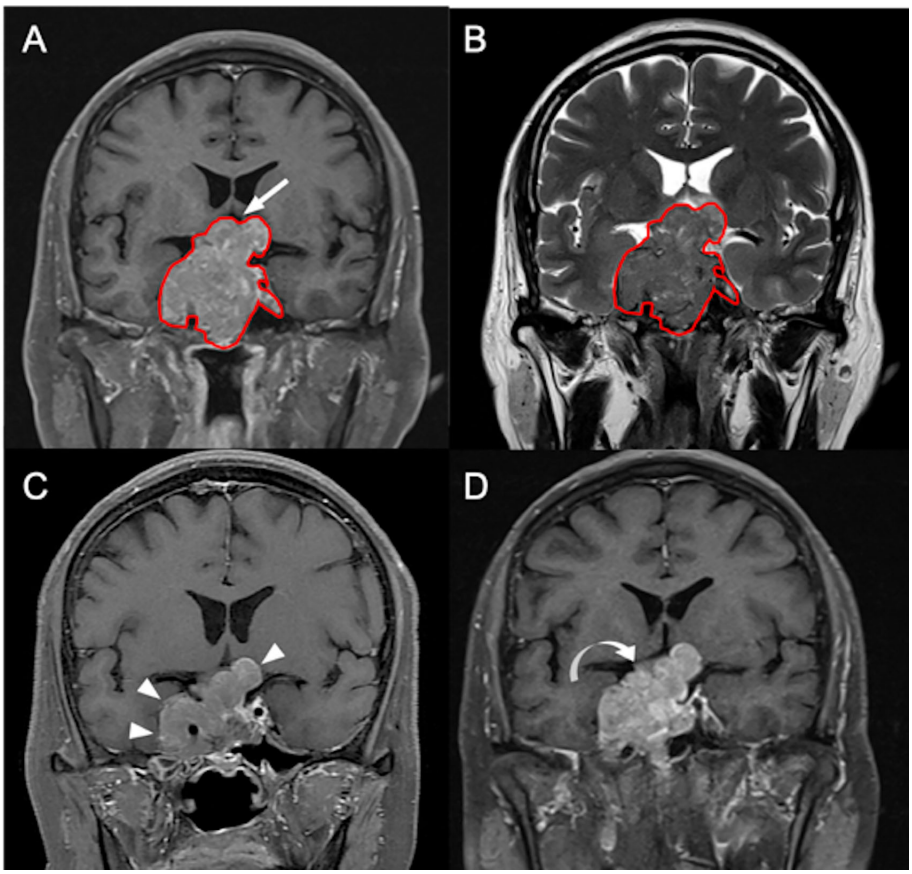

FIGURE 2 | A 55-year-old male patient with left hemianopia and pathologically confirmed NFPA. **(A)** Coronal CE T1WI shows an enhancing sellar tumor (red outline) with upward suprasellar extension and bilateral cavernous sinus invasion, causing compression of the optic chiasm and the third ventricle (arrow indicates area of optic chiasm and third ventricle). **(B)** The tumor (red outline) is segmented on coronal CE T1WI **(A)** and then mapped to the coronal T2WI **(B)**. **(C)** Improvement of blurred vision after subtotal tumor resection *via* transsphenoidal approach is clinically documented, and the maximum height of the residual tumor (arrowheads) measured from coronal CE T1WI is 38 mm. **(D)** Recurrent visual deterioration with enlargement of the residual tumor (curved arrow) with maximum height up to 48 mm is observed 19 months after surgical resection.

(ICCs) of the three imaging features were 0.90, 0.80, and 0.87 respectively.

The SVM classification results by the original mask shows 25 TP, 16 TN, 6 FP, and 3 FN cases (**Figure 4**) with accuracy of 82% and AUC of 0.78 (**Table 3**). The optimal cut-off value of SVM score for differentiation of P/R was 0.537, with AUC of 0.87 (**Figure 5**). When tumor progression trends were compared, patients with high SVM score (more than the cut-off value of 0.537) were found to exhibit shorter PSF ($p < 0.001$) (**Figure 5**).

DISCUSSION

In this study, we developed a radiomics model to predict P/R in NFPAs. Three tumor ROIs, including the original mask and mask with binary erosions, were used. Three features were selected by SVM algorithm to build the final predication model: two from CE T1WI and one from T2WI. The overall accuracy was 82% with AUC of 0.78, and there was no significant difference amongst the three tumor ROIs methods. This study also calculated SVM score for prediction of P/R in NFPAs, and patients with higher SVM score were found to exhibit shorter PSF. In multivariate Cox hazards analysis, symptoms of sex hormones, hypopituitarism, and SVM score were high risk factors of P/R in NFPAs.

Although more than 90% of NFPAs are benign according to the 2017 WHO classification system (4), 25–55% may exhibit early P/R within 5 years after surgical resection (5–8). The Ki-67 index, mitotic count, and tumor invasion are all associated with aggressive clinical behavior in NFPAs (4). However, the invasive growth of NFPAs is not clearly defined in the WHO criteria, and it is usually underestimated if the corresponding information from MR imaging is not taken into consideration (8). A meta-analysis including 143 studies by Roelfsema et al. (8) showed that postoperative hormone concentration is an important predictor for P/R in functioning pituitary adenomas, but no specific factor is found for NFPAs.

Recently, low apparent diffusion coefficient (ADC) on diffusion-weight MR imaging (DWI), indicating a higher

TABLE 2 | Cox proportional hazards analysis for P/R.

	Univariate Analysis		Multivariate Analysis	
	HR (95% CI) for P/R	***p***	**HR (95% CI) for P/R**	***p***
Sex (fraction male)	1.980 (0.861, 4.551)	0.108		
Age (years)	1.020 (0.996, 1.045)	0.098		
Visual disturbance	3.378 (0.797, 14.311)	0.098		
Headache	0.825 (0.361, 1.889)	0.649		
Symptoms of sex hormones	5.792 (2.000, 16.777)	0.001*	10.713 (2.884, 39.800)	< 0.001*
Incidental	0.642 (0.152, 2.721)	0.548		
Hypopituitarism	2.772 (1.27, 6.052)	0.01*	2.680 (1.121, 6.49)	0.027*
Hyperprolactinemia	1.162 (0.504, 2.679)	0.724		
Non-GTR	1.311 (0.389, 4.418)	0.662		
Successful chiasmatic decompression	0.400 (0.180, 0.888)	0.024*	1.012 (0.404, 2.537)	0.979
Cavernous sinus invasion (Knosp grades 3–4)	1.460 (0.647, 3.295)	0.363		
Extrasellar extension (Hardy's grade 3–4)	1.728 (0.792, 3.768)	0.169		
Compression of optic chiasm	3.354 (0.454, 24.766)	0.236		
Compression of the third ventricle	1.769 (0.74, 4.228)	0.199		
Hydrocephalus	2.117 (0.483, 9.275)	0.32		
Giant NFPA (>40 mm)	2.964 (1.277, 6.883)	0.011*	2.061 (0.562, 7.560)	0.276
Maximum tumor height (mm)	1.164 (1.046, 1.296)	0.005*	1.060 (0.889, 1.264)	0.518
Tumor volume (cm^3)	1.031 (1.011, 1.051)	0.002*	0.988 (0.954, 1.024)	0.506
SVM score	10.037 (2.252, 44.740)	0.002*	6.879 (1.328, 35.621)	0.022*

**Statistical difference ($p < 0.05$).*

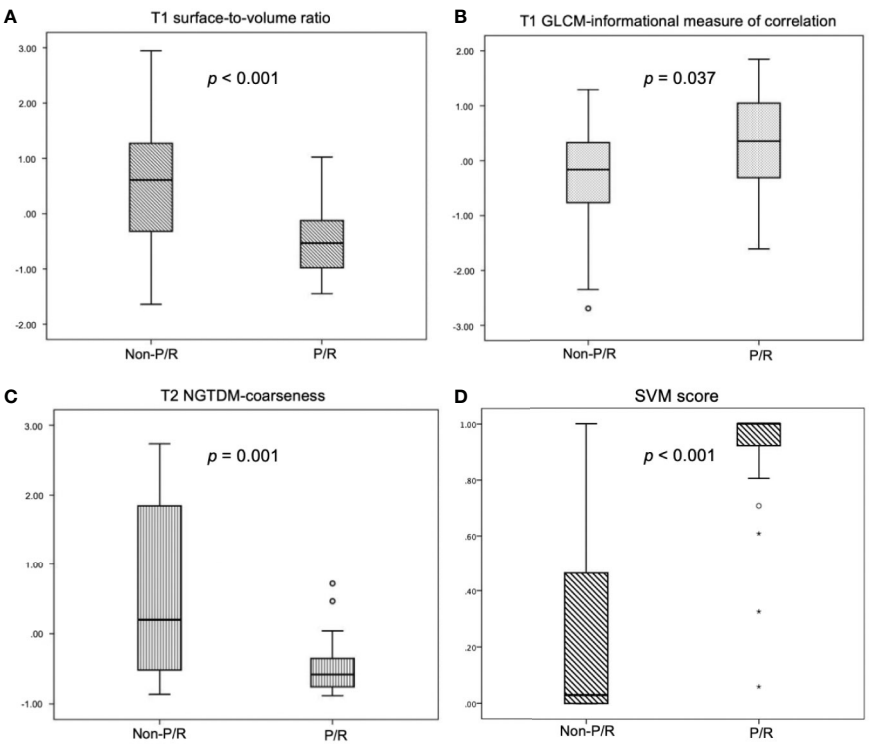

FIGURE 3 | Box plot of **(A)** T1 surface-to-volume ratio, **(B)** T1 GLCM-informational measure of correlation, **(C)** T2 NGTDM-coarseness, and **(D)** SVM score for prediction of P/R in NFPAs. Statistically significant differences ($p < 0.05$) (Mann-Whitney U test) in the selected features and SVM score are observed. Boxes indicate the interquartile range (IQR), and whiskers indicate the range. The horizontal line represents the median in each box. Circles represent outliers, which are defined as distances greater than 1.5 times the IQR below the first quartile or above the third quartile. Stars represent extreme values, defined as distances greater than three times the IQR below the first quartile.

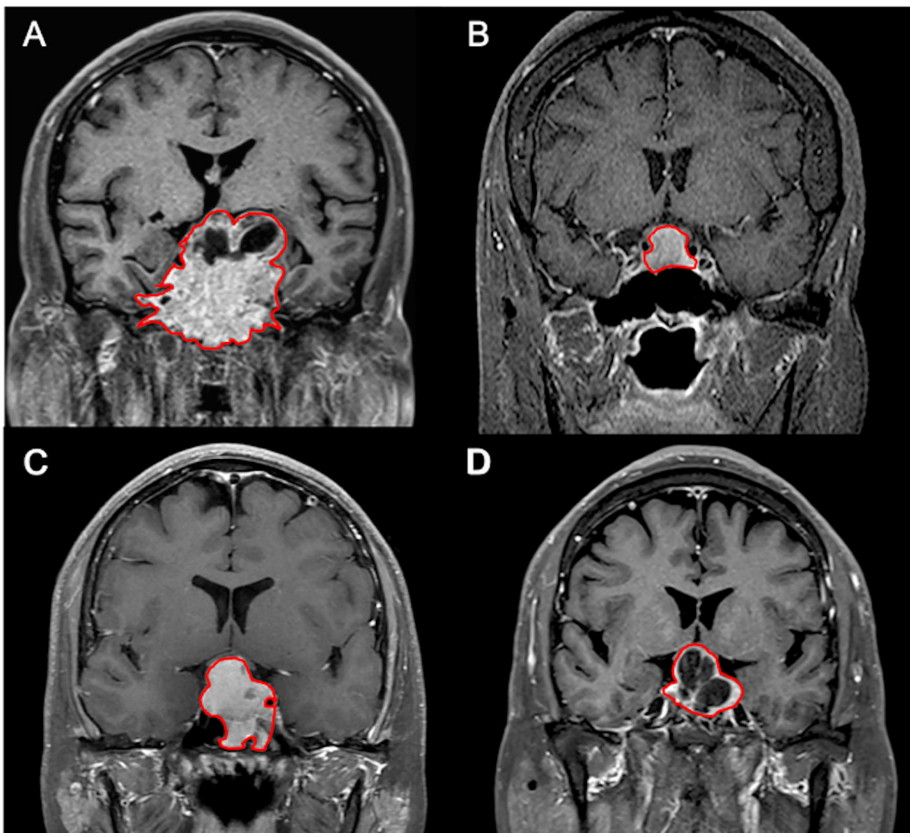

FIGURE 4 | Examples of NFPAs (red outline) on coronal CE T1WI showing **(A)** true positive (TP), **(B)** true negative (TN), **(C)** false positive (FP), and **(D)** false negative (FN) results in the prediction model. **(A)** In the TP group, larger tumor sizes with more surrounding bone invasion are observed. **(B)** In contrast, smaller tumor sizes without bone invasion are found in most TN cases. **(C)** Most FP cases showed relatively homogeneous contrast enhancement without apoplexy or cystic change. **(D)** Two of the three FN cases exhibit macrocystic components or apoplexy.

TABLE 3 | Performance in prediction models with and without binary erosions.

	TP	TN	FP	FN	Accuracy	AUC
Original mask	25	16	6	3	82%	0.78
With 0.25 *cm* erosion	24	16	6	4	80%	0.80
With 0.5 *cm* erosion	24	17	5	4	82%	0.79

cellular density, is reported to be associated with tumor progression in NFPAs (26, 39). However, the ADC values may be affected by susceptibility artifacts from blood products because of apoplexy or necrosis; therefore, they could only be measured for solid NFPAs without hemorrhage or cystic changes (9, 26, 40). The radiomics analysis can be applied to the whole tumor to obtain reproducible, objective, and quantitative data from different imaging sequences, thus providing a more comprehensive method in the approach of various acquired information (13–15). For application of radiomics in pituitary tumors, Saha et al. (41) reported a review article including 16 studies from the past 10 years (2009–2019). Ten of these studies were undertaken from 2018 to 2019, most of which utilized single-centered, retrospective data, semi-automatic pipelines, and binary classifications as in our study. Zhang et al. (19) applied preoperative radiomics to distinguish null cell adenomas from other subtypes in NFPAs with AUC of 0.8 to 0.83. Rui et al. (18), Zeynalova et al. (31), and Cuocolo et al. (42) used preoperative radiomics texture and histogram analysis to predict consistency in pituitary macroadenomas with AUCs of 0.836, 0.71, and 0.99 respectively. Fan et al. (20, 29) and Kocak et al. (30) used radiomics to predict response to radiotherapy and somatostatin analogues in acromegaly with AUCs of 0.96 and 0.845 respectively. Niu et al. (21) used radiomics to predict cavernous sinus invasion in NFPAs with AUC of 0.826 to 0.852. An SVM or radiomics score is a novel concept in clinical applications. An individualized SVM (radiomics) score could be calculated based on selected features (43–45). Xu et al. (43) used SVM score to preoperative lymph node metastasis in intrahepatic cholangiocarcinoma, with AUC of 0.87. Liu et al. (44) reported excellent performance in SVM score for prediction of treatment response in locally advanced rectal cancer, with AUC of 0.98. Park et al. (45) reported radiomics score improved the performance in MR prognostic model for glioblastoma. Zheng et al. (46) reported radiomics score is an independent prognostic factor for the postoperative outcome in solitary hepatocellular carcinoma. These studies suggest that radiomics

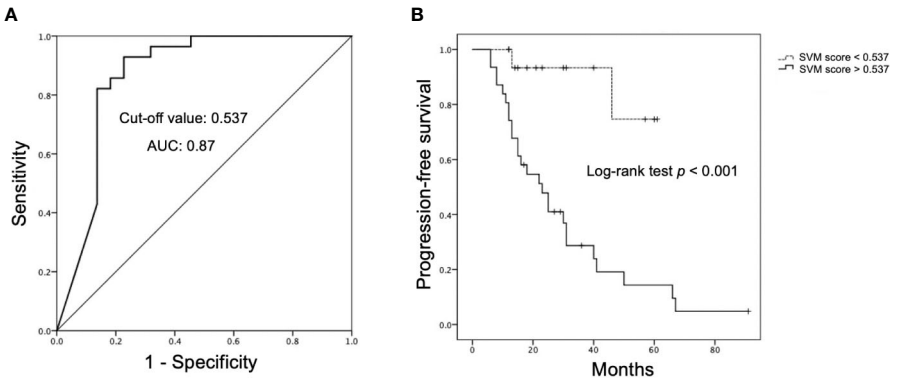

FIGURE 5 | Receiver operating characteristic (ROC) and Kaplan-Meier survival curves of SVM score. **(A)** ROC curve of SVM score for prediction of P/R in NFPAs, with optimal cut-off value of 0.537 and AUC of 0.87. **(B)** Kaplan-Meier survival curves showing significant difference ($p < 0.05$) (Log-tank test) in overall trend of progression-free survival based on cut-off value of SVM score.

features might be a useful tool in predicting recurrences in NFPAs, but no reports regarding this concept have been published as of yet.

To the best of our knowledge, preoperative radiomics approach for prediction of P/R in NFPAs is rarely reported. The SVM algorithm was utilized for feature selection and classification in this study. Three selected features were T1 surface-to-volume ratio, T1 GLCM-informational measure of correlation, and T2 NGTDM-coarseness. The surface-to-volume ratio is a shape index related to tumor infiltration. T1 GLCM-information measure of correlation is a texture feature related to the joint probability occurrence of the pixel pairs entropy. If the distribution of the intensities is more homogeneous, the value of this feature can be higher. T2 NGTDM-coarseness is an inverse measure of the level of the spatial rate of change in intensity. A higher value indicates a lower spatial change rate and a locally more uniform texture (47). In this study, three ROI methods were implemented, including the original tumor mask and two masks with differential erosion of the boundary pixels. The goal was to evaluate whether the potential inclusion of normal pituitary glandular tissue and other surrounding, non-tumorous structures would affect the prediction. The obtained results, however, turned out to be similar. One possible reason was that the eroded pixels were minimal compared to the whole tumor mask, thus accounting for the minimal overall effects on produced results.

In recent years, study of computer-extracted imaging radiomic features has become an active research field. However, the robustness and reproducibility of the selected quantitative imaging features need to be extensively studied before their clinical applications. Factors affecting the robustness of radiomic approach are modality dependent. So far only few studies have investigated the robustness of radiomic features in MRI (48–51). How different imaging sequences and imaging parameters will affect the reproducibility of radiomic features is still not clearly known. A recent phantom study noted that remarkable differences exist among different MRI sequences in the number of robust and reproducible features (52). Nevertheless, more than 30% (15 of 45) features still showed excellent robustness across all sequences and demonstrate excellent reproducibility. It was supposed that these 15 features can reliably be applied for the design of radiomics signatures within clinical studies. Among these features, the shape-related feature was noted to be robust. Another study of repeatability and reproducibility of MRI-based radiomic features also showed that shape features emerged as the most stable features among all the selected features (53). It was suggested that radiomics extracted from T1W and T2W imaging should be used with caution, and only robust and reproducible features should be selected for building a radiomics signature (52). However, it was also true that through fully automatic image segmentation as our study did, the effect of operators' dependent bias of radiomic features can be reduced (52).

There were 41 true and 9 false predictions using the model developed with the original tumor mask. For most TP and FN cases, large tumor sizes with heterogeneous enhancement and surrounding bone invasion were observed. In contrast, small tumor sizes without bone invasion were found in most TN cases. Homogeneous contrast enhancement without apoplexy or cystic change was observed in most FP cases. Based on our results, macrocystic components or apoplexy may be an important factor leading to FN. Further studies involving a larger sample size is necessary to establish a better understanding regarding factors related to true and false predictions.

It is known that the extent of tumor resection is an important determining factor affecting recurrence rates in NFPAs (11). Although no statistical difference is demonstrated between GTR and P/R in our study, it may be due to the relatively small sample size. In our study, tumor recurrence was present in three patients despite having undergone GTR. In contrast, stable disease was observed in 16 patients after receiving STR only. Since most NFPAs are benign tumors, preoperative prediction of P/R in NFPAs offers clinically valuable information regarding treatment options. On the other hand, a significant correlation between the number of surgical resections and complication rates in NFPAs is reported (54). Anterior pituitary insufficiency and diabetes

insipidus are the most commonly encountered postoperative complications in NFPAs with occurrence rates of 19.4 and 17.8% respectively (54). For patients with high possibilities of tumor recurrence, aggressive resection combined with postoperative adjuvant RT and close MR imaging follow-up should be considered. In contrast, for patients with lower possibilities of disease recurrence, the aim of surgery would be to relieve clinical symptoms by decreasing tumor mass effects. Optimal surgical planning for low risk patients could reduce potential complications of endocrine disorders while maintaining a good treatment outcome.

It is known that postoperative adjuvant RT offers excellent tumor control in 96% of patients with non-secreting adenomas (55). However, whether postoperative RT is beneficial for patients with low possibility of recurrence is controversial because RT may increase risks of complications such as visual deterioration, hypopituitarism, cerebrovascular accident, and dementia in NFPAs (55, 56). Because adjuvant RT may affect the independent predictive value of the preoperative MR radiomics analysis for P/R, patients who have received adjuvant RT before P/R were excluded from our study.

The study had several limitations. Selection bias may exist due to its retrospective nature. All MR images were acquired at a single site with a single protocol, and lack of external validation. Future testing with multi-institutional data and varying imaging protocols is necessary to determine whether the trained classifier is generalizable. Due to the relatively small sample size, only a few imaging features can be selected to build the classification model in order to avoid over-fitting. More advanced statistical analysis methods that can take all clinical and imaging factors into account need to be considered in the future. When more cases become available, other machine learning strategies, such as a fully automatic convolutional neural network able to perform end-to-end learning may be applied to improve the performance of prediction.

CONCLUSIONS

In summary, our preliminary study of MR radiomics analyses based on CE T1WI and T2WI in preoperative MRI was able to achieve an accuracy of 82% and AUC of 0.78 in predicting recurrence in NFPAs. For SVM score based on selective features, an AUC of 0.87 was obtained in differentiation of P/R. The features extracted based on automatic segmentation and imaging registration were objective and quantitative. Because the robustness and reproducibility of MR radiomic features may be affected by imaging sequences and imaging parameters, more studies in this field are needed to know which reproducible radiomic features can be consistently used across imaging sequences and different institutions. The results in our study offer useful clinical information to aid in the preoperative as well as postoperative planning in the management of NFPAs, such as the extent of surgical resection, implementation of postoperative adjuvant RT, and the time interval of MR imaging follow-up. Nevertheless, this approach still needs to be validated with a larger-scale study and long-term follow-up.

DATA AVAILABILITY STATEMENT

The original contributions presented in the study are included in the article/**Supplementary Material**. Further inquiries can be directed to the corresponding author.

ETHICS STATEMENT

The studies involving human participants were reviewed and approved by Chi Mei Medical Center Institutional Review Board (IRB no. 10902-009). Written informed consent for participation was not required for this study in accordance with the national legislation and the institutional requirements.

AUTHOR CONTRIBUTIONS

Conceived and designed the experiments: C-CK, J-HC. Performed the experiments: C-CK, YZ. Analyzed the data: C-CK, YZ, J-HC, K-TC, T-YC, S-WL. Contributed reagents/materials/analysis tools: T-YC, Y-KT. Wrote the paper: C-CK, YZ. Critically revised the article: J-HC, M-YS. All authors contributed to the article and approved the submitted version.

SUPPLEMENTARY MATERIAL

The Supplementary Material for this article can be found online at: https://www.frontiersin.org/articles/10.3389/fonc.2020.590083/full#supplementary-material

REFERENCES

1. Sivakumar W, Chamoun R, Nguyen V, Couldwell WT. Incidental pituitary adenomas. *Neurosurgical Focus* (2011) 31(6):E18. doi: 10.3171/2011.9.Focus11217
2. Greenman Y, Stern N. Non-functioning pituitary adenomas. *Best Pract Res Clin Endocrinol Metab* (2009) 23(5):625–38. doi: 10.1016/j.beem.2009.05.005
3. Molitch ME. Nonfunctioning pituitary tumors and pituitary incidentalomas. *Endocrinol Metab Clinics North Am* (2008) 37(1):151–71, xi. doi: 10.1016/j.ecl.2007.10.011
4. Lloyd RV, Osamura RY, Klöppel G, Rosai J. *WHO Classification of Tumours of Endocrine Organs, 4th ed.* Lyon: World Health Organization Press (2017).
5. Dekkers OM, Hammer S, de Keizer RJ, Roelfsema F, Schutte PJ, Smit JW, et al. The natural course of non-functioning pituitary macroadenomas. *Eur J Endocrinol* (2007) 156(2):217–24. doi: 10.1530/eje.1.02334
6. Ferrante E, Ferraroni M, Castrignano T, Menicatti L, Anagni M, Reimondo G, et al. Non-functioning pituitary adenoma database: a useful resource to improve the clinical management of pituitary tumors. *Eur J Endocrinol* (2006) 155(6):823–9. doi: 10.1530/eje.1.02298

7. O'Sullivan EP, Woods C, Glynn N, Behan LA, Crowley R, O'Kelly P, et al. The natural history of surgically treated but radiotherapy-naive nonfunctioning pituitary adenomas. *Clin Endocrinol* (2009) 71(5):709–14. doi: 10.1111/j.1365-2265.2009.03583.x
8. Roelfsema F, Biermasz NR, Pereira AM. Clinical factors involved in the recurrence of pituitary adenomas after surgical remission: a structured review and meta-analysis. *Pituitary* (2012) 15(1):71–83. doi: 10.1007/s11102-011-0347-7
9. Boxerman JL, Rogg JM, Donahue JE, Machan JT, Goldman MA, Doberstein CE. Preoperative MRI evaluation of pituitary macroadenoma: imaging features predictive of successful transsphenoidal surgery. *AJR Am J Roentgenol* (2010) 195(3):720–8. doi: 10.2214/ajr.09.4128
10. Snead FE, Amdur RJ, Morris CG, Mendenhall WM. Long-term outcomes of radiotherapy for pituitary adenomas. *Int J Radiat Oncol Biol Phys* (2008) 71(4):994–8. doi: 10.1016/j.ijrobp.2007.11.057
11. Brochier S, Galland F, Kujas M, Parker F, Gaillard S, Raftopoulos C, et al. Factors predicting relapse of nonfunctioning pituitary macroadenomas after neurosurgery: a study of 142 patients. *Eur J Endocrinol* (2010) 163(2):193–200. doi: 10.1530/eje-10-0255
12. Losa M, Mortini P, Barzaghi R, Ribotto P, Terreni MR, Marzoli SB, et al. Early results of surgery in patients with nonfunctioning pituitary adenoma and analysis of the risk of tumor recurrence. *J Neurosurg* (2008) 108(3):525–32. doi: 10.3171/jns/2008/108/3/0525
13. Zhou M, Scott J, Chaudhury B, Hall L, Goldgof D, Yeom KW, et al. Radiomics in Brain Tumor: Image Assessment, Quantitative Feature Descriptors, and Machine-Learning Approaches. *AJNR Am J Neuroradiol* (2018) 39(2):208–16. doi: 10.3174/ajnr.A5391
14. Huang YQ, Liang CH, He L, Tian J, Liang CS, Chen X, et al. Development and Validation of a Radiomics Nomogram for Preoperative Prediction of Lymph Node Metastasis in Colorectal Cancer. *J Clin Oncol* (2016) 34(18):2157–64. doi: 10.1200/jco.2015.65.9128
15. Wu J, Aguilera T, Shultz D, Gudur M, Rubin DL, Loo BWJr., et al. Early-Stage Non-Small Cell Lung Cancer: Quantitative Imaging Characteristics of (18)F Fluorodeoxyglucose PET/CT Allow Prediction of Distant Metastasis. *Radiology* (2016) 281(1):270–8. doi: 10.1148/radiol.2016151829
16. Park YW, Han K, Ahn SS, Choi YS, Chang JH, Kim SH, et al. Whole-Tumor Histogram and Texture Analyses of DTI for Evaluation of IDH1-Mutation and 1p/19q-Codeletion Status in World Health Organization Grade II Gliomas. *AJNR Am J Neuroradiol* (2018) 39(4):693–8. doi: 10.3174/ajnr.A5569
17. Park YW, Oh J, You SC, Han K, Ahn SS, Choi YS, et al. Radiomics and machine learning may accurately predict the grade and histological subtype in meningiomas using conventional and diffusion tensor imaging. *Eur Radiol* (2018) 29(8):4068–76. doi: 10.1007/s00330-018-5830-3
18. Rui W, Wu Y, Ma Z, Wang Y, Wang Y, Xu X, et al. MR textural analysis on contrast enhanced 3D-SPACE images in assessment of consistency of pituitary macroadenoma. *Eur J Radiol* (2019) 110:219–24. doi: 10.1016/j.ejrad.2018.12.002
19. Zhang S, Song G, Zang Y, Jia J, Wang C, Li C, et al. Non-invasive radiomics approach potentially predicts non-functioning pituitary adenomas subtypes before surgery. *Eur Radiol* (2018) 28(9):3692–701. doi: 10.1007/s00330-017-5180-6
20. Fan Y, Hua M, Mou A, Wu M, Liu X, Bao X, et al. Preoperative Noninvasive Radiomics Approach Predicts Tumor Consistency in Patients With Acromegaly: Development and Multicenter Prospective Validation. *Front Endocrinol (Lausanne)* (2019) 10:403. doi: 10.3389/fendo.2019.00403
21. Niu J, Zhang S, Ma S, Diao J, Zhou W, Tian J, et al. Preoperative prediction of cavernous sinus invasion by pituitary adenomas using a radiomics method based on magnetic resonance images. *Eur Radiol* (2019) 29(3):1625–34. doi: 10.1007/s00330-018-5725-3
22. Ugga L, Cuocolo R, Solari D, Guadagno E, D'Amico A, Somma T, et al. Prediction of high proliferative index in pituitary macroadenomas using MRI-based radiomics and machine learning. *Neuroradiology* (2019) 61(12):1365–73. doi: 10.1007/s00234-019-02266-1
23. Galm BP, Martinez-Salazar EL, Swearingen B, Torriani M, Klibanski A, Bredella MA, et al. MRI texture analysis as a predictor of tumor recurrence or progression in patients with clinically non-functioning pituitary adenomas. *Eur J Endocrinol* (2018) 179(3):191–8. doi: 10.1530/eje-18-0291
24. Hong JW, Lee MK, Kim SH, Lee EJ. Discrimination of prolactinoma from hyperprolactinemic non-functioning adenoma. *Endocrine* (2010) 37(1):140–7. doi: 10.1007/s12020-009-9279-7
25. Wang S, Lin S, Wei L, Zhao L, Huang Y. Analysis of operative efficacy for giant pituitary adenoma. *BMC Surg* (2014) 14:59. doi: 10.1186/1471-2482-14-59
26. Ko CC, Chen TY, Lim SW, Kuo YT, Wu TC, Chen JH. Prediction of recurrence in solid nonfunctioning pituitary macroadenomas: additional benefits of diffusion-weighted MR imaging. *J Neurosurg* (2019) 132(2):351–9. doi: 10.3171/2018.10.Jns181783
27. Knosp E, Steiner E, Kitz K, Matula C. Pituitary adenomas with invasion of the cavernous sinus space: a magnetic resonance imaging classification compared with surgical findings. *Neurosurgery* (1993) 33(4):610–7; discussion 7-8. doi: 10.1227/00006123-199310000-00008
28. Hardy J. Acromegaly: Surgical treatment by transsphenoidal microsurgical removal of the pituitary adenoma. In: Tindall GT, Collins WF, editors. *Clinical Management of Pituitary Disorder, 1st ed*. New York, Raven Press (1979). 209–17.
29. Fan Y, Jiang S, Hua M, Feng S, Feng M, Wang R. Machine Learning-Based Radiomics Predicts Radiotherapeutic Response in Patients With Acromegaly. *Front Endocrinol (Lausanne)* (2019) 10:588. doi: 10.3389/fendo.2019.00588
30. Kocak B, Durmaz ES, Kadioglu P, Polat Korkmaz O, Comunoglu N, Tanriover N, et al. Predicting response to somatostatin analogues in acromegaly: machine learning-based high-dimensional quantitative texture analysis on T2-weighted MRI. *Eur Radiol* (2019) 29(6):2731–9. doi: 10.1007/s00330-018-5876-2
31. Zeynalova A, Kocak B, Durmaz ES, Comunoglu N, Ozcan K, Ozcan G, et al. Preoperative evaluation of tumour consistency in pituitary macroadenomas: a machine learning-based histogram analysis on conventional T2-weighted MRI. *Neuroradiology* (2019) 61(7):767–74. doi: 10.1007/s00234-019-02211-2
32. Guyon I, Elisseeff A. An introduction to variable and feature selection. *J Mach Learn Res* (2003) 3(Mar):1157–82. doi: 10.1162/153244303322753616
33. Nasrabadi NM. Pattern recognition and machine learning. *J Electronic Imaging* (2007) 16(4):049901. doi: 10.1117/1.2819119
34. Jenkinson M, Bannister P, Brady M, Smith S. Improved optimization for the robust and accurate linear registration and motion correction of brain images. *Neuroimage* (2002) 17(2):825–41. doi: 10.1006/nimg.2002.1132
35. Gonzalez RC, Woods RE, Eddins SL. *Digital Image processing using MATLAB®*. United States: Gatesmark Publishing (2009).
36. Drucker H, Burges CJ, Kaufman L, Smola AJ, Vapnik V. Support vector regression machines. In: Jordan MI, LeCun Y, Solla SA, editors. *Advances in neural information processing systems*. London, MIT Press (1997). 155–61.
37. Tong S, Chang E. Support vector machine active learning for image retrieval. In: *Proceedings of the ninth ACM international conference on Multimedia*. New York: Association for Computing Machinery (ACM) (2001).
38. Hastie T, Tibshirani R, Friedman J. *The Elements of Statistical Learning: Data Mining, Inference, and Prediction. 2nd ed*. New York: Springer (2009).
39. Tamrazi B, Pekmezci M, Aboian M, Tihan T, Glastonbury CM. Apparent diffusion coefficient and pituitary macroadenomas: pre-operative assessment of tumor atypia. *Pituitary* (2017) 20(2):195–200. doi: 10.1007/s11102-016-0759-5
40. Bradley WGJr. MR appearance of hemorrhage in the brain. *Radiology* (1993) 189(1):15–26. doi: 10.1148/radiology.189.1.8372185
41. Saha A, Tso S, Rabski J, Sadeghian A, Cusimano MD. Machine learning applications in imaging analysis for patients with pituitary tumors: a review of the current literature and future directions. *Pituitary* (2020) 23(3):273–93. doi: 10.1007/s11102-019-01026-x
42. Cuocolo R, Ugga L, Solari D, Corvino S, D'Amico A, Russo D, et al. Prediction of pituitary adenoma surgical consistency: radiomic data mining and machine learning on T2-weighted MRI. *Neuroradiology* (2020) 62(12):1649–56. doi: 10.1007/s00234-020-02502-z
43. Xu L, Yang P, Liang W, Liu W, Wang W, Luo C, et al. A radiomics approach based on support vector machine using MR images for preoperative lymph node status evaluation in intrahepatic cholangiocarcinoma. *Theranostics* (2019) 9(18):5374–85. doi: 10.7150/thno.34149
44. Liu Z, Zhang XY, Shi YJ, Wang L, Zhu HT, Tang Z, et al. Radiomics Analysis for Evaluation of Pathological Complete Response to Neoadjuvant Chemoradiotherapy in Locally Advanced Rectal Cancer. *Clin Cancer Res* (2017) 23(23):7253–62. doi: 10.1158/1078-0432.Ccr-17-1038

45. Park JE, Kim HS, Jo Y, Yoo RE, Choi SH, Nam SJ, et al. Radiomics prognostication model in glioblastoma using diffusion- and perfusion-weighted MRI. *Sci Rep* (2020) 10(1):4250. doi: 10.1038/s41598-020-61178-w
46. Zheng BH, Liu LZ, Zhang ZZ, Shi JY, Dong LQ, Tian LY, et al. Radiomics score: a potential prognostic imaging feature for postoperative survival of solitary HCC patients. *BMC Cancer* (2018) 18(1):1148. doi: 10.1186/s12885-018-5024-z
47. Haralick RM, Shanmugam K. Textural features for image classification. *IEEE Trans systems man cybernetics* (1973) (6):610–21. doi: 10.1109/TSMC.1973.4309314
48. Mayerhoefer ME, Szomolanyi P, Jirak D, Berg A, Materka A, Dirisamer A, et al. Effects of magnetic resonance image interpolation on the results of texture-based pattern classification: a phantom study. *Invest Radiol* (2009) 44 (7):405–11. doi: 10.1097/RLI.0b013e3181a50a66
49. Collewet G, Strzelecki M, Mariette F. Influence of MRI acquisition protocols and image intensity normalization methods on texture classification. *Magn Reson Imaging* (2004) 22(1):81–91. doi: 10.1016/j.mri.2003.09.001
50. Park JE, Kim HS. Radiomics as a Quantitative Imaging Biomarker: Practical Considerations and the Current Standpoint in Neuro-oncologic Studies. *Nucl Med Mol Imaging* (2018) 52(2):99–108. doi: 10.1007/s13139-017-0512-7
51. Saha A, Harowicz MR, Mazurowski MA. Breast cancer MRI radiomics: An overview of algorithmic features and impact of inter-reader variability in annotating tumors. *Med Phys* (2018) 45(7):3076–85. doi: 10.1002/mp.12925
52. Baeßler B, Weiss K, Pinto Dos Santos D. Robustness and Reproducibility of Radiomics in Magnetic Resonance Imaging: A Phantom Study. *Invest Radiol* (2019) 54(4):221–8. doi: 10.1097/rli.0000000000000530
53. Fiset S, Welch ML, Weiss J, Pintilie M, Conway JL, Milosevic M, et al. Repeatability and reproducibility of MRI-based radiomic features in cervical cancer. *Radiother Oncol* (2019) 135:107–14. doi: 10.1016/j.radonc.2019.03.001
54. Ciric I, Ragin A, Baumgartner C, Pierce D. Complications of transsphenoidal surgery: results of a national survey, review of the literature, and personal experience. *Neurosurgery* (1997) 40(2):225–36; discussion 36-7. doi: 10.1097/00006123-199702000-00001
55. Rim CH, Yang DS, Park YJ, Yoon WS, Lee JA, Kim CY. Radiotherapy for pituitary adenomas: long-term outcome and complications. *Radiat Oncol J* (2011) 29(3):156–63. doi: 10.3857/roj.2011.29.3.156
56. Sebastian P, Balakrishnan R, Yadav B, John S. Outcome of radiotherapy for pituitary adenomas. *Rep Pract Oncol Radiother* (2016) 21(5):466–72. doi: 10.1016/j.rpor.2016.06.002

Conflict of Interest: The authors declare that the research was conducted in the absence of any commercial or financial relationships that could be construed as a potential conflict of interest.

frontiers in Oncology

ORIGINAL RESEARCH
published: 29 January 2021
doi: 10.3389/fonc.2020.600327

A Quantitative Assessment of Pre-Operative MRI Reports in Glioma Patients: Report Metrics and IDH Prediction Ability

*Hang Cao[1], E. Zeynep Erson-Omay[2], Murat Günel[2], Jennifer Moliterno[2] and Robert K. Fulbright[3]**

[1] Department of Neurosurgery, Xiangya Hospital, Central South University, Changsha, China, [2] Department of Neurosurgery, Yale School of Medicine, New Haven, CT, United States, [3] Department of Radiology and Biomedical Imaging, MRRC, Yale School of Medicine, New Haven, CT, United States

OPEN ACCESS

Edited by:
Harrison Bai,
Brown University, United States

Reviewed by:
Matthew Tate,
Northwestern University,
United States
Jesse Liu,
Oregon Health and Science University,
United States

***Correspondence:**
Robert K. Fulbright
robert.fulbright@yale.edu

Specialty section:
This article was submitted to Neuro-Oncology and Neurosurgical Oncology, a section of the journal Frontiers in Oncology

Received: 29 August 2020
Accepted: 26 November 2020
Published: 29 January 2021

Citation:
Cao H, Erson-Omay EZ, Günel M, Moliterno J and Fulbright RK (2021) A Quantitative Assessment of Pre-Operative MRI Reports in Glioma Patients: Report Metrics and IDH Prediction Ability. Front. Oncol. 10:600327. doi: 10.3389/fonc.2020.600327

Objectives: To measure the metrics of glioma pre-operative MRI reports and build IDH prediction models.

Methods: Pre-operative MRI reports of 144 glioma patients in a single institution were collected retrospectively. Words were transformed to lowercase letters. White spaces, punctuations, and stop words were removed. Stemming was performed. A word cloud method applied to processed text matrix visualized language behavior. Spearman's rank correlation assessed the correlation between the subjective descriptions of the enhancement pattern. The T1-contrast images associated with enhancement descriptions were selected. The keywords associated with IDH status were evaluated by $\chi 2$ value ranking. Random forest, k-nearest neighbors and Support Vector Machine algorithms were used to train models based on report features and age. All statistical analysis used two-tailed test with significance at $p < .05$.

Results: Longer word counts occurred in reports of older patients, higher grade gliomas, and wild type IDH gliomas. We identified 30 glioma enhancement descriptions, eight of which were commonly used: peripheral, heterogeneous, irregular, nodular, thick, rim, large, and ring. Five of eight patterns were correlated. IDH mutant tumors were characterized by words related to normal, symmetric or negative findings. IDH wild type tumors were characterized words by related to pathological MR findings like enhancement, necrosis and FLAIR foci. An integrated KNN model based on report features and age demonstrated high-performance (AUC: 0.89, 95% CI: 0.88–0.90).

Conclusion: Report length depended on age, glioma grade, and IDH status. Description of glioma enhancement was varied. Report descriptions differed for IDH wild and mutant gliomas. Report features can be used to predict glioma IDH status.

Keywords: glioma, magnetic resonance imaging, electronic health records, quality improvement, biomarkers

INTRODUCTION

The pre-operative MRI scan of patients with glioma plays both a critical role in aiding diagnosis (1), the surgical approach, and also in serving as a baseline reference for future management. MR signal intensity data is easily available, and the MR scan data have been the subject of intense focus as researchers seek to analyze MR data in a qualitative and quantitative manner (2). Through advanced MR imaging method and radiomics analysis, the pre-operative genotype (3), immune phenotype (4), and prognosis prediction (5) become possible. These findings based on image data greatly expand the clinician's vision on glioma pathogenesis and treatment strategies.

The value and properties of another very important part of the pre-operative MRI data, the radiology report, have not been so well appreciated. Previous studies have put efforts into certain aspects of reports including tumor volume estimation (6) and treatment response evaluation (7), but the deconstruction and analysis of the full text are still lacking. In clinical practice, the qualitative and quantitative comments contained in MRI report remain the major point of reference for many diagnostic and treatment decisions. The major difficulties of using MRI reports data could be divided into three parts. First, the text reports are of non-structured data, which is largely due to the natural language used in reports. The practice years, personal habit, and language background may change the focus and sentence order of text reports. Second, the heterogeneous MRI appearance of glioma results in a variable subjective description of imaging findings. Third, the general properties of disease-specific reports have not been established using quantitative analyses designed to analyze natural language. Interestingly, the above-mentioned difficulties could also be advantages to study radiology reports. Unlike the neural network models and many machine learning models, the models based on natural language-based reports have inherent interpretability. Also, the reports as unchangeable medical record could better reflect real-world judgement and largely diminish the possible retrospective bias.

Our study objectives were to characterize glioma pre-operative MRI reports and to assess the IDH prediction ability of report features. We collected the pre-operative MRI reports on glioma patients and analyzed them with automatic natural language processing algorithm. The processed and tokenized report features were then used to build IDH prediction models. The success rate of the prediction algorithm was calculated using the IDH status identified in the cases with whole exome sequencing or by targeted sequencing.

MATERIALS AND METHODS

Patients and Reports

We performed a retrospective review of 144 consecutive cases between 2011 and 2018. For inclusion, patients who consented for clinical research had a confirmed pathological diagnosis of astrocytic or oligodendroglial tumor at our institution and underwent routine pre-operative MRI brain scan at the same institution. Full-length text reports of pre-operative MRI scans were collected from the picture archival and communication system. If the patient underwent more than one pre-operative MRI, the first report was included to prevent retrospective bias.

MRI Protocol

See **Supplementary File 1**.

Histology Subtypes and IDH Status

Surgical tumor samples underwent post-operative histology assessment, in which the integrated diagnosis was made based on the histological features, the initial IDH R132H status (provided by immunohistochemical IHC method), and MGMT promoter status (determined by PCR spell out method). The subsequent IDH mutation status was determined by targeted or whole exome sequencing.

The Extraction of Meta Data From Text Reports

MRI text reports included study indication, clinical history, comparison studies, imaging technique, findings, impression, dictating radiologist, and co-signing radiologist. To minimize the experience related bias and privacy exposure, only the findings section was used for building the text report or corpus. Meta data of the text reports was extracted through manual or automatic methods. Manual extraction was performed for scan date, dictating radiologist and co-signing radiologist. Automatic extraction was performed for word count and sentence count using R package quanteda (version 2.0.1) (8).

Detection and Correction of Misspellings

Misspellings were identified and corrected *via* R package hunspell (version 3.0) (9) with plug-in medical term dictionary and by manually checking. The corrected text matrix was used for the next analysis, below.

Processing and Visualization of the Text Reports

Reports underwent lowercase transformation, number removal, punctuation removal, stopword removal and stemming processing to build sparse document-feature matrix (DFM) *via* R package quanteda (version 2.0.1). The DFM was used to generate a word cloud with the top 100 frequent tokens. A token is the word after the above processing was performed.

Detection of Abbreviations

The R package clean-NLP (version 3.0.0) with udpipe annotation algorithm was used for abbreviation identification. After ranking the annotated tokens by length, tokens with less than 10 letters were manually checked. For potential abbreviations, the original sentence was inspected to confirm the full word and original meaning.

Abbreviations: 2HG, 2-Hydroxyglutarate; GBM, Glioblastoma; IDH, Isocitrate dehydrogenase; KNN, K nearest neighbors; MRS, Magnetic resonance spectroscopy; MGMT, O6-methylguanine-DNA methyl-transferase; PWI, Perfusion-weighted imaging.

Frequency and Redundancy Analysis of the Subjective Description of Enhancement Patterns

We manually labeled sentences containing the enhancement description from each report. Enhancement pattern modifiers were extracted from sentences. The frequency of enhancement pattern modifiers was summarized. Modifiers used in at least five or more reports underwent spearman correlation test. We collected T1-contrast images corresponding to enhancement patterns described in reports.

Analysis of Keywords Associated With IDH Status

Keywords associated with IDH status were analyzed based on the extracted document feature matrix (DFM). Keyword preference was evaluated by the keyness score, which equals the calculated chi-square value (Yates correction applied). The positive or negative keyness score sign was based on the relationship between observed value and expected value of target token relative to the IDH-MT corpus (**Supplementary File 1**). We summarized keywords with the 10 largest absolute keyness scores in the positive and negative sign groups. Since word counts with very low-frequency could also have high absolute chi-square value by coincidence, words occurring no more than five times were labeled. The p-values of all chi-square tests (Yates correction applied) were given.

Establishment of IDH Status Prediction Model Based on Pre-Operative MRI Reports

Report-based glioma IDH prediction models were built *via* Orange software datamining tool (10) (version 3.25). Tokens were used as input features for model training. Samples were separated into 70% training set (97 patients) and 30% test set (42 patients) for 100 times. Machine learning methods included support vector machine, random forest, and k-nearest neighbors. Machine learning model parameters are provided in **Supplementary File 1**. Average performance of the models was evaluated by AUC, sensitivity and specificity, by setting the IDH mutant type as target class. Since age is a predictive factor for IDH status, we generated age logistic regression model and integrated machine learning models, using age and report features. The threshold of 0.5 (<0.5, IDH wild type ≥0.5, IDH mutant type.) was selected for all models.

Statistical Analysis

The normality of continuous variables was first assessed by the Kolmogorov–Smirnov test. Due to insignificant results, non-parametric statistics tests were used to compare group differences. Pearson chi-square test, Fisher's exact test and likelihood-ratio test were used for categorical variables (sex, histology subtype, WHO grade, IDH, and MGMT status) according to expected count range and contingency table type. Statistical tests were performed with SPSS software (version 22.0; IBM). For model performance evaluation, MedCalc (version 19.0.7; MedCalc Software) was used to assess AUC, sensitivity, specificity, and to compare ROC curves.

RESULTS

Patient Characteristics

The characteristics of the 144 patients (84 men, 60 women) for which the median age and interquartile range were 59 years and 19 years, respectively are summarized in **Table 1**. Differences were found in age, initial histology reading, WHO grade, MGMT status between IDH mutant and wild type groups (P <.001). IDH wild type tumors were in older patients and were more commonly Grade IV tumors. IDH mutant tumors were more likely to be methylated with respect to MGMT. The inconsistency of diagnosis of oligodendroglioma and IDH status based on initial histology reading *versus* subsequent whole exome sequencing was found in one patient labeled as having anaplastic oligodendroglioma. There was an imbalance between IDH subtype distributions (31 IDH mutant *vs* 107 wild type patients).

General Characteristics of Reports

A total of 144 MRI reports signed by academic neuroradiologists were included in this study. The radiologist numbers are summarized in **Table 1**. All reports were generated using microphones with voice recognition software. A dictation template was used that had headings of study, date, study indication, and clinical history, whether comparison studies were available, imaging technique, findings, and impression. The date was auto-populated. There were sentences included in the template about normal structures that could be used or changed. Findings were dictated by the radiologists into the appropriate fields. The findings part of the reports started with the lesion location and size description, followed by routine conventional sequence (T1, T1-contrast, T2, FLAIR) appearance and optional advanced sequence (DWI, SWI, PWI, MRS) characteristics. The report findings ended with negative findings (findings not present) and assessment of normal structures.

One hundred twenty of one hundred forty-four reports included measurements of the glioma. In 13 of 144 reports, the statement that the study was limited was found at the beginning (10), middle (two) or end (one) of the reports. The evaluation of negative findings included transtentorial herniation, hydrocephalus, ventricle asymmetry, midline shift, global parenchymal volume loss, acute infarct, and acute intracranial hemorrhage. Evaluation of normal structure included extra axial space, ventricular system, osseous structure, orbits, and paranasal sinuses. One hundred thirty-three reports that used free-text description in evaluation of normal structures. One misspelled word was found in all 144 reports ("tthe", should be "the"). This misspelling was corrected before further analysis.

Processing of the 144 MRI reports generated a text corpus for each report, resulting in 144 processed corpora (1,476 sentences, 21,357 words). The word and sentence count characteristics were summarized in **Table 2**. Word counts were longer in older patients ($p < 0.05$). In all samples, patients with WHO grade II glioma were younger ($p < 0.001$) and had reports with lower word counts ($p = 0.01$) when compared with patients with WHO grade III and IV gliomas. In cases with an available IDH status, patients with an IDH mutant glioma were younger ($p < 0.001$)

TABLE 1 | Clinical characteristics of the study samples.

Item		Study cohort (n = 144)	IDH mutant glioma (n = 31)	IDH wild type glioma (n = 107)	p value
Age					
	Median (Q1–Q3)	59 (50–69)	39 (33–51)	63 (54–71)	<.001
Sex					
	Women	60	16	42	0.22
	Men	84	15	65	
Histology					
	Diffuse astrocytoma	12	10	2	<.001
	Oliogoastrocytoma	2	2	0	
	Oligodendroglioma	8	7	0	
	Anaplastic astrocytoma	8	4	3	
	Anaplastic oligoastrocytoma	2	1	1	
	Anaplastic oligodendroglioma	6	5	1	
	Diffuse midline glioma, H3 K27M-mutant	2	0	2	
	Glioblastoma	104	2	98	
WHO grade					
	Grade II	21	19	2	<.001
	Grade III	16	10	5	
	Grade IV	106	2	100	
IDH status					
	Wild type	107	0	107	NA
	Mutant type	31	31	0	
	NA	6	0	0	
MGMT status					
	Methylated	70	26	42	<.001
	Unmethylated	68	3	62	
	NA	6	2	3	
Reports meta feature: Radiologists					
	Report radiologist (persons)	47	17	38	NA
	Co-sign radiologist (persons)	22	14	20	
	Total radiologist (persons)	68	31	57	

and had lower word counts in reports (p = 0.027) when compared with IDH wild type gliomas. Patients with WHO grade III glioma were younger (p = 0.006) but had similar word counts (p = 0.873) when compared with patients with WHO grade IV glioma. The largest word count interquartile range was found in WHO grade III glioma reports (median and interquartile range, 161.5 and 85.5). No difference was found in sentence count according to age, gender. WHO grade, IDH status, or MGMT status. The median sentence count of 10 was found in all groups.

TABLE 2 | The word and sentence count of the study reports.

Item	Word count	p value	Sentence count	p value
	Median (Q1–Q3)		Median (Q1–Q3)	
Total study samples (n = 144)	144.5 (111.5–176.5)	NA	10 (8–12)	NA
Age (n = 144)				
≤40 years (n = 23)	113 (98–173)	0.02*	10 (8–12)	0.42
>40 and ≤60 years (n = 54)	140.5 (105–168)		10 (8–11)	
>60 years (n = 67)	155 (121–185)		10 (8–12)	
Sex (n = 144)				
Woman (n = 60)	147.5 (120.5–181.5)	0.20	10 (9–12)	0.17
Man (n = 84)	138 (107.5–172)		10 (8–11)	
WHO grade (n = 144)				
Grade II (n = 22)	110 (103–148)	0.04*	10 (9–12)	0.91
Grade III (n = 16)	161.5 (104–189.5)		10 (8.5–12.5)	
Grade IV (n = 106)	146.5 (120–178)		10 (8–12)	
IDH status (n = 138)				
Wild type (n = 107)	147 (120–181)	0.03*	10 (8–12)	0.74
Mutant type (n = 31)	113 (102–168)		10 (9–12)	
MGMT status (n = 138)				
Methylated (n = 70)	137 (107–177)	0.60	10 (8–12)	0.96
Unmethylated (n = 68)	146.5 (118–178.5)		10 (8–12)	

**Significant.*

The top 100 tokens (processed words) are shown in **Figure 1**. The most frequent words were related to body side, tumor size measurement ("x"), anatomical location, enhancement and other MR signal descriptions. The brain ventricle was also frequently mentioned in mass effect and infiltrated region.

Abbreviations

A total of 27 abbreviations were found in all reports. The abbreviation frequency, full word and category are summarized in **Table 3**. The abbreviations used could be classified into six categories including MRI term, CT term, anatomy, pathology, chemistry, and direction of imaging plane. The word transverse was found to have the most variant abbreviation presentations, which included TR, TRV, TV.

Subjective Description of Enhancement Patterns

There were 112 of 144 reports (77.8%) that included a subjective description of enhancement. Thirty subjective descriptions were identified and are summarized in **Supplementary File 1**. Eight of 30 (26.7%) subjective descriptions that occurred in at least five reports were taken to be major enhancement patterns. These included peripheral, heterogeneous, irregular, nodular, thick, rim, large, and ring. The frequency and Spearman's rank correlation coefficient of major enhancement patterns are shown in **Figure 2** (the coefficient was only shown when $p < .05$). The largest absolute correlation coefficient was found between peripheral and heterogeneous enhancement ($r = -0.38$, $p < .001$). Thick enhancement demonstrated positive correlation with peripheral enhancement description ($r = 0.29$, $p = .002$). Nodular enhancement showed negative correlation with heterogeneous enhancement description ($r = -0.30$, $p = .001$). Thick enhancement was positively correlated with irregular enhancement description ($r = 0.24$, $p = .01$). Interestingly, irregular enhancement showed both positive correlation with peripheral enhancement ($r = 0.21$, $p = .03$) and negative correlation with heterogeneous enhancement description ($r = -0.26$, $p = .004$). The representative T1-contrast images corresponding to the subjective descriptions of the major enhancement patterns are in **Figure 3**.

Keywords Associated With IDH Status

The keywords occurring differentially based on in IDH mutant and wild type gliomas are shown in **Figure 4A** (all grade

FIGURE 1 | The wordcloud of 144 pre-operative glioma MRI reports generated by R package quanteda. The top 100 tokens were selected. X means tumor measurement.

TABLE 3 | The abbreviations used in the MRI reports.

Abbreviations	Full word	Category	Count
FLAIR	Fluid-attenuated inversion recovery	MRI term	170
T2	T2 relaxation	MRI term	111
AP	Anterior-posterior	Direction	56
CC	Craniocaudal	Direction	47
T1	T1 relaxation	MRI term	28
TR	Transverse	Direction	21
TRV	Transverse	Direction	20
CT	Computed tomography	CT term	13
TV	Transverse	Direction	7
CSF	Cerebrospinal fluid	Anatomy	6
A2	Second segment of the anterior cerebral artery	Anatomy	4
M1	First segment of the middle cerebral artery	Anatomy	3
M2	Second segment of the middle cerebral artery	Anatomy	3
MCA	Middle cerebral artery	Anatomy	3
SWI	Susceptibility weighted imaging	MRI term	3
DTI	Diffusion Tensor Imaging	MRI term	2
DWI	Diffusion weighted imaging	MRI term	2
C2	Second cervical vertebra	Anatomy	1
ADC	Apparent diffusion coefficient	MRI term	1
C1	First cervical vertebra	Anatomy	1
CTA	Computed tomography angiography	CT term	1
DVA	Developmental venous anomaly	Pathology	1
MPRAGE	Magnetization-prepared rapid gradient-echo	MRI term	1
NAA	N-acetylaspartate	Chemistry	1
rCBV	Relative cerebral blood volume	MRI term	1
SI	Superior-inferior	Direction	1
VIII	Eight	Anatomy	1

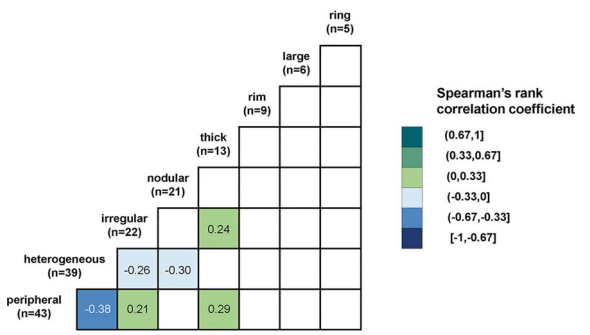

FIGURE 2 | The correlations between major descriptions of enhancement patterns.

samples) and **Figure 4B** (Grade III and IV samples). IDH mutant type gliomas were characterized by keyness values with positive signs. Keywords associated with IDH mutant tumors were associated with normal findings, symmetric ventricles, normal gray matter, no appreciable enhancement, no intracranial findings, normal appearance, or intact structures. IDH wild type gliomas were characterized with keyness values with negative signs. Keywords associated with IDH wild type gliomas were associated with effacement, irregular enhancement or shape, necrosis, foci of abnormal findings, peripheral enhancement, extension of signal, FLAIR findings, T2 findings, and peripheral enhancement.

IDH Status Prediction Based on Pre-Operative Reports

The overall test set results of model performance are summarized in **Table 4**. The integrated KNN model which used both age and report feature achieved the highest test set AUC (0.89, 95% CI: 0.88–0.90). The age only logistic regression model achieved the second highest test set AUC (0.87, 95% CI: 0.86–0.88). The pairwise comparison of ROC curves between integrated model (age and report feature) and age only model showed statistical difference ($p < 0.001$). The integrated KNN model showed higher sensitivity than age only logistic regression model (Target class: IDH mutant type. 58.9 *vs* 21.3%). For report feature models, SVM model showed highest AUC (0.75, 95% CI: 0.73–0.76). All models showed high specificity (>85%) and low sensitivity (<60%).

DISCUSSION

The pre-operative MRI reports of gliomas read by neuroradiologists in an academic institution were analyzed to provide report metrics and IDH prediction ability. Longer word counts were found in older patients and in patients with high grade (WHO grades III and IV) gliomas and wild type IDH tumors. The patients with WHO grade III glioma were younger and showed similar word counts compared with patients with WHO grade IV glioma. We identified 30 different subjective enhancement descriptions, in which eight descriptions were commonly used in at least five reports. These included

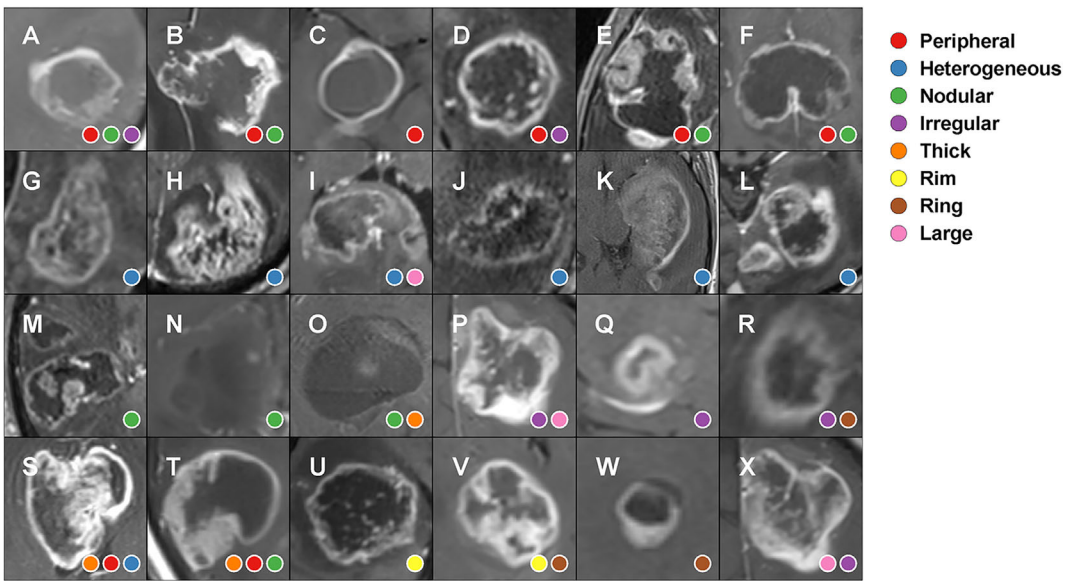

FIGURE 3 | Glioma enhancement patterns and how radiologists described them in pre-operative MRI reports. **(A–F)** peripheral enhancement; **(G–L)** heterogeneous enhancement; **(M–O)** nodular enhancement; **(P–R)** irregular enhancement; **(S, T)** thick enhancement; **(U, V)** rim enhancement; **(W)** ring enhancement; **(X)** large enhancement.

"peripheral", "heterogeneous", "irregular", "nodular", "thick", "rim", "large", and "ring". Five of these eight descriptions were correlated ($p < 0.05$). Reports in IDH mutant gliomas used words like normal, symmetric, and intact. Reports in IDH wild type gliomas used words like enhancement, necrosis, and abnormal signal intensity on FLAIR sequences. The prediction model generated by age and report features *via* KNN method showed better performance than age only model (AUC, 0.89 *vs* 0.87. IDH mutant detection sensitivity, 58.9 *vs* 21.3%).

During the past decades, efforts have been made to improve brain tumor MRI reporting. The major approaches included a focus on structured reporting and general quality. For structured reporting, Mamlouk et al (11). in 2018 introduced a series of neuroradiology structured templates that contained key points to report based on specific indications. In the report template for head and neck cancer, the findings part of the report required the radiologist to report tumor and nodal characteristics. Apart from pre-designed options, the template still has the free-text description part. In our reports, we found the structured system resulted in nearly similar sentence count for all reports. Andrea et al (12). in 2018 compared the reporting with an expert designed tumor MRI report template with free-text reporting. Findings were more completely reported when using a template. Our reports covered the majority of template fields suggested by Andrea et al., but the lesion size was usually measured on single sequence instead of both T1-contrast and FLAIR. Our reports contained more detailed tumor components' (enhancing tumor, necrosis, edema) pattern description, which have been found to correlate with glioma molecular subtypes.

For general quality, we found our reports were satisfactory as there were few misspellings, and abbreviations were easy to understand. However, the enhancement patterns were described in a variable way and may not be fully objective. For example, the word "irregular" was found preferably used with "peripheral" and not used with "heterogeneous". This finding suggested there is the potential risk of biased description caused by language habits. The variable appearance of glioma enhancement on MR leads to a multiplicity of language-based descriptions, in part due to using synonyms or related words to describe a similar imaging feature (**Figure 3**). The varied descriptions seen in **Figure 3** suggest that a more standardized manner of describing contrast enhancement might be useful to the field.

Among various genomic alternations of glioma, the IDH mutation has attracted attention due to its diagnosis and prognosis prediction value. MRI features including enhancement ratio (13), MRS 2HG signal (14), radiomics features (15), and deep learning features (16) have been used to build pre-operative prediction models. However, processing procedures like drawing tumor region or additional scanning are required to generate such features for prediction models. In our study, the language features of report findings were directly extracted without image processing procedures. The keyword analysis suggested IDH mutation status was associated with different descriptions in reports. The keywords differentiating mutant and wild types were mainly about negative imaging findings, enhancement, necrosis, edema, and anatomy. When used with age information, the report features generated a satisfactory prediction model. This type of model could be directly implemented in the daily workflow without requiring extra imaging analysis. Additional research could explore other features that radiology reports might have in providing information about brain tumors.

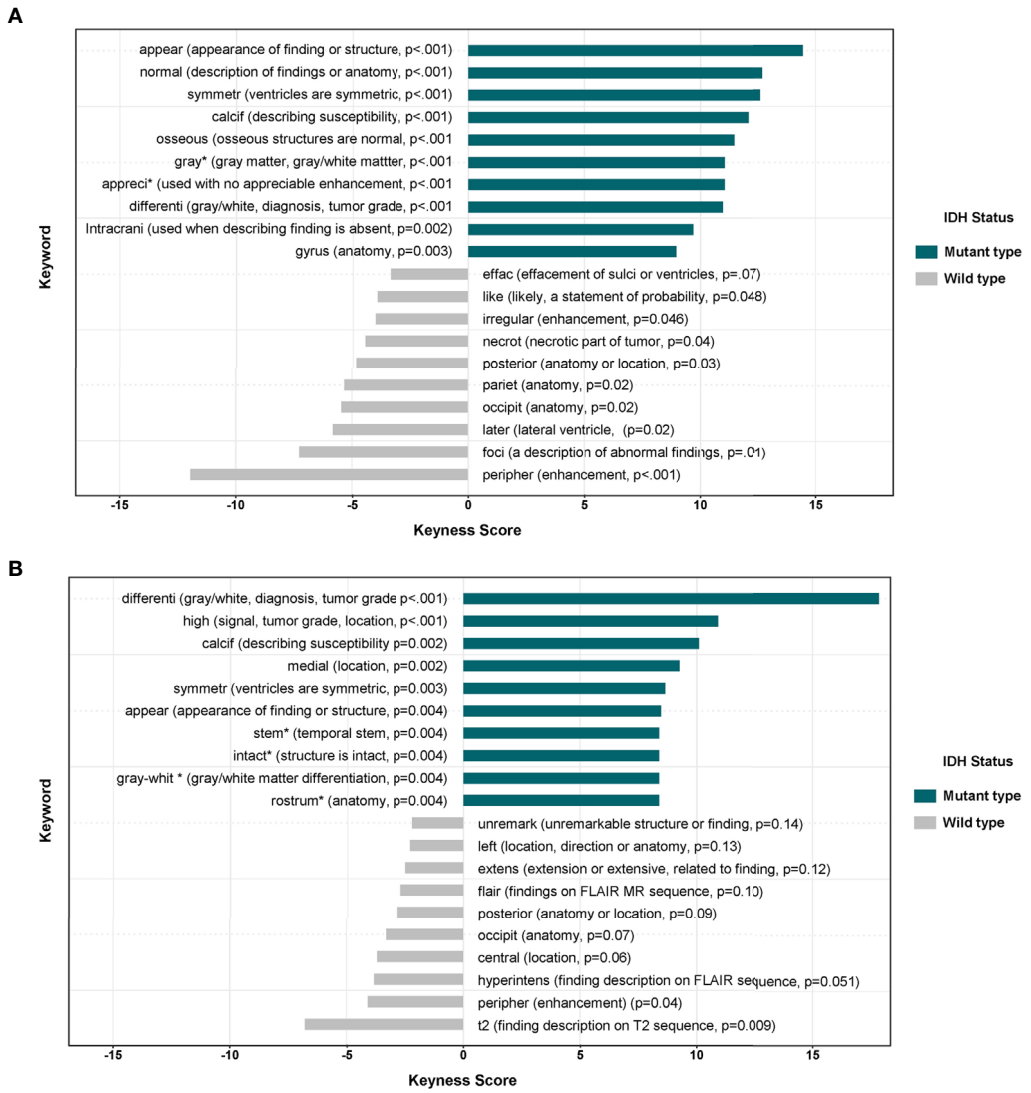

FIGURE 4 | **(A)** The differential associations of keywords in MRI reports in IDH mutant and wild type gliomas (grades II–IV, n = 138). The positive keyness score was correlated with IDH-mutant type glioma. *Infrequent description in reports (n < 5 reports). **(B)** The differential associations of keywords in MRI reports in IDH mutant and wild type gliomas (grades III–IV, n = 117). The positive keyness score was correlated with IDH-mutant type glioma. *Infrequent description in reports (n < 5 reports).

TABLE 4 | The performance of the IDH prediction model from 100 test sets.

Feature group	Modeling method	AUC	95% CI	Sensitivity	95% CI	Specificity	95% CI
Age	Logistic Regression	0.87	0.86–0.88	21.3% (192/900)	18.7–24.2%	96.1% (3170/3300)	95.3–96.7%
Report text feature	KNN	0.65	0.63–0.66	26.4% (238/900)	23.6–29.5%	88.4% (2916/3300)	87.2–89.4%
	SVM	0.75	0.73–0.76	16.4% (148/900)	14.1–19.0%	97.2% (3209/3300)	96.6–97.8%
	RF	0.65	0.64–0.67	9.4% (85/900)	7.6–11.5%	97.7% (3225/3300)	97.2–98.2%
Report text feature + Age	KNN	0.89	0.88–0.90	58.9% (530/900)	55.6–62.1%	90.6% (2988/3300)	89.5–91.5%
	SVM	0.77	0.76–0.79	22.3% (201/900)	19.7–25.2%	96.6% (3188/3300)	95.9–97.2%
	RF	0.73	0.72–0.75	14.8% (133/900)	12.5–17.3%	97.2% (3207/3300)	96.6–97.7%

Our study has several limitations. First, the study cohort was retrospectively collected from a single institution. Second, the imbalance of IDH status distribution in the study cohort might be a result of referral bias of our institution. This imbalance could affect the specific keyword analysis and prediction model training. A more balanced and larger cohort would be helpful for further research. Third, the selection procedure of representative T1 contrast images could contain subjective bias since all imaging

sequences were not analyzed. Finally, all of the radiologists who signed the final report were academic neuroradiologists. Our findings might not be applicable to a general radiology practice.

MRI reports were longer in older patients, high grade gliomas, and IDH wild type gliomas. Patients with WHO grade III glioma were younger but had similar word counts compared to patients with WHO grade IV glioma. The descriptions of glioma enhancement were variable. Five of the most common descriptions of enhancement patterns were correlated. Keyword analysis of radiology reports demonstrated different descriptions were used for IDH wild and IDH mutant gliomas. Text features of reports were used to build a model that could predict glioma IDH status.

DATA AVAILABILITY STATEMENT

The original contributions presented in the study are included in the article/**Supplementary Material**; further inquiries can be directed to the corresponding author.

ETHICS STATEMENT

The studies involving human participants were reviewed and approved by the Yale Human Investigative Committee, Biomedical Board, Yale University School of Medicine. The patients/participants provided their written informed consent to participate in this study.

AUTHOR CONTRIBUTIONS

RF's contributor roles include conceptualization (lead), development of the methodology (lead), supervision (lead), and writing, reviewing, and editing of the manuscript (lead). HC's contributor roles include data curation (lead), formal analysis (Lead), development of the methodology (lead), visualization (lead), and writing of the original draft (lead). EE-O's contributor roles include supervision (supporting), and writing, reviewing, and editing the manuscript (supporting). MG's contributor role includes supervision (supporting). JM's contributor role includes supervision (supporting). All authors contributed to the article and approved the submitted version.

SUPPLEMENTARY MATERIAL

The Supplementary Material for this article can be found online at: https://www.frontiersin.org/articles/10.3389/fonc.2020.600327/full#supplementary-material

REFERENCES

1. Anzalone N, Castellano A, Cadioli M, Conte GM, Cuccarini V, Bizzi A, et al. Brain gliomas: multicenter standardized assessment of dynamic contrast-enhanced and dynamic susceptibility contrast MR images. *Radiology* (2018) 287(3):933–43. doi: 10.1148/radiol.2017170362
2. Gillies RJ, Kinahan PE, Hricak H. Radiomics: images are more than pictures, they are data. *Radiology* (2016) 278(2):563–77. doi: 10.1148/radiol.2015151169
3. Smits M, van den Bent MJ. Imaging correlates of adult glioma genotypes. *Radiology* (2017) 284(2):316–31. doi: 10.1148/radiol.2017151930
4. Sun R, Limkin EJ, Vakalopoulou M, Dercle L, Champiat S, Han SR, et al. A radiomics approach to assess tumour-infiltrating CD8 cells and response to anti-PD-1 or anti-PD-L1 immunotherapy: an imaging biomarker, retrospective multicohort study. *Lancet Oncol* (2018) 19(9):1180–91. doi: 10.1016/S1470-2045(18)30413-3
5. Bae S, Choi YS, Ahn SS, Chang JH, Kang S-G, Kim EH, et al. Radiomic MRI phenotyping of glioblastoma: improving survival prediction. *Radiology* (2018) 289(3):797–806. doi: 10.1148/radiol.2018180200
6. Gui C, Lau JC, Kosteniuk SE, Lee DH, Megyesi JF. Radiology reporting of low-grade glioma growth underestimates tumor expansion. *Acta Neurochir* (2019) 161(3):569–76. doi: 10.1007/s00701-018-03783-3
7. Yang D. Standardized MRI assessment of high-grade glioma response: a review of the essential elements and pitfalls of the RANO criteria. *Neuro Oncol Pract* (2016) 3(1):59–67. doi: 10.1093/nop/npv023
8. Benoit K, Watanabe K, Wang H, Nulty P, Obeng A, Müller S, et al. quanteda: An R package for the quantitative analysis of textual data. *J Open Source Softw* (2018) 3(30):774. doi: 10.21105/joss.00774
9. Ooms J. *hunspell: High-Performance Stemmer, Tokenizer, and Spell Checker*. (2018) CRAN - Package hunspell. Available at: https://CRAN.R-project.org/package=hunspell [Accessed Jan 11, 2021].
10. Demšar J, Curk T, Erjavec A, Gorup Č, Hočevar T, Milutinovič M, et al. Orange: data mining toolbox in Python. *J Mach Learn Res* (2013) 14(1):2349–53. doi: 10.5555/2567709.2567736
11. Mamlouk M, Chang P, Saket R. Contextual radiology reporting: a new approach to neuroradiology structured templates. *Am J Neuroradiol* (2018) 39(8):1406–14. doi: 10.3174/ajnr.A5697
12. Bink A, Benner J, Reinhardt J, Vere-Tyndall D, Stieltjes B, Hainc N, et al. Structured reporting in neuroradiology: intracranial tumors. *Front Neurol* (2018) 9:32. doi: 10.3389/fneur.2018.00032
13. Park Y, Han K, Ahn S, Bae S, Choi Y, Chang J, et al. Prediction of IDH1-mutation and 1p/19q-codeletion status using preoperative MR imaging phenotypes in lower grade gliomas. *Am J Neuroradiol* (2018) 39(1):37–42. doi: 10.3174/ajnr.A5421
14. Branzoli F, Di Stefano AL, Capelle L, Ottolenghi C, Valabrègue R, Deelchand DK, et al. Highly specific determination of IDH status using edited in vivo magnetic resonance spectroscopy. *Neuro Oncol* (2018) 20(7):907–16. doi: 10.1093/neuonc/nox214
15. Wu S, Meng J, Yu Q, Li P, Fu S. Radiomics-based machine learning methods for isocitrate dehydrogenase genotype prediction of diffuse gliomas. *J Cancer Res Clin Oncol* (2019) 145(3):543–50. doi: 10.1007/s00432-018-2787-1
16. Bangalore Yogananda CG, Shah BR, Vejdani-Jahromi M, Nalawade SS, Murugesan GK, Yu FF, et al. A novel fully automated MRI-based deep-learning method for classification of IDH mutation status in brain gliomas. *Neuro Oncol* (2020) 22(3):402–11. doi: 10.1101/757385

Conflict of Interest: The authors declare that the research was conducted in the absence of any commercial or financial relationships that could be construed as a potential conflict of interest.

frontiers in Oncology

ORIGINAL RESEARCH
published: 11 February 2021
doi: 10.3389/fonc.2020.606741

Radiomics Features Predict *Telomerase Reverse Transcriptase* Promoter Mutations in World Health Organization Grade II Gliomas *via* a Machine-Learning Approach

Shengyu Fang[1†], Ziwen Fan[2†], Zhiyan Sun[1], Yiming Li[2], Xing Liu[3], Yuchao Liang[2], Yukun Liu[2], Chunyao Zhou[2], Qiang Zhu[2], Hong Zhang[2], Tianshi Li[2], Shaowu Li[4], Tao Jiang[1,2], Yinyan Wang[1,2‡] and Lei Wang[2*‡]*

[1] Beijing Neurosurgical Institute, Capital Medical University, Beijing, China, [2] Department of Neurosurgery, Beijing Tiantan Hospital, Capital Medical University, Beijing, China, [3] Department of Pathology, Beijing Tiantan Hospital, Capital Medical University, Beijing, China, [4] Department of Neuroradiology, Beijing Tiantan Hospital, Capital Medical University, Beijing, China

The detection of mutations in telomerase reverse transcriptase promoter (p*TERT*) is important since preoperative diagnosis of p*TERT* status helps with evaluating prognosis and determining the surgical strategy. Here, we aimed to establish a radiomics-based machine-learning algorithm and evaluated its performance with regard to the prediction of mutations in p*TERT* in patients with World Health Organization (WHO) grade II gliomas. In total, 164 patients with WHO grade II gliomas were enrolled in this retrospective study. We extracted a total of 1,293 radiomics features from multi-parametric magnetic resonance imaging scans. Elastic net (used for feature selection) and support vector machine with linear kernel were applied in nested 10-fold cross-validation loops. The predictive model was evaluated by receiver operating characteristic and precision-recall analyses. We performed an unpaired t-test to compare the posterior predictive probabilities among patients with differing p*TERT* statuses. We selected 12 valuable radiomics features using nested 10-fold cross-validation loops. The area under the curve (AUC) was 0.8446 (95% confidence interval [CI], 0.7735–0.9065) with an optimal summed value of sensitivity of 0.9355 (95% CI, 0.8802–0.9788) and specificity of 0.6197 (95% CI, 0.5071–0.7371). The overall accuracy was 0.7988 (95% CI, 0.7378–0.8598). The F1-score was 0.8406 (95% CI, 0.7684–0.902) with an optimal precision of 0.7632 (95% CI, 0.6818–0.8364) and recall of 0.9355 (95% CI, 0.8802–0.9788). Posterior probabilities of p*TERT* mutations were significantly different between patients with wild-type and mutant *TERT* promoters. Our findings suggest that a radiomics analysis with a machine-learning algorithm can be useful for predicting p*TERT* status in patients with WHO grade II glioma and may aid in glioma management.

Keywords: low-grade glioma, machine-learning, nested cross-validation, radiomics, *TERT* promoter mutation

OPEN ACCESS

Edited by:
Harrison Bai,
Brown University, United States

Reviewed by:
Wenbin Ma,
Peking Union Medical College Hospital (CAMS), China
Jiaojian Wang,
University of Electronic Science and Technology of China, China

****Correspondence:***
Lei Wang
wanglei_tiantan@163.com
Yinyan Wang
tiantanyinyan@126.com

[†]These authors have contributed equally to this work and share first authorship

[‡]These authors have contributed equally to this work and share last authorship

Specialty section:
This article was submitted to Neuro-Oncology and Neurosurgical Oncology, a section of the journal Frontiers in Oncology

Received: *15 September 2020*
Accepted: *24 December 2020*
Published: *11 February 2021*

Citation:
Fang S, Fan Z, Sun Z, Li Y, Liu X, Liang Y, Liu Y, Zhou C, Zhu Q, Zhang H, Li T, Li S, Jiang T, Wang Y and Wang L (2021) Radiomics Features Predict Telomerase Reverse Transcriptase Promoter Mutations in World Health Organization Grade II Gliomas via a Machine-Learning Approach. Front. Oncol. 10:606741. doi: 10.3389/fonc.2020.606741

INTRODUCTION

Large-scale tumor genomics research has altered the perspective of tumor research by revealing a novel method for classification of central nervous system (CNS) tumors, especially for the most malignant primary brain tumor: gliomas. Currently, gliomas are primarily classified based on the molecular characteristics of tumor tissues according to the 2016 World Health Organization (WHO) classification of CNS tumors (1), with the status of these molecular biomarkers guiding the chemotherapy and radiation therapy strategies after surgical resection. Based on these new classification standards, glioblastomas and oligodendrogliomas often exhibit mutations in the telomerase reverse transcriptase promoter (p*TERT*) (1, 2). The function of *TERT* is to maintain telomere length, which shortens with each division of normal cells (3, 4). When p*TERT* is mutated, *TERT* is upregulated, resulting in maintenance of cellular growth (5). Mutations in p*TERT* can be detected in a variety of tumors. In high-grade glioma glioblastoma and low-grade glioma oligodendroglioma, mutations in p*TERT* can be detected with a high probability. According to the cIMPACT-NOW update, mutations in p*TERT* usually suggest a better prognosis in *IDH*-mutant diffuse gliomas. Conversely, mutations in p*TERT* in *IDH*-wild-type diffuse gliomas and glioblastomas suggest a poor prognosis (6). Thus, determining p*TERT* status can be helpful for predicting prognosis and optimizing clinical treatment targets.

Radiomics analysis has been widely adopted in the field of preoperative prediction in gliomas. The use of radiomics to analyze the WHO grades, molecular characteristics, and clinical outcomes of tumor tissue *via* preoperative magnetic resonance imaging (MRI) has produced good results (7–10). However, the predominant focus of many prior studies has been the prediction of the subtype combination of p*TERT* and *IDH*, which has demonstrated moderate performance (11, 12), rather than the status of p*TERT* alone. Other studies have exhibited superior performance at predicting p*TERT* status in patients, including those with higher-grade gliomas (WHO grade III or IV) (13, 14). In this regard, p*TERT* status in WHO grade II gliomas has rarely been predicted directly. In addition, the limited sample sizes used in previous prediction models pose several issues arising from overfitting when generalizing to other patient populations.

In the present study, we aimed to investigate the potential association between radiomics features and p*TERT* mutations by selecting valuable radiomics-based features. Based on extracted radiomics features from conventional MRI sequences used in most hospitals and clinical centers, we attempt to preoperatively predict the p*TERT* mutation status of WHO grade II gliomas by developing a machine-learning-based predictive model with limited overfitting and bias *via* a nested 10-fold cross-validation.

MATERIALS AND METHODS

Patients

The clinical histories of 275 patients with pathologically confirmed primary WHO grade II gliomas were retrospectively collected from the CGGA database from June 2014 to June 2019. The following inclusion criteria were used: (a) adult (age ≥18 years); (b) histopathological diagnosis of primary grade II glioma; (c) no history of preoperative therapy or biopsy; and (d) available preoperative conventional MRI sequences, including T1-weighted images (T1WIs), T2-weighted images (T2WIs), and contrast-enhancement T1WIs (CE-T1WIs). Information on *IDH* and 1p/19q statuses was acquired from the CGGA database (http://www.cgga.org.cn/), and the details of the measurements and relationship among molecular biomarkers are shown in the **Supplementary Materials** and **Supplementary Table S1**, respectively.

Ethics Statement

All clinical information was retrospectively collected from the institutional medical database, and the retrospective study was approved by the local institutional review board.

Telomerase Reverse Transcriptase Promoter Mutation

Polymerase chain reaction (PCR) and Sanger sequencing were used to identify mutations in p*TERT* (15). The genomic mutational hotspots in the core promoter region of *TERT* were covered by sequences, including the nucleotide positions 1,295,228 [C228T] and 1,295,250 [C250T]. Nested PCR was performed for amplification based on the human genome reference sequence (grCh37 February 2009; http://genome.ucsc.edu/). To remove any unused primers, PCR products were purified using Illustra ExoProStar system (GE Healthcare, Buckinghamshire, UK) after amplification. The quality of PCR products was analyzed by electrophoresis on 2% agarose gels before sequencing. Then, PCR products were directly sequenced using a BigDye Terminator cycle sequencing kit on an ABI 3100 PRISM DNA sequencer (Applied Biosystems, Foster City, CA, USA).

Magnetic Resonance Imaging Acquisition and Preprocessing

Regions of interest (ROIs) were drawn in slices presenting with tumors based on T2WI, in which the abnormal area could accurately represent the region implicated in low-grade gliomas (16–19). MRI was mainly performed using a Trio 3.0-T scanner (Siemens, Erlangen, Germany). T2WIs were obtained with the following imaging parameters: TR = 5,500 ms; TE = 120 ms; field of view = 240 × 240 mm^2; flip angle = 150°; and voxel size = 0.65 × 0.65 × 5 mm^3. T1WIs were obtained with the following parameters: TR = 450 ms; TE = 15 ms; field of view = 240 × 240 mm^2; voxel size = 0.65 ×0.65 × 5 mm^3. Patients were injected with gadopentetate dimeglumine intravenously (0.1 mM/kg), and CE-T1WIs were collected after contrast injection. To delineate tumor masks, two neurosurgeons (>5 years of experience, ZF and ZS) who were blinded to the patients' clinical information used MRIcro (http://www.mccauslandcenter.sc.edu/mricro/) to draw the ROIs. Regions with hyperintense signals on T2WI were considered tumor areas. The T2WI and ROI for each patient were then registered to the high-resolution (1.0-mm isotropic) MNI (Montreal Neurological Institute) brain space using the SPM8 software (http://www.fil.ion.ucl.ac.uk/spm/software/spm8). A senior neuroradiologist (>20 years of

experience, SL) made the final decision when the inter-neurosurgeon's discrepancies of tumor masks exceeded 5% (DICE coefficient).

Quantitative Radiological Feature Extraction

To avoid heterogeneity bias, various MRI signal intensity values were transformed into standardized intensity ranges *via* z-score transformation. Radiomics features were then extracted from tumor masks based on the different types of MRI sequences using an automated approach (details are provided in the **Supplementary Material**) (20). For each sequence, 431 radiomics features were extracted and classified into four types (**Figure 1**): (1) first-order statistics features (n = 14), which quantitatively delineate the distribution of voxel intensities with the MRI scan through commonly used and basic metrics; (2) shape- and size-based features (n = 8), which used three dimensional features to reflect the shape and size of the ROI; (3) textural features (n = 33), which are calculated from gray-level run-length and gray level co-occurrence texture metrics and reflect the intra-tumoral heterogeneity differences; and (4) wavelet features (n = 376), which were transferred from intensity and texture features.

Feature Selection and Model Development

We developed a commonly used machine-learning algorithm, the linear support vector machine (linear SVM), to build predictive models. A linear SVM, which specified the use of a linear kernel, aimed to identify the best hyperplane that maximizes the margin between the data points of two classes (21–25). The *fitcsvm* function in MATLAB was used to build the linear SVM model. To optimize the predictive models, we varied the box constraint and kernel scale parameters in a 10-fold cross-validation (CV). In the CV, predictive models with minimal loss were considered as the optimal model.

The linear SVM was evaluated with a nested k-fold CV approach. Nested CV is widely employed in the machine-learning analysis of neuro-imaging (12, 26–29). Compared to simple CV, nested CV can reduce overfitting and limit optimistic biases, especially in relatively small samples (30, 31). These methods can make full use of all the information in the dataset and prevent circular analysis. After the dataset is split into 10 non-overlapping subsets, one selected subset (test dataset) is used to estimate the performance of a model that is trained by the remaining nine subsets (training dataset), which used another 10-fold CV for hyperparameter tuning (inner loop). These processes are repeated 10 times (outer loop), each time selecting an independent subset as the test dataset for model evaluation. We performed a 10-fold CV in

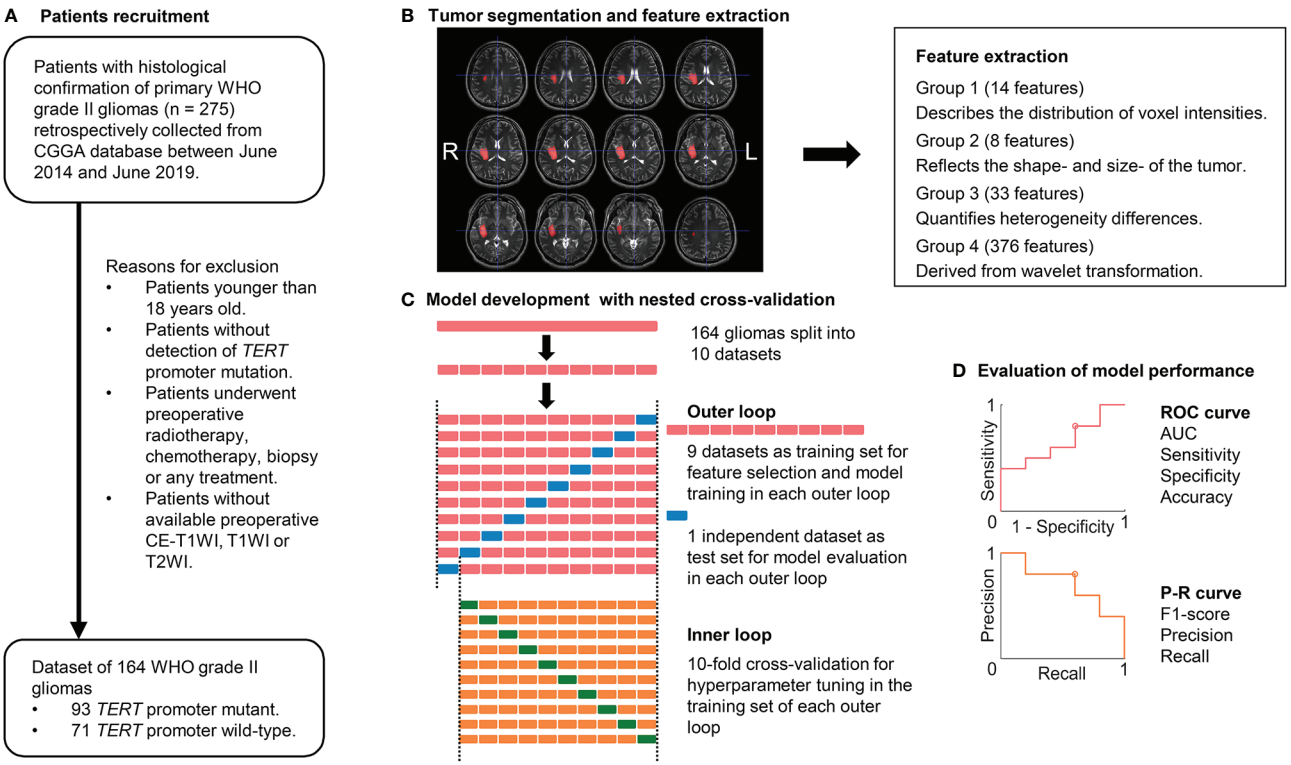

FIGURE 1 | Workflow of patient recruitment, image processing, and machine-learning. **(A)** Patient recruitment process. **(B)** Image processing. Tumor segmentation was performed with T2-weighted images (T2WIs). Radiomics features were extracted from T1-weighted images (T1WIs), T2WIs, and contrast-enhanced T1WI using region-of-interest masks. **(C)** Feature selection and machine-learning were computed in a nested 10-fold cross-validation scheme, which comprised an inner and outer loop. The inner loop included hyperparameter tuning and feature selection. The outer loop was performed for the evaluation of model performance. **(D)** ROC analysis and P-R analysis were used for model performance evaluation. *AUC*, area under the curve; *CGGA*, Chinese Glioma Genome Atlas database; *TERT*, telomerase reverse transcriptase; *P-R analysis*, precision and recall analysis; *ROC*, receiver operating characteristic.

the outer loops and computed the model performance, which was evaluated by ROC and PR analyses, using posterior probabilities.

Feature selection using elastic net (E-net) was conducted in the training component with nine datasets of each outer loop. The E-net penalty was regarded as a weighted sum of the least absolute shrinkage and selection operator penalty (LASSO) and ridge penalty (32, 33). λ and α, ranging from 0 to 1 in steps of 0.1, were selected using 10-fold CV *via* minimum or minimum plus one standard error criteria in the E-net model. We then selected the valuable features with non-zero coefficient resulting from the optimal λ and α for further analysis. After feature selection, a linear SVM was trained using the training dataset with an inner 10-fold CV loop for hyperparameter tuning. Grid searches were used for all of the hyperparameter tuning processes. Thus, 10 different linear SVM models were built with specific sets of features and hyperparameters.

Statistical Analyses

The entire nested 10-fold CV process was computed in MATLAB 2019b (MathWorks, Natick, MA, USA). Receiver operating characteristic (ROC) and precision-recall analyses were conducted to determine the performance of models in the prediction of p*TERT* status. The optimal threshold was identified when the sum of sensitivity and specificity was maximal. The 95% confidence interval (CI) of performance was evaluated using bootstrapping. We report the correlation coefficients and corresponding *p* values of the point-biserial-correlation between the true labels and posterior probabilities of *TERT* status, which were transformed from the decision values of SVM (34). The linear SVM model decision values of patients with wild-type or mutant p*TERT* were compared using unpaired t-test. Data are presented as means ± standard deviations. Differences were considered statistically significant at a P-value (p) <0.05.

RESULTS

Clinical Characteristics

Overall, 275 patients with pathological confirmed primary WHO grade II gliomas were retrospectively collected from the CGGA database. We excluded 26 patients younger than 18 years of age; 11 patients without results of *TERT* promoter mutation; eight patient received radiotherapy; chemotherapy, biopsy, or any treatment before preoperative MRI examinations; and 66 patients without available preoperative MRIs. As a result, we retrospectively enrolled 164 patients with primary WHO grade II gliomas (89 men and 75 women; age range, 20–80 years; **Table 1**). The proportion of patients with a mutation in p*TERT* was 56.7% (93/164). The proportion of patients with a mutation in *IDH* and a 1p/19q codeletion were 86% (141/164) and 48.2% (79/164), respectively. The mean (± standard deviation) age and tumor volume were 41.6 ± 10.4 years and 61.4 ± 55.3 cm^3, respectively.

Radiomics Feature Selection

We extracted 431 features from each sequence and a total of 1,293 radiomics features from all conventional sequences for each patient. The radiomics features selected by E-net in each outer loop ranged from 12 to 234. Features that were selected in at least nine of the 10 loops were considered to be the most valuable (**Table 2**). The 12 valuable radiomics features that were retained were textual features (Group 3) and their wavelet-transformed features (Group 4), such as CE-T1WI_Cluster Tendency, T1WI_Contrast, T1WI_Long Run Low Gray Level Emphasis_1, T1WI_Low Gray Level Run Emphasis, T2WI_Long Run High Gray Level Emphasis_1, *etc.* The z-score-transformed value of each important radiomics feature and p*TERT* status were compared, revealing that all valuable radiomics features in patients with mutations in p*TERT* were significantly different from patients with wild-type p*TERT* ($p < 0.05$).

Model Performance

Ten predictive models were built in this study. Model parameters are shown in **Table 3**, and the performance of each predictive model in each loop are summarized in **Supplementary Table S2**. The box constraints and kernel scale ranged from 10 to 1,000 and 0.46 to 215.4, respectively. The ROC analysis revealed an AUC value of 0.8446 (95% CI, 0.7735–0.9065), with optimal summed values of sensitivity of 0.9355 (95% CI, 0.8802–0.9788) and specificity of 0.6197 (95% CI, 0.5071–0.7371) (**Figure 2**). The overall accuracy was 0.7988 (95% CI, 0.7378–0.8598). The P-R analysis displayed an F1-score value of 0.8406 (95% CI, 0.7684–0.902) with an optimal precision of 0.7632 (95% CI, 0.6818–0.8364) and optimal recall of 0.9355 (95% CI, 0.8802–0.9788). A total of 34 patients were misclassified. There were 27 (79.4%) patients with wild-type p*TERT*, 28 (82.4%) patients with wild-type *IDH*, and 26 (76.5%) patients with 1p/19q non-codeletion. To evaluate the association between posterior probability and true labels, we computed point-biserial-correlations, revealing r and p values of 0.59 and <0.0001, respectively. Further, we compared the posterior probability between wild-type and mutant p*TERT*, revealing a p-value <0.0001, which indicated that our model can be used to predict the p*TERT* status of WHO grade II gliomas (**Figure 3**).

Furthermore, the performances of the prediction model in the subgroup of *IDH* and 1p/19q were evaluated. Although the AUCs

TABLE 1 | Baseline demographics and clinical characteristics of patients.

Variable	Value
Number of Patients	164
Sex	
Male	89
Female	75
Age (years)*	41.6 ± 10.4
IDH	
Wild-type	23
Mutant	141
1p/19q	
Codeletion	79
Non-codeletion	85
p*TERT*	
Wild-type	71
Mutant	93
Tumor volume (cm^3)	61.4 ± 55.3

**Data are presented as means ± standard deviations.*
IDH, isocitrate dehydrogenase; NOS, not otherwise specified; pTERT, telomerase reverse transcriptase promoter.

TABLE 2 | Selected valuable features.

Feature name	Selected times	*p**
CE-T1WI_Cluster Tendency (Group 3)	10	0.0025
T1WI_Contrast (Group 3)	10	<0.0001
T1WI_Long Run Low Gray Level Emphasis_1 (Group 4)	10	<0.0001
T1WI_Low Gray Level Run Emphasis (Group 3)	10	0.0066
T2WI_Long Run High Gray Level Emphasis_1 (Group 4)	10	<0.0001
CE-T1WI_Homogeneity 2_4 (Group 4)	9	0.0055
CE-T1WI _Sum Entropy_1 (Group 4)	9	<0.0001
CE-T1WI _Sum Variance_2 (Group 4)	9	0.0056
CE-T1WI _Variance_2 (Group 4)	9	<0.0001
T1WI_Cluster Prominence (Group 3)	9	<0.0001
T1WI_ Inverse Difference Moment Normalized (Group 3)	9	0.0006
T2WI_Homogeneity 2 (Group 3)	9	0.0007

**P-value of comparison between TERT promoter mutant and wild-type using unpaired t-test.*

TABLE 3 | Optimal model parameters in each outer loop.

Loops	Box constraint	Kernel scale
Loop 1	1,000	215.4
Loop 2	215.4	46.4
Loop 3	46.4	46.4
Loop 4	1000	215.4
Loop 5	215.4	10
Loop 6	10	10
Loop 7	1,000	46.4
Loop 8	46.4	46.4
Loop 9	1,000	215.4
Loop 10	10	0.46

of the ROC analysis reached a value of 0.853 (95% CI, 0.7834–0.9153), 0.8333 (95% CI, 0.6445–0.9732), and 0.8868 (95% CI, 0.8094–0.9501) for mutant *IDH*, wild-type *IDH*, and 1p/19q non-deletion groups, respectively, the AUC for the 1p/19q codeletion showed a rather low value of 0.4595 (95% CI, 0.1638–0.7114). Regarding the high rate of p*TERT* mutations in the 1p/19q codeletion (74/79), the P–R Curve, which is suitable for describing imbalances in binary data, showed a more reliable result to evaluate the model performance. The precision, recall, and F1-score in 1p/19q codeletion group were 0.9367 (95% CI, 0.8797–0.9873), 1 (95% CI, 1–1), and 0.9673 (95% CI, 0.936–0.9936), respectively. In addition, the accuracies were 0.8085 (95% CI, 0.7447–0.8652), 0.7826 (95% CI, 0.6087–0.913), 0.9367 (95% CI, 0.8734–0.9873), and 0.8706 (95% CI, 0.8–0.9412) in mutant *IDH*, wild-type *IDH*, 1p/19q codeletion, and 1p/19q non-deletion groups, respectively. The detailed prediction model performances in molecular subgroups are shown in **Supplementary Table S3**.

DISCUSSION

The clinical characteristics of patients with mutations in p*TERT* were associated with poor prognosis with glioblastomas and a good prognosis with oligodendroglioma (6, 35, 36). Based on the presence of p*TERT* mutations, *IDH1/2* mutations, and 1p/19q codeletion status, gliomas were divided into five subtypes with different overall survival (37). Since patients with lower-grade gliomas (LGGs) who carry mutations in p*TERT* always have a better survival, the determination of p*TERT* status by a non-invasive MRI scan may help patients make better decisions regarding their treatment plan. The development of an efficient method to accurately and preoperatively identify the p*TERT* status of the tumor before surgery is a critical unmet need. In this regard, radiomics offers a promising approach. To predict p*TERT* mutation status preoperatively, we built a preoperative model based on radiomics analysis that exhibited good performance and robustness.

Based on artificial intelligence, radiomics showed its potential to connect radiological images and tumor metadata (38). Radiological images contain tumor features, such as shape, volume, density, structure, and other characteristics, which are associated with tumor genomics (39). In this study, data from 164 patients with WHO grade II gliomas, whose p*TERT* status and preoperative MRIs were available, were included into the dataset. We used E-net to reduce dimensionality, identified the main features of the data, and attempted to eliminate the overfitting phenomenon of the model caused by excessive features (40). In total, 12 important radiomics features were selected more than nine times by E-net in the loops. These valuable radiomics features were predominantly textual information that could not be fully identified by the human eye in imaging and reflected the internal tissue characteristics of tumor imaging, such as internal density, morphological cell proliferation state, and infiltration degree (41–44). Among the five top radiomics features selected by the loops (10 times), three features were selected from T1WIs, and one feature was selected from CE-T1WIs and T2WIs, respectively. These results indicated that T1WIs provide the most valuable information for predictions given that WHO grade II gliomas are rarely contrast-enhanced.

By analyzing the textures extracted from patients' radiological images, substantial progress has been made with regard to WHO grade and genotype prediction of gliomas (7, 9, 16, 45–48). On one hand, since the classification of p*TERT* status has predominantly been associated with *IDH* and 1p/19q alterations, previous studies have aimed at combining subtypes of mutations in p*TERT* and *IDH* mutations for predictions. However, these attempts did not achieve a satisfactory result. Based on the radiomics analysis of conventional MRI, a LASSO regression model was used for predicting molecular subtypes of LGGs including mutant *IDH1/2*, mutant *IDH1/2* with *p*TERT mutations, and wild-type *IDH* (11). The accuracies of the prediction model reached 0.74 in the training set and 0.56 in the validation set. Another study showed lower performance based on the combination of patient age, radiomics features, and convolutional neural network features; a linear SVM model was used for predicting three subtypes of LGGs, and the accuracy reached 0.63 ± 0.08 (12). On the other hand, some studies presenting radiomics analysis focus on p*TERT* mutations only. A previous study compared three machine-learning methods in predicting p*TERT* mutations in LGGs, including random forest, SVM, and adaboost methods (13). The results showed that the

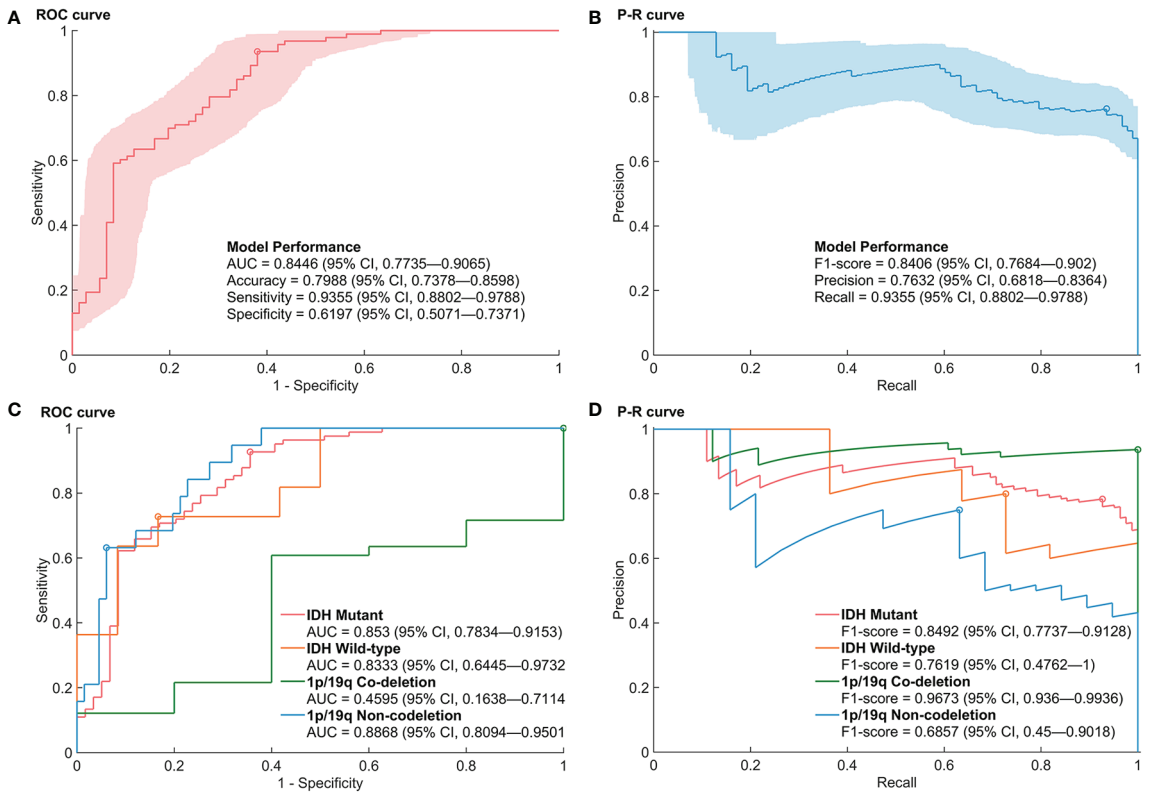

FIGURE 2 | Performance of the prediction model for mutations in the promoter region of *TERT* (p*TERT*) in WHO grade II gliomas. **(A, B)** The receiver operating characteristic (ROC) curve and P–R curve in the prediction of mutations in p*TERT* in WHO grade II gliomas. **(C, D)** The ROC curve and P–R curve in the prediction of mutations in p*TERT* in the subgroups of molecular biomarkers in WHO grade II gliomas.

random forest method had the best performance after feature selection using LASSO, and the AUC value reached 0.827 (95% CI, 0.667–0.988) in the validation group. An extreme gradient boosting model with recursive feature selection showed similarity AUC of 0.82 ± 0.04 (29), which was similar to our prediction models. In addition, based on the convolutional neural network features described above, the linear SVM model reached an accuracy of 0.84 ± 0.09 (12). Further, the prediction of mutations in p*TERT* in the subgroup of *IDH* also reached stable performances, where the random forest model achieved an AUC of 0.824 (95% CI, 0.639–1) and 0.750 (95% CI, 0.260–1) in the mutant *IDH* and wild-type *IDH* groups, respectively (13).

Although the above radiomics-based analysis achieved good performance in the predication of mutations in p*TERT*, previous studies have focused on LGGs, which are composed of WHO grades II and III gliomas, with limited sample sizes (11–13, 29). However, gliomas in WHO grade II and HGG showed differences in biological and radiomics features (49). Thus, the present study focuses on WHO grade II gliomas, which decreased the sample size but improved the consistency and practicality of the results. As a result, we enrolled 164 patients with WHO grade II gliomas and used nested CV to fully utilize the information of the enrolled patients. In addition, the performance of the prediction was also evaluated in the subgroups with *IDH* and 1p/19q alterations, which reached high and stable accuracies. However, because of the highly skewed dataset of the 1p/19q codeletion group (74 p*TERT* mutant and five wild-type samples), the ROC curve was limited, and the P–R curve gave a more informative picture of performance (50), which showed a high F1-score of 0.9673 (95% CI, 0.936–0.9936) and a high accuracy of 0.9367 (95% CI, 0.8734–0.9873).

There are some limitations of this study. First, as all patients enrolled were from a single hospital, multi-center data verification is lacking. In subsequent experiments, we will include other clinical centers or glioma imaging datasets, such as TCIA, to eliminate potential systematic errors caused by using different equipment to collect image information. Second, ROI labeling in this study relied on manual labeling by imaging scientists, which inevitably resulted in differences in ROI interpretation and affected subsequent analysis and processing. To overcome this limitation, artificial intelligence labeling should be introduced in future research to automatically label ROIs and improve the efficiency and consistency of the prediction system.

In conclusion, our results demonstrate the clinical utility of radiomics analysis for predicting p*TERT* mutation status preoperatively. Through nested CV, we developed an efficient

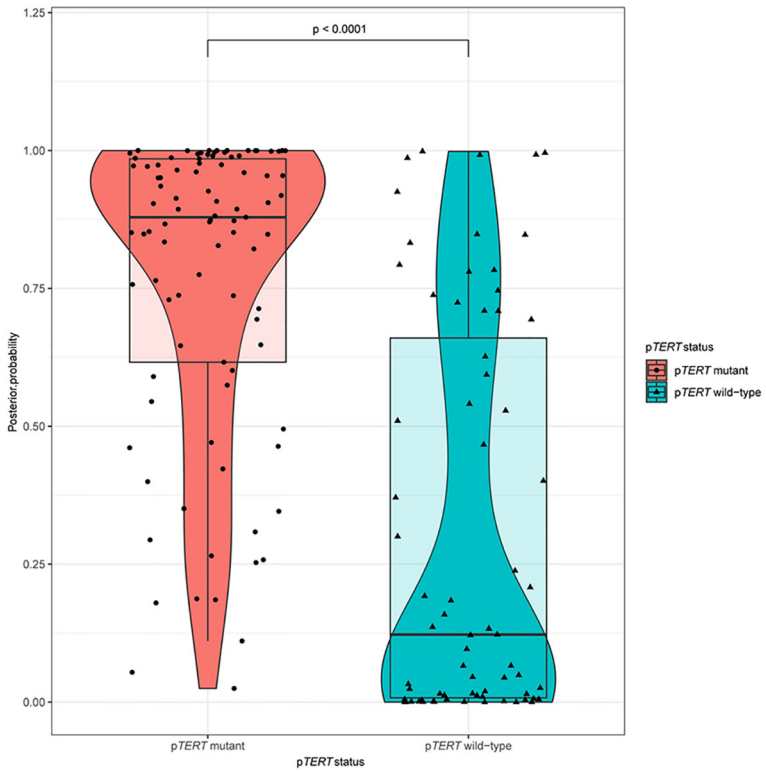

FIGURE 3 | A violin plot comparing the differences in posterior probabilities between mutants and wild-types promoter regions of *TERT*.

machine-learning-based model with robust performance. Given that p*TERT* mutation status plays an important role in glioma patients' outcomes, our predictive model will facilitate the optimization of clinical management strategies for patients with gliomas.

DATA AVAILABILITY STATEMENT

The raw data supporting the conclusions of this article will be made available by the authors, without undue reservation.

ETHICS STATEMENT

The studies involving human participants were reviewed and approved by the ethics committee of Beijing Tiantan Hospital (Beijing Tiantan Hospital, Capital Medical University, Beijing 100070, China). The patients/participants provided their written informed consent to participate in this study.

AUTHOR CONTRIBUTIONS

YW, TJ, and LW conceptualized and designed the study. SF, XL, YCL, YKL, CZ, QZ, TL, and HZ acquired the data. ZF, SF, ZS, YKL, SL, and YW analyzed and interpreted the data. SF and ZF drafted the manuscript. YW and LW critically revised the manuscript. All authors contributed to the article and approved the submitted version.

FUNDING

This study was supported by grants from the Beijing Nova Program (No. Z181100006218064), Beijing Municipal Natural Science Foundation (No. 7202021), and Capital's Funds for Health Improvement and Research (CFH 2018-2-1072).

ACKNOWLEDGMENTS

The authors would like to acknowledge the support of Zitong Zhao.

SUPPLEMENTARY MATERIAL

The Supplementary Material for this article can be found online at: https://www.frontiersin.org/articles/10.3389/fonc.2020.606741/full#supplementary-material

REFERENCES

1. Louis DN, Perry A, Reifenberger G, von Deimling A, Figarella-Branger D, Cavenee WK, et al. The 2016 World Health Organization Classification of Tumors of the Central Nervous System: a summary. *Acta Neuropathol* (2016) 131(6):803–20. doi: 10.1007/s00401-016-1545-1
2. Cancer Genome Atlas Research N, Brat DJ, Verhaak RG, Aldape KD, Yung WK, Salama SR, et al. Comprehensive, Integrative Genomic Analysis of Diffuse Lower-Grade Gliomas. *N Engl J Med* (2015) 372(26):2481–98. doi: 10.1056/NEJMoa1402121
3. Blackburn EH. Structure and function of telomeres. *Nature* (1991) 350 (6319):569–73. doi: 10.1038/350569a0
4. Liu L, Lai S, Andrews LG, Tollefsbol TO. Genetic and epigenetic modulation of telomerase activity in development and disease. *Gene* (2004) 340(1):1–10. doi: 10.1016/j.gene.2004.06.011
5. Chiba K, Lorbeer FK, Shain AH, McSwiggen DT, Schruf E, Oh A, et al. Mutations in the promoter of the telomerase gene TERT contribute to tumorigenesis by a two-step mechanism. *Science* (2017) 357(6358):1416–20. doi: 10.1126/science.aao0535
6. Brat DJ, Aldape K, Colman H, Holland EC, Louis DN, Jenkins RB, et al. cIMPACT-NOW update 3: recommended diagnostic criteria for "Diffuse astrocytic glioma, IDH-wildtype, with molecular features of glioblastoma, WHO grade IV". *Acta Neuropathol* (2018) 136(5):805–10. doi: 10.1007/s00401-018-1913-0
7. Li Y, Liu X, Xu K, Qian Z, Wang K, Fan X, et al. MRI features can predict EGFR expression in lower grade gliomas: A voxel-based radiomic analysis. *Eur Radiol* (2018) 28(1):356–62. doi: 10.1007/s00330-017-4964-z
8. Qian Z, Li Y, Sun Z, Fan X, Xu K, Wang K, et al. Radiogenomics of lower-grade gliomas: a radiomic signature as a biological surrogate for survival prediction. *Aging* (2018) 10(10):2884–99. doi: 10.18632/aging.101594
9. Liu X, Li Y, Li S, Fan X, Sun Z, Yang Z, et al. IDH mutation-specific radiomic signature in lower-grade gliomas. *Aging* (2019) 11(2):673–96. doi: 10.18632/aging.101769
10. Liu X, Li Y, Qian Z, Sun Z, Xu K, Wang K, et al. A radiomic signature as a non-invasive predictor of progression-free survival in patients with lower-grade gliomas. *NeuroImage Clin* (2018) 20:1070–7. doi: 10.1016/j.nicl.2018.10.014
11. Arita H, Kinoshita M, Kawaguchi A, Takahashi M, Narita Y, Terakawa Y, et al. Lesion location implemented magnetic resonance imaging radiomics for predicting IDH and TERT promoter mutations in grade II/III gliomas. *Sci Rep* (2018) 8(1):11773. doi: 10.1038/s41598-018-30273-4
12. Fukuma R, Yanagisawa T, Kinoshita M, Shinozaki T, Arita H, Kawaguchi A, et al. Prediction of IDH and TERT promoter mutations in low-grade glioma from magnetic resonance images using a convolutional neural network. *Sci Rep* (2019) 9(1):20311. doi: 10.1038/s41598-019-56767-3
13. Jiang C, Kong Z, Zhang Y, Liu S, Liu Z, Chen W, et al. Conventional magnetic resonance imaging-based radiomic signature predicts telomerase reverse transcriptase promoter mutation status in grade II and III gliomas. *Neuroradiology* (2020) 62(7):803–13. doi: 10.1007/s00234-020-02392-1
14. Tian H, Wu H, Wu G, Xu G. Noninvasive Prediction of TERT Promoter Mutations in High-Grade Glioma by Radiomics Analysis Based on Multiparameter MRI. *BioMed Res Int* (2020) 2020:3872314. doi: 10.1155/2020/3872314
15. Arita H, Narita Y, Fukushima S, Tateishi K, Matsushita Y, Yoshida A, et al. Upregulating mutations in the TERT promoter commonly occur in adult malignant gliomas and are strongly associated with total 1p19q loss. *Acta Neuropathol* (2013) 126(2):267–76. doi: 10.1007/s00401-013-1141-6
16. Li Y, Qian Z, Xu K, Wang K, Fan X, Li S, et al. MRI features predict p53 status in lower-grade gliomas via a machine-learning approach. *NeuroImage Clin* (2018) 17:306–11. doi: 10.1016/j.nicl.2017.10.030
17. Wang Y, Fan X, Li H, Lin Z, Bao H, Li S, et al. Tumor border sharpness correlates with HLA-G expression in low-grade gliomas. *J Neuroimmunol* (2015) 282:1–6. doi: 10.1016/j.jneuroim.2015.02.013
18. Kinoshita M, Sakai M, Arita H, Shofuda T, Chiba Y, Kagawa N, et al. Introduction of high throughput magnetic resonance T2-weighted image texture analysis for WHO grade 2 and 3 gliomas. *PLoS One* (2016) 11(10): e0164268. doi: 10.1371/journal.pone.0164268
19. Mandonnet E, Delattre JY, Tanguy ML, Swanson KR, Carpentier AF, Duffau H, et al. Continuous growth of mean tumor diameter in a subset of grade II gliomas. *Ann Neurol* (2003) 53(4):524–8. doi: 10.1002/ana.10528
20. Aerts HJ, Velazquez ER, Leijenaar RT, Parmar C, Grossmann P, Carvalho S, et al. Decoding tumour phenotype by noninvasive imaging using a quantitative radiomics approach. *Nat Commun* (2014) 5:4006. doi: 10.1038/ncomms5644
21. Hastie T, Tibshirani R, Friedman J. *The Elements of Statistical Learning, Ed*. New York: Spriner (2008).
22. Cristianini N, Shawe-Taylor J. *An introduction to support vector machines and other kernel-based learning methods*. Cambridge, England: Cambridge University Press (2000). doi: 10.1017/CBO9780511801389
23. Schölkopf B, Smola AJ, Bach F. *Learning with kernels: support vector machines, regularization, optimization, and beyond*. Cambridge, MA, London, England: MIT Press (2002).
24. Fan R-E, Chen P-H, Lin C-J. Working set selection using second order information for training support vector machines. *J Mach Learn Res* (2005) 6 (Dec):1889–918. doi: 10.1115/1.1898234
25. Kecman V, Huang T-M, Vogt M. *Iterative single data algorithm for training kernel machines from huge data sets: Theory and performance. Support vector machines: Theory and Applications*. Berlin, Germany: Springer (2005). p. 255–74. doi: 10.1007/10984697_12
26. Laurent J, Watts R, Adise S, Allgaier N, Chaarani B, Garavan H, et al. Associations Among Body Mass Index, Cortical Thickness, and Executive Function in Children. *JAMA Pediatr* (2020) 174(2):170–7. doi: 10.1001/jamapediatrics.2019.4708
27. Castillo-Barnes D, Su L, Ramírez J, Salas-Gonzalez D, Martinez-Murcia F, Illan I, et al. Autosomal Dominantly Inherited Alzheimer Disease: Analysis of genetic subgroups by Machine Learning. *Int J Inf Fusion* (2020) 58:153–67. doi: 10.1016/j.inffus.2020.01.001
28. Hahn T, Kircher T, Straube B, Wittchen H, Konrad C, Ströhle A, et al. Predicting treatment response to cognitive behavioral therapy in panic disorder with agoraphobia by integrating local neural information. *JAMA Psychiatry* (2015) 72(1):68–74. doi: 10.1001/jamapsychiatry.2014.1741
29. Shboul Z, Chen J M, Iftekharuddin K. Prediction of Molecular Mutations in Diffuse Low-Grade Gliomas using MR Imaging Features. *Sci Rep* (2020) 10 (1):3711. doi: 10.1038/s41598-020-60550-0
30. Varoquaux G, Raamana PR, Engemann DA, Hoyos-Idrobo A, Schwartz Y, Thirion B. Assessing and tuning brain decoders: cross-validation, caveats, and guidelines. *NeuroImage* (2017) 145:166–79. doi: 10.1016/j.neuroimage.2016.10.038
31. Cawley GC, Talbot NL. On over-fitting in model selection and subsequent selection bias in performance evaluation. *J Mach Learn Res* (2010) 11:2079–107. doi: 10.1007/s10846-010-9395-x
32. Friedman J, Hastie T, Tibshirani R. Regularization Paths for Generalized Linear Models via Coordinate Descent. *J Stat Softw* (2010) 33(1):1–22. doi: 10.18637/jss.v033.i01
33. Zou H, Hastie T. Regularization and variable selection via the elastic net. *J R Stat Soc: Ser B Stat Methodol* (2005) 67(2):301–20. doi: 10.1111/j.1467-9868.2005.00503.x
34. De Cáceres M, Legendre P. Associations between species and groups of sites: indices and statistical inference. *Ecology* (2009) 90(12):3566–74. doi: 10.1890/08-1823.1
35. Nonoguchi N, Ohta T, Oh JE, Kim YH, Kleihues P, Ohgaki H. TERT promoter mutations in primary and secondary glioblastomas. *Acta Neuropathol* (2013) 126(6):931–7. doi: 10.1007/s00401-013-1163-0
36. Louis DN, Aldape K, Brat DJ, Capper D, Ellison DW, Hawkins C, et al. Announcing cIMPACT-NOW: the Consortium to Inform Molecular and Practical Approaches to CNS Tumor Taxonomy. *Acta Neuropathol* (2017) 133(1):1–3. doi: 10.1007/s00401-016-1646-x
37. Eckel-Passow JE, Lachance DH, Molinaro AM, Walsh KM, Decker PA, Sicotte H, et al. Glioma Groups Based on 1p/19q, IDH, and TERT Promoter Mutations in Tumors. *N Engl J Med* (2015) 372(26):2499–508. doi: 10.1056/NEJMoa1407279
38. Gillies RJ, Kinahan PE, Hricak H. Radiomics: Images Are More than Pictures, They Are Data. *Radiology* (2016) 278(2):563–77. doi: 10.1148/radiol.2015151169
39. Lambin P, Rios-Velazquez E, Leijenaar R, Carvalho S, van Stiphout RG, Granton P, et al. Radiomics: extracting more information from medical images using advanced feature analysis. *Eur J Cancer* (2012) 48(4):441–6. doi: 10.1016/j.ejca.2011.11.036

40. Qian Z, Li Y, Wang Y, Li L, Li R, Wang K, et al. Differentiation of glioblastoma from solitary brain metastases using radiomic machine-learning classifiers. *Cancer Lett* (2019) 451:128–35. doi: 10.1016/j.canlet.2019.02.054
41. Aerts HJ. The Potential of Radiomic-Based Phenotyping in Precision Medicine: A Review. *JAMA Oncol* (2016) 2(12):1636–42. doi: 10.1001/jamaoncol.2016.2631
42. Joo L, Park JE, Park SY, Nam SJ, Kim YH, Kim JH, et al. Extensive Peritumoral Edema and Brain-to-Tumor Interface MR Imaging Features Enable Prediction of Brain Invasion in Meningioma: Development and Validation. *Neuro-oncology* (2020) noaa190. doi: 10.1093/neuonc/noaa190
43. Tang X. Texture information in run-length matrices. *IEEE Trans Image Process* (1998) 7(11):1602–9. doi: 10.1109/83.725367
44. Lambin P, Leijenaar RTH, Deist TM, Peerlings J, de Jong EEC, van Timmeren J, et al. Radiomics: the bridge between medical imaging and personalized medicine. *Nat Rev Clin Oncol* (2017) 14(12):749–62. doi: 10.1038/nrclinonc.2017.141
45. Li Y, Liu X, Qian Z, Sun Z, Xu K, Wang K, et al. Genotype prediction of ATRX mutation in lower-grade gliomas using an MRI radiomics signature. *Eur Radiol* (2018) 28(7):2960–8. doi: 10.1007/s00330-017-5267-0
46. Qian J, Herman MG, Brinkmann DH, Laack NN, Kemp BJ, Hunt CH, et al. Prediction of MGMT Status for Glioblastoma Patients Using Radiomics Feature Extraction From (18)F-DOPA-PET Imaging. *Int J Radiat Oncol Biol Phys* (2020) 108(5):1339–46. doi: 10.1016/j.ijrobp.2020.06.073
47. Zhang Z, Xiao J, Wu S, Lv F, Gong J, Jiang L, et al. Deep Convolutional Radiomic Features on Diffusion Tensor Images for Classification of Glioma Grades. *J Digit Imaging* (2020) 33(4):826–37. doi: 10.1007/s10278-020-00322-4
48. Kocak B, Durmaz ES, Ates E, Sel I, Turgut Gunes S, Kaya OK, et al. Radiogenomics of lower-grade gliomas: machine learning-based MRI texture analysis for predicting 1p/19q codeletion status. *Eur Radiol* (2020) 30(2):877–86. doi: 10.1007/s00330-019-06492-2
49. Tian Q, Yan L, Zhang X, Zhang X, Hu Y, Han Y, et al. Radiomics strategy for glioma grading using texture features from multiparametric MRI. *J Magn Reson Imaging JMRI* (2018) 48(6):1518–28. doi: 10.1002/jmri.26010
50. Davis J, Goadrich M eds. "The relationship between Precision-Recall and ROC curves". In: *Proceedings of the 23rd international conference on Machine learning* New York, NY, USA: Association for Computing Machinery (2006) 233–40. doi: 10.1145/1143844.1143874

Conflict of Interest: The authors declare that the research was conducted in the absence of any commercial or financial relationships that could be construed as a potential conflict of interest.

frontiers in Oncology

ORIGINAL RESEARCH
published: 11 February 2021
doi: 10.3389/fonc.2020.610691

Computer Tomography Radiomics-Based Nomogram in the Survival Prediction for Brain Metastases From Non-Small Cell Lung Cancer Underwent Whole Brain Radiotherapy

Ji Zhang[1†], Juebin Jin[1†], Yao Ai[1], Kecheng Zhu[1], Chengjian Xiao[1], Congying Xie[1,2] and Xiance Jin[1*]*

[1] Department of Radiotherapy Center, The First Affiliated Hospital of Wenzhou Medical University, Wenzhou, China, [2] Department of Radiation and Medical Oncology, The Second Affiliated Hospital of Wenzhou Medical University, Wenzhou, China

Prognostic parameters and models were believed to be helpful in improving the treatment outcome for patients with brain metastasis (BM). The purpose of this study was to investigate the feasibility of computer tomography (CT) radiomics based nomogram to predict the survival of patients with BM from non-small cell lung cancer (NSCLC) treated with whole brain radiotherapy (WBRT). A total of 195 patients with BM from NSCLC who underwent WBRT from January 2012 to December 2016 were retrospectively reviewed. Radiomics features were extracted and selected from pretherapeutic CT images with least absolute shrinkage and selection operator (LASSO) regression. A nomogram was developed and evaluated by integrating radiomics features and clinical factors to predict the survival of individual patient. Five radiomics features were screened out from 105 radiomics features according to the LASSO Cox regression. According to the optimal cutoff value of radiomics score (Rad-score), patients were stratified into low-risk (Rad-score <= −0.14) and high-risk (Rad-score > −0.14) groups. Multivariable analysis indicated that sex, karnofsky performance score (KPS) and Rad-score were independent predictors for overall survival (OS). The concordance index (C-index) of the nomogram in the training cohort and validation cohort was 0.726 and 0.660, respectively. An area under curve (AUC) of 0.786 and 0.788 was achieved for the short-term and long-term survival prediction, respectively. In conclusion, the nomogram based on radiomics features from CT images and clinical factors was feasible to predict the OS of BM patients from NSCLC who underwent WBRT.

Keywords: brain metastasis, non-small cell lung cancer, whole brain radiotherapy, overall survival, radiomics, nomogram

OPEN ACCESS

Edited by:
Xuejun Li,
Central South University, China

Reviewed by:
Yuming Jiang,
Stanford University, United States
Giovanni Raffa,
University of Messina, Italy

****Correspondence:***
Congying Xie
wzxiecongying@163.com
Xiance Jin
jinxc1979@hotmail.com

[†]These authors have contributed equally to this work

Specialty section:
This article was submitted to Neuro-Oncology and Neurosurgical Oncology, a section of the journal Frontiers in Oncology

Received: *27 September 2020*
Accepted: *14 December 2020*
Published: *11 February 2021*

Citation:
Zhang J, Jin J, Ai Y, Zhu K, Xiao C, Xie C and Jin X (2021) Computed Tomography Radiomics-Based Nomogram in the Survival Prediction for Brain Metastases From Non-Small Cell Lung Cancer Underwent Whole Brain Radiotherapy. Front. Oncol. 10:610691. doi: 10.3389/fonc.2020.610691

INTRODUCTION

Brain metastasis (BM) is the most frequent intracranial malignancy and remains a leading cause of morbidity and mortality in both men and woman despite advances in surgical, systemic, and radiotherapy treatments (1). Lung cancer is the most common primary origin for patients with BM, where non-small cell lung cancer (NSCLC) accounts for approximately 80% of all lung cancers (2). The prognosis of NSCLC patients with BM has significantly worsened with the median overall survival (OS) varying from 2.8 to 25.3 months (3). Studies indicated that the prognosis of individual BM patients may be affected by a few clinical factors, such as the type of primary cancer, systemic control, treatment modality, treatment response, *etc* (4, 5). The identification of these prognostic factors before or early after the beginning of treatment was believed to be helpful in improving the treatment outcome for patients with BM by adjusting and choosing the right management strategy (6).

In the past decades, several prognostic models had been suggested to predict the survival of BM patients (7–9). Recently, prognostic models such as Golden Grading System (GGS), Disease-Specific Graded Prognostic Assessment (DS-GPA), Score Index for Radiosurgery (SIR) in brain metastases, *etc.* have been published (10–12). Although these models and the suggested prognostic factors have facilitated the prediction of survival, lack of individualized survival probability and disproportional size of prognostic groups observed in these models hindered their wide application for clinical use (9). Biomarkers derived from genomic and proteomic data in primary cancers had also been reported to stratify patients into different diagnostic/prognostic groups and lead to more effective treatment paths (13, 14). However, the procedures of acquiring genomic and proteomic biomarkers are usually invasive and are not always technically feasible (15). Studies also pointed out core biopsy specimens may not represent the entirety of the tumor due to the spatial heterogeneity of tumors (16, 17).

As an emerging quantitative analysis technique, radiomics has been used to provide valuable information from medical images pertaining to tumor phenotype and microenvironment, which had been used for cancer diagnosis, treatment response monitoring, and outcome prediction for various cancers (18). Recently, Della et al. demonstrated that three-dimensional (3D) quantitative tissue enhancement in pre-treatment cranial magnetic resonance imaging (MRI) may be a radiomic marker to predict the survival of patients with singular BM treated with stereotactic radiation therapy (SRT) (19). Karami et al. also investigated that feasibility of using quantitative MRI (qMRI) biomarkers to predict the outcome of local failure for BM patients treated with SRT (20). Huang et al. pointed out that radiomic features from T1 MRI could potentially be used as surrogate biomarkers for tumor prognosis prediction following gamma knife radiosurgery (GKRS) (21).

The management options for patients with BM have been diverse in the present era, including whole brain radiation therapy (WBRT), hypo-fractionated SRT, stereotactic radiosurgery (SRS), surgical resection, and systemic therapy (22). WBRT is a standard treatment modality for NSCLC patients with multiple BM and remains the cornerstone of management of BM for many years (23). Despite the availability of diverse scoring systems, there is still a lack of consensus regarding the prognostic factors that can help the treatment decision-making concerning the use of WBRT in NSCLC patients with BM (24). On the other hand, although MRI is a more sensitive than computer tomography (CT) for BM detection, contrast enhanced CT (CECT) has been recommended on equal footing with MRI in the 2007 evidence-based ACCP guidelines for the detection of asymptomatic NSCLC metastases (25), as no improvement in survival has been reported based on screening with MRI versus CT (26). CT is also a standard modality in the radiation treatment planning for BM. So the purpose of this study is to investigate the feasibility and sensitivity of CT radiomics based nomogram to predict the survival of patients with BM from NSCLC treated with WBRT.

Abbreviations: NSCLC, non-small cell lung cancer; BM, brain metastases; WBRT, whole brain radiotherapy; LASSO, least absolute shrinkage and selection operator; CECT, contrast enhanced computer tomography; OS, overall survival; AUC, area under curve; MRI, magnetic resonance imaging.

MATERIALS AND METHODS

Patients and Computer Tomography Acquisition

Patients with BM treated in our institute from January 2012 to December 2016 were retrospectively reviewed in this study. The including criteria were 1) BM metastasized from original NSCLC; 2) BM treated with WBRT; 3) The number of metastases is less than ten; 4) Patients with pretherapeutic CECT images. BM metastasized from other origins and treated with other radiotherapy techniques was excluded. The Ethics Committee in Clinical Research of our institute approved this retrospective study and waived the need of written informed consent (ECCR#2019059). The study was conducted according to the Declaration of Helsinki with confirmation of patient data confidentiality.

BM patients were immobilized with a thermal plastic in supine position for radiotherapy. Cerebral CECT images were acquired using a 16-detector row CT simulator (Brilliance, Phillips, Cleveland OH, USA). The scanning parameters were set identical for these patients at 100 kV, 180–280 mA and a field of view of 450 mm with a 3 mm reconstructed section thickness. Before the CT scan, 100 ml of iodinated contrast material was injected into vein *via* a high pressure injector at a rate of 3.0 to 4.0 ml/s.

Radiomics Feature Extraction

No preprocessing or normalization was performed for the DICOM CT images. The tumors were manually contoured by a junior radiation oncologist and verified by a senior

radiation oncologist *via* a 3D Slicer software (version 4.2.1, https://www.slicer.org). For patients with two or more metastases, all the metastatic tumors were contoured regarding as an individual tumor.

CECT images with contoured target volumes were then imported into python3.0(https://www.python.org). An in-house algorithm in Python was coded to extract texture features automatically from each segmented region of interest (ROI) using Python package (PyRadiomics). A total of 105 radiomics features were extracted from individual BM lesion quantifying phenotypic differences on the basis of shape (n = 13), first-order (n = 18), and texture (n = 74) features. Detailed information on the feature extraction algorithms was shown in **Supplementary Material 1**.

Feature Selection and Radiomics Signature

For individual patient, radiomics features were analyzed based on the sum of the radiomics values of each lesion divided by the number of lesions. The least absolute shrinkage and selection operator (LASSO) is a computationally attractive alternative to standard covariance selection for sparse high-dimensional graphs and an effective approach for the biomarker selection of high-dimensional data. The LASSO Cox regression model was used to select the effective prognostic radiomics features. Depending on the regulation weight λ, LASSO shrinks all regression coefficients towards zero and sets the coefficients of many irrelevant features exactly to zero. A radiomics signature was generated *via* a linear combination of selected features weighted by their respective coefficients.

Survival Assessment and Nomogram

Kaplan–Meier survival analysis was applied to assess the association between radiomics signature and survival. Patients were divided into high-risk and low-risk groups based on a threshold of the radiomics score (Rad-score). The threshold was estimated based on the training cohort using an optimal cut-point analysis with X-tile software (version 3.6.1, Yale University School of Medicine, New Haven, Conn), and tested on the validation cohort. A weighted log-rank test (G-rho rank test, rho = 1) was used to test the difference between the high-risk and low-risk groups.

Clinical factors that associated with OS were also investigated with univariate analysis and multivariate Cox regression analysis. Factors with a p value less than 0.1 in the univariate analysis were included in the multivariate analysis. A nomogram was developed by integrating radiomics features and clinical factors to evaluate quantitatively the survival of individual patient. The performance of radiomics signature and nomogram was evaluated with Harrell concordance index (C-index) (1 indicates perfect concordance; 0.5 indicates no better concordance than chance).

Statistical Analysis

The OS was defined as the time from the date of first WBRT until death or the last follow-up. Patients were randomly divided into training data set (70%) and validation data set (30%). Categorical variables were compared using the x^2 test or Fisher exact test. Continuous variables were compared by using the Student t test or Mann–Whitney U test, when appropriate. Selection of radiomics features and logistic regression model building were done using the "glmnet" package. The receiver operating characteristics (ROC) curve was performed using "pROC" package. The nomogram was achieved using "rms" and "survival" packages. The statistical analyses were conducted with R software (version 3.0.1, http://www.R-project.org), SPSS software (version 19.0, IBM, Armonk, NY, USA) and Origin 2018. For all tests, $p < 0.05$ was considered as statically significant.

RESULTS

Patients' Characteristics

A total of 195 patients (male 132, female 63) with BM from lung cancer were enrolled in this retrospective study, as shown in the flowchart for patient selection in **Figure 1**. Patients were divided into training (133) and validation (62) cohorts with a median and mean age of 62.0, 61.9 years, and 63.0, 63.0 years, respectively. The median and mean OS were 8.7, 13.5 months and 8.8, 12.6 month for the training and validation data sets, respectively. The clinical characteristics were well balanced between the training and validation data sets, as shown in **Table 1**.

Feature Selection and Radiomics Signature

As shown in **Figure 2**, 10-fold cross validation was performed in the elastic net to tune parameter λ, so as to select the radiomics features that were associated with OS. Five radiomics features were screened out from 105 radiomics features according to the LASSO Cox regression analysis. They were one first order feature, two gray-level run length matrix (GLRLM) features, one gray-level size zone matrix (GLSZM) feature and one gray-level different matrix (GLDM) feature. The radiomics signature was constructed based on the Rad-score. Rad-score of individual patients was computed through a linear combination of the selected features weighted by their respective coefficients, as shown in the **Supplementary Data File 2**.

An optimal cutoff value of −0.14 was calculated by the X-tile plot based the Rad-scores of patients in the training cohort. The patients were then stratified into low-risk (Rad-score < =−0.14) and high-risk (Rad-score > −0.14) groups. **Figures 3A, B** shows the distribution of Rad-scores in the training cohort and the validation cohort for patients with low and high risk, respectively. Significant survival differences were observed between patients of low and high-risk groups according to the log-rank test, as shown in **Figure 4**. The performance of selected individual radiomics features and the radiomics signature in the prediction of low and high-risk patients was shown in **Table 2**. A C-index of 0.635 was achieved with radiomics score.

Risk Factors and Nomogram

Table 3 shows the results of univariate and multivariate Cox analysis of the risk factors associated with OS in the training

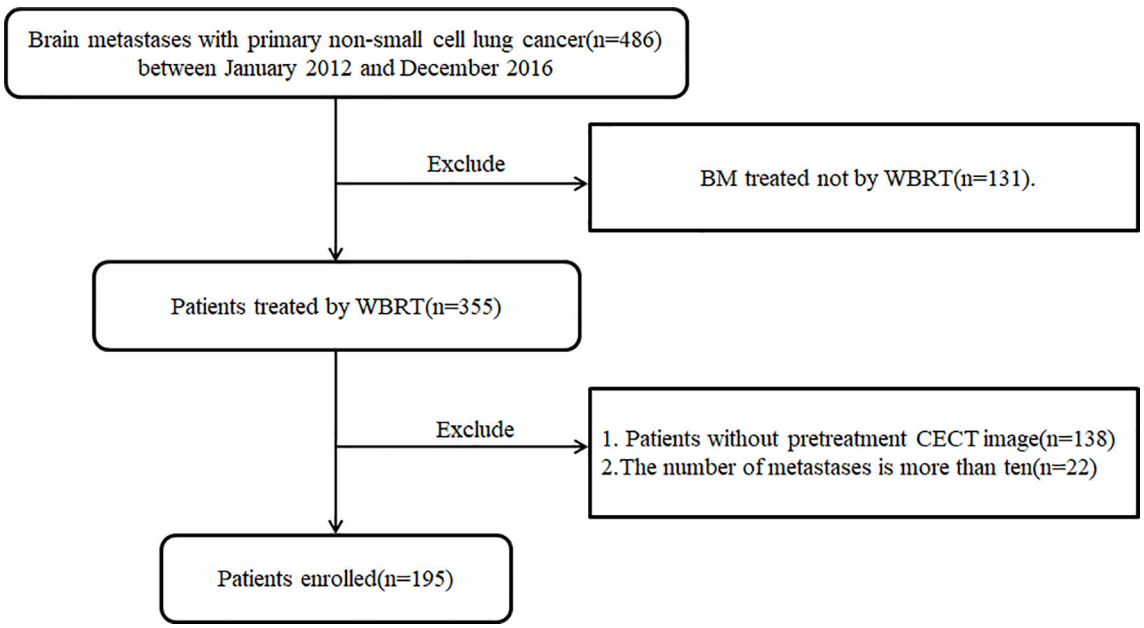

FIGURE 1 | The flowchart of patients' selection for this retrospective study.

TABLE 1 | Characteristics of patients in the training and validation cohorts.

Characteristic	Training cohort (N = 133)	Validation cohort (N = 62)	*P* value
Sex, No. (%)			0.99
Male	90(67.7%)	42(67.7%)	
Female	43(32.3%)	20(32.3%)	
Age			0.85
Range	35-88	40-83	
Median	63.0	61.5	
Mean	61.87	61.82	
Karnofsky performance score			0.73
Median	70	70	
No. of metastases lesions, No. (%)			0.38
single	62(46.6%)	24(38.7%)	
multiple	71(53.4%)	38(61.3%)	
Extracranial metastasis, No. (%)			0.92
Yes	77(57.9%)	29(53.2%)	
No	56(42.1%)	23(46.8%)	
Smoking, No. (%)			0.94
Yes	62(46.6%)	30(48.4%)	
No	71(53.4%)	32(51.6%)	
Hypertension, No. (%)			0.019
Yes	52(39.1%)	13(21.0%)	
No	81(60.9%)	49(79.0%)	
Glycuresis, No. (%)			1.00
Yes	20(15.0%)	10(16.1%)	
No	113(85.0%)	52(83.9%)	
Overall Survival(d)			0.56
Range	4-1778	16-1765	
Median	260	247.5	
Mean	403.17	455.29	

cohort. According to the multivariable analysis, sex (HR = 1.733; 95% CI: 1.125–2.794; p = 0.014), karnofsky performance score (KPS) (HR = 3.204; 95% CI: 2.003–5.125; $p < 0.001$) and Rad-score (HR = 10.866; 95%CI: 1.711–68.981; p = 0.011) were independent predictors for OS.

A nomogram was constructed by integrating the clinical factors and radiomics signature (**Figure 5A**) to predict the probability of 3-month OS and 1-year OS after treatment for patients with BM. **Figures 5B, C** demonstrated the calibration curves for the evaluation of agreement between nomogram prediction and actual observation for 3-month and 1-year OS with validation data set, respectively. The C-index of nomogram in training cohort and validation cohort were 0.726, 0.660, respectively. Further verification with ROC was shown in **Figure 6**. An AUC of 0.786 (95% CI: 0.671–0.901) and 0.788 (95% CI: 0.657–0.918) was achieved for the short-term and long-term survival prediction, respectively.

DISCUSSION AND CONCLUSIONS

In this study, the feasibility and sensitivity of a CT based radiomics nomogram were investigated in the prediction of 3-month and 1-year survival for patients with BM from NSCLC. Sex, KPS and Rad-score were associated with the OS and integrated into the nomogram. A C-index of 0.660 was achieved by the nomogram in survival prediction for BM patients from NSCLC. An AUC of 0.786 and 0.788 was achieved for the 3-month and 1-year survival prediction, respectively.

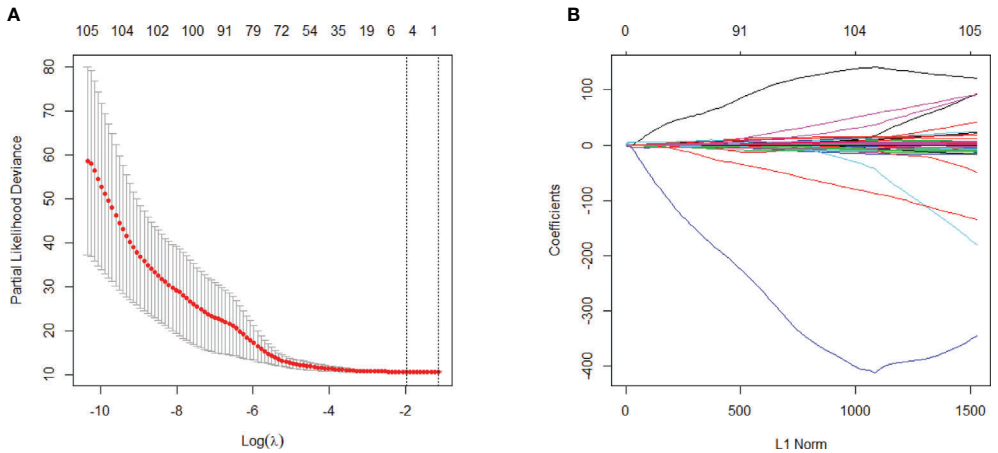

FIGURE 2 | Selection of survival associated radiomics features using the elastic net method, **(A)** Tuning parameter (λ) in the elastic net used 10-fold cross-validation *via* maximum area under curve and criterion of minimum standard deviation were followed; **(B)** The coefficient profiles of 105 radiomics features against the L1 norm (inverse proportional to log λ).

More than 20% of patients with NSCLC are affected by BM and are associated with poor prognosis (2, 3). Patients with BM were usually reported with remarkable heterogeneity. BM patients may have one or dozens of metastases with varied response or resistance to radiation therapy or chemotherapy (27). Similarly, in this study, there were about 55% (109/195) patients with more than one metastasis with a mean OS around 13 months. Due to this heterogeneity, prognostic features and treatment options for patients with BM should be carefully investigated on an individual basis. Although there is still controversy for the palliative treatment for BM patients with poor prognosis, multidisciplinary palliative therapy must be administered to increase the OS rates of patients with good prognosis (28).

The prediction of survival for BM is usually difficult due to a plethora of factors associated with survival. In the literature, multiple factors, such as control of primary disease, number of metastasis, KPS, age, tumor volume, presence of extracranial metastases *etc.*, were investigated for the prediction of survival of patients with BM (4). The type of treatment is certainly a significant prognostic factor for patients with BM. Whole brain volume reduction and neurocognitive function decline were the major concerns with WBRT (29), while with the development of hippocampal-sparing technique, neurocognitive function and patient-reported symptoms were improved (30). In this study, sex and KPS were correlated with the OS with a HR of 1.733 and 3.204, respectively, according to the multivariate Cox analysis for BM patients treated with WBRT. This is consistent with previously reported models (4, 8, 9).

In this study, radiomics features extracted from CT images were also closely associated with the survival of BM patients as it demonstrated that the HR of Rad-score was 10.866 with a p value

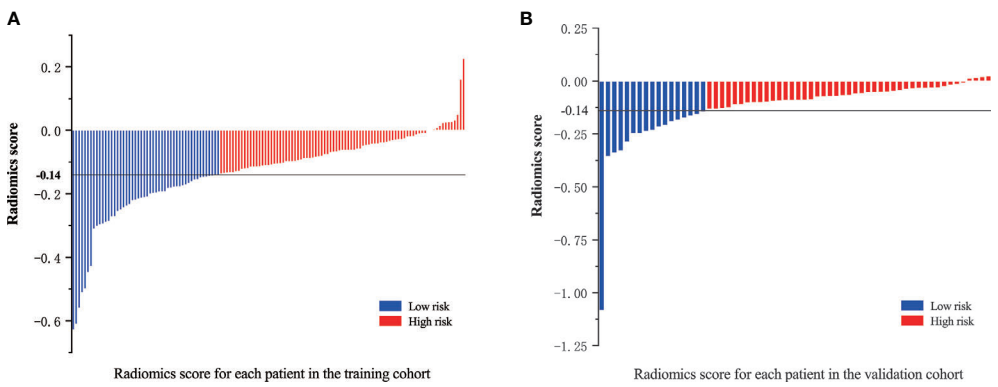

FIGURE 3 | Radiomics scores for each patient in the **(A)** training cohort and **(B)** validation cohort; patients were classified into high and low risk groups with a threshold of –0.14.

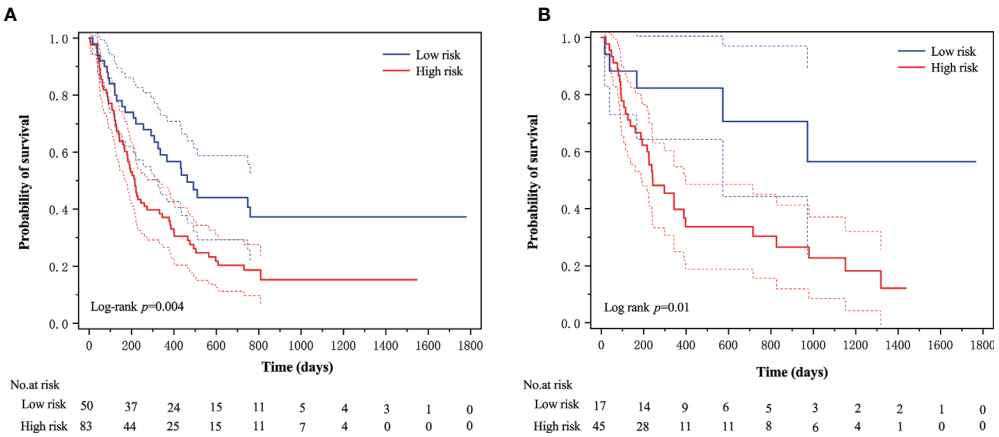

FIGURE 4 | The Kaplan–Meier survival curves of the low- and high-risk groups according to the log-rank test for patients in **(A)** training cohort and **(B)** validation cohort. The vertical dashed line is 95% confidence interval.

TABLE 2 | The performance of the selected radiomics features and constructed radiomics signatures.

Radiomics features	Training cohort			Validation cohort		
	C-index	95%CI	*P* value	C-index	95%CI	*P* value
Firstorder_Skewness	0.547	(0.486,0.608)	0.14	0.541	(0.436,0.646)	0.45
GLRLM_LowGrayLevelRunEmphasis	0.546	(0.487,0.605)	0.13	0.570	(0.468,0.679)	0.18
GLRLM_ShortRunLowGrayLevelEmphasis	0.549	(0.489,0.609)	0.11	0.582	(0.482,0.682)	0.11
GLSZM_GrayLevelNonUniformity	0.522	(0.455,0.589)	0.51	0.589	(0.496,0.682)	0.060
GLDM_DependenceNonUniformityNormalized	0.534	(0.471,0.597)	0.29	0.584	(0.478,0.690)	0.77
Radiomics score	0.581	(0.523,0.639)	0.0059*	0.635	(0.536,0.734)	0.0074*

**Statistical significance.*

TABLE 3 | Univariate and multivariate Cox regression analysis for risk factors associated with overall survival.

Variable	Univariate analysis			Multivariable analysis		
	HR	95%CI	*p* value	HR	95%CI	*p* value
Sex	1.656	(1.059,2.590)	0.027	1.733	(1.125,2.794)	0.014*
Age (<=56, >56)	0.991	(0.662,1.484)	0.97			
KPS (<=70, >70)	3.450	(2.185,5.447)	<0.001	3.204	(2.003,5.125)	<0.001*
Extracranial met	0.514	(0.338,0.783)	0.002	0.682	(0.441,1.053)	0.084
Smoking	0.778	(0.520,1.165)	0.22			
Hypertension	1.052	(0.695,1.594)	0.81			
Glycuresis	0.771	(0.443,1.341)	0.36			
Rad-score	14.006	(2.233,87.845)	0.005	10.866	(1.711,68.981)	0.011*

KPS, Karnofsky performance score; met, metastasis; Rad-score, radiomics score.
**Statistical significance.*

of 0.011. Similarly, Huang et al. demonstrated that radiomics features extracted from pre-treatment T1 MRI was an independent prognostic factor of local control for BM patients who underwent gamma knife radiosurgery (21). Karami et al. found it was possible to use MRI based radiomics features to predict local failure early for BM patients treated with SRT (20). Huang et al. also reported that the radiomics features extracted from chest CT images were independent of clinical-pathologic risk factors and significantly correlated with the disease free survival of patients with early-stage NSCLC (31).

With radiomics features alone, a C-index of 0.635 was achieved in the prediction of survival of BM patients who underwent WBRT in this study. This was better than a nomogram integrating clinical factors of primary site, histology, status of primary disease, metastatic spread, age, KPS, and number of brain lesions by Barnholtz-Sloan et al., in which a C-index of 0.60 was reported in the prediction of survival of 2,350 BM patients from seven Radiation Therapy Oncology Group (RTOG) randomized trials (32). Pietrantonio et al. developed a survival prediction nomogram for BM from

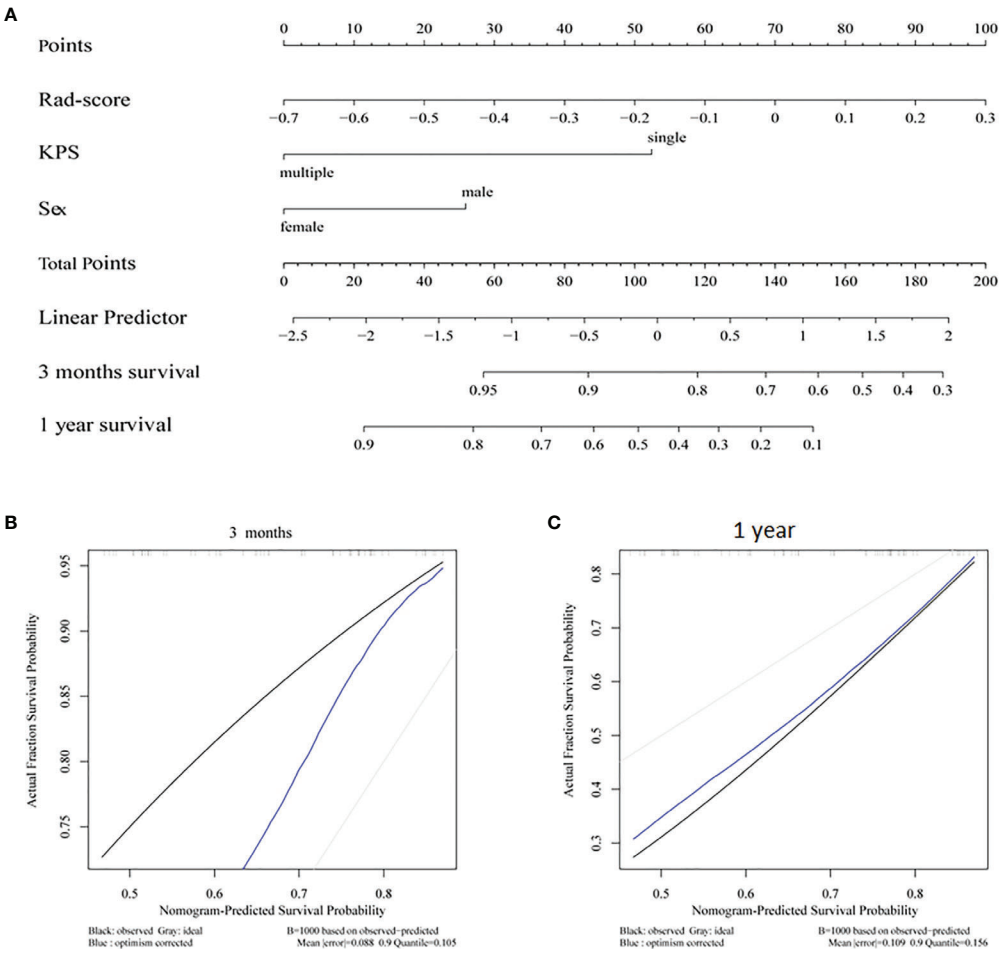

FIGURE 5 | **(A)** Radiomics nomogram integrated with radiomics signature and clinical factor; calibration curves of the radiomics nomogram for **(B)** 3 months survival and **(C)** 1 year survival.

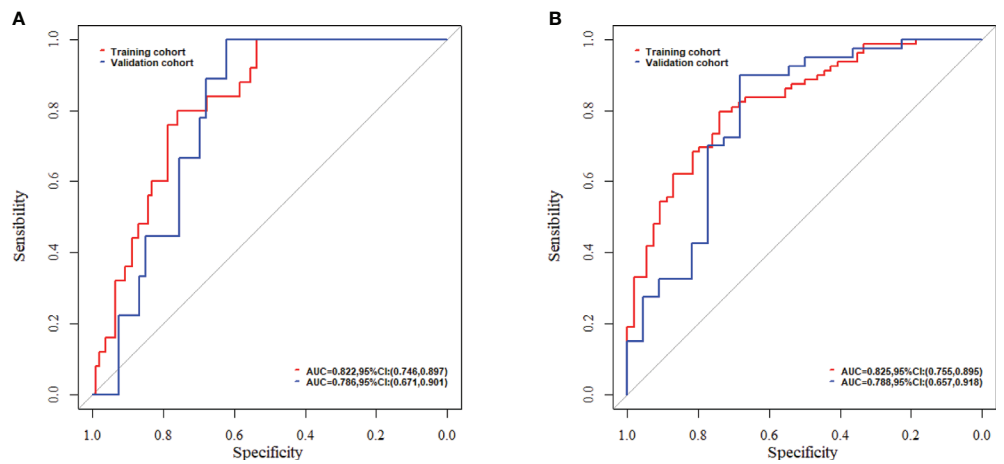

FIGURE 6 | The evaluation of nomogram with receiver operating characteristic curves for **(A)** short-term survival prediction model; **(B)** long-term survival prediction model.

colorectal cancer and achieved a similar C-index of 0.64 and external validation C-index of 0.73 with the integrating of age, KPS, site of BM and number of BM (33).

With the integrating of radiomics features and clinical factors, the nomogram constructed in this study achieved a C-index of 0.726 and 0.660 for the training and validation cohorts, respectively. This was close to the reported C-index of 0.74 in a study of Park et al. in which the survival prediction of BM patients from hepatocellular carcinoma treated with WBRT with or without resection/radiosurgery was investigated (34). The AUC of our radiomics based nomogram for short-term and long-term survival was 0.786 and 0.788, respectively. These were better than the reported two nomograms for the prediction of early death (<3 months) and long-term survival (>1 year), which was investigated by Zindler et al. with an AUC of 0.70 and 0.67 for early dearth and long-term survival, respectively, for BM patients from NSCLC treated with SRS (35).

Some limitations of the current study are its retrospective design and the risk of selection bias. The nomogram was built and validated internally with data from our institution only; external validations with additional independent data are needed to further evaluate the performance of this nomogram. BM patients from primary sites other than NSCLC were not included in this study, such as breast, colorectal cancer, *etc.* With the development of medical imaging technologies, immobilization methods, and radiotherapy techniques, more and more BM patients were treated with SRT and SRS. A more comprehensive nomogram for patients treated with other than WBRT and based on other image modality radiomics will greatly improve our survival prediction ability and guide tailored treatment for patients with BM.

In conclusion, a nomogram based on radiomics features from CT images and clinical factors was constructed to predict the OS for patients with BM from NSCLC who underwent WBRT. The predicted short-term and long-term survival of BM patients who underwent WBRT will help to adjust and choose the right management strategy, so as to improve the outcome for these patients.

DATA AVAILABILITY STATEMENT

The original contributions presented in the study are included in the article/**Supplementary Material**; further inquiries can be directed to the corresponding author.

ETHICS STATEMENT

The studies involving human participants were reviewed and approved by The Ethics Committee in Clinical Research of the 1st Affiliated Hospital of Wenzhou Medical University. The informed consent from patients/participants was waived by the Ethics Committee for this retrospective study.

AUTHOR CONTRIBUTIONS

JZ, YA, and XJ conceived and designed the study. JZ, KM, and ChX acquired and managed the patients. JZ and JJ analyzed and interpreted the data (e.g., statistical analysis, biostatistics, and computational analysis). JZ, XJ, and CoX wrote, reviewed, and/or revised the manuscript. All authors contributed to the article and approved the submitted version.

FUNDING

This work was partially funded by the Wenzhou Municipal Science and Technology Bureau (Nos. 2018ZY016 and H20180003) and National Natural Science Foundation of China under Grant No. 11675122.

SUPPLEMENTARY MATERIAL

The Supplementary Material for this article can be found online at: https://www.frontiersin.org/articles/10.3389/fonc.2020.610691/full#supplementary-material

REFERENCES

1. Ostrom QT, Wright CH, Barnholtz-Sloan JS. Brain metastases: epidemiology. *Handb Clin Neurol* (2018) 149:3–23. doi: 10.1016/B978-0-12-811161-1.00002-5
2. Schuette W. Treatment of brain metastases from lung cancer: chemotherapy. *Lung Cancer* (2004) 45:S253–7. doi: 10.1016/j.lungcan.2004.07.967
3. Sensen J, Hansen H, Hansen M, Dombernowsky P. Brain metastases in adenocarcinoma of the lung: frequency, risk groups, and prognosis. *J Clin Oncol* (1988) 6:1474–80. doi: 10.1200/JCO.1988.6.9.1474
4. Sperduto PW, Chao ST, Sneed PK, Luo X, Suh J, Roberge D, et al. Diagnosis specific prognostic factors, indexes, and treatment outcomes for patients with newly diagnosed brain metastases: a multi-institutional analysis of 4,259 patients. *Int J Radiat Oncol Biol Phys* (2010) 77:655–61. doi: 10.1016/j.ijrobp.2009.08.025
5. Rades D, Gerdan L, Segedin B, Nagy V, Khoa MT, Trang NT, et al. Brain metastasis. Prognostic value of the number of involved extracranial organs. *StrahlentherOnkol* (2013) 189:996–1000. doi: 10.1007/s00066-013-0442-y
6. Jenkinson MD, Haylock B, Shenoy A, Husband D, Javadpour M. Management of cerebral metastasis: evidence-based approach for surgery, stereotactic radiosurgery and radiotherapy. *Eur J Cancer* (2011) 47:649–55. doi: 10.1016/j.ejca.2010.11.033
7. Lagerwaard FJ, Levendag PC, Nowak PJ, Eijkenboom WM, Hanssens PE, Schmitz PI. Identification of prognostic factors in patients with brain metastases: a review of 1292 patients. *Int J Radiat Oncol Biol Phys* (1999) 43:795–803. doi: 10.1016/S0360-3016(98)00442-8
8. Sperduto PW, Berkey B, Gaspar LE, Mehta M, Curran W. A new prognostic index and comparison to three other indices for patients with brain metastases: an analysis of 1,960 patients in the RTOG database. *Int J Radiat Oncol Biol Phys* (2008) 70:510–4. doi: 10.1016/j.ijrobp.2007.06.074
9. Nieder C, Mehta MP. Prognostic indices for brain metastases – usefulness and challenges. *RadiatOncol* (2009) 4:10. doi: 10.1186/1748-717X-4-10
10. Rades D, Janssen S, Bajrovic A, Veninga T, Fischer D, Schild SE. A new scoring tool to assess overall survival in patients with intracerebral metastases from gynecological cancers. *Int J Gynecol Cancer* (2017) 27:597–602. doi: 10.1097/IGC.0000000000000899

11. Joshi R, Johnson MD, Maitz A, Marvin KS, Olson RE, Grills IS. Utility of graded prognostic assessment in evaluation of patients with brainstem metastases treated with radiosurgery. *Clin Neurol Neurosurg* (2106) 147:30–3. doi: 10.1016/j.clineuro.2016.05.001
12. Sehmisch L, Schild SE, Rades D. Development of a survival score for patients with cerebral metastases from melanoma. *Anticancer Res* (2017) 37:249–52. doi: 10.21873/anticanres.11314
13. Lee JM, Kohn EC. Proteomics as a guiding tool for more effective personalized therapy. *Ann Oncol* (2010) 21:1–6. doi: 10.1093/annonc/mdq375
14. Szopa W, Burley TA, Kramer-Marek G, Kaspera W. Diagnostic and therapeutic biomarkers in glioblastoma: Current status and future perspectives. *BioMed Res Int* (2017) 2017:8013575. doi: 10.1155/2017/8013575
15. Diamandis EP. The failure of protein cancer biomarkers to reach the clinic: why, and what can be done to address the problem? *BMC Med* (2012) 10:87. doi: 10.1186/1741-7015-10-87
16. Jamal-Hanjani M, Quezada SA, Larkin J, Swanton C. Translational implications of tumor heterogeneity. *Clin Cancer Res* (2015) 21:1258–66. doi: 10.1158/1078-0432.CCR-14-1429
17. Cyll K, Ersvær E, Vlatkovic L, Pradhan M, Kildal W, Avranden Kjær M, et al. Tumour heterogeneity poses a significant challenge to cancer biomarker research. *Br J Cancer* (2017) 117(3):367–75. doi: 10.1038/bjc.2017.171
18. Kniep HC, Madesta F, Schneider T, Hanning U, Schönfeld MH, Schön G, et al. Radiomics of brain MRI: utility in prediction of metastatic tumor type. *Radiology* (2019) 290:479–87. doi: 10.1148/radiol.2018180946
19. Della Seta M. Collettini F, Chapiro J, etal.A 3D quantitative imaging biomarker in pre-treatment MRI predicts overall survival after stereotactic radiation therapy of patients with a singular brain metastasis. *Acta Radiol* (2019) 60(11):1496–503. doi: 10.1177/0284185119831692
20. Karami E, Soliman H, Ruschin M, Sahgal A, Myrehaug S, Tseng CL, et al. Quantitative MRI Biomarkers of Stereotactic Radiotherapy Outcome in Brain Metastasis. *Sci Rep* (2019) 9(1):19830. doi: 10.1038/s41598-019-56185-5
21. Huang CY, Lee CC, Yang HC, Lin CJ, Wu HM, Chung WY, et al. Radiomics as prognostic factor in brain metastases treated with Gamma Knife radiosurgery. *J Neuro Oncol* (2020) 146(3):439–49. doi: 10.1007/s11060-019-03343-4
22. Tsao M, Xu W, Sahgal A. A meta-analysis evaluating stereotactic radiosurgery, whole-brain radiotherapy, or both for patients presenting with a limited number of brain metastases. *Cancer* (2012) 118:2486–93. doi: 10.1002/cncr.26515
23. Taimur S, Edelman MJ. Treatment options for brain metastases inpatients with non-small-cell lung cancer. *Curr Oncol Rep* (2003) 5:342–6. doi: 10.1007/s11912-003-0077-8
24. Mulvenna P, Nankivell M, Barton R, Faivre-Finn C, Wilson P, McColl E, et al. Dexamethasone and supportive care with or without whole brain radiotherapy intreating patients with non-small cell lung cancer with brain metastasesunsuitable for resection or stereotactic radiotherapy (QUARTZ): results from a phase 3, non-inferiority, randomizedtrial. *Lancet* (2016) 388:2004–14. doi: 10.1016/S0140-6736(16)30825-X
25. Silvestri GA, Gould MK, Margolis ML, Tanoue LT, McCrory D, Toloza E, et al. Noninvasive staging of non-small cell lung cancer: ACCP evidenced-based clinical practice guidelines. *Chest* (2007) 132(3 suppl):178S–201. doi: 10.1378/chest.07-1360
26. Yokoi K, Kamiya N, Matsuguma H, Machida S, Hirose T, Mori K, et al. Detection of brain metastasis in potentially operable non-small cell lung cancer: a comparison of CT and MRI. *Chest* (1999) 115:714–9. doi: 10.1378/chest.115.3.714
27. Oh Y, Taylor S, Bekele BN, Debnam JM, Allen PK, Suki D, et al. Number of metastatic sites is a strong predictor of survival in patients with nonsmall cell lung cancer with or without brain metastases. *Cancer* (2009) 115(13):2930–8. doi: 10.1002/cncr.24333
28. Liubota R, Cheshuk V, Vereshchako R, Zotov O, Zaichuk V, Anikusko N, et al. The impact of locoregional treatment on survival of patients with primary metastatic breast cancer. *Exp Oncol* (2017) 39(1):75–7. doi: 10.31768/2312-8852.2017.39(1):75-77
29. Gui C, Chintalapati N, Hales RK, Voong KR, Sair HI, Grimm J, et al. A prospective evaluation of whole brain volume loss and neurocognitive decline following hippocampal-sparing prophylactic cranial irradiation for limited-stage small-cell lung cancer. *J Neuro Oncol* (2019) 144(2):351–8. doi: 10.1007/s11060-019-03235-7
30. Brown PD, Gondi V, Pugh S, Tome WA, Wefel JS, Armstrong TS, et al. Hippocampal Avoidance During Whole-Brain Radiotherapy Plus Memantine for Patients With Brain Metastases: Phase III Trial NRG Oncology CC001. *J Clin Oncol* (2020) 38(10):1019–29. doi: 10.1200/JCO.19.02767
31. Huang Y, Liu Z, He L, Chen X, Pan D, Ma Z, et al. Radiomics Signature: A Potential Biomarker for the Prediction of Disease-Free Survival in Early-Stage (I or II) Non–Small Cell Lung Cancer. *Radiology* (2016) 281(3):947–57. doi: 10.1148/radiol.2016152234
32. Barnholtz-Sloan JS, Yu C, Sloan AE, Vengoechea J, Wang M, Dignam JJ, et al. A nomogram for individualized estimation of survival among patients with brain metastasis. *Neuro Oncol* (2012) 14:910–8. doi: 10.1093/neuonc/nos087
33. Pietrantonio F, Aprile G, Rimassa L, Franco P, Lonardi S, Cremolini C, et al. A new nomogram for estimating survival in patients with brainmetastases secondary to colorectal cancer. *RadiotherOncol* (2015) 117:315–21. doi: 10.1016/j.radonc.2015.08.023
34. Park Y, Kim KS, Kim K, Chie EK, Kim JH, Kim JS, et al. Nomogram prediction of survival in patients with brain metastases from hepatocellular carcinoma treated with whole-brain radiotherapy: a multicenter retrospective study. *J Neuro Oncol* (2015) 125:377–83. doi: 10.1007/s11060-015-1926-7
35. Zindler JD, Jochems A, Lagerwaard FJ, Beumer R, Troost EGC, Eekers DBP. Individualized early death and long-term survival prediction afterstereotactic radiosurgery for brain metastases of non-small cell lung cancer:Two externally validated nomograms. *Radiother Oncol* (2017) 123:189–94. doi: 10.1016/j.radonc.2017.02.006

Conflict of Interest: The authors declare that the research was conducted in the absence of any commercial or financial relationships that could be construed as a potential conflict of interest.

frontiers in Oncology

ORIGINAL RESEARCH
published: 17 February 2021
doi: 10.3389/fonc.2020.599888

Non-Invasive Radiomics Approach Predict Invasiveness of Adamantinomatous Craniopharyngioma Before Surgery

*Guofo Ma[1], Jie Kang[1], Ning Qiao[1], Bochao Zhang[1], Xuzhu Chen[2], Guilin Li[3], Zhixian Gao[1] and Songbai Gui[1]**

[1] Department of Neurosurgery, Beijing Tiantan Hospital, Capital Medical University, Beijing, China, [2] Department of Radiology, Beijing Tiantan Hospital, Capital Medical University, Beijing, China, [3] Neuropathology Department, Beijing Neurosurgical Institute, Capital Medical University, Beijing, China

OPEN ACCESS

Edited by:
Harrison Bai,
Brown University, United States

Reviewed by:
Jiaojian Wang,
University of Electronic Science and Technology of China, China
Wei Wei,
Xi'an Polytechnic University, China

***Correspondence:**
Songbai Gui
guisongbai@yeah.net

Specialty section:
This article was submitted to Cancer Imaging and Image-directed Interventions, a section of the journal Frontiers in Oncology

Received: 28 August 2020
Accepted: 30 December 2020
Published: 17 February 2021

Citation:
Ma G, Kang J, Qiao N, Zhang B, Chen X, Li G, Gao Z and Gui S (2021) Non-Invasive Radiomics Approach Predict Invasiveness of Adamantinomatous Craniopharyngioma Before Surgery. Front. Oncol. 10:599888. doi: 10.3389/fonc.2020.599888

Purpose: Craniopharyngiomas (CPs) are benign tumors, complete tumor resection is considered to be the optimal treatment. However, although histologically benign, the local invasiveness of CPs commonly contributes to incomplete resection and a poor prognosis. At present, some advocate less aggressive surgery combined with radiotherapy as a more reasonable and effective means of protecting hypothalamus function and preventing recurrence in patients with tight tumor adhesion to the hypothalamus. Hence, if a method can be developed to predict the invasiveness of CP preoperatively, it will help in the development of a more personalized surgical strategy. The aim of the study was to report a radiomics-clinical nomogram for the individualized preoperative prediction of the invasiveness of adamantinomatous CP (ACPs) before surgery.

Methods: In total, 1,874 radiomics features were extracted from whole tumors on contrast-enhanced T1-weighted images. A support vector machine trained a predictive model that was validated using receiver operating characteristic (ROC) analysis on an independent test set. Moreover, a nomogram was constructed incorporating clinical characteristics and the radiomics signature for individual prediction.

Results: Eleven features associated with the invasiveness of ACPs were selected by using the least absolute shrinkage and selection operator (LASSO) method. These features yielded area under the curve (AUC) values of 79.09 and 73.5% for the training and test sets, respectively. The nomogram incorporating peritumoral edema and the radiomics signature yielded good calibration in the training and test sets with the AUCs of 84.79 and 76.48%, respectively.

Conclusion: The developed model yields good performance, indicating that the invasiveness of APCs can be predicted using noninvasive radiological data. This reliable, noninvasive tool can help clinical decision making and improve patient prognosis.

Keywords: craniopharyngioma, adamantinomatous, invasiveness, radiomics, machine learning, nomogram

INTRODUCTION

Craniopharyngiomas (CPs) are rare and non-neuroepithelial entities arising from a malformation of embryonal tissue, with an incidence of 0.5–2 cases per million persons per year (1–3). Two histological subtypes have been identified: adamantinomatous CPs (ACPs) and papillary CPs (PCPs). They are commonly located in the suprasellar region and can cause devastating neuroendocrine dysfunction by mass effect and/or invasion to the optic apparatus, pituitary gland and hypothalamus. Complete tumor resection with improvement in visual function, and no further deterioration of neuroendocrine and cognitive function is considered the optimal treatment outcome. However, although these massed are of a benign histological nature, the abovementioned ideal treatment goal is not always achievable due to the potential close adhesion of CPs to surrounding brain tissue.

Pathological studies have confirmed that the histology of the interface between CPs and surrounding brain tissue can be classified into two types, including finger-like invasion and no finger-like invasion (4–6). Numerous investigators have deemed that such local invasion resulting in adhesion could be associated with the failure of complete resection and poor prognosis (7–9). Therefore, a preoperative noninvasive method for identifying the invasiveness of CPs could help in the development of more individualized treatment decisions. Addressing this problem, we developed a machine learning radiomics model to predict the invasiveness of ACPs before surgery.

Radiomics is an emerging research method that can effectively evaluate the heterogeneity of tumors by extracting a large number of image features from medical images. Its applicability and utility have already been validated in several tumor types; Zhang et al. focused on the preoperative prediction of nonfunctioning pituitary adenoma subtypes before surgery (10); Li et al. predicted P53 status, progression-free survival (PFS), phosphatase and tensin homolog (PTEN) and vascular endothelial growth factor (VEGF) expression in patients with gliomas (11–14). Furthermore, radiomics approaches have also been validated in meningiomas (15), lung cancer (16) and skull base chordomas (17).

In the current study, we extracted a large number of radiomics features from preoperative MRI scans of ACPs with known local invasiveness. We hypothesized that a radiomics model could predict the invasiveness of ACPs via a machine-learning algorithm.

METHODS

Patients

We retrospectively reviewed the medical records of patients who underwent surgery for craniopharyngioma from 2002 to 2019, and a total 335 cases of ACPs were included in this study. Their radiographic and pathological data were collected from picture archiving and communications systems. The pathological sections were reviewed by two individual senior neuropathologists to confirm the histology of the interface between the ACPs and surrounding brain tissue (**Figures S2** and **S4**). Potential candidates were excluded if their pathological sections could not reflect the relationship between the ACP and brain tissues. Furthermore, MRI images were reviewed by two experienced radiologists to identify whether peritumor edema was present on T2-weighted images. Any disagreement was resolved by a consultation. The inclusion criteria were as follows: 1) histologically confirmed as ACPs; 2) the definite invasiveness of each tumor; 3) complete preoperative MRI data [including T2-weighted, T1-weighted and contrast enhanced (CE)-T1 images]; 4) no history of surgical treatment; and 5) available clinical characteristics. Among 335 patients, 225 patients who were treated between January 2002 and December 2015 were allocated to the training set, and 110 patients who were treated between January 2016 and December 2019 were allocated to the validating set. The training set was used to establish a stable model to predict the invasiveness of ACPs via radiomics features, while the validation set was used to assess the prediction accuracy of the model. The study was approved and reviewed by the institutional review board.

MRI Acquisition and Tumor Segmentation

CE-T1 images were used for the extraction of radiomics features, as these images are optimal for identifying the tumor border. MRI was performed in the head-first supine position on a 3-T scanner (Tim Trio, Siemens) using a head coil. The acquisition parameters for precontrast T1-weighted sequences were as follows: repetition time, 156–2,520 ms; echo time, 2–19.7 ms; flip angle:150°; field of view: 240×188 mm^2; acquisition matrix: 384×300 and slice thickness: 5 mm. The study was repeated immediately after the rapid injection of contrast agent gadolinium-DTPA (0.1 mmol/kg Gadovist; Beijing Beilu Pharmaceutical Co., Beijing China). The regions of interest (ROI), i.e., whole tumors, were manually delineated by two neuroradiologists on the CE-T1 images using MRIcron software (http://www.mccauslandcenter.sc.edu/mricro) (**Figure S1** and **S3**). The two neuroradiologists were blinded to the patients' clinical characteristics. Next, a third senior neuroradiologist reevaluated the ROIs and made final decisions when discrepancies were ≥ 5%.

Feature Extraction

First, we homogenized the image intensity on all MR images by z-score transformation (MATLAB version 2014a; The Mathworks, Natick, MA, USA) to avoid heterogeneity bias. In this study, a total of 1,874 features were acquired (**Table S1**). The features were divided into eight categories: (a) first-order statistics, (b) shape-based, (c) Gray Level Cooccurence Matrix (GLCM), (d) Gray Level Run Length Matrix (GLRLM), (e) Gray Level Size Zone Matrix (GLSZM), (f) Neighboring Gray Tone Difference Matrix (NGTDM), (g) Gray Level Dependence Matrix (GLDM), and (h) wavelet features, they were derived from first-order statistics and texture features via wavelet decomposition (using directional low-pass and high-pass filtering.

Feature Selection and Classification

We used the least absolute shrinkage and selection operator (LASSO) algorithm, which is a suitable and powerful method for

the regression of high-dimensional data, to screen the most predictive features in the training set. In this procedure, the tuning parameter (lambda) was selected by the cross-validation method; the optimal lambda was confirmed as that which resulted in the smallest cross-validation error. Then, a support vector machine (SVM) classifier was used to establish a machine-learning model for invasiveness prediction. The performance of the classification model was evaluated and validated by employing 10-fold cross-validation. Receiver operator characteristic (ROC) curve analysis was performed for both the training and validation sets to evaluate the discriminative ability of the machine-learning model.

Radiomics-Clinical Nomogram Construction and Performance Assessment

To provide a more individualized predictive model, a nomogram was built from the training set data. First, a radiomics signature was constructed using the selected features, and represented by a radiomics score. The score was calculated for each patient as a linear combination of the selected features weighted by their respective coefficients. Second, the radiomics signature and other clinical predictors (age, sex, peritumoral edema, tumor size) were tested using a multivariate logistic regression algorithm in the training set. The final selection of the model for the nomogram was conducted using a backward step-down selection process based on the Akaike information criterion. The performance of the nomogram was estimated with the training cohort and then tested with the validation cohort.

Statistics

The Mann–Whitney U test and chi-square test were used to evaluate whether age, sex, tumor invasiveness and peritumoral edema were significantly different between the training set and validation set. They were performed by using SPSS software version 22.0 (IBM Corp.) Statistical significance was set as $p < 0.05$. The LASSO algorithm, SVM classifier, ROC curve analysis and nomogram were performed based on "glmnet", "e1071", "pROC", and "rms" packages in R software version 3.3.2 (The R Foundation, Salt Lake City, UT, USA), respectively.

RESULTS

Clinical Characteristics

A total 187 male and 148 female patients was enrolled in the study, with 51 pediatric patients (mean age 14.3 years, range 6–17 years) and 284 adult patients (mean age 41.6 years, range 18–71 years). Among these patients, 129 men and 96 women were allocated to the training group and 58 men and 52 women were allocated to the validation group via random assignment. The ratios of invasiveness to noninvasiveness were 65/160 in the training group and 31/79 in the validation set. The distributions of the characteristics of the two groups were compared using the Mann–Whitney U test and the chi-square test, and there were no significant differences in age ($p = 0.61$), sex ($p = 0.43$), peritumoral edema ($p = 0.38$), tumor size or invasiveness ($p = 0.22$). Detailed information pertaining to the clinical characteristics of the patients is shown in **Table 1**.

TABLE 1 | Patient characteristics.

	Training	Validation	P value
Age(years, mean)	37.2	35.63	0.61[a]
Sex(Male/Female)	129/96	58/52	0.43[b]
Peritumoral edema	48/177	19/91	0.38[b]
Tumor invasiveness	65/120	31/79	0.22[b]

[a]*Mann-Whitney U test,* [b]*Chi-square test.*

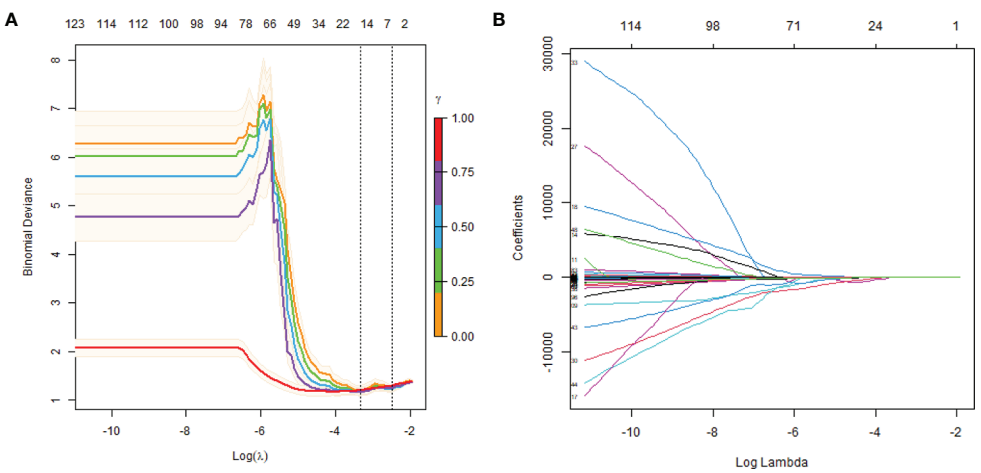

FIGURE 1 | Texture feature selection using LASSO logistic regression. **(A)** Selection of the tuning parameter (lambda). The dotted vertical lines are plotted at the optimal λ values based on the minimum criteria and 1 standard error of the minimum criteria. **(B)** LASSO coefficient profiles are shown for the 1874 texture features. A vertical line is drawn at the value where the optimal lambda results in 11 nonzero coefficients.

Machine-Learning Model for Predicting the Invasiveness of ACPs

In this study, the LASSO algorithm was used to select features with nonzero coefficients, and a subset of 11 features were screened from a total of 1,874 radiomic features (**Figures 1A, B**). The names and descriptions of these 11 selected features are shown in **Table 2**.

A machine-learning model was constructed based on the selected features and the SVM classifier with the training set data. The AUC was 79.09% following ROC curve analysis, and the sensitivity, specificity, and accuracy were 81.97%, 66.74 and 75%, respectively at the optimal cutoff point (0.609) (**Figure 2A**). Then, the model was applied to the validation set, and the invasiveness of the ACPs was effectively predicted. In the ROC curve analysis, the AUC was 73.5%. In addition, the optimal cutoff value (0.568) yielded a sensitivity, specificity, and accuracy of 69.53, 72.44, and 66.53%, respectively (**Figure 2B**). Hence, the 11 radiological features that constituted our model were regarded as an effective radiomics signature for the invasiveness of ACPs.

Development and Validation of the Individualized Predictive Nomogram

The radiomics signature and peritumoral edema were identified as independent predictors of ACP invasiveness based on the multivariate logistic regression algorithm (**Table 3**). The nomogram showed favorable discrimination with an AUC of 84.79% [95% confidence interval (CI), 84.12–85.46%] in the training set (**Figures 3A, B**). The radiomic nomogram also showed good discrimination with an AUC of 76.48% (95% CI, 74.13–78.83%) in the testing set (**Figure 3C**).

DISCUSSION

Although the history of surgical treatment for CPs has been spanned the course of more than 100 years, these masses still pose a surgical challenge even after the application of modern neurosurgical techniques (18–22). Numerous studies have revealed that quality of life (QoL) and cognitive performance

TABLE 2 | Eleven prognostic radiomics features selected by the LASSO algorithm.

Features	Descriptions	Coefficients
First order_ Skewness	Skewness measures the asymmetry of the distribution of values about the Mean value.	-2.7×10^{-1}
GLSZM_ Gray Level Variance	Measuring the variance in gray level intensities for the zones.	4.32×10^{-1}
Shape _Sphericity	Measuring the roundness of the shape of the tumor region relative to a circle	1.13×10^{-1}
Shape _ Surface Volume Ratio	A lower value indicates a more compact (sphere-like) shape and dependent on the volume of the ROI.	2.46×10^{-2}
GLCM _ Contrast	Measuring the local intensity variation, favoring values away from the diagonal.	2.87×10^{-3}
wavelet-HLL_ GLDM_ DNU	Describing the homogeneity among dependencies in the image. The value is low if the image has more similarity.	-5.1×10^{-1}
wavelet-LHL_GLCM_ Autocorrelation	Describing the magnitude of the fineness and coarseness of texture.	-6.72×10^{-2}
wavelet-HLH_ NGTDM_ Busyness	Describing the change from a pixel to its neighbor. The value is high if the changes of intensity between pixels and its neighborhood is rapid.	-1.91
wavelet-LLL_ NGTDM _Complexity	Describing the complexity of the image. The value is high if there are many rapid changes in gray level intensity.	4.09×10^{-3}
wavelet-HLL_ GLSZM_ SAHGLE	Describing the distribution of smaller size zones with higher gray-level values.	-1.17×10^{-1}
wavelet-LLH_ GLSZM _ SZNUN	Describing the variability of size zone volumes throughout the image.	-7.42×10^{-2}

DNU, Dependence Non Uniformity; SAHGLE, Small Area High Gray Level Emphasis; SZNUN, Size Zone Non Uniformity Normalized.

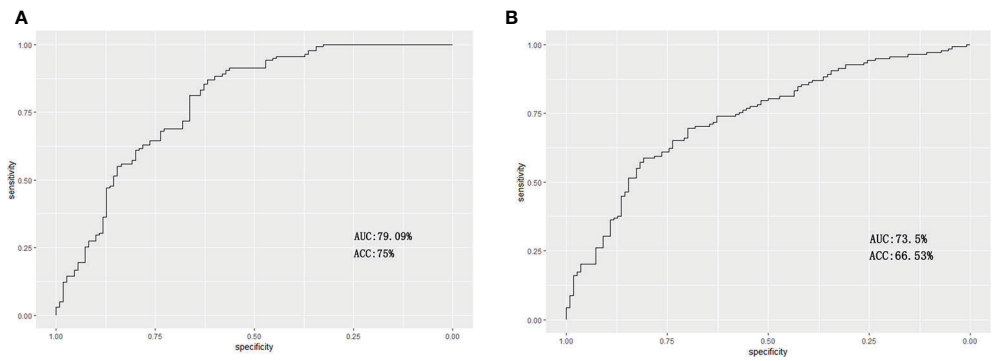

FIGURE 2 | Receiver operating characteristic curves for the prediction of invasiveness of ACPs in the training and validation sets. **(A)** For the training set, the area under the curve (AUC) was 79.09% with a sensitivity, specificity and accuracy of 81.97, 66.74, and 75%, respectively. **(B)** For the validation set, the AUC was 73.5% with a sensitivity, specificity and accuracy of 69.53, 72.44, and 66.53%, respectively.

TABLE 3 | Multivariate logistic regression analysis of the radiomics score and clinical predictors in the training set.

	Univariate logistic regression			Multivariate logistic regression		
	HR	95% CI	P value	HR	95% CI	P value
Age, per 1 year increase	0.927	0.552–1.556	0.77			
Sex (male)	0.988	0.972–1.005	0.16			
Peritumoral edema	2.499	1.351–4.624	0.014	1.964	1.018–3.788	0.036
Tumor size, per 1cm increase	1.719	1.899–3.288	0.101			
Radiomics score, per 0.1 increase	1.583	1.079–2.458	<0.001	1.257	1.072–1.473	0.005

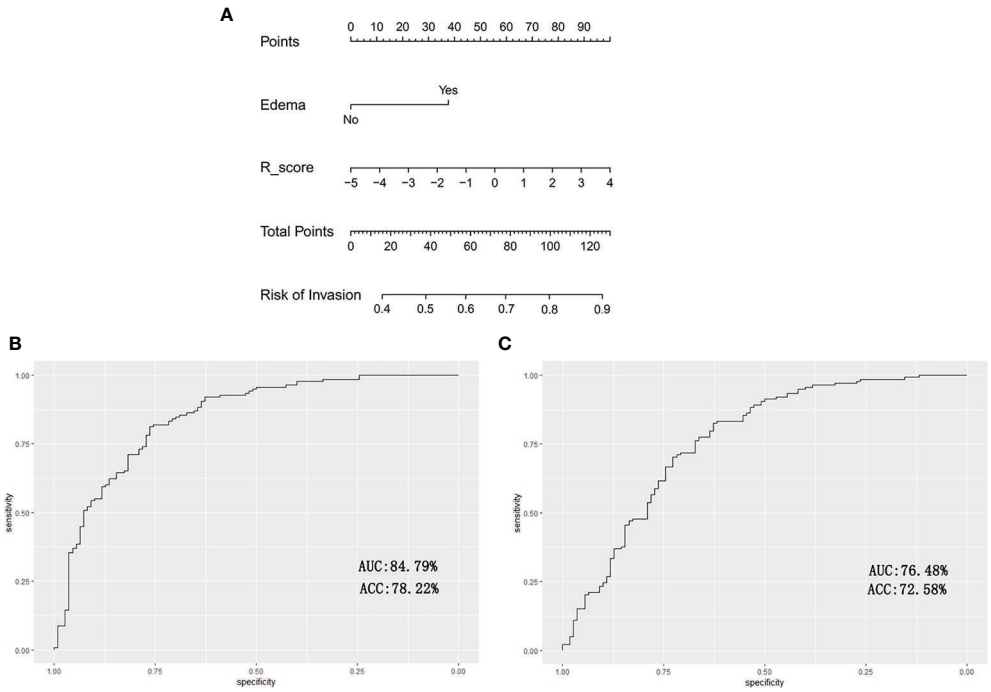

FIGURE 3 | The radiomic-clinical nomogram and its performance are illustrated. **(A)** The radiomics-clinical nomogram developed to predict the invasiveness of ACPs is illustrated. **(B)** For the training set, the AUC was 84.79% with the sensitivity, specificity and accuracy of 83.27, 76.05, and 78.22%, respectively. **(C)** For the validation set, the AUC was 76.48% with a sensitivity, specificity and accuracy of 71.24, 72.33, and 72.58%, respectively.

are frequently impaired in long-term survivors after surgery due to the anatomical proximity of the CPs to the optic nerve and to the hypothalamic-pituitary axes (23–25). Some researchers have advocated less aggressive surgery combined with radiotherapy as a more reasonable and effective means of protecting hypothalamus function and preventing recurrence in the patients with tight tumor adhesion to the hypothalamus (26–28). Therefore, it is important to assess the aggressiveness of the tumor before surgery. In the present study, we used the noninvasive radiomics method to predict the invasiveness of ACPs before surgery, which made it possible to develop a personalized surgical protocol. Note that to avoid heterogeneity between the two histopathological CP subtypes, only ACPs were included in the study.

In our cohort, there were more male patients (n = 187, 55.82%) than female patients (n = 148, 44.18%), consistent with previous reports (29–31). Although CPs were more common among child patients, the proportion of adult patients was higher in this study (84.78 vs. 15.22%); because adult patients were the main group of patients in our ward.

To date, radiomics studies on craniopharyngiomas are rare. Yue et al. proposed a machine learning model for discriminating BRAF mutation and wild type among craniopharyngiomas with sensitivity of 1.00 and specificity of 0.91 (32). Chen et al. predicted the pathological subtype and gene mutations in craniopharyngiomas with radiomics (33).

Radiomics is an emerging diagnostic technique, and the potential ability of improving clinical decision support systems has been well verified. Some successful precedents have been demonstrated in radiomics studies for identifying the invasiveness of tumors. For example, a previous report showed that preinvasive pulmonary adenocarcinomas and invasive pulmonary adenocarcinomas could be distinguished by constructing a radiomics-clinical nomogram predictive model

with an AUC of 0.903 (34). Another report revealed that the muscular invasiveness of bladder cancer could be evaluated by a noninvasive radiomics model (35). Furthermore, Zhu et al. proposed a learning radiomics model for preoperative grading in meningioma (36). In the present study, we employed a radiomics approach to provide preoperatively predict the invasiveness of ACPs. The high-throughput features applied in our radiomics model were extracted from the whole tumor on preoperative CE-T1 images, which could reflect the heterogeneity of the tumor. Subsequently, 11 invasiveness-associated features were screened by using the LASSO algorithm, consisting of one first-order feature, two shape-based features, two texture features, and six wavelet features. Most of these selected features were also reported in previous studies of tumor invasiveness (35, 37). Our predicted model constructed by using an SVM classifier achieved AUCs of 79.09% in the training set data and 73.5% in the validation set data. The results indicate that the invasiveness of APCs can be predicted using noninvasive radiological data, and the proposed radiomics signature performed well in the training and validation sets.

Tumor invasiveness is closely associated with gene mutations and/or relative protein expression levels. However, owing to its rarity and benign histological nature, studies of the genomics and molecular pathology of CPs are limited. A previous study revealed that the expression of claudin-1, a tight junction protein expressed in epithelial tissues that plays important roles in cell polarity and adhesion, could be strongly associated with the invasiveness of CPs (38). The authors found that the invasive CPs exhibited significantly lower claudin-1 expression than their noninvasive counterparts regardless of CP subtype. We suggest that this difference may be the basis of the molecular pathology for distinguishing invasive and noninvasive ACPs by using the radiomics method.

The individualized predictive nomogram, incorporated the radiomics signature and peritumoral edema into a model, which facilitated the individualized prediction of the invasiveness of ACPs. The radiomic-clinical nomogram showed better discrimination in the training and validation sets with AUCs of 84.79 and76.48%, respectively. This revealed that combining multiple clinical risk factors to estimate and determine follow-up treatment, rather than focusing on a single radiological feature, is very necessary.

There are some limitations in our study. First, to build the radiomics signature and predictive model, we analyzed axial CE-T1 images, which are usually referred to clinically; however, combinations with other sequences such as fluid attenuated inversion recovery (FLAIR) imaging and T2-weighted imaging may have provided additional information and improved the performance of the predictive model. Second, potential selection biases might have occurred because of the retrospective nature of the study. Third, the imaging protocols used were not fully consistent in that the imaging data were acquired with different MRI scanners.

CONCLUSION

We proposed a radiomics-clinical nomogram for the individualized preoperative prediction of the invasiveness of ACPs. This reliable, noninvasive tool can help clinical decision making and improve patient prognosis.

DATA AVAILABILITY STATEMENT

The raw data supporting the conclusions of this article will be made available by the authors, without undue reservation.

ETHICS STATEMENT

The studies involving human participants were reviewed and approved by The Ethics Committee of Beijing Tiantan Hospital affiliated to Capital Medical University. Written informed consent to participate in this study was provided by the participants' legal guardian/next of kin.

AUTHOR CONTRIBUTIONS

GM collected and analyzed clinical data, and prepared the manuscript. SG designed the trial and revised the manuscript. NQ and BZ collected clinical data. XC supervised the tumor segmentation. GL supervised the evaluation of the histology of the interface between CPs and surrounding brain tissue. All authors contributed to the article and approved the submitted version.

SUPPLEMENTARY MATERIAL

The Supplementary Material for this article can be found online at: https://www.frontiersin.org/articles/10.3389/fonc.2020.599888/full#supplementary-material

REFERENCES

1. Garrè ML, Cama A. Craniopharyngioma: modern concepts in pathogenesis and treatment. *Curr Opin Pediatr* (2007) 19(4):471–9. doi: 10.1097/MOP.0b013e3282495a22
2. Nielsen EH, Feldt-Rasmussen U, Poulsgaard L, Kristensen LO, Astrup J, Jørgensen JO, et al. Incidence of craniopharyngioma in Denmark (n = 189) and estimated world incidence of craniopharyngioma in children and adults. *J Neuro-Oncol* (2011) 104(3):755–63. doi: 10.1007/s11060-011-0540-6
3. Bunin GR, Surawicz TS, Witman PA, Preston-Martin S, Davis F, Bruner JM. The descriptive epidemiology of craniopharyngioma. *J Neurosurg* (1998) 89(4):547–51. doi: 10.3171/jns.1998.89.4.0547
4. Kawamata T, Kubo O, Hori T. Histological findings at the boundary of craniopharyngiomas. *Brain Tumor Pathol* (2005) 22(2):75–8. doi: 10.1007/s10014-005-0191-4
5. Liu Y, Qi ST, Wang CH, Pan J, Fan J, Peng JX, et al. Pathological Relationship Between Adamantinomatous Craniopharyngioma and Adjacent Structures Based on QST Classification. *J Neuropathol Exp Neurol* (2018) 77(11):1017–23. doi: 10.1093/jnen/nly083

6. Burghaus S, Hölsken A, Buchfelder M, Fahlbusch R, Riederer BM, Hans V, et al. A tumor-specific cellular environment at the brain invasion border of adamantinomatous craniopharyngiomas. *Virchows Archiv an Int J Pathol* (2010) 456(3):287–300. doi: 10.1007/s00428-009-0873-0
7. Sterkenburg AS, Hoffmann A, Gebhardt U, Warmuth-Metz M, Daubenbüchel AM, Müller HL. Survival, hypothalamic obesity, and neuropsychological/psychosocial status after childhood-onset craniopharyngioma: newly reported long-term outcomes. *Neuro-oncology* (2015) 17(7):1029–38. doi: 10.1093/neuonc/nov044
8. Gautier A, Godbout A, Grosheny C, Tejedor I, Coudert M, Courtillot C, et al. Markers of recurrence and long-term morbidity in craniopharyngioma: a systematic analysis of 171 patients. *J Clin Endocrinol Metab* (2012) 97(4):1258–67. doi: 10.1210/jc.2011-2817
9. Fjalldal S, Holmer H, Rylander L, Elfving M, Ekman B, Osterberg K, et al. Hypothalamic involvement predicts cognitive performance and psychosocial health in long-term survivors of childhood craniopharyngioma. *J Clin Endocrinol Metab* (2013) 98(8):3253–62. doi: 10.1210/jc.2013-2000
10. Zhang S, Song G, Zang Y, Jia J, Wang C, Li C, et al. Non-invasive radiomics approach potentially predicts non-functioning pituitary adenomas subtypes before surgery. *Eur Radiol* (2018) 28(9):3692–701. doi: 10.1007/s00330-017-5180-6
11. Li Y, Qian Z, Xu K, Wang K, Fan X, Li S, et al. MRI features predict p53 status in lower-grade gliomas via a machine-learning approach. *NeuroImage Clin* (2018) 17:306–11. doi: 10.1016/j.nicl.2017.10.030
12. Liu X, Li Y, Qian Z, Sun Z, Xu K, Wang K, et al. A radiomic signature as a non-invasive predictor of progression-free survival in patients with lower-grade gliomas. *NeuroImage Clin* (2018) 20:1070–7. doi: 10.1016/j.nicl.2018.10.014
13. Li Y, Liang Y, Sun Z, Xu K, Fan X, Li S, et al. Radiogenomic analysis of PTEN mutation in glioblastoma using preoperative multi-parametric magnetic resonance imaging. *Neuroradiology* (2019) 61(11):1229–37. doi: 10.1007/s00234-019-02244-7
14. Sun Z, Li Y, Wang Y, Fan X, Xu K, Wang K, et al. Radiogenomic analysis of vascular endothelial growth factor in patients with diffuse gliomas. *Cancer Imaging Off Publ Int Cancer Imaging Soc* (2019) 19(1):68. doi: 10.1186/s40644-019-0256-y
15. Zhang J, Yao K, Liu P, Liu Z, Han T, Zhao Z, et al. A radiomics model for preoperative prediction of brain invasion in meningioma non-invasively based on MRI: A multicentre study. *EBioMedicine* (2020) 58. doi: 10.1016/j.ebiom.2020.102933 102933.
16. Shi L, He Y, Yuan Z, Benedict S, Valicenti R, Qiu J, et al. Radiomics for Response and Outcome Assessment for Non-Small Cell Lung Cancer. *Technol Cancer Res Treat* (2018) 17. doi: 10.1177/1533033818782788 1533033818782788.
17. Wei W, Wang K, Liu Z, Tian K, Wang L, Du J, et al. Radiomic signature: A novel magnetic resonance imaging-based prognostic biomarker in patients with skull base chordoma. *Radiother Oncol J Eur Soc Ther Radiol Oncol* (2019) 141:239–46. doi: 10.1016/j.radonc.2019.10.002
18. Gardner PA, Prevedello DM, Kassam AB, Snyderman CH, Carrau RL, Mintz AH. The evolution of the endonasal approach for craniopharyngiomas. *J Neurosurg* (2008) 108(5):1043–7. doi: 10.3171/jns/2008/108/5/1043
19. Yang I, Sughrue ME, Rutkowski MJ, Kaur R, Ivan ME, Aranda D, et al. Craniopharyngioma: a comparison of tumor control with various treatment strategies. *Neurosurg Focus* (2010) 28(4):E5. doi: 10.3171/2010.1.Focus09307
20. Jeswani S, Nuño M, Wu A, Bonert V, Carmichael JD, Black KL, et al. Comparative analysis of outcomes following craniotomy and expanded endoscopic endonasal transsphenoidal resection of craniopharyngioma and related tumors: a single-institution study. *J Neurosurg* (2016) 124(3):627–38. doi: 10.3171/2015.3.Jns142254
21. Chakrabarti I, Amar AP, Couldwell W, Weiss MH. Long-term neurological, visual, and endocrine outcomes following transnasal resection of craniopharyngioma. *J Neurosurg* (2005) 102(4):650–7. doi: 10.3171/jns.2005.102.4.0650
22. Ozgural O, Kahilogullari G, Dogan I, Al-Beyati ESM, Bozkurt M, Tetik B, et al. Single-Center Surgical Experience of the Treatment of Craniopharyngiomas With Emphasis on the Operative Approach: Endoscopic Endonasal and Open Microscopic Transcranial Approaches. *J Craniofac Surg* (2018) 29(6):e572–8. doi: 10.1097/scs.0000000000004592
23. Müller HL. Childhood craniopharyngioma–current concepts in diagnosis, therapy and follow-up. *Nat Rev Endocrinol* (2010) 6(11):609–18. doi: 10.1038/nrendo.2010.168
24. Müller HL. Childhood craniopharyngioma: current controversies on management in diagnostics, treatment and follow-up. *Expert Rev Neurother* (2010) 10(4):515–24. doi: 10.1586/ern.10.15
25. Muller HL. Childhood craniopharyngioma. Recent advances in diagnosis, treatment and follow-up. *Horm Res* (2008) 69(4):193–202. doi: 10.1159/000113019
26. Wen BC, Hussey DH, Staples J, Hitchon PW, Jani SK, Vigliotti AP, et al. A comparison of the roles of surgery and radiation therapy in the management of craniopharyngiomas. *Int J Radiat Oncol Biol Phys* (1989) 16(1):17–24. doi: 10.1016/0360-3016(89)90005-9
27. Hetelekidis S, Barnes PD, Tao ML, Fischer EG, Schneider L, Scott RM, et al. 20-year experience in childhood craniopharyngioma. *Int J Radiat Oncol Biol Phys* (1993) 27(2):189–95. doi: 10.1016/0360-3016(93)90227-m
28. Rajan B, Ashley S, Gorman C, Jose CC, Horwich A, Bloom HJ, et al. Craniopharyngioma–a long-term results following limited surgery and radiotherapy. *Radiother Oncol: J Eur Soc Ther Radiol Oncol* (1993) 26(1):1–10. doi: 10.1016/0167-8140(93)90019-5
29. Feng Y, Ni M, Wang YG, Zhong LY. Comparison of neuroendocrine dysfunction in patients with adamantinomatous and papillary craniopharyngiomas. *Exp Ther Med* (2019) 17(1):51–6. doi: 10.3892/etm.2018.6953
30. Goschzik T, Gessi M, Dreschmann V, Gebhardt U, Wang L, Yamaguchi S, et al. Genomic Alterations of Adamantinomatous and Papillary Craniopharyngioma. *J Neuropathol Exp Neurol* (2017) 76(2):126–34. doi: 10.1093/jnen/nlw116
31. Kiliç M, Can SM, Özdemir B, Tanik C. Management of Craniopharyngioma. *J Craniofac Surg* (2019) 30(2):e178–83. doi: 10.1097/scs.0000000000005136
32. Yue Q, Yu Y, Shi Z, Wang Y, Zhu W, Du Z, et al. Prediction of BRAF mutation status of craniopharyngioma using magnetic resonance imaging features. *J Neurosurg* (2018) 129(1):27–34. doi: 10.3171/2017.4.Jns163113
33. Chen X, Tong Y, Shi Z, Chen H, Yang Z, Wang Y, et al. Noninvasive molecular diagnosis of craniopharyngioma with MRI-based radiomics approach. *BMC Neurol* (2019) 19(1):6. doi: 10.1186/s12883-018-1216-z
34. Zhao W, Xu Y, Yang Z, Sun Y, Li C, Jin L, et al. Development and validation of a radiomics nomogram for identifying invasiveness of pulmonary adenocarcinomas appearing as subcentimeter ground-glass opacity nodules. *Eur J Radiol* (2019) 112:161–8. doi: 10.1016/j.ejrad.2019.01.021
35. Zheng J, Kong J, Wu S, Li Y, Cai J, Yu H, et al. Development of a noninvasive tool to preoperatively evaluate the muscular invasiveness of bladder cancer using a radiomics approach. *Cancer* (2019) 125(24):4388–98. doi: 10.1002/cncr.32490
36. Zhu Y, Man C, Gong L, Dong D, Yu X, Wang S, et al. A deep learning radiomics model for preoperative grading in meningioma. *Eur J Radiol* (2019) 116:128–34. doi: 10.1016/j.ejrad.2019.04.022
37. Zhao S, Su Y, Duan J, Qiu Q, Ge X, Wang A, et al. Radiomics signature extracted from diffusion-weighted magnetic resonance imaging predicts outcomes in osteosarcoma. *J Bone Oncol* (2019) 19:100263. doi: 10.1016/j.jbo.2019.100263
38. Stache C, Hölsken A, Fahlbusch R, Flitsch J, Schlaffer SM, Buchfelder M, et al. Tight junction protein claudin-1 is differentially expressed in craniopharyngioma subtypes and indicates invasive tumor growth. *Neuro-oncology* (2014) 16(2):256–64. doi: 10.1093/neuonc/not195

Conflict of Interest: The authors declare that the research was conducted in the absence of any commercial or financial relationships that could be construed as a potential conflict of interest.

frontiers in Oncology

ORIGINAL RESEARCH
published: 05 March 2021
doi: 10.3389/fonc.2021.621088

Predicting Survival Duration With MRI Radiomics of Brain Metastases From Non-small Cell Lung Cancer

Bihong T. Chen[1], Taihao Jin[1], Ningrong Ye[1], Isa Mambetsariev[2], Tao Wang[3], Chi Wah Wong[4], Zikuan Chen[1], Russell C. Rockne[5], Rivka R. Colen[6], Andrei I. Holodny[7], Sagus Sampath[8] and Ravi Salgia[2]*

[1] Department of Diagnostic Radiology, City of Hope National Medical Center, Duarte, CA, United States, [2] Department of Medical Oncology and Therapeutics Research, City of Hope Comprehensive Cancer Center and Beckman Research Institute, Duarte, CA, United States, [3] Departments of Interventional Radiology, Nanjing First Hospital, Nanjing Medical University, Nanjing, China, [4] Applied AI and Data Science, City of Hope National Medical Center, Duarte, CA, United States, [5] Division of Mathematical Oncology, City of Hope National Medical Center, Duarte, CA, United States, [6] Department of Radiology, Hillman Cancer Center, University of Pittsburgh Medical Center, Pittsburgh, PA, United States, [7] Department of Radiology, Memorial Sloan-Kettering Cancer Center, New York, NY, United States, [8] Department of Radiation Oncology, City of Hope National Medical Center, Duarte, CA, United States

OPEN ACCESS

Edited by:
Xuejun Li,
Central South University, China

Reviewed by:
Bo Gao,
Affiliated Hospital of Guizhou Medical University, China
Minghao Dong,
Xidian University, China

***Correspondence:**
Bihong T. Chen
Bechen@coh.org
orcid.org/0000-0002-3127-0711

Specialty section:
This article was submitted to Neuro-Oncology and Neurosurgical Oncology, a section of the journal Frontiers in Oncology

Received: *25 October 2020*
Accepted: *08 February 2021*
Published: *05 March 2021*

Citation:
Chen BT, Jin T, Ye N, Mambetsariev I, Wang T, Wong CW, Chen Z, Rockne RC, Colen RR, Holodny AI, Sampath S and Salgia R (2021) Predicting Survival Duration With MRI Radiomics of Brain Metastases From Non-small Cell Lung Cancer. Front. Oncol. 11:621088. doi: 10.3389/fonc.2021.621088

Background: Brain metastases are associated with poor survival. Molecular genetic testing informs on targeted therapy and survival. The purpose of this study was to perform a MR imaging-based radiomic analysis of brain metastases from non-small cell lung cancer (NSCLC) to identify radiomic features that were important for predicting survival duration.

Methods: We retrospectively identified our study cohort via an institutional database search for patients with brain metastases from EGFR, ALK, and/or KRAS mutation-positive NSCLC. We segmented the brain metastatic tumors on the brain MR images, extracted radiomic features, constructed radiomic scores from significant radiomic features based on multivariate Cox regression analysis ($p < 0.05$), and built predictive models for survival duration.

Result: Of the 110 patients in the cohort (mean age 57.51 ± 12.32 years; range: 22–85 years, M:F = 37:73), 75, 26, and 15 had NSCLC with EGFR, ALK, and KRAS mutations, respectively. Predictive modeling of survival duration using both clinical and radiomic features yielded areas under the receiver operative characteristic curve of 0.977, 0.905, and 0.947 for the EGFR, ALK, and KRAS mutation-positive groups, respectively. Radiomic scores enabled the separation of each mutation-positive group into two subgroups with significantly different survival durations, i.e., shorter vs. longer duration when comparing to the median survival duration of the group.

Conclusion: Our data supports the use of radiomic scores, based on MR imaging of brain metastases from NSCLC, as non-invasive biomarkers for survival duration. Future research with a larger sample size and external cohorts is needed to validate our results.

Keywords: radiomics, machine learning, survival, lung cancer, brain metastases, brain MRI, artificial intelligence

INTRODUCTION

Lung cancer is the second most commonly diagnosed cancer (1). Non-small cell lung cancer (NSCLC) makes up ∼85–90% of all lung cancer cases, and 30–50% of patients with NSCLC develop brain metastases (2, 3). Despite advancements in treatment, the survival duration of patients with lung cancer brain metastases remains short, with a poor median survival of 4–8 months after diagnosis (4). Molecular characteristics help to determine whether patients with cancer will respond to targeted therapies thus prolong survival (5). The molecular testing of lung cancer usually screens for genes encoding epidermal growth factor receptor (EGFR), anaplastic lymphoma kinase (ALK) and Kirsten rat sarcoma viral oncogene homolog (KRAS) (6–8). Molecularly targeted medications that can penetrate the central nervous system have improved outcomes in patients with brain metastases from lung cancers with actionable mutations. For example, tyrosine kinase inhibitors, such as erlotinib, have been effective in treating brain metastases in NSCLC patients with EGFR mutations (9). Therefore, the knowledge of molecular mutation status is essential for planning individualized treatments and for predicting survival.

Pathological tissue confirmation and molecular characterization of brain metastases through invasive biopsy or surgical resection are not always possible or practical. In contrast, neuroimaging methods, such as brain magnetic resonance imaging (MRI), are commonly used to non-invasively assess the entire brain to diagnose and to plan treatments for patients with brain metastases. In addition, brain metastases may present with various imaging features depending on the mutation status of the primary NSCLC (10). However, little is known about the relationship between the neuroimaging features of brain metastases and the NSCLC mutation subtypes for survival prediction. There is an unmet need to identify non-invasive neuroimaging biomarkers to predict survival duration for NSCLC patients with brain metastases who may have one of the three most common mutations, i.e., EGFR, ALK, or KRAS.

Radiomics is a computerized method to extract high-dimensional data from non-invasive standard-of-care medical images (11). It can provide a detailed characterization of tumors, in terms of tumor heterogeneity in relation to aggressiveness, which are not perceptible to the human eye (12, 13). In addition, linking imaging features with molecular and immune characteristics will contribute valuable information that is critical for cancer treatment and prognosis (14). Furthermore, the radiomic approach allows the non-invasive analysis of treatment response and prognosis at multiple time points, which is not feasible or practical using invasive biopsies. Radiomic scores, which incorporate information about key imaging features, have shown potential as biomarkers for predicting survival in patients with lung cancer and breast cancers (13, 15, 16). However, to the best of our knowledge, no published studies have used radiomic analysis of brain metastases to predict survival duration of patients with NSCLC according to their mutation status.

Here, we performed a MRI radiomic analysis of brain metastases for survival duration in patients with NSCLC. We hypothesize that MRI radiomics of brain metastases could be used to predict survival duration in patients with NSCLC. Our objective was to use radiomic features extracted from MR images of the brain metastases to build machine learning models for predicting survival durations of patients with NSCLC according to the specific mutation status of their primary NSCLC, i.e., EGFR, ALK, or KRAS. In addition, we constructed a radiomic score for each mutation-positive group to predict whether the patients survived longer or shorter than the median survival duration for each group.

METHODS

Patient Selection and Imaging Acquisition

We retrospectively identified consecutive patients for this study by searching the Thoracic Oncology Registry for all lung cancer patients treated at City of Hope National Medical Center (Duarte, CA, USA) between 2009 and 2017. Eligibility criteria included the following: diagnosis of NSCLC; confirmation via genotype testing of an EGFR, ALK, and/or KRAS mutation in the primary NSCLC tumors; and having brain MRI scans performed to diagnose brain metastases but before initiating treatment for the brain metastases. Patient demographic data, survival information including date of death or last follow-up, and mutation status were abstracted from electronic medical records (**Table 1**). The Institutional Review Board at City of Hope National Medical Center approved this study and waived informed consent due to its retrospective nature. The study was conducted in accordance with the Declaration of Helsinki.

Brain MR images including both the T1-weighted contrast-enhanced (T1C) and T2-weighted fluid-attenuated inversion recovery (FLAIR) sequences were retrieved from our Picture Archiving and Communication System. Brain MR scans were obtained from the same in-house 3T VERIO Siemens scanner

TABLE 1 | Demographic information for the study cohort.

	EGFR (+) *N* = 75	*ALK* (+) *N* = 21	*KRAS* (+) *N* = 15	*p*-value
Age				
Mean ± SD	57.43 ± 12.09	53.81 ± 14.79	63.67 ± 6.40	0.09
Race				
Caucasian	34 (45.33%)	13(61.90%)	11 (73.33%)	
Asian	35 (46.67%)	7 (33.33%)	1 (6.67%)	0.016
Other[1]	6 (8%)	1 (0.04%)	3 (20%)	
Gender				
Male	24 (32%)	8 (38.10%)	5 (33.33%)	0.83
Female	51 (68%)	13 (61.90%)	10 (66.67%)	
History of Smoking				
Yes	20 (26.67%)	5 (23.80%)	12 (80%)	<0.001
No	55 (73.33%)	16 (76.19%)	3 (20%)	

[1]*American Indian or Alaska Native, African American, Native Hawaiian, or Pacific Islander. EGFR, epidermal growth factor receptor; ALK, anaplastic lymphoma kinase; KRAS, Kirsten rat sarcoma viral oncogene homolog.*

(Siemens, Erlangen, Germany). T1C sequence was acquired with axial T1-weighted three-dimensional (3D) magnetization prepared rapid gradient echo (MPRAGE) imaging after intravenous administration of MultiHance® (gadobenate dimeglumine) at 0.1 mmol/Kg. The FLAIR sequence for the peritumoral edema was acquired with routine imaging protocol. Detailed scanning parameters have been reported in our previous study (10).

Brain Tumor Segmentation

For image segmentation, we co-registered T1C and FLAIR images into the same geometric space under an affine transformation as established by the elastix toolbox (17). We segmented the T1C and FLAIR images for enhancing tumor and peritumoral edema, respectively. We performed image transformation and re-slicing with FSL scripts (https://fsl.fmrib.ox.ac.uk/fsl/fslwiki/).

Subsequently, we used ITK-SNAP, an open-source 3D image analysis software (www.itksnap.org) to contour the tumor boundaries of both T1C (for the enhancing tumor) and FLAIR (for the peritumoral edema) images in a semi-automated fashion on a slice-by-slice basis (18). This semi-automated method consisted of the two steps. First, the ITK-SNAP software automatically placed a region of interest box around the tumors. Second, the tumor boundaries were manually drawn slice-by-slice by our trained research personnel (NY, TW, and BC). One researcher (NY) was a neuroimaging researcher with 2 years of experience in tracing tumors for radiomic research. The other two researchers (TW and BC) were neuroradiologists with a combined 20 years of experience in neuroimaging. Discrepancy during tumor segmentation was resolved by consensus of the research group. We have reported the details of brain tumor segmentation previously (10). The imaging delineation (mask) of the two segmented phenotypes (enhancing tumor and peritumoral edema) were exported for radiomic analysis. Our analysis included up to 10 of the largest tumors from each patient, limited to tumors >5 mm in diameter because smaller tumors could not be reliably segmented for 3D analysis. Our dataset consisted of 452 lesions from 110 patients. **Figure 1** presents the schema for brain tumor segmentation, radiomic feature extraction, and predictive modeling for survival duration.

To assess the consistency of image segmentation and the stability of radiomic features extracted for modeling, two researchers (NY and TW) independently performed tumor segmentation on the brain images from 20 randomly selected patients with the results being blinded to each other. We then used their segmentation results to test the inter-observer variability. In addition, one researcher (NY) repeated the brain tumor segmentation twice with 1 month apart for testing the intra-observer variability. We used the interclass correlation coefficient (ICC) test to assess the consistency of the radiomic features for both inter-observer and intra-observer variability. An inter-observer and intra-observer ICC > 0.80 was considered stable for tumor segmentation and radiomic feature extraction. The inter-observer ICC between the two researchers (NY and TW) for tumor segmentation achieved at 0.96 ± 0.04 in a range from 0.87 to 0.99 and for edema segmentation achieved at 0.95 ± 0.05 in a range from 0.80 to 0.99. The intra-observer ICC between the two measurements by the same researcher (NY) achieved 0.99 ± 0.006 (range from 0.97 to 1.00), and 0.99 ± 0.007 (range from 0.97 to 1.00) for segmentation of tumor and edema, respectively. The results indicated favorable inter- and intra-observer reproducibility and stability for tumor segmentation and subsequent radiomic feature extraction.

Radiomic Feature Extraction and Selection

The image preprocessing and radiomic feature extraction have been previously reported by our group (10). Briefly, we preprocessed each of the T1C or FLAIR images using a pipeline consisting of three steps: (i) skull-stripping using the Brain Extraction Tool (BET; http://fsl.fmrib.ox.ac.uk/fsl/fslwiki/BET) and Free Surfer (https://surfer.nmr.mgh.harvard.edu/); (ii) bias field correction using the routine N4ITKBiasFieldCorrection of nipype (https://nipype.readthedocs.io/en/0.12.0/users/index.html); (iii) image intensity normalization using an algorithm to standardize the intensity scales across MR images of the same contrast (19). Subsequently, we applied six different filters (Wavelet, Laplacian of Gaussian, Square, Square Root, Logarithm, or Exponential) to each of the preprocessed images, generating six derived images. Therefore, there were 12 derived images associated with each brain lesion, 6 for each of the two original (T1C and FLAIR) images. Finally, we performed radiomic feature extraction using an open-source python package PyRadiomics (https://pyradiomics.readthedocs.io/en/latest/) (20) on each derived image by applying a tumor or edema mask based on the modality of the original image, i.e., applying the tumor mask on the six images derived from the original T1C image, and applying the edema mask on the six images derived from the original FLAIR image. We extracted three types of radiomic features from each image including: (i) textural features, including Gray Level Co-occurrence Matrix (GLCM), Gray Level Run Length Matrix (GLRLM), Gray Level Size Zone Matrix (GLSZM), Neighboring Gray Tone Difference Matrix (NGTDM), and Gray Level Dependence Matrix (GLDM); (ii) shape-based features, including Volume, Surface Area, and Sphericity; and (iii) intensity-based features, such as Minimum, Maximum, and Mean. We extracted a total of 2,786 radiomic features from the 12 derived images for each lesion.

We performed feature selection in two steps. First, we selected 2,520 stable features from the total of 2,786 features based on the inter-observer ICC test with a threshold of 0.8 (corrected $p < 0.05$). Second, from those 2,520, the 50 most relevant features for model building were selected using a minimum redundancy and maximum relevance (MRMR) algorithm (21).

Building Predictive Models for Survival Duration

We dichotomized the patients in each mutation-positive group into two subgroups, i.e., shorter and longer survival subgroups, by assigning the patients with survival duration shorter than the median of the mutation-positive group to the shorter survival subgroup and the remaining patients to the longer survival subgroup. Subsequently we built independent machine learning models for each mutation-positive group to predict

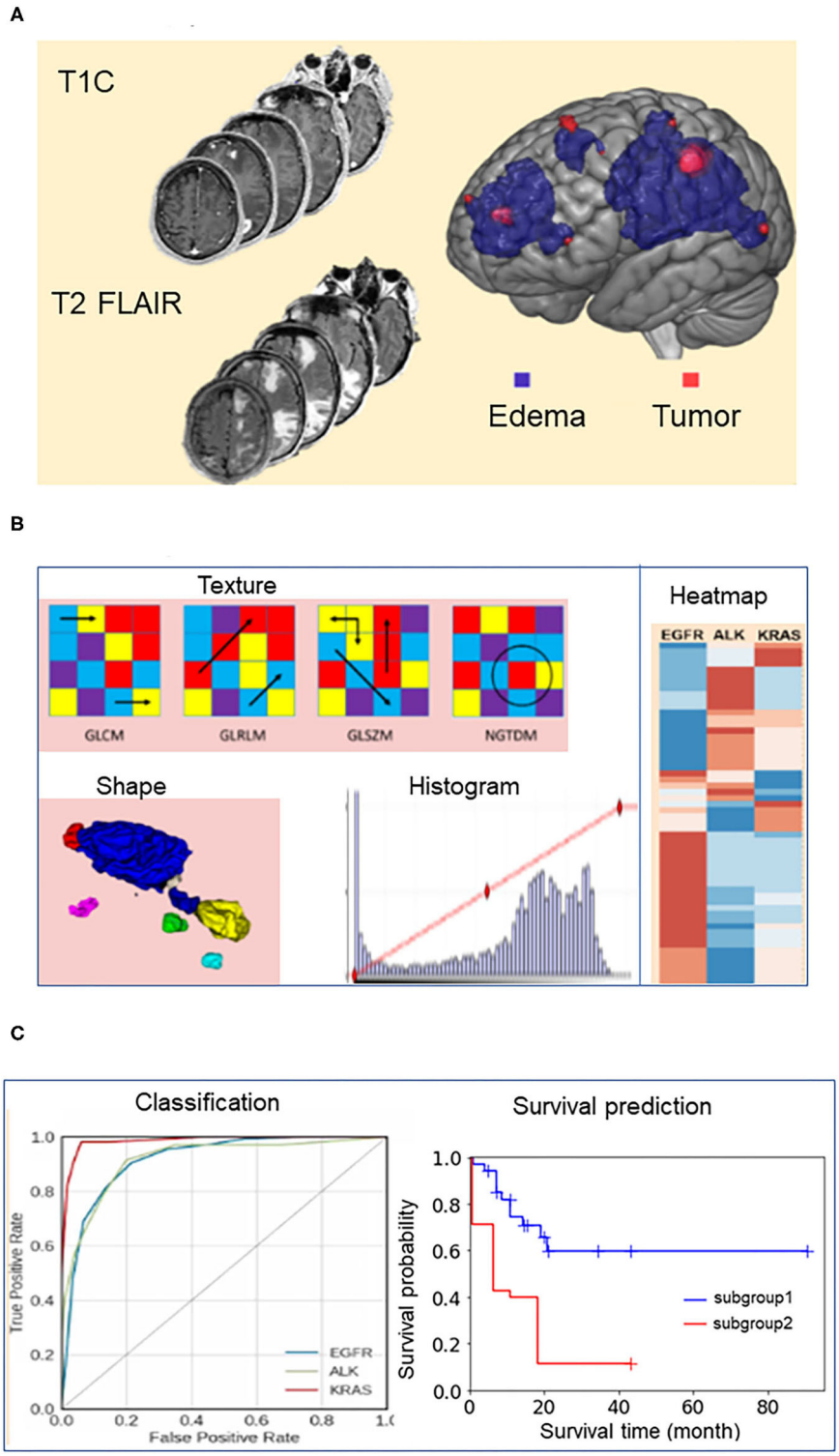

FIGURE 1 | Schema for brain tumor segmentation, radiomic feature extraction, and predictive modeling. **(A)** Representative tumor segmentation images from post-contrast T1-weighted (T1C) and T2-weighted fluid-attenuated inversion recovery (FLAIR) data. **(B)** Illustrations of radiomic features extracted from the brain tumor images, including texture, shape, and intensity. GLCM, Gray Level Co-occurrence Matrix; GLRLM, Gray Level Run Length Matrix; GLSZM, Gray Level Size Zone Matrix; NGTDM, Neighboring Gray Tone Difference Matrix. **(C)** Receiver operating characteristic (ROC) curves for the models predicting the survival durations of patients in each of the three mutation-positive groups (EGFR, ALK, and KRAS mutation-positive groups) and representative survival duration analysis.

whether a patient survived longer than the median survival duration of the group. We evaluated the predictive performance of the machine learning models through leave one out cross validation (LOOCV) using four commonly used performance metrics including the area under the curve (AUC) of the receiver operating characteristic curves (ROC), the specificity, sensitivity and the prediction accuracy (22). We used an open source software scikit-learn for the machine learning model training and evaluation (23). Model training and prediction were tumor-based rather than patient-based, meaning each tumor was treated as an independent instance. The synthetic minority over-sampling technique (SMOTE) was used to improve learning using imbalanced datasets (24).

We built the predictive models using the 50 radiomic features alone or together with 18 additional features including demographic, clinical, and tumor information. Demographic information included gender (male, female), race (Caucasian, Asian, and other), and smoking history (yes, no). Clinical information included the presence or absence of extracranial metastases at 11 sites (bone, lymph, liver, lung, kidney, pancreas, breast, spinal cord, mediastinum, pericardium, and pleura). Tumor information included the number of tumors, the volume of the enhancing tumor core, and the edema/tumor volume ratio. The MRMR-based feature selection was performed in each round of LOOCV process, i.e., 50 most relevant radiomic features were selected using the MRMR algorithm using the training dataset (sample size equals $N-1$ for a N sample dataset) after leaving one sample out as the test dataset.

Selection of Machine Learning Algorithm

We used the gradient boosting classifier to build the machine learning models for predicting the survival durations of all three mutation groups. We selected this algorithm using a model selection process that has been previously described (10). Briefly, (a) we tested 30 classifiers implemented in Scikit-Learn software (23) and evaluated their performance using leave-one-out cross validation (LOOCV), (b) we subsequently ranked their performances according to the area under the curve (AUC) of the receiver operating characteristic curve (ROC) of each model, and (c) we selected the algorithm, Gradient boosting classifier, because it was the only one ranked among top three algorithms for modeling each of the three patient groups.

Table 2 presents the performance data for the top three algorithms for each of the three mutation groups. The performance metrics include accuracy, AUC, sensitivity, and specificity. A total of five classifiers (ada boosting, random forest, extra tree, bagging, and gradient boosting) ranked among the top three classifiers for modeling at least one of the three mutation groups. Gradient boosting classifier was the only classifier ranked among top three for all three mutation-positive groups, therefore, we used this algorithm to build the predictive models for all three mutation groups.

TABLE 2 | Performance metrics for the top three machine learning algorithms for predicting whether patients survive longer than the group median in the EGFR, ALK, and KRAS mutation-positive groups using radiomic features only.

Mutation	Classifier	Accuracy	AUC*	Sensitivity	Specificity
EGFR	Ada Boost Classifier	84.30%	0.905	86.00%	82.00%
	Bagging Classifier	84.00%	0.915	90.00%	79.00%
	Gradient Boosting Classifier	88.10%	0.95	90.00%	87.00%
ALK	Gradient Boosting Classifier	85.70%	0.92	88.00%	83.00%
	Random Forest Classifier	77.80%	0.93	95.00%	68.00%
	Extra Trees Classifier	85.70%	0.936	90.00%	81.00%
KRAS	Extra Trees Classifier	78.70%	0.913	84.00%	75.00%
	Gradient Boosting Classifier	85.10%	0.955	83.00%	87.00%
	Ada Boost Classifier	95.70%	0.957	100.00%	92.00%

**AUC, area under the receiver operating characteristic curve. EGFR, epidermal growth factor receptor; ALK, anaplastic lymphoma kinase; KRAS, Kirsten rat sarcoma viral oncogene homolog.*

Statistical Analysis and Radiomic Score

Demographic Data

We used analysis of variance (ANOVA) to determine the statistical significance of group differences in age. The normality of the distribution was tested using the Shapiro-Wilk test, and the homoscedasticity (the three groups have equal variance) was tested using Bartlett's test implemented in SciPy. We used Fisher's exact test to determine the statistical significance of group differences in the distributions of the categorical variables, including gender, race, smoking history, histology, and other metastatic sites. $P < 0.05$ were considered statistically significant. We used the statistical analysis package in the SciPy: open source scientific tools for Python library (https://www.scipy.org/) for the analysis described above.

Survival Analysis and Radiomic Score

We selected radiomic and clinical features that were important for patients' survival duration and subsequently computed radiomic score for each patient by sequentially performing univariate and multivariate Cox proportional hazard regression through the following steps (**Figure 2**): **(A)** Selecting 20 radiomic features potentially associated with patients' survival duration. In this step, we computed the feature importance of the 50 radiomic features used in the machine learning models using scikit learn software as described in the Section: Building Predictive Models for Survival Duration) and selected the top 20 radiomic features according to the feature importance value (**Supplementary Table 1**, Supplementary Material); **(B)** Performing univariate Cox regression using each of the selected top 20 radiomic features (one by one) and selected those with $p < 0.05$ in the analysis; **(C)** Performing multivariate Cox regression using the above selected radiomic features together with the 18 clinical feature (described in Section Building Predictive Models for Survival Duration) and chose those with $p < 0.05$ in the analysis as the final selected radiomic and clinical features; **(D)** Computing radiomic score for each patient in each mutation-positive group using a linear combination of the features selected in step C weighted by the coefficients determined by the multivariate Cox regression. We divided each mutation group

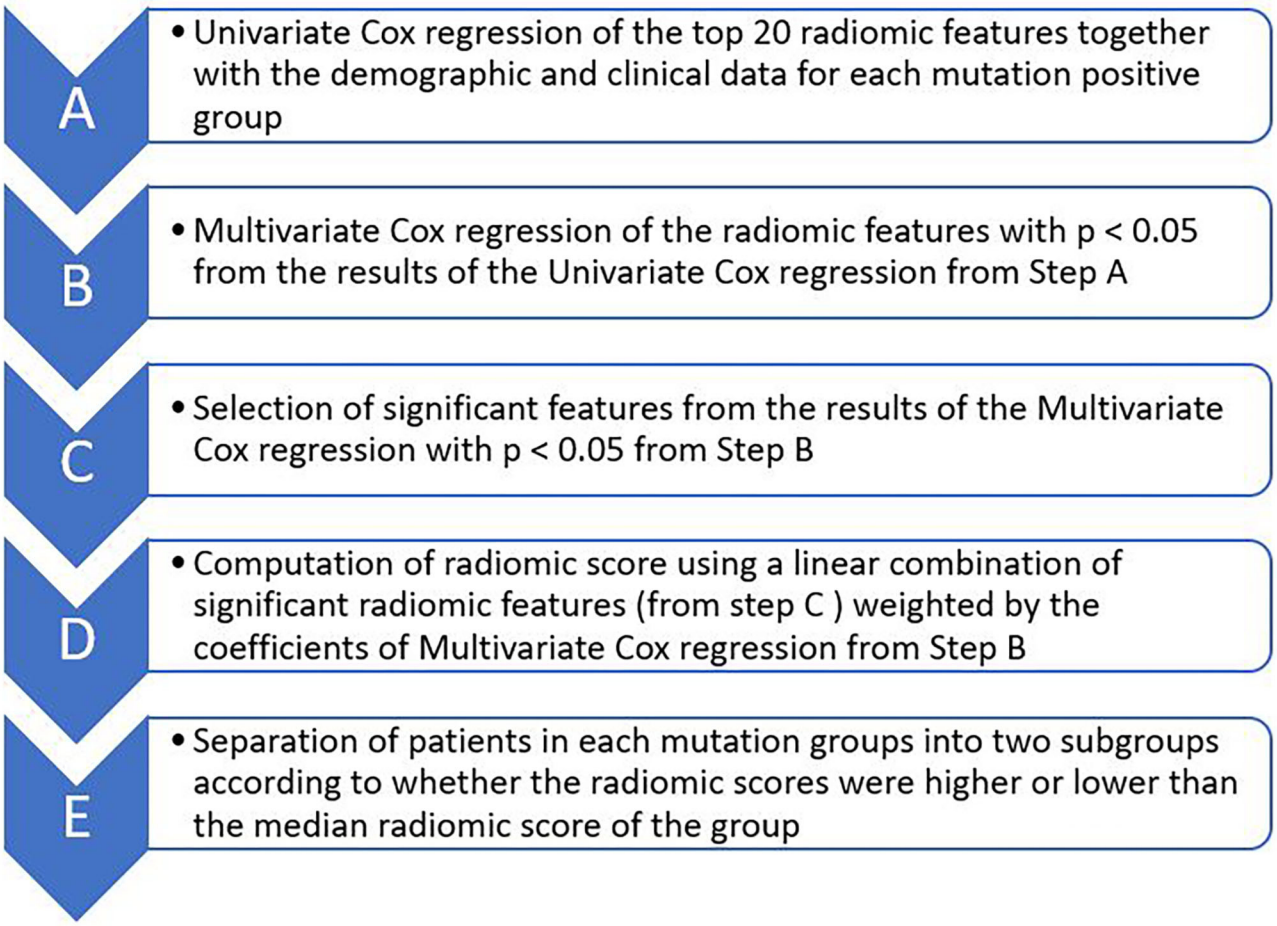

FIGURE 2 | Major steps of Cox proportional hazard regression analysis for determining the effects of radiomic features on survival durations of patients for each of the three mutation-positive group (EGFR, ALK, and KRAS mutation-positive groups). The top 20 radiomic features (step A) were selected based on the feature importance as determined by the multivariate Cox regression during classifier training.

into two subgroups according to the radiomic scores. In each mutation group, those patients with higher radiomic scores than the group median were assigned into the high radiomic score subgroup, and the rest of the patients in the mutation-positive group were assigned into the subgroup with lower radiomic score. We tested the statistical significance of the differences in the median survival durations between the two subgroups in each mutation-positive group using log rank test. We used log rank test to compare the median survival durations of patients in the EGFR, ALK, and KRAS mutation-positive groups. We used Lifelines, an open source software in Python (https://lifelines.readthedocs.io/en/latest/), for the survival analysis and presentation described in this section.

RESULTS

Patient Information

The 110 patients in this study cohort [mean age: 57.51 ± 12.32 years (range: 22 to 85 years), M:F = 37:73] were separated into three groups according to mutation status of the three oncogenes EGFR, ALK, and KRAS. In this cohort, 75 patients had EGFR mutation, 21 had ALK mutation, and 15 had KRAS mutation in their primary NSCLC, respectively (**Table 1**). There was one patient who was positive for both ALK and EGFR mutations. A detailed summary of the demographic and clinical information for the cohort has been reported previously focusing on classification of mutation status from lung cancer brain metastases (10). Briefly, there were statistically significant group differences for the two categorical variables, race ($p < 0.05$) and smoking history ($p < 0.001$). There was a significant difference in the racial distribution of the EGFR and KRAS groups ($p = 0.005$), and the KRAS group had a higher percentage of smokers than the EGFR ($p = 0.0002$) and ALK ($p = 0.0036$) groups.

We also compared the demographic data between the mutation-positive group and the mutation-negative groups for each gene mutation, i.e., EGFR (+) vs. EGFR (–), ALK (+) vs. ALK (–), and KRAS (+) vs. KRAS (–). There was a significantly greater percentage of Asian patients in the EGFR (+) group than

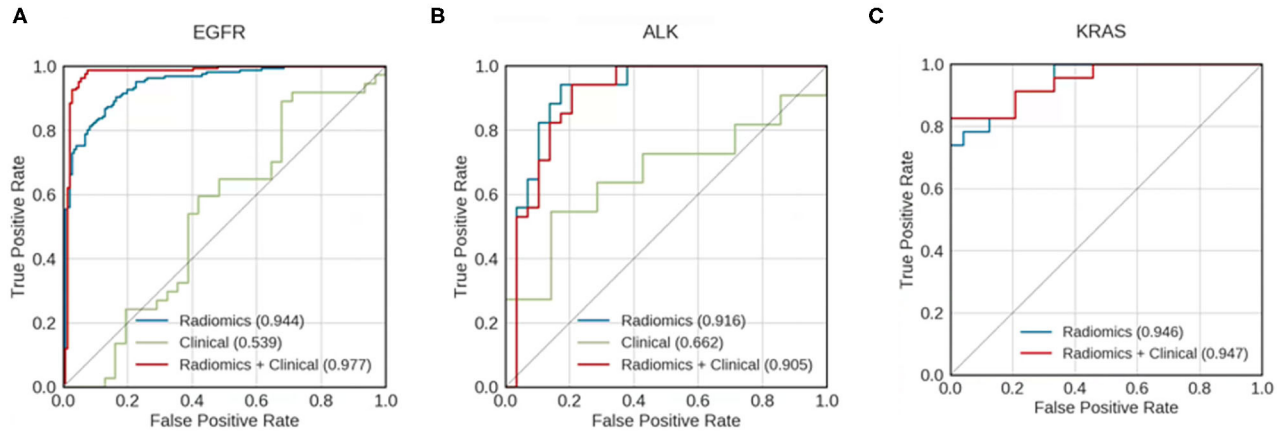

FIGURE 3 | Receiver operating characteristic (ROC) curves for models predicting whether patients with mutations of **(A)** EGFR, **(B)** ALK, and **(C)** KRAS survived longer than the median survival duration of the mutation-positive group. Curves are shown for models using clinical data only (green), radiomics features only (blue), and a combination of both clinical data and radiomic features (red). The areas under the receiver operating characteristic curves (AUCs) are indicated in each panel. KRAS mutation−positive group has too small a sample size to build the predictive model using clinical data alone.

the EGFR (−) group ($p = 0.042$). The KRAS (+) group was significantly older than the KRAS (−) group ($p = 0.002$). There was a higher percentage of smokers in the KRAS (+) group than the KRAS (−) group ($p = 0.0001$).

The median survival durations for EGFR, ALK, and KRAS mutation-positive groups were 12.7, 20.9, and 17.0 months, respectively. The pair-wise log-rank test indicated that the median survival duration of the ALK mutation-positive group was significantly longer than that of the EGFR mutation-positive group ($p = 0.011$), whereas the difference between the ALK and KRAS mutation-positive groups was not significant ($p > 0.05$).

TABLE 3 | Performance metrics for predicting whether patients survive longer than the group median in EGFR, ALK, and KRAS mutation-positive groups.

Mutation	Accuracy	AUC*	Sensitivity	Specificity
EGFR	94.90%	0.977	96.00%	94.00%
ALK	84.10%	0.905	88.00%	81.00%
KRAS	83.00%	0.947	83.00%	83.00%

**AUC, area under the receiver operating characteristic curve.*
EGFR, epidermal growth factor receptor; ALK, anaplastic lymphoma kinase; KRAS, Kirsten rat sarcoma viral oncogene homolog.
Both clinical data and radiomics features were used for predictive modeling.

Prediction of Survival Duration

For all mutation-positive groups, the predictive performance of models built with radiomic features alone was better than that of models built with clinical data alone. Combining radiomic features and clinical data resulted in the most accurate prediction results (**Figure 3**). When using both clinical data and radiomic features in the modeling, the AUCs for predicting whether patients survived longer than the median survival duration of the group was 0.977, 0.905, and 0.947 for EGFR, ALK, and KRAS, respectively. **Table 3** shows the accuracy, AUC, sensitivity, and specificity of the survival duration predictions for the patients in EGFR, ALK, or KRAS mutation-positive group, respectively. Both radiomic features and clinical data were combined to generate the performance data in **Table 3**. The accuracy was 94.9%, 84.1%, and 83.0% for the survival duration predictions for EGFR, ALK, and KRAS mutation-positive group, respectively. The sensitivity was 96.0, 88.0, and 83.0% for the survival duration predictions of EGFR, ALK, and KRAS mutation-positive group, respectively. The specificity was 94.0, 81.0, and 83.0% for the survival duration predictions of the patients in the EGFR, ALK, and KRAS mutation-positive groups, respectively.

Cox Regression Analysis and Radiomic Score Calculation

Table 4 presents multivariate Cox regression results for the three mutation-positive groups. The demographic and radiomic features that were statistically significantly associated with survival duration ($p < 0.05$) are listed in **Table 4**. The features with positive coefficients were associated with shorter survival duration while those with negative coefficients were associated with longer survival duration. For the EGFR mutation-positive group, the radiomic score consisted of age {[Coefficient (coef): 2.76]}, Caucasian race (coef: 0.961), male sex (coef: 0.89), edema/tumor volume ratio (coef: −3.71), tumor number (coef: 1.78), an intensity feature exacted from edema area (coef: 1.37) and a textual feature exacted from tumor area (coef: −1.41). For the ALK mutation-positive group, the radiomic score consisted of the tumor number (coef: 3.05), and an intensity feature exacted from edema area (coef: −1.76). For the KRAS mutation-positive group, the radiomic score consisted of the edema/tumor volume ratio (coef: −16.8) and the tumor number (coef: −1.06). The feature names and

TABLE 4 | Demographic and radiomic features significantly associated with survival duration for each mutation-positive group as determined by multivariate Cox regression analysis.

Group	Features	coef	se(coef)	*z*	*p*	Lower 0.95	Upper 0.95
EGFR	Age	2.76	0.42	6.56	<0.001	1.93	3.58
	Race Caucasian	0.96	0.14	6.83	<0.001	0.69	1.24
	Sex Male	0.89	0.14	6.34	<0.001	0.62	1.17
	Edema/Tumor Ratio	−3.71	0.99	−3.74	<0.001	−5.65	−1.76
	Tumor Number	1.78	0.38	4.75	<0.001	1.05	2.52
	Edema Median Intensity*	1.37	0.43	3.21	0.001	0.54	2.21
	Tumor Texture**	−1.41	0.59	−2.40	0.016	−2.56	−0.26
ALK	Tumor Number	3.05	0.60	5.12	<0.001	1.88	4.21
	Edema Median Intensity*	−1.76	0.88	−2.00	0.045	−3.48	−0.04
KRAS	Edema/Tumor Ratio	−16.80	3.89	−4.33	<0.001	−24.50	−9.22
	Tumor Number	−1.06	0.45	−2.32	0.020	−1.95	−0.17

*Coef, Cox regression coefficient; se(coef), standard error of the Cox regression coefficient; lower 0.95, the lower bound of the 95% confidence interval; upper 0.95, the upper bound of the 95% confidence interval; *Edema Median Intensity, Edema_Intensity_squareroot_Intensity_Median; **Tumor Texture, Tumor Texture log_sigma_3-mm_3D GLRLM LongRunHighGrayLevelEmphasis; EGFR, epidermal growth factor receptor; ALK, anaplastic lymphoma kinase; KRAS, Kirsten rat sarcoma viral oncogene homolog.*

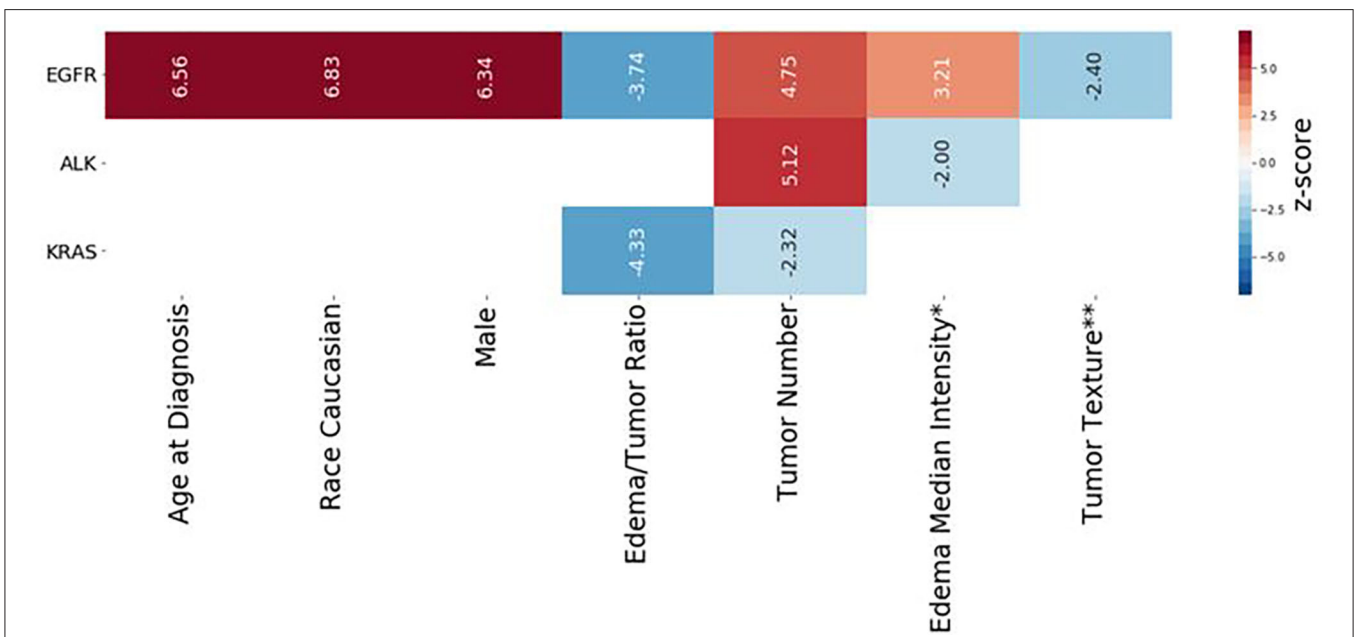

FIGURE 4 | Radiomic scores of survival durations for EGFR, ALK, and KRAS mutation-positive groups. Each column represents the components of the radiomic score for survival prediction for each mutation-positive group, as indicated on the left end. The color indicates the z-score for each feature, based on multivariate Cox regression analysis, according to the scale shown on the right end. The numerical value of each Wald statistics is indicated with imbedded texts. Features with positive values (red) are associated with shorter survival duration, while those with negative values are associated with longer survival duration. The corresponding Cox regression coefficients of the features are shown in **Table 4**. *Edema Median Intensity: Edema_Intensity_squareroot_Intensity_Median. **Tumor Texture: Tumor Texture log-sigma-3-mm-3D GLRLM LongRunHighGrayLevelEmphasis.

the z score listed in **Table 4** are graphically presented in **Figure 4**.

To assess the collective prognostic power of the features that were statistically significantly associated with the patients' survival, we constructed radiomic scores through a linear combination of the significant radiomic features listed in **Table 4** which were weighted by the coefficients. We then divided each of the three patient groups into two subgroups based on the radiomic scores, i.e., assigning those patients with the radiomic scores lower than the median radiomic score of the group into a lower score subgroup and assigning the rest of the patients in the group into a higher score group. **Figure 5** shows Kaplan–Meier

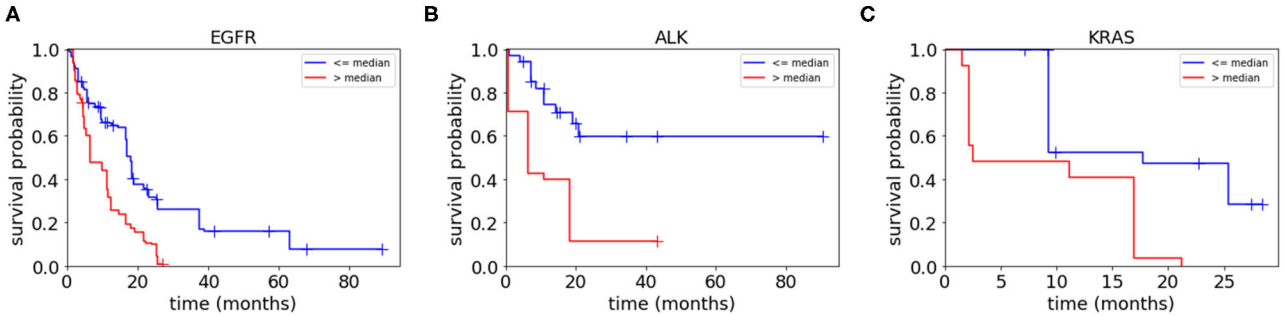

FIGURE 5 | Kaplan–Meier plots for each mutation-positive group **(A–C)** separated into two subgroups by their radiomic scores (higher than or lower than the median radiomic score for each mutation-positive group). The subgroup with radiomic score values higher than the median radiomic score of each mutation-positive group had significantly shorter survival duration than the subgroup with values lower than the median radiomic score. The radiomic scores were computed as the weighted average of the features shown in **Table 4** (weighted by Cox regression coefficients).

plots of the two subgroups within each mutation-positive group based on radiomic scores. In each of the three mutation-positive groups, the subgroup with lower radiomic score had longer median survival duration than that of the subgroup with higher radiomic score.

DISCUSSION

In this study, we built machine learning models to predict whether patients with EGFR, ALK, or KRAS mutation-positive primary NSCLC survived longer than the median survival duration for each specific mutation group. The final models of our study used 50 radiomic features together with 18 clinical features and achieved AUC of 0.977, 0.905, and 0.947 for the three mutation-positive groups, i.e., EGFR, ALK, and KRAS groups, respectively. Subsequently, we identified radiomic and clinical features significantly associated with survival duration for the patients in the three mutation-positive groups. Finally, we constructed radiomic scores using linear combinations of these features weighted with their coefficients in the multivariate regression. After dividing each of the three mutation groups into two subgroups according to radiomic scores, our study showed that the subgroup with lower radiomic scores had statistically significant longer median survival duration, indicating strong association between radiomic scores and the patients' survival duration.

The performance of our predictive models compared favorably to those of published predictive models based on the computed tomography (CT) images of primary lung cancer (25–28). Hosny et al. (29) used a 3D convolutional neural network (CNN) to study prognostic stratification in a multi-cohort radiomic study using the lung CT images of 1,194 patients with NSCLC. Their models predicted whether patients could survive longer than 2 years after treated either with radiotherapy or surgery, and achieved AUC of 0.70 and 0.71, respectively. It is challenging to compare our results, which were based on the MRI radiomics of brain metastases, to the results of the deep learning study which was based on lung CT images. Nevertheless, judging by AUC values alone, the performance of our predictive models was comparable to the work performed by deep learning networks (29).

Our predictive models achieved reasonable performance as compared to other studies using radiomic features from MR images of brain metastases (30–33). For example, Béresová et al. (33) demonstrated that using MR image-based textural radiomic analysis could distinguish brain metastases originating from lung cancer vs. breast cancer, achieving AUC of 0.70. In another study, Ortiz-Ramon et al. (32) used radiomic features extracted from MR images of brain metastases to predict whether the primary cancer being lung cancer or melanoma, achieving AUC of 0.95. Recently, Kniep et al., build predictive models using radiomic features from MR images to predict whether brain metastases originated from primary breast cancer, small cell lung cancer, NSCLC, gastrointestinal cancer, or melanoma. The AUC of their predictive models were between 0.64 for NSCLC and 0.82 for breast cancer (34).

Our approach using radiomic scores to predict survival duration of NSCLC patients with brain metastases was novel. We constructed radiomic scores with linear combinations of 2–7 significant radiomic features for each mutation-positive group, weighted by their Cox coefficients. Our radiomic score calculations indicated that different sets of radiomic features were significantly associated with survival duration in different mutation groups. For example, an edema feature, the Edema_Intensity_squareroot_Intensity_Median, was significantly associated with survival duration of patients in the EGFR and ALK mutation-positive groups, but not in the KRAS mutation-positive group. Edema Tumor Volume ratio on the other hand, was significantly associated with survival duration in the EGFR and KRAS mutation-positive groups, but not in ALK mutation-positive group. Our findings indicated the potential mutation-specific association between the radiomic features and survival durations. These results were not unexpected since our radiomic scores were consisted of features reflecting tumor heterogeneity such as edema intensity and tumor texture which have been known to affect survival (35).

Our findings regarding the relationship between peritumoral edema of brain metastases and the survival durations is generally in line with published literature (35, 36). Spanberger et al. studied the prognostic value of the extent of peritumoral brain edema in the patients operated for single brain metastasis. They reported a strong correlation between the extent of peritumoral edema on brain MRI scans and overall survival, i.e., patients with small peritumoral edema have longer survival than patients with large peritumoral edema (35). Our current study showed similar findings, i.e., lower edema/tumor ratio in our radiomic scores indicated longer survival duration. In addition, Berghoff et al. studied the role of tumor-infiltrating lymphocytes (TIFs) in the immune microenvironment of 116 specimen of brain metastases originating from different primary cancers including lung cancer, breast cancer, melanoma, and renal cell carcinoma. They found that dense TIFs correlated with peritumoral brain edema and the overall survival (36). A recent study by Nardone et al. (37) has also shown that the peritumoral edema and tumor volume of brain metastases were correlated with overall survival in patients with NSCLC undergoing radiosurgery. Taken together of the prior published reports and our current study, there is supporting evidence for incorporating brain tumor characteristics such as edema and tumor volume into survival analysis of patients with brain metastases.

The multivariate Cox regression in our study showed that age at diagnosis, Caucasian race, and male gender, were highly correlated with survival duration in the EGFR mutation-positive group. This result was consistent with literature indicating that age, active extracranial disease, and EGFR mutation are independently associated with survival (9). However, it is challenging to compare our analysis of survival duration with others because of differences in study cohorts, systemic disease status and treatment regimen for both the primary cancers and brain metastases. Nevertheless, it is reasonable to evaluate survival in terms of mutation status since molecular targeted therapy based on mutation information may improve prognosis and survival (38). For instance, the progression-free and overall survival of patients with EGFR and ALK mutations may be improved by treatment with tyrosine kinase inhibitors and ALK inhibitors specifically targeting these two mutations (38). Our study results provide the pilot data supporting radiomic scores as non-invasive biomarkers for assessment of survival duration in lung cancer brain metastases according to the mutation status. Nevertheless, independent validation is needed to substantiate our results.

There were several limitations to this study. First, this was a retrospective study focusing on NSCLC patients with brain metastases who were treated at a single institution over a 9-year interval. Our study design was inherently limited by various confounding variables, such as patient characteristics, imaging parameters, and treatment regimens for the primary NSCLC. Second, our sample size was modest, which might have limited our ability to build more robust predictive models with radiomic features. Third, the mutation status for this cohort was obtained from the primary NSCLC. Since most patients in our cohort did not undergo invasive biopsy or surgery of the brain metastases, the brain metastases could not be directly genotyped and we therefore assumed that brain metastases having the same mutation status as the primary NSCLC. We recognize this limitation with the understanding that mutation status in the primary NSCLC and distant metastases may not always be concordant (39). Lastly, this pilot study did not evaluate or control for all the potential confounding factors that might have contributed to survival duration, such as primary tumor status, systematic disease status, neurological deficits, and treatment regimen for the primary NSCLC and brain metastases. This was because we did not have the statistical power in this retrospective study with a modest sample size to control for all the highly variable confounding factors affecting survival. We recognize our approach for building predictive models with the potential uncontrolled variables may have affected our model performance. We will consider those confounding factors in our future large-scale multicenter research.

Despite these limitations, our study had strengths. First, to the best of our knowledge, our study was the first to use MRI radiomics of brain metastases and machine learning algorithms to predict the survival durations of patients with NSCLC, accounting for their mutation status. Second, we used a 3D slice-by-slice approach to segment brain metastases in their entirety, which we believe should have provided a more detailed characterization of tumor heterogeneity than what could be achieved using a 2D method (32). Third, we constructed radiomic scores using both radiomic features and clinical data, which improved predictive power compared to the scores constructed using either clinical data or radiomic data alone. Therefore, our study has merit as an exploratory, proof-of-concept pilot study from which to generate hypotheses for future large-scale, multicenter studies using imaging biomarkers to predict survival durations of patients with brain metastases from NSCLC and other primary cancers.

In summary, our study showed that a MRI radiomic approach capturing the critical radiological features of brain metastases in patients with primary NSCLC may be used to predict survival durations according to mutation status. Our data supports the concept of using radiomic scores as non-invasive imaging biomarkers for survival analysis, which is important for personalized treatment and prognostic assessment for cancer patients with metastatic disease.

DATA AVAILABILITY STATEMENT

The raw data supporting the conclusions of this article will be made available by the authors to qualified researchers, without undue reservation.

ETHICS STATEMENT

The studies involving human participants were reviewed and approved by the Institutional Review Board at City

of Hope National Medical Center which approved this study and waived informed consent due to its retrospective nature. Written informed consent for participation was not required for this study in accordance with the institutional requirements.

AUTHOR CONTRIBUTIONS

BC and RS designed and conducted the study. NY, TJ, IM, TW, BC, and RS analyzed the brain MR imaging data. NY, TW, and BC performed tumor segmentation and reviewed the segmented images for consistency. TJ developed the pipeline for predictive modeling and machine learning. TJ and NY performed statistical analysis. BC, TJ, NY, IM, CW, TW, ZC, RR, RC, AH, SS, and RS contributed to data interpretation. BC, TJ, NY, IM, and RS contributed to the manuscript writing process and BTC prepared the first draft of the entire manuscript. All authors approved the final manuscript.

FUNDING

This work was supported by the National Cancer Institute of the National Institutes of Health under Grants No. P30CA033572 and 1U54CA209978-01A1. TJ was partially supported by the Center for Cancer and Aging Pilot Project Award at City of Hope to BC. This work was also supported by the City of Hope Research Initiative Health Equity Pilot Grant (Awarded to BC and RS).

ACKNOWLEDGMENTS

The authors thank Kerin K. Higa, Ph.D. for editing this manuscript.

SUPPLEMENTARY MATERIAL

The Supplementary Material for this article can be found online at: https://www.frontiersin.org/articles/10.3389/fonc.2021.621088/full#supplementary-material

REFERENCES

1. Fenske DC, Price GL, Hess LM, John WJ, Kim ES. Systematic review of brain metastases in patients with non-small-cell lung cancer in the United States, European Union, and Japan. *Clin Lung Cancer.* (2017) 18:607–14. doi: 10.1016/j.cllc.2017.04.011
2. Hu C, Chang EL, Hassenbusch SJ 3rd, Allen PK, Woo SY, Mahajan A, et al. (2006). Nonsmall cell lung cancer presenting with synchronous solitary brain metastasis. *Cancer.* 106, 1998–2004. doi: 10.1002/cncr.21818
3. Chen Z, Fillmore CM, Hammerman PS, Kim CF, Wong KK. Non-small-cell lung cancers: a heterogeneous set of diseases. *Nat Rev Cancer.* (2014) 14:535–46. doi: 10.1038/nrc3775
4. Mak KS, Gainor JF, Niemierko A, Oh KS, Willers H, Choi NC, et al. Significance of targeted therapy and genetic alterations in EGFR, ALK, or KRAS on survival in patients with non-small cell lung cancer treated with radiotherapy for brain metastases. *Neuro Oncol.* (2015) 17:296–302. doi: 10.1093/neuonc/nou146
5. Ellison G, Zhu G, Moulis A, Dearden S, Speake G, Mccormack R. EGFR mutation testing in lung cancer: a review of available methods and their use for analysis of tumour tissue and cytology samples. *J Clin Pathol.* (2013) 66:79–89. doi: 10.1136/jclinpath-2012-201194
6. Riely GJ, Marks J, Pao W. KRAS mutations in non-small cell lung cancer. *Proc Am Thorac Soc.* (2009) 6:201–5. doi: 10.1513/pats.200809-107LC
7. Kwak EL, Bang YJ, Camidge DR, Shaw AT, Solomon B, Maki RG, et al. Anaplastic lymphoma kinase inhibition in non-small-cell lung cancer. *N Engl J Med.* (2010) 363:1693–703. doi: 10.1056/NEJMoa1006448
8. Siegelin MD, Borczuk AC. Epidermal growth factor receptor mutations in lung adenocarcinoma. *Lab Invest.* (2014) 94:129–37. doi: 10.1038/labinvest.2013.147
9. Porta R, Sanchez-Torres JM, Paz-Ares L, Massuti B, Reguart N, Mayo C, et al. Brain metastases from lung cancer responding to erlotinib: the importance of EGFR mutation. *Eur Respir J.* (2011) 37:624–31. doi: 10.1183/09031936.00195609
10. Chen BT, Jin T, Ye N, Mambetsariev I, Daniel E, Wang T, et al. Radiomic prediction of mutation status based on MR imaging of lung cancer brain metastases. *Magn Reson Imaging.* (2020) 69:49–56. doi: 10.1016/j.mri.2020.03.002
11. Kuo MD, Jamshidi N. Behind the numbers: Decoding molecular phenotypes with radiogenomics–guiding principles and technical considerations. *Radiology.* (2014) 270:320–5. doi: 10.1148/radiol.13132195
12. Lambin P, Rios-Velazquez E, Leijenaar R, Carvalho S, Van Stiphout RG, Granton P, et al. Radiomics: extracting more information from medical images using advanced feature analysis. *Eur J Cancer.* (2012) 48:441–6. doi: 10.1016/j.ejca.2011.11.036
13. Aerts HJ, Velazquez ER, Leijenaar RT, Parmar C, Grossmann P, Carvalho S, et al. Decoding tumour phenotype by noninvasive imaging using a quantitative radiomics approach. *Nat Commun.* (2014) 5:4006. doi: 10.1038/ncomms5006
14. Sun R, Limkin EJ, Vakalopoulou M, Dercle L, Champiat S, Han SR, et al. A radiomics approach to assess tumour-infiltrating CD8 cells and response to anti-PD-1 or anti-PD-L1 immunotherapy: an imaging biomarker, retrospective multicohort study. *Lancet Oncol.* (2018) 19:1180–91. doi: 10.1016/S1470-2045(18)30413-3
15. Shen C, Liu Z, Guan M, Song J, Lian Y, Wang S, et al. 2D and 3D CT radiomics features prognostic performance comparison in non-small cell lung cancer. *Transl Oncol.* (2017) 10:886–94. doi: 10.1016/j.tranon.2017.08.007
16. Park H, Lim Y, Ko ES, Cho HH, Lee JE, Han BK, et al. Radiomics signature on magnetic resonance imaging: association with disease-free survival in patients with invasive breast cancer. *Clin Cancer Res.* (2018) 24:4705–14. doi: 10.1158/1078-0432.CCR-17-3783
17. Klein S, Staring M, Murphy K, Viergever MA, Pluim JP. elastix: a toolbox for intensity-based medical image registration. *IEEE Trans Med Imaging.* (2010) 29:196–205. doi: 10.1109/TMI.2009.2035616
18. Yushkevich PA, Piven J, Hazlett HC, Smith RG, Ho S, Gee JC, et al. User-guided 3D active contour segmentation of anatomical structures: significantly improved efficiency and reliability. *Neuroimage.* (2006) 31:1116–28. doi: 10.1016/j.neuroimage.2006.01.015
19. Shinohara RT, Sweeney EM, Goldsmith J, Shiee N, Mateen FJ, Calabresi PA, et al. Statistical normalization techniques for magnetic resonance imaging. *Neuroimage Clin.* (2014) 6:9–19. doi: 10.1016/j.nicl.2014.08.008
20. Van Griethuysen JJM, Fedorov A, Parmar C, Hosny A, Aucoin N, Narayan V, et al. Computational radiomics system to decode the radiographic phenotype. *Cancer Res.* (2017) 77:e104–e107. doi: 10.1158/0008-5472.CAN-17-0339
21. Peng H, Long F, Ding C. Feature selection based on mutual information: criteria of max-dependency, max-relevance, and min-redundancy. *IEEE Trans Pattern Anal Mach Intell.* (2005) 27:1226–38. doi: 10.1109/TPAMI.2005.159
22. Arlot S, Celisse A. A survey of cross-validation procedures for model selection. *Statist Surv.* (2010) 4:40–79. doi: 10.1214/09-SS054
23. Pedregosa F, Varoquaux G, Gramfort A, Michel V, Thirion B, Grisel O, et al. Scikit-learn: machine learning in Python. *J Mach Learn Res.* (2011) 12:2825–30. doi: 10.1016/j.patcog.2011.04.006

24. Chawla NV, Bowyer KW, Hall LO, Kegelmeyer WP. SMOTE: synthetic minority over-sampling technique. *J Artif Intell Res.* (2002) 16:321–57. doi: 10.1613/jair.953
25. Liu Y, Kim J, Balagurunathan Y, Li Q, Garcia AL, Stringfield O, et al. (2016). Radiomic features are associated with EGFR mutation status in lung adenocarcinomas. *Clin Lung Cancer.* 17:441–8.e446. doi: 10.1016/j.cllc.2016.02.001
26. Rizzo S, Petrella F, Buscarino V, De Maria F, Raimondi S, Barberis M, et al. CT radiogenomic characterization of EGFR, K-RAS, and ALK mutations in non-small cell lung cancer. *Eur Radiol.* (2016) 26:32–42. doi: 10.1007/s00330-015-3814-0
27. Gevaert O, Echegaray S, Khuong A, Hoang CD, Shrager JB, Jensen KC, et al. Predictive radiogenomics modeling of EGFR mutation status in lung cancer. *Sci Rep.* (2017) 7:41674. doi: 10.1038/srep41674
28. Zhang L, Chen B, Liu X, Song J, Fang M, Hu C, et al. Quantitative biomarkers for prediction of epidermal growth factor receptor mutation in non-small cell lung cancer. *Transl Oncol.* (2018) 11:94–101. doi: 10.1016/j.tranon.2017.10.012
29. Hosny A, Parmar C, Coroller TP, Grossmann P, Zeleznik R, Kumar A, et al. Deep learning for lung cancer prognostication: a retrospective multi-cohort radiomics study. *PLoS Med.* (2018) 15:e1002711. doi: 10.1371/journal.pmed.1002711
30. Li Z, Mao Y, Li H, Yu G, Wan H, Li B. Differentiating brain metastases from different pathological types of lung cancers using texture analysis of T1 postcontrast MR. *Magn Reson Med.* (2016) 76:1410–9. doi: 10.1002/mrm.26029
31. Nardone V, Tini P, Biondi M, Sebaste L, Vanzi E, De Otto G, et al. Prognostic value of MR imaging texture analysis in brain non-small cell lung cancer oligo-metastases undergoing stereotactic irradiation. *Cureus.* (2016) 8:e584. doi: 10.7759/cureus.584
32. Ortiz-Ramon R, Larroza A, Arana E, Moratal D. A radiomics evaluation of 2D and 3D MRI texture features to classify brain metastases from lung cancer and melanoma. *Conf Proc IEEE Eng Med Biol Soc.* (2017) 2017:493–6. doi: 10.1109/EMBC.2017.8036869
33. Béresová M, Larroza A, Arana E, Varga J, Balkay L, Moratal D. 2D and 3D texture analysis to differentiate brain metastases on MR images: proceed with caution. *Magn Reson Mater Phys Biol Med.* (2018) 31:285–94. doi: 10.1007/s10334-017-0653-9
34. Kniep HC, Madesta F, Schneider T, Hanning U, Schonfeld MH, Schon G, et al. Radiomics of brain MRI: utility in prediction of metastatic tumor type. *Radiology.* (2019) 290:479–87. doi: 10.1148/radiol.2018180946
35. Spanberger T, Berghoff AS, Dinhof C, Ilhan-Mutlu A, Magerle M, Hutterer M, et al. Extent of peritumoral brain edema correlates with prognosis, tumoral growth pattern, HIF1a expression and angiogenic activity in patients with single brain metastases. *Clin Exp Metastasis.* (2013) 30:357–68. doi: 10.1007/s10585-012-9542-9
36. Berghoff AS, Fuchs E, Ricken G, Mlecnik B, Bindea G, Spanberger T, et al. Density of tumor-infiltrating lymphocytes correlates with extent of brain edema and overall survival time in patients with brain metastases. *Oncoimmunology.* (2016) 5:e1057388. doi: 10.1080/2162402X.2015.1057388
37. Nardone V, Nanni S, Pastina P, Vinciguerra C, Cerase A, Correale P, et al. Role of perilesional edema and tumor volume in the prognosis of non-small cell lung cancer (NSCLC) undergoing radiosurgery (SRS) for brain metastases. *Strahlenther Onkol.* (2019) 195:734–44. doi: 10.1007/s00066-019-01475-0
38. Di Lorenzo R, Ahluwalia MS. Targeted therapy of brain metastases: latest evidence and clinical implications. *Ther Adv Med Oncol.* (2017) 9:781–96. doi: 10.1177/1758834017736252
39. Bozzetti C, Tiseo M, Lagrasta C, Nizzoli R, Guazzi A, Leonardi F, et al. Comparison between epidermal growth factor receptor (EGFR) gene expression in primary non-small cell lung cancer (NSCLC) and in fine-needle aspirates from distant metastatic sites. *J Thorac Oncol.* (2008) 3:18–22. doi: 10.1097/JTO.0b013e31815e8ba2

Conflict of Interest: The authors declare that the research was conducted in the absence of any commercial or financial relationships that could be construed as a potential conflict of interest.

frontiers in Oncology

ORIGINAL RESEARCH
published: 17 March 2021
doi: 10.3389/fonc.2021.595259

A Voxel-Based Radiographic Analysis Reveals the Biological Character of Proneural-Mesenchymal Transition in Glioblastoma

Tengfei Qi[1†], *Xiangqi Meng*[1†], *Zhenyu Wang*[1], *Xinyu Wang*[1], *Nan Sun*[1], *Jianguang Ming*[1], *Lejia Ren*[1], *Chuanlu Jiang*[1*] and *Jinquan Cai*[1,2*]

[1] Department of Neurosurgery, The Second Affiliated Hospital of Harbin Medical University, Harbin, China, [2] Department of Microbiology, Tumor and Cell Biology (MTC), Biomedicum, Karolinska Institutet, Stockholm, Sweden

OPEN ACCESS

Edited by:
Xuejun Li,
Central South University, China

Reviewed by:
Liang Wang,
Fourth Military Medical University, China
Guihua Wang,
Huazhong University of Science and Technology, China

***Correspondence:**
Chuanlu Jiang
jcl6688@163.com
Jinquan Cai
jinquan.cai@ki.se;
caijinquan@hrbmu.edu.cn

[†]These authors share first authorship

Specialty section:
This article was submitted to Cancer Imaging and Image-directed Interventions, a section of the journal Frontiers in Oncology

Received: 15 August 2020
Accepted: 16 February 2021
Published: 17 March 2021

Citation:
Qi T, Meng X, Wang Z, Wang X, Sun N, Ming J, Ren L, Jiang C and Cai J (2021) A Voxel-Based Radiographic Analysis Reveals the Biological Character of Proneural-Mesenchymal Transition in Glioblastoma. Front. Oncol. 11:595259. doi: 10.3389/fonc.2021.595259

Introduction: Proneural and mesenchymal subtypes are the most distinct demarcated categories in classification scheme, and there is often a shift from proneural type to mesenchymal subtype in the progression of glioblastoma (GBM). The molecular characters are determined by specific genomic methods, however, the application of radiography in clinical practice remains to be further studied. Here, we studied the topography features of GBM in proneural subtype, and further demonstrated the survival characteristics and proneural-mesenchymal transition (PMT) progression of samples by combining with the imaging variables.

Methods: Data were acquired from The Cancer Imaging Archive (TCIA, http://cancerimagingarchive.net). The radiography image, clinical variables and transcriptome subtype from 223 samples were used in this study. Proneural and mesenchymal subtype on GBM topography based on overlay and Voxel-based lesion-symptom mapping (VLSM) analysis were revealed. Besides, we carried out the comparison of survival analysis and PMT progression in and outside the VLSM-determined area.

Results: The overlay of total GBM and separated image of proneural and mesenchymal subtype revealed a correlation of the two subtypes. By VLSM analysis, proneural subtype was confirmed to be related to left inferior temporal medulla, and no significant voxel was found for mesenchymal subtype. The subsequent comparison between samples in and outside the VLSM-determined area showed difference in overall survival (OS) time, tumor purity, epithelial-mesenchymal transition (EMT) score and clinical variables.

Conclusions: PMT progression was determined by radiography approach. GBM samples in the VLSM-determined area tended to harbor the signature of proneural subtype. This study provides a valuable VLSM-determined area related to the predilection site, prognosis and PMT progression by the association between GBM topography and molecular characters.

Keywords: voxel-based lesion-symptom mapping, proneural subtype, mesenchymal subtype, magnetic resonance imaging, glioblastoma

INTRODUCTION

Glioblastoma (GBM), mainly diagnosed by magnetic resonance imaging (MRI) and accurate pathological examination, is the most aggressive brain tumor and indicates a poor prognosis (1). The current standard of care refers to maximal surgical resection followed by local radiotherapy and chemotherapy. However, the tumor evolves rapidly in the progression, which is linked to resistance to adjuvant treatment (2, 3).

As a non-invasive checking method, MRI is capable of conducting qualitative and quantitative analysis with specific phenotypic imaging features, to associate with potential prognosis and characteristics (4). The genomic characteristics of heterogeneous MRI features in GBM are investigated and determined by scholars in a growing number of studies, which provide chances for grouping, prognostication and innovation of targeted therapies (5, 6). As a newly developed terminology, Visually Accessible Rembrandt Images (VASARI) feature set (https://wiki.nci.nih.gov/display/CIP/VASARI) incorporates various visible subjective imaging features, which is designed to normalize grading of the distinct features of gliomas on MRI, containing different grades criteria corresponding to diverse score to depict severity (7).

GBM with specific anatomical region shows similarity in genomic alterations and gene expression patterns (8). Voxel-based lesion-symptom mapping (VLSM) approach is one of the most common method to explore the relationship between GBM topography in MRI and lesion-behavior based on voxel-by-voxel method (9). In consideration of tumorigenesis and progression characteristics of GBM, VLSM is widely used to investigate tumor location involved in occupation and other affected secondary diseases (10). VLSM analysis is reported to identify the genomic alterations and the object-action dissociation in studies (11, 12).

Both MRI features and transcriptome analysis reveal distinct subtypes of GBM with different clinical and molecular characteristics (13). The Cancer Genome Atlas (TCGA, https://portal.gdc.cancer.gov/) has described a robust gene expression-based molecular classification of GBM including proneural, mesenchymal, neural, and classical subtypes (14). Notably, there is a consensus that proneural and mesenchymal subtypes are the most distinct demarcated categories among different subtypes (15–17). Proneural subtype is generally regarded as a common precursor of several molecular subtypes, while mesenchymal subtype indicates worst prognosis and lowest tumor purity (18–20). It is worth noting that there is plasticity for proneural subtype, and it has been proved to be with a tendency toward proneural-mesenchymal transition (PMT) progression during glioma progression (21, 22). Halliday found that a marked shift away from a proneural expression pattern toward a mesenchymal one in GBM (23). PMT progression may represent for GBM the equivalent of epithelial–mesenchymal transition (EMT) process associated with other aggressive cancers (24). The EMT process refers to transdifferentiation of epithelial cells into motile mesenchymal cells in tumor progression and metastasis, which is mediated by plenty of key transcription factors (25). To date, GBM topography in proneural or mesenchymal subtypes is not elaborately analyzed in previous studies.

In our study, we screened 223 samples in TCIA (The Cancer Imaging Archive, TCIA, http://cancerimagingarchive.net) database and elucidated the radiogenomic signatures in GBM via common MRI alignment. As for GBM topography for subtypes is not clear to date, we used VLSM method to evaluate the predilection sites of proneural and mesenchymal subtypes. The combination of VLSM method and VASARI features was applied to analyze overall survival (OS) and other significant information based on the VLSM-determined area, contributing to understand the genomics pathogenesis potentially.

RESULTS

Demographic Characteristics

The distribution of 223 samples enrolled into the study were illustrated in **Figure 1** (**Supplementary Table 1**). In the age distribution of patients, there were 65 patients (29% of 223) were between 50 and 60 years old. In the gender distribution of patients, there were 90 females (40% of 223) and 133 males (60% of 223). As high as 81 an d84% of the patients had received pharmaceutical and radiation treatment, respectively, while only 5 and 2% lack relevant information, respectively. Karnofsky performance status (KPS) value of 80 was in 49% of the patients. The OS time was in a range of 4–1,730 days. The survival of 100–300 days (34%) harbored the highest proportion. The patients who had received tumor resection procedure were 91%, and 19% of the patients only experienced excisional biopsy to acquire pathologic information. In the molecular subtypes distribution, mesenchymal subtype had a proportion of 33%, whereas proneural, neural and classical subtypes were 23, 18, and 26% of total, respectively.

GBM topography at lobe level was summarized in **Table 1**. The predilection site of samples involved with temporal lobe (75.34% of total, 80.77% of proneural subtype, 68.50% of mesenchymal subtype, 82.50% of neural subtype, 74.13% of classical subtype). The proportion of single temporal lobe (21.92%) involved in mesenchymal subtype was a little higher than other subtypes. Samples with mesenchymal subtype had the highest percentage outside temporal lobes (31.51%). There were 103 samples with tumor located in the right hemisphere and 104 samples with tumor located in the left. All the subtypes indicated no obvious inclination in tumor side.

To further explore characteristics of GBM topography, the Volume of interests (VOIs) of the whole patient cohort were overlapped on the standard template (**Figure 2**). GBM topography was evenly distributed in periventricular zone and adjacent to the subventricular zone. In addition, there was no significant discrepancy between tumors in the left and those in the right side.

VLSM-Determined Area

Firstly, separated tumor overlays were performed to detect GBM topography of proneural and mesenchymal subtypes, and we finally found that compared with integral overlay displayed in **Figure 2**, the overlays of two subtypes had diversities (**Figures 3A,B**). On one hand, overlay on the right side of the two subtypes resembled each other and showed a favorable agreement

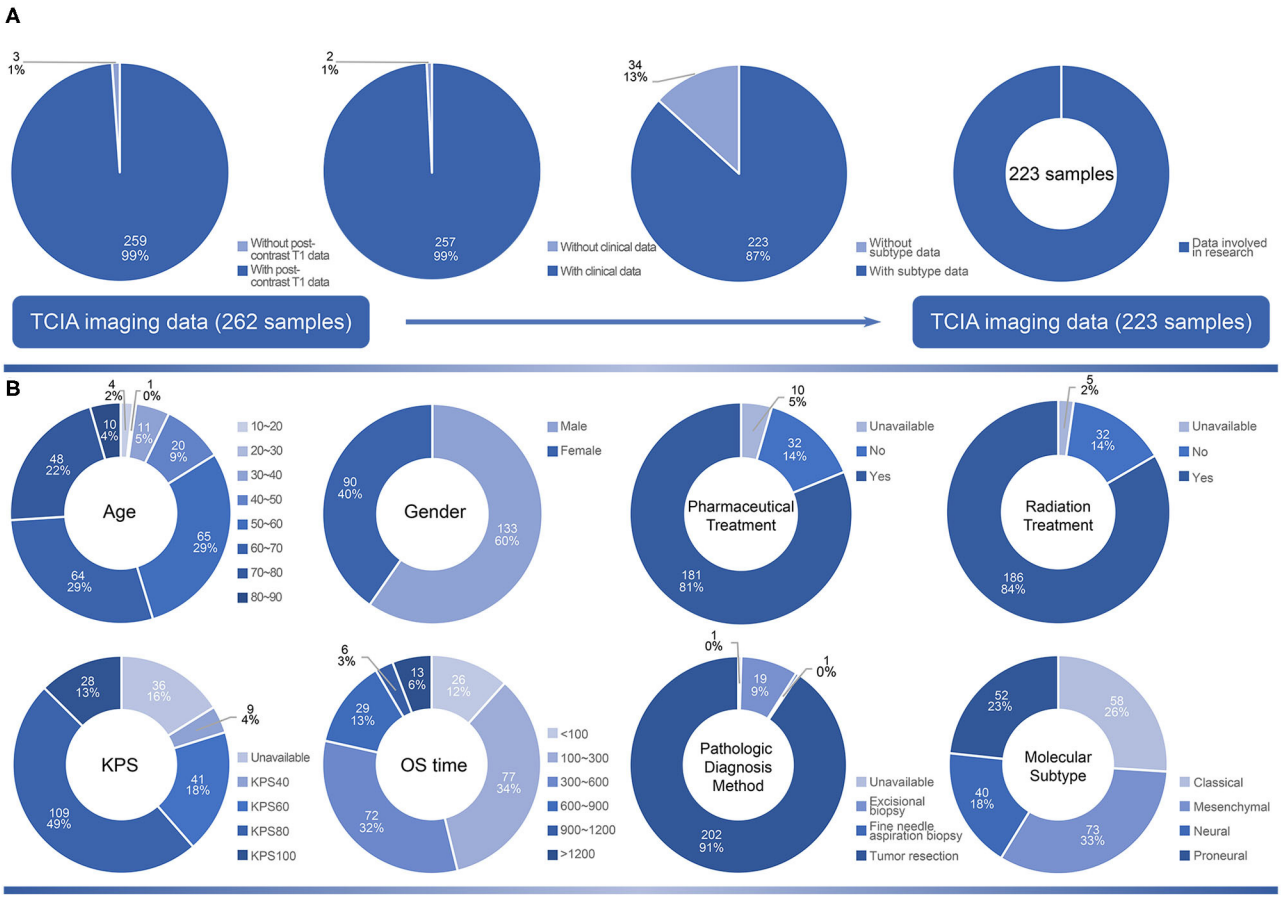

FIGURE 1 | The selection criteria of the study and demographic characteristics of samples. **(A)** The original 262 samples collected from TCIA. According to the availability of post-contrast T1 image, clinical data and subtype data, 223 samples were included in the study. **(B)** The distribution of clinical variables including age, gender, pharmaceutical treatment, radiation treatment, KPS, OS time, pathologic diagnosis method and molecular subtype in 223 samples.

to integral overlay. On the other hand, two groups indicated different distribution on the left side. High frequency of tumor occurrence of the mesenchymal subtype located forward and close to frontal lobe, while hotspot of the proneural subtype located backwards in cerebral hemisphere and near occipital lobe. These results suggested that the two subtypes had a different tumorigenesis in topography but an intimate relation in progression.

To further explore PMT progression, we selected 125 samples comprised of 52 proneural and 73 mesenchymal subtypes to conduct VLSM analysis. The normalized lesion maps in proneural and mesenchymal subtypes were calculated independently. VLSM specifically associated proneural subtype with lesions to a cluster of the left inferior temporal medulla, while no significant voxel was found for mesenchymal subtype (**Figure 4**). The results of significant clusters of proneural subtype accorded with previous overlay map of the proneural subtype. According to whether the tumors were in or outside the VLSM-determined area of proneural subgroup, the samples were classified into two groups. Of the 125 samples, there were 33 samples in the VLSM-determined area, and 22 samples (67% of 33) were proneural subtype while 11 samples (33% of 33) were mesenchymal subtype. Among 92 samples that were outside the VLSM-determined area, 30 samples (33% of 92) were proneural subtype, whereas 62 samples (67% of 92) were mesenchymal subtype. We also observed that among 52 proneural samples, 22 samples (42% of 52) were in the VLSM-determined area while 30 samples (58% of 52) were outside the VLSM-determined area. Among 73 mesenchymal samples, 11 samples (15% of 73) were in the VLSM-determined area and 62 samples (85% of 73) were outside the VLSM-determined area (**Table 2**).

Survival Analysis

Survival analysis was carried out to find whether the VLSM-determined area could serve as a prognostic role. Initially, to exclude some recognized factors that influence survival outcome obviously, we included samples with standard tumor resection, radiotherapy and pharmaceutical treatment to make the survival result more persuasive. Since contrast enhancement of MRI was associated with survival (26), we

TABLE 1 | The distribution of different subtypes based on tumor locations.

	Total (n = 223)	Proneural (n = 52)	Mesenchymal (n = 73)	Neural (n = 40)	Classical (n = 58)
Single temporal lobe, *n* (%)	38 (17.04)	10 (19.23)	16 (21.92)	4 (10.00)	8 (13.79)
Multiple lobes including temporal lobe, *n* (%)	130 (58.30)	32 (61.54)	34 (46.58)	29 (72.5)	35 (60.34)
Other locations, *n* (%)	55 (24.66)	10 (19.23)	23 (31.51)	7 (17.5)	15 (25.86)
Left, *n* (%)	103 (46.19)	29 (55.77)	36 (49.32)	14 (35.00)	24 (41.38)
Right, *n* (%)	104 (46.64)	21 (40.38)	33 (45.21)	21 (52.50)	29 (50.00)
Bilateral, *n* (%)	16 (7.17)	2 (3.85)	4 (5.48)	5 (12.50)	5 (8.62)

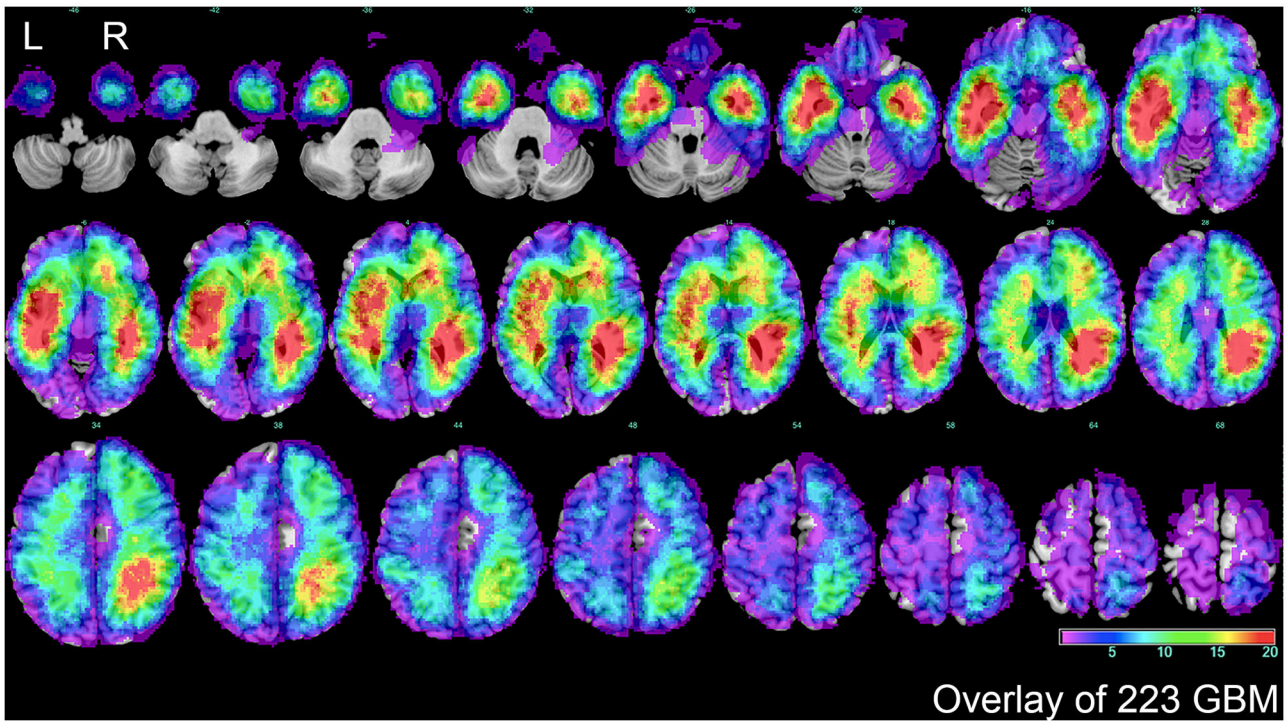

FIGURE 2 | The overlap of total GBM lesions. VOIs of 223 GBM samples included in the study were overlaid on standard template. The color scale indicated the amount of the VOIs overlap from violet (1 case) to red (more than 20 cases). The distribution showed that a majority of GBM located in periventricular or subventricular region. L represented left side, and R represented right side.

selected variable F5 of VASARI feature set to remove the bias of contrast enhancement on survival. In this study, 95% proportion of enhancing area is defined as the cut-off value of striking enhancement. Another variable F1 was also chosen as a reference, and GBM samples involved with temporal lobe were selected (**Figure 5A**). Kappa consistency test was executed before survival analysis. The results of inter-rater analysis for VASARI features indicated excellent agreement, and kappa values of F1 and F5 were 0.923 and 0.842, respectively (**Table 3**). Log-rank survival analysis showed that GBM samples in the VLSM-determined area had longer OS time compared with those outside the VLSM-determined area (P = 1.20E-2, **Figure 5B**). Then the data based on proneural or mesenchymal subtype were subdivided to find the significant difference of survival outcome. Proneural subtype in the VLSM-determined area predicted a longer OS time (P = 3.00E-03, **Figure 5C**), while in mesenchymal subtype, there was no significant difference between GBM samples in and outside the VLSM-determined area in survival analysis (P = 1.28E-01, **Figure 5D**).

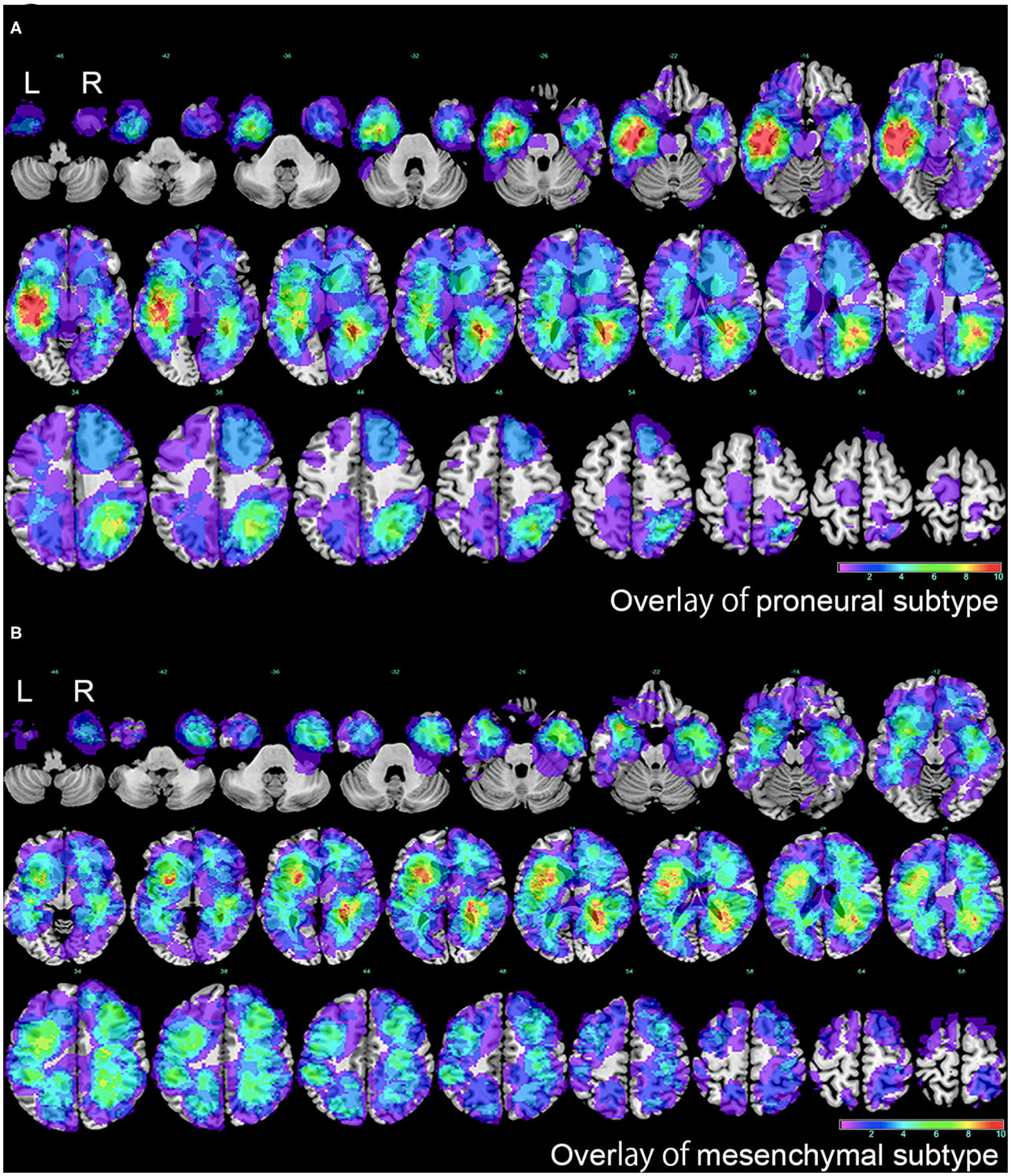

FIGURE 3 | The overlap of proneural and mesenchymal subtypes of GBM. **(A)** The overlap of proneural subtype of GBM. The color scale indicated the amount of the VOIs overlap, from violet (1 case) to red (more than 10 cases). **(B)** The overlap of mesenchymal subtype of GBM. The color scale indicated the amount of the VOIs overlap, from violet (1 case) to red (more than 10 cases). L represented left side, and R represented right side.

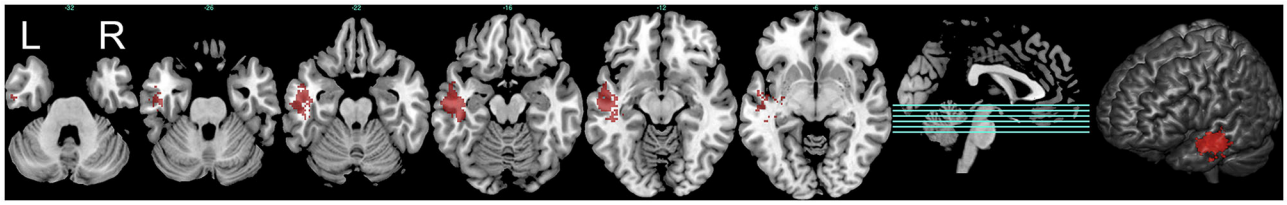

FIGURE 4 | The predilection region of proneural subtype defined by VLSM analysis. The VLSM analysis determined the predilection regions of proneural subtype in the left inferior temporal medulla (marked in red). Three-dimensional render of the VLSM-determined area was also illustrated. L represented left side, and R represented right side. This figure only showed the result below an FDR-adjusted threshold ($P < 0.05$).

Clinical Variables, EMT Process, and Tumor Purity

Apart from clinical variables, the expression profiling data in TCGA was used to calculate the corresponding signal pathway score by single-sample Gene Set Enrichment Analysis (ssGSEA) to evaluate EMT process and tumor purity of samples (**Figure 6**). For clinicopathological characteristics, age, subtype, EMT score and tumor purity were of significant association in and outside the region (**Figure 6A**). VOI, KPS, MGMT and gender showed no significant difference (**Supplementary Table 2**). VLSM/VOI was illustrated as histogram in descending order. Age distribution showed that patients with GBM outside the VLSM-determined area were older than those in the VLSM-determined area. The proportion of proneural subtype was higher in the VLSM-determined area, while samples in mesenchymal subtype had preference locating outside the VLSM-determined area. Compared with samples in the VLSM-determined area, samples outside the VLSM-determined area had a higher EMT score, which indicated a tendency to mesenchymal phenotype. As for tumor purity, we calculated immune signature and stromal signature together. The top 10 genes with significant differential expression were presented in the image (**Figure 6B**, **Supplementary Table 3**). In EMT gene set, KLHL12, HDAC2, STRAP, and FUZ were over-expressed in VLSM-determined area, and other genes such as CTNNB1, HIF1A, and IL6 were over-expressed outside the VLSM-determined area. These results demonstrated that there were significant differences of EMT process and tumor purity between GBM in and outside the VLSM-determined area, indicating the potential PMT progression. We also analyzed the immune cells infiltration between GBM in and outside the VLSM-determined area to further discuss the changes of microenvironment in PMT progression. The infiltrations of T cells CD8 and T cells follicular helper were significantly down-regulated in GBM outside the VLSM-determined area compared with those in GBM in the VLSM-determined area (T cells CD8, $P = 1.00E\text{-}02$; T cells follicular helper, $P = 1.00E\text{-}02$; Student's *t*-test, **Supplementary Table 4**).

TABLE 2 | The distribution of proneural and mesenchymal subtypes in and outside the VLSM-determined area.

	Proneural subtype	Mesenchymal subtype	Total
In the VLSM-determined area	22	11	33
Outside the VLSM-determined area	30	62	92
Total	52	73	125

DISCUSSION

GBM is categorized into four subtypes (proneural subtype, mesenchymal subtype, classical subtype and neural subtype) based on molecular and phenotypic differences. For instance, mesenchymal subtype has higher rates of proliferation *in vitro* and is markedly resistant to radiotherapy compared with proneural subtype (27). PMT progression widely exists in the process of GBM progression due to the invasive mechanism and activation potential of mesenchymal feature of proneural subtype (19). In this study, we found potential relevance between proneural subtype and mesenchymal subtype on GBM topography based on overlay and VLSM analysis, and survival analysis revealed that patients with GBM in the VLSM-determined area survived longer than patients with GBM outside the VLSM-determined area. Furthermore, the results of EMT score and tumor purity suggested a potential PMT progression between GBM in and outside the VLSM-determined area further. Samples with GBM in and outside the VLSM-determined area harbored the signature of proneural subtype and mesenchymal subtype in PMT progression, respectively. In previous study, the PMT progression is determined by specific genomic methods generally, while this study discussed the subject in radiography approach and presented ideas related to different subtypes (28, 29).

The non-invasive method of MRI materials provides effective mean to explore different molecular genetic signatures (4). Tumor location can be associated with the genetic profile of tumor precursor cells (14). In our study, 223 samples with definite subtypes were selected to conduct tumor overlay maps. The original GBM overlay result indicated the overlays with higher proportion were around periventricular or subventricular zone, which suggested the result was associated with the origin of brain tumors (30). Proneural subtype and mesenchymal subtype are the most distinct subtypes, which suggests a biological significance in tumor biology and overall survival (31–33). According to overlay of the VOIs in proneural and mesenchymal

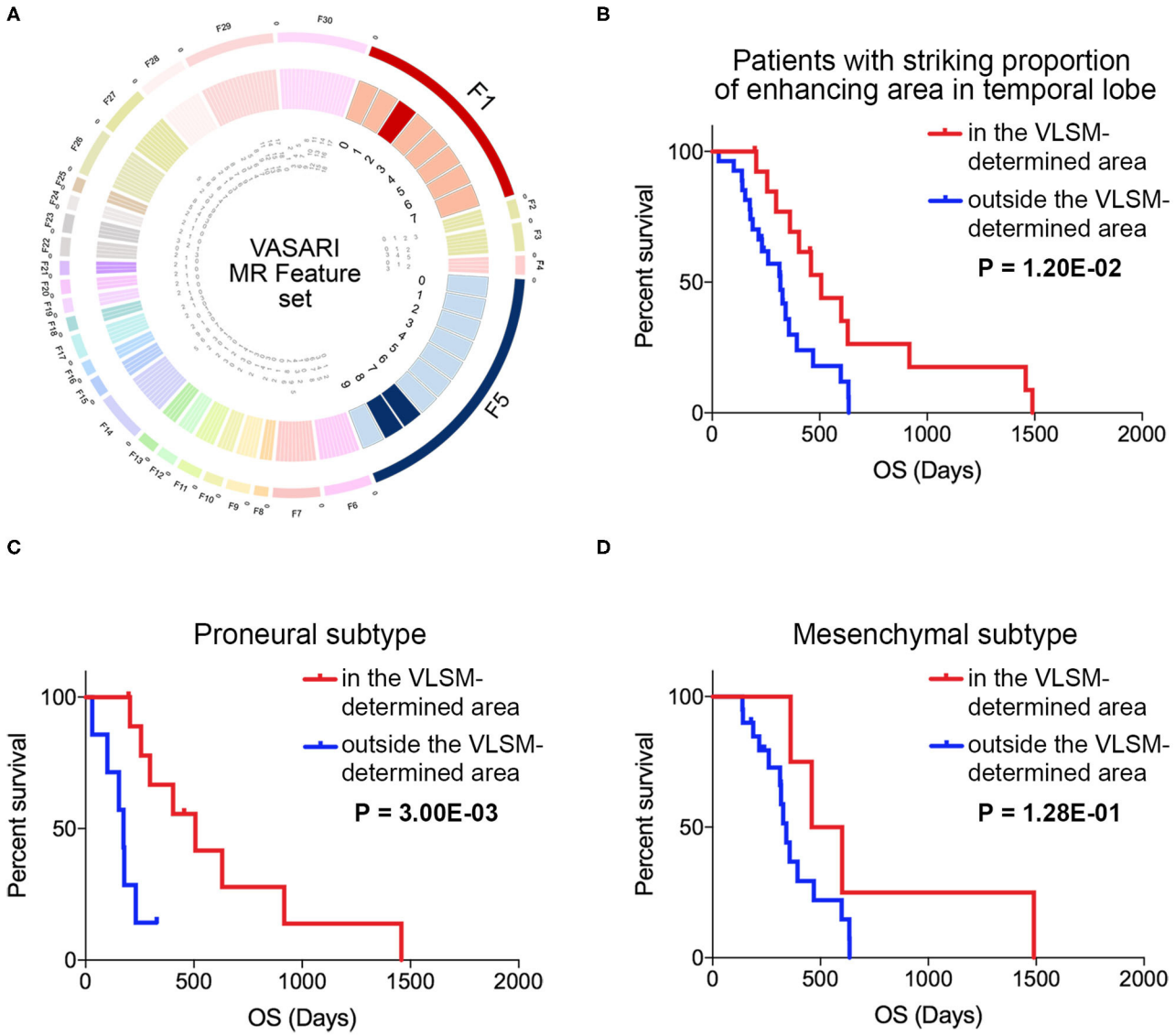

FIGURE 5 | The VASARI feature set used for screening samples and survival analysis in and outside the VLSM-determined area. **(A)** The F1 and F5 in VASARI feature sets were applied. Patients with GBM involved temporal lobe with over 95% proportion of enhancing area were carried out for survival analysis. **(B)** Survival analysis illustrated the significantly different prognosis of patients with GBM in and outside the VLSM-determined area (P = 1.20E-02). **(C)** Survival analysis illustrated the significantly different prognosis of patients with proneural subtype of GBM in and outside the VLSM-determined area (P = 3.00E-03). **(D)** Survival analysis illustrated the prognosis of patients with mesenchymal subtype of GBM in and outside the VLSM-determined area (P = 1.28E-01). P-value was determined by log-rank test.

subtypes gathered with diverse predilection site, we explored the anatomical characteristics of the two subtypes. The predilection area of proneural glioma was involved with left middle and left inferior temporal gyrus. The brain temporal lobe plays a role in recognition of specific objects and processing with visual stimuli (34), and is one of the most predilection sites for GBM in adults (35). Proneural subtype has classical events in the robust classification scheme including TP53 mutation, and can be a driver of initial oncogenic events and influenced by a variety of genomic factors in tumor initialization and progression (14, 18). The predilection area of mesenchymal glioma located forward and close to brain frontal lobe. Gliomas located in the frontal lobe have symptoms including dementia, personality change, gait disturbance, expressive aphasia and others (36). The mesenchymal gliomas expressed properties such as reduced cell polarity, increased pseudopodia formation, cell motility and invasion, upregulation of EMT markers (19). The overlays of the VOIs in proneural and mesenchymal subtypes gathered with diverse predilection site. Therefore, we employed VLSM analysis to explore the anatomical characteristics of the two subtypes. The overlays of the VOIs in proneural subtype and mesenchymal subtype gathered with diverse predilection site.

TABLE 3 | Inter-observer analysis for VASARI imaging features used in the study.

VASARI imaging features	Description	Options	Kappa value
Tumor location (F1)	Location of lesion geographic epicenter	0 = – 1 = Frontal 2 = Temporal 3 = Insular 4 = Parietal 5 = Occipital 6 = Brainstem 7 = Cerebellum	0.923
Proportion enhancing (F5)	Enhancing proportion of the entire tumor	0 = – 1 = n/a 2 = None (0%) 3 = < 5% 4 = 6–33% 5 = 34–67% 6 = 68–95% 7 = > 95% 8 = All (100%) 9 = Indeterminate	0.842

Therefore, we employed VLSM analysis to explore the anatomical characteristics of the two subtypes.

VLSM is a different method from overlay, which can provide statistical significance for the observed difference based on voxel level and bring forward to evaluate the relationship between lesions and clinical symptoms (37). In present study, proneural subtype was confirmed to be related to left inferior temporal medulla. We morphologically defined a VLSM-determined area as inclination tumorigenesis of proneural subtype. However, no significant voxel was detected in mesenchymal subtype. The overlay images provided evidence that mesenchymal subtype GBM had a relative diffused distribution. This characteristic might be explained by the absence of diffused growing patterns of mesenchymal subtype (38).

In the analysis of MRI radiography, tumor contrast enhancement is applied to predict GBM prognosis and malignancy, which can be easily distinguished, resulting to the narrowing of subjective error of visual inspection and facilitating feasibility or availability (39, 40). In this study, we employed VASARI feature set to formulate proportion of enhancing area for ensuring the normalized visual feature. GBM involved temporal lobe with over 95% proportion of enhancing area, as well as other potential factors involved in patient's prognosis such as tumor resection, radiation treatment and pharmaceutical adjuvant, were used for sample filtration to further analysis of VLSM-determined area. GBM samples in the VLSM-determined area had longer OS time compared with those outside the VLSM-determined area. For proneural subtype, samples in the VLSM-determined area had longer survival time than those outside the VLSM-determined area. However, there was no significant difference for mesenchymal subtype, which could be explained by the limited amount of data.

Different metastasis and immune related genes manifest differential expression patterns among GBM subtypes (41, 42). Mesenchymal subtype is characterized by an increased immune cell presence compared to proneural subtype (43). The existence of PMT progression can influence survival time, the sensitivity to radiotherapy and chemotherapy, potential target in gene therapy and tumor immunity (44). Quiescent GBM cells gain malignant potency by engaging a mesenchymal shift that resembles EMT process and increases invasive behaviors (45). Tumor purity refers to the proportion of cancer cells in a tumor sample and is negatively correlated with EMT process and immune activity (46). Cases with low tumor purity are more likely to be related to malignant entities and have reduced survival time, which resembles PMT progression, indicating a worsening process and enabling the tumor incline to obtain characters of mesenchymal subtype (24). Besides, PMT progression indicates a worsening process and enables the tumor incline to obtain characters of mesenchymal subtype (24, 47). Compared with proneural subtypes, mesenchymal subtype had the lower purity score, indicating a lower tumor purity with the infiltration of non-neoplastic cells into this subtype (19, 48). In order to assess the PMT progression of GBM, we compared EMT process and tumor purity by expression profiling data of samples in and outside the VLSM-determined area via ssGSEA. Samples outside the VLSM-determined area had higher EMT scores than those in the VLSM-determined area, representing that the EMT process were upregulated in GBM outside the VLSM-determined area. Low tumor purity, indicating poor prognosis and an intense immune phenotype (49), was detected in samples outside the VLSM-determined area. The diverse pattern of the presence of stromal and immune cells across tumor types more broadly illustrates the impact of the tumor microenvironment on tumorigenesis and homeostasis (46). In our study, the samples outside the VLSM-determined area had lower tumor purity, higher stromal and immune signature gene expression than samples in the VLSM-determined area, indicating a higher infiltration of stromal and immune cells in glioma tissues (50). Immune signature genes, such as S100A8, had been shown to be pro-tumorigenic by inducing infiltration of myeloid derived suppressor cells (MDSCs) (51) or suppressing T cell function at the tumor site (52). High expression of stromal signature genes, such as COL3A1, is correlated with poor prognosis in glioblastoma (53). These results demonstrated that the different microenvironment could regulate the malignant progression between GBM in and outside the VLSM-determined. In addition, the microenvironment plays a key role in PMT progression. GBM subtypes shift from one to another one upon changes in the microenvironment. The average percentage of the different ratio in 22 types immune cells between GBM in and outside the VLSM-determined area were calculated and displayed. According to the result, GBM outside the VLSM-determined area had lower infiltrations of T cells CD8 and T cells follicular helper compared with GBM in the VLSM-determined area. The immune response of patients with glioma are characterized by defects in poor tumor antigen-specific CD8+ T cell responses, and elevated programmed death 1 (PD-1) in CD8+ T cells contributing to the poor prognosis of these patients (54, 55). Low tumor-infiltrating CD8+ T cells were associate with poor progression-free survival (56). T follicular helper cell could activate B cells to facilitate

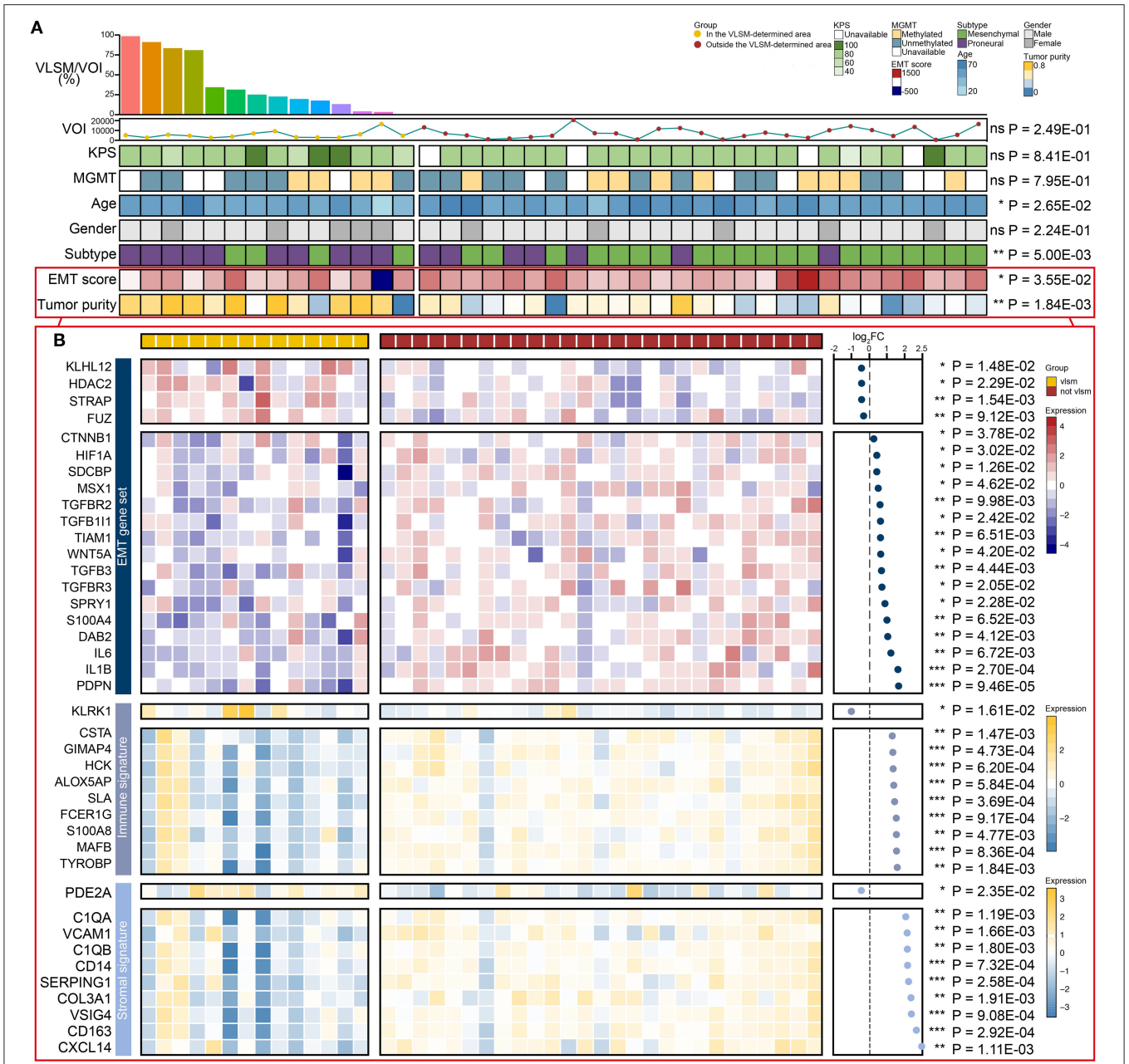

FIGURE 6 | The comparison of EMT score, tumor purity, clinical variables and differential expressed genes between GBM in and outside the VLSM-determined area. **(A)** The EMT score, tumor purity and the clinical variables including VLSM/VOI, VOI, KPS, MGMT, age, gender, subtype were used. The histogram presented VLSM/VOI in descending order. The line chart presented the VOIs. The heatmaps presented differences between GBM in and outside the VLSM-determined area. **(B)** The heatmaps showed the differential expressed genes of EMT gene set, immune signature and stromal signature of GBM in and outside the VLSM-determined area. The scatter plot presented the fold change of differential expressed genes in logarithmic form. *P*-value was determined by Student's *t*-test. Significant results were presented as ns non-significant, $^{*}P < 0.05$, $^{**}P < 0.01$, or $^{***}P < 0.001$.

the anti-tumor response (57). These results demonstrated that the different immune cells infiltration between GBM in and outside the VLSM-determined area could regulate the malignant progression of glioma.

In present study, the difference of gene expression patterns between GBM in and outside the VLSM-determined area provided reference to molecular targeting treatment according to different topography (58). Among 141 genes of EMT gene set, 16 genes including CTNNB1, HIF1A, and IL6 were upregulated. CTNNB1, the downstream effector of the canonical WNT signaling pathway, is a key feature of EMT process, which has been identified as a therapeutic target

for GBM (59). Multiple HIF1A-responsive EMT regulators in cancers is sufficient to induce all stages of cancer spread, including invasion, intravasation, and distant extravasation (60). Cytokines such as IL6 are capable of inducing EMT process by downregulation of E-cadherin and upregulation of Vimentin (61–63). The top 10 genes of differential expressed genes in stromal signature and immune signature were also of vital significance in PMT progression of GBM. Single cell analysis of immune cells in GBM showed that S100A8/9 (macrophages markers) was highly expressed in immune cells in the tumor core, indicating that the infiltration of immune cells within the mesenchymal subtype (19). CXCL14 enhances the sphere-forming ability of GBM cells, overexpresses in mesenchymal tumors and is responsible for tumor onset, growth and recurrence (64).

We realized the limitations of our techniques. Firstly, the VLSM method regarded each voxel as being independent and separated from other adjacent voxels, which may influence the calculation of involved regions. In addition, although the general MR imaging sequences ensure the reliability or reproducibility of the study, senior scans (such as DWI, DTI, MRS) are beneficial for further study of intratumoural transcriptional heterogeneity with novel algorithm.

Our study demonstrated a valuable VLSM-determined area related to the predilection site, prognosis and PMT progression by radiography approach. GBM involved in VLSM-determined area exhibited the characters of proneural subtype. The results also revealed the differences of EMT process and tumor purity among GBM in and outside the VLSM-determined area.

MATERIALS AND METHODS

Data Collection

Original data used in this research were provided by TCGA, an open resource containing comprehensive genomics information on various cancers. TCGA data collection founded by the cooperation between National Cancer Institute (NCI) and several institutions, publicly available in TCIA database, was selected to explore the connection between GBM phenotypes and radiographs, for data were matched to store in TCGA and TCIA (65). All information was available in an open manner, and no institutional review board or Act approval was essential. Imaging data comprised various general sequences such as T1-weighted, T2-weighted images, and other advanced MRI scans. Among different original pre-operative multimodal MRI scans, post-contrast T1-weighted and other available sequences such as T2-weighted images were employed in present study. Clinical data and molecular genetic data included gender, OS time, age, KPS, and other information (66).

MRI data of total 262 GBM samples including multiple sequences were acquired initially. The exclusion criteria referred to sample lacks post-contrast T1-weighted, subtype classification, and clinical features. After summarizing the entire data together, we identified 223 samples who had relevant variables available finally. A flowchart of the number of samples included or excluded for each analysis was shown in **Supplementary Figure 1**.

Imaging Processing

Prior to imaging processing, the original imaging dataset was evaluated by VASARI feature set, which served as a semi-quantitative imaging analysis for describing visual features on MRI (67). In this study, two variables describing topography of brain lobes of lesion and proportion of enhancing area were used, which were visually estimated by observers and divided into separate categories. For each sample, the images were evaluated by a neurosurgeon and a neuroradiologist independently and they knew nothing about other data. The third experienced neurosurgeon made the final decision judged by multiple MRI sequences when there was a discrepancy. All the observers learned the visual examples of scoring consensus in advance to ensure agreement. Kappa consistency test was used to check inter-observer variation.

After radiography materials were downloaded, format transformation was carried out to acquire NIfTI format profiles. The neurosurgeon and neuroradiologist manually draw the lesion map on post-contrast T1-weighted image in each axial slice by the usage of MRIcron (http://www.sph.sc.edu/comd/rorden/mricron) to delineate the boundary of the tumor. If there was an evident discrepancy (the ratio of VOI between two observers > 0.05), the VOIs of the samples would be rechecked by another neurosurgeon to make the final decision. Then VOIs of all samples were collected. The sequences were normalized into the stereotactic Montreal Neurological Institute (MNI) standard space. With Statistical Parametric Mapping 8 (SPM 8, http://www.fil.ion.ucl.ac.uk/spm/software/spm8) implemented in MATrix LABoratory (MATLAB, Mathworks, Natick, MA), images and generated VOIs were registered to brain atlas and normalized at the MNI space using the standard normalization algorithm followed by examination of visual inspection (68). To explore the distribution of GBM and correlations among different subtypes, all normalized VOIs were summed up together to get the overlay maps on ch2bet template.

VLSM Method

VLSM method was applied to relate lesion map to manifestation of proneural and mesenchymal subtype in MRIcron software by Non-parametric Mapping Statistics (NPM, http://www.mccauslandcenter.sc.edu/mricro/mricron/) (69). Subsequently, a spreadsheet was generated to link the lesion to subtype of each sample. Non-parametric Liebermeister test was used to perform statistical comparisons on voxel-wise base, which were performed at each voxel using specific subtypes as dependent variable (binary measure). *Z*-value corresponding to significant *P* level indicated the minimum threshold of significant topography, and a higher statistical output meant stronger association between predilection site of GBM and specific subtypes. Analysis was only computed on voxels damaged $> 5\%$. NPM false discovery rate (FDR) correction for multiple comparisons was applied. VLSM maps were displayed on ch2bet template with a statistical significance ($P < 0.05$).

Estimation of EMT Process and Tumor Purity

Expression profiling data from TCGA was used to evaluate EMT enrichment and tumor purity (70). SsGSEA was applied to get the enrichment scores of EMT gene set and tumor purity associated gene sets for each sample (71). A single sample's genes expression profiling data from the space of single genes were projected onto the space of every gene set by ssGSEA, and each enrichment score was on behalf of the degree to which the genes in every gene set were coordinately up-regulated or down-regulated within a sample (72).

Statistics

Statistical analysis (VLSM analysis excluded) was carried out by IBM SPSS statistics and GraphPad Prism. All results were shown as mean ± standard deviation or number of observations and percentages. Kappa consistency test was applied to evaluate consistency in the diagnosis of VASARI scores between different observers (73), and the kappa values > 0.8, in the range of 0.6–0.8, and < 0.6 indicated excellent, good and poor agreement, respectively. χ^2-test was used to detect the distribution of several attributes on categorical variables, while Student's *t*-test checked the differences between two groups on continuous variables. *R* packages, such as pheatmap, limma and affy, were used to produce figures and calculate differential expressed genes. Regarding to survival analysis, Kaplan-Meier curve and log-rank test were applied to describe OS time. $P < 0.05$ was considered statistically significant.

DATA AVAILABILITY STATEMENT

Publicly available datasets were analyzed in this study. This data can be found at: http://cancerimagingarchive.net, TCIA.

ETHICS STATEMENT

Ethical review and approval was not required for the study on human participants in accordance with the local legislation and institutional requirements. Written informed consent for participation was not required for this study in accordance with the national legislation and the institutional requirements.

AUTHOR CONTRIBUTIONS

CJ and JC designed the experiments. TQ and XM performed the experiments. TQ, XM, and JC analyzed the data and wrote the manuscript. ZW, XW, NS, JM, and LR contributed to materials and analysis tools. All authors revised the manuscript.

FUNDING

This study was supported by the National Natural Science Foundation of China (Nos: 81874204, 81772666, 81972817, 82073298, and 82003022); Excellent Young Talents Project of Central Government Supporting Local University Reform and Development Fund (No: 0202-300011190006); Karolinska Institutet Research Foundation Grants 2020-2021 (No. FS-2020:0007); the China Postdoctoral Science Foundation (Nos. 2019M660074 and 2020T130157); the Heilongjiang Postdoctoral Science Foundation (LBH-Z19029); and the Research Project of the Health and Family Planning Commission of Heilongjiang Province (2019-102).

SUPPLEMENTARY MATERIAL

The Supplementary Material for this article can be found online at: https://www.frontiersin.org/articles/10.3389/fonc.2021.595259/full#supplementary-material

REFERENCES

1. Li WB, Tang K, Chen Q, Li S, Qiu XG, Li SW, et al. MRI manifestions correlate with survival of glioblastoma multiforme patients. *Cancer Biol Med.* (2012) 9:120–3. doi: 10.3969/j.issn.2095-3941.2012.02.007
2. Wu P, Cai J, Chen Q, Han B, Meng X, Li Y, et al. Lnc-TALC promotes O(6)-methylguanine-DNA methyltransferase expression via regulating the c-Met pathway by competitively binding with miR-20b-3p. *Nat Commun.* (2019) 10:2045. doi: 10.1038/s41467-019-10025-2
3. Meng X, Zhao Y, Han B, Zha C, Zhang Y, Li Z, et al. Dual functionalized brain-targeting nanoinhibitors restrain temozolomide-resistant glioma via attenuating EGFR and MET signaling pathways. *Nat Commun.* (2020) 11:594. doi: 10.1038/s41467-019-14036-x
4. Gutman DA, Cooper LA, Hwang SN, Holder CA, Gao J, Aurora TD, et al. MR imaging predictors of molecular profile and survival: multi-institutional study of the TCGA glioblastoma data set. *Radiology.* (2013) 267:560–9. doi: 10.1148/radiol.13120118
5. Itakura H, Achrol AS, Mitchell LA, Loya JJ, Liu T, Westbroek EM, et al. Magnetic resonance image features identify glioblastoma phenotypic subtypes with distinct molecular pathway activities. *Sci Transl Med.* (2015) 7:303ra138. doi: 10.1126/scitranslmed.aaa7582
6. Bakas S, Akbari H, Sotiras A, Bilello M, Rozycki M, Kirby JS, et al. Advancing the cancer genome atlas glioma MRI collections with expert segmentation labels and radiomic features. *Sci Data.* (2017) 4:170117. doi: 10.1038/sdata.2017.117
7. Lee M, Han K, Ahn SS, Bae S, Choi YS, Hong JB, et al. The added prognostic value of radiological phenotype combined with clinical features and molecular subtype in anaplastic gliomas. *J Neuro-Oncol.* (2019) 142:129–38. doi: 10.1007/s11060-018-03072-0
8. Puchalski RB, Shah N, Miller J, Dalley R, Nomura SR, Yoon JG, et al. An anatomic transcriptional atlas of human glioblastoma. *Science.* (2018) 360:660–3. doi: 10.1126/science.aaf2666
9. Kimberg DY, Coslett HB, Schwartz MF. Power in voxel-based lesion-symptom mapping. *J Cognit Neurosci.* (2007) 19:1067–80. doi: 10.1162/jocn.2007.19.7.1067
10. Sagnier S, Sibon I. The new insights into human brain imaging after stroke. *J Neurosci Res.* (2019) doi: 10.1002/jnr.24525
11. Darlix A, Deverdun J, Menjot de Champfleur N, Castan F, Zouaoui S, Rigau V, et al. IDH mutation and 1p19q codeletion distinguish two radiological patterns of diffuse low-grade gliomas. *J Neuro-Oncol.* (2017) 133:37–45. doi: 10.1007/s11060-017-2421-0
12. Pisoni A, Mattavelli G, Casarotti A, Comi A, Riva M, Bello L, et al. Object-action dissociation: a voxel-based lesion-symptom mapping study on 102 patients after glioma removal. *NeuroImage Clin.* (2018) 18:986–95. doi: 10.1016/j.nicl.2018.03.022
13. Rathore S, Akbari H, Rozycki M, Abdullah KG, Nasrallah MP, Binder ZA, et al. Radiomic MRI signature reveals three distinct subtypes of glioblastoma

with different clinical and molecular characteristics, offering prognostic value beyond IDH1. *Sci Rep.* (2018) 8:5087. doi: 10.1038/s41598-018-22739-2
14. Verhaak RG, Hoadley KA, Purdom E, Wang V, Qi Y, Wilkerson MD, et al. Integrated genomic analysis identifies clinically relevant subtypes of glioblastoma characterized by abnormalities in PDGFRA, IDH1, EGFR, and NF1. *Cancer cell.* (2010) 17:98–110. doi: 10.1016/j.ccr.2009.12.020
15. Jakovlevs A, Vanags A, Gardovskis J, Strumfa I. Molecular classification of diffuse gliomas. *Polish J Pathol.* (2019) 70:246–58. doi: 10.5114/pjp.2019.93126
16. Pan YB, Wang S, Yang B, Jiang Z, Lenahan C, Wang J, et al. Transcriptome analyses reveal molecular mechanisms underlying phenotypic differences among transcriptional subtypes of glioblastoma. *J Cell Mol Med.* (2020) 24:3901–16. doi: 10.1111/jcmm.14976
17. Sharma A, Bendre A, Mondal A, Muzumdar D, Goel N, Shiras A. Angiogenic gene signature derived from subtype specific cell models segregate proneural and mesenchymal glioblastoma. *Front Oncology.* (2017) 7:146. doi: 10.3389/fonc.2017.00146
18. Ozawa T, Riester M, Cheng YK, Huse JT, Squatrito M, Helmy K, et al. Most human non-GCIMP glioblastoma subtypes evolve from a common proneural-like precursor glioma. *Cancer Cell.* (2014) 26:288–300. doi: 10.1016/j.ccr.2014.06.005
19. Behnan J, Finocchiaro G, Hanna G. The landscape of the mesenchymal signature in brain tumours. *Brain.* (2019) 142:847–66. doi: 10.1093/brain/awz044
20. Cai J, Zhang J, Wu P, Yang W, Ye Q, Chen Q, et al. Blocking LINC00152 suppresses glioblastoma malignancy by impairing mesenchymal phenotype through the miR-612/AKT2/NF-kappaB pathway. *J Neuro-Oncol.* (2018) 140:225–36. doi: 10.1007/s11060-018-2951-0
21. Waker CA, Lober RM. Brain tumors of glial origin. *Adv Experi Med Biol.* (2019) 1190:281–97. doi: 10.1007/978-981-32-9636-7_18
22. Murata H, Yoshimoto K, Hatae R, Akagi Y, Mizoguchi M, Hata N, et al. Detection of proneural/mesenchymal marker expression in glioblastoma: temporospatial dynamics and association with chromatin-modifying gene expression. *J Neuro-Oncol.* (2015) 125:33–41. doi: 10.1007/s11060-015-1886-y
23. Halliday J, Helmy K, Pattwell SS, Pitter KL, LaPlant Q, Ozawa T, et al. In vivo radiation response of proneural glioma characterized by protective p53 transcriptional program and proneural-mesenchymal shift. *Proc Natl Acad Sci USA.* (2014) 111:5248–53. doi: 10.1073/pnas.1321014111
24. Fedele M, Cerchia L, Pegoraro S, Sgarra R, Manfioletti G. Proneural-mesenchymal transition: phenotypic plasticity to acquire multitherapy resistance in glioblastoma. *Int J Mol Sci.* (2019) 20:2746. doi: 10.3390/ijms20112746
25. Yang J, Weinberg RA. Epithelial-mesenchymal transition: at the crossroads of development and tumor metastasis. *Dev Cell.* (2008) 14:818–29. doi: 10.1016/j.devcel.2008.05.009
26. Nicolasjilwan M, Hu Y, Yan C, Meerzaman D, Holder CA, Gutman D, et al. Addition of MR imaging features and genetic biomarkers strengthens glioblastoma survival prediction in TCGA patients. *J Neuroradiol.* (2015) 42:212–21. doi: 10.1016/j.neurad.2014.02.006
27. Mao P, Joshi K, Li J, Kim SH, Li P, Santana-Santos L, et al. Mesenchymal glioma stem cells are maintained by activated glycolytic metabolism involving aldehyde dehydrogenase 1A3. *Proc Natl Acad Sci USA.* (2013) 110:8644–9. doi: 10.1073/pnas.1221478110
28. Bhat KPL, Balasubramaniyan V, Vaillant B, Ezhilarasan R, Hummelink K, Hollingsworth F, et al. Mesenchymal differentiation mediated by NF-kappaB promotes radiation resistance in glioblastoma. *Cancer Cell.* (2013) 24:331–46. doi: 10.1016/j.ccr.2013.08.001
29. Tan MSY, Sandanaraj E, Chong YK, Lim SW, Koh LWH, Ng WH, et al. A STAT3-based gene signature stratifies glioma patients for targeted therapy. *Nat Commun.* (2019) 10:3601. doi: 10.1038/s41467-019-11614-x
30. Sanai N, Alvarez-Buylla A, Berger MS. Neural stem cells and the origin of gliomas. *N Engl J Med.* (2005) 353:811–22. doi: 10.1056/NEJMra043666
31. Huse JT, Phillips HS, Brennan CW. Molecular subclassification of diffuse gliomas: seeing order in the chaos. *Glia.* (2011) 59:1190–9. doi: 10.1002/glia.21165
32. Nakano I. Stem cell signature in glioblastoma: therapeutic development for a moving target. *J Neurosurg.* (2015) 122:324–30. doi: 10.3171/2014.9.Jns132253
33. Lin N, Yan W, Gao K, Wang Y, Zhang J, You Y. Prevalence and clinicopathologic characteristics of the molecular subtypes in malignant glioma: a multi-institutional analysis of 941 cases. *PLoS ONE.* (2014) 9:e94871. doi: 10.1371/journal.pone.0094871
34. Chillemi G, Calamuneri A, Morgante F, Terranova C, Rizzo V, Girlanda P, et al. Spatial and temporal high processing of visual and auditory stimuli in cervical dystonia. *Front Neurol.* (2017) 8:66. doi: 10.3389/fneur.2017.00066
35. Nizamutdinov D, Stock E, Dandashi J, Vasquez E, Mao Y, Dayawansa S, et al. Prognostication of survival outcomes in patients diagnosed with glioblastoma. *World Neurosurg.* (2018) 109:e67–74. doi: 10.1016/j.wneu.2017.09.104
36. Chandana SR, Movva S, Arora M, Singh T. Primary brain tumors in adults. *Am Fam Phys.* (2008) 77:1423–30. doi: 10.1016/S0140-6736(03)12328-8
37. Bates E, Wilson SM, Saygin AP, Dick F, Sereno MI, Knight RT, et al. Voxel-based lesion-symptom mapping. *Nat Neurosci.* (2003) 6:448–50. doi: 10.1038/nn1050
38. Steed TC, Treiber JM, Patel K, Ramakrishnan V, Merk A, Smith AR, et al. Differential localization of glioblastoma subtype: implications on glioblastoma pathogenesis. *Oncotarget.* (2016) 7:24899–907. doi: 10.18632/oncotarget.8551
39. Moulding HD, Friedman DP, Curtis M, Kenyon L, Flanders AE, Paek SH, et al. Revisiting anaplastic astrocytomas I: an expansive growth pattern is associated with a better prognosis. *J Magnet Reson Imaging: JMRI.* (2008) 28:1311–21. doi: 10.1002/jmri.21593
40. Chaichana KL, Kosztowski T, Niranjan A, Olivi A, Weingart JD, Laterra J, et al. Prognostic significance of contrast-enhancing anaplastic astrocytomas in adults. *J Neurosurg.* (2010) 113:286–92. doi: 10.3171/2010.2.Jns091010
41. Cai J, Zhang W, Yang P, Wang Y, Li M, Zhang C, et al. Identification of a 6-cytokine prognostic signature in patients with primary glioblastoma harboring M2 microglia/macrophage phenotype relevance. *PLoS ONE.* (2015) 10:e0126022. doi: 10.1371/journal.pone.0126022
42. Zha C, Meng X, Li L, Mi S, Qian D, Li Z, et al. Neutrophil extracellular traps mediate the crosstalk between glioma progression and the tumor microenvironment via the HMGB1/RAGE/IL-8 axis. *Cancer Biol Med.* (2020) 17:154–68. doi: 10.20892/j.issn.2095-3941.2019.0353
43. Kaffes I, Szulzewsky F, Chen Z, Herting CJ, Gabanic B, Velazquez Vega JE, et al. Human mesenchymal glioblastomas are characterized by an increased immune cell presence compared to proneural and classical tumors. *Oncoimmunology.* (2019) 8:e1655360. doi: 10.1080/2162402X.2019.1655360
44. Tejero R, Huang Y, Katsyv I, Kluge M, Lin JY, Tome-Garcia J, et al. Gene signatures of quiescent glioblastoma cells reveal mesenchymal shift and interactions with niche microenvironment. *EBioMedicine.* (2019) 42:252–69. doi: 10.1016/j.ebiom.2019.03.064
45. Phillips HS, Kharbanda S, Chen R, Forrest WF, Soriano RH, Wu TD, et al. Molecular subclasses of high-grade glioma predict prognosis, delineate a pattern of disease progression, and resemble stages in neurogenesis. *Cancer Cell.* (2006) 9:157–73. doi: 10.1016/j.ccr.2006.02.019
46. Yoshihara K, Shahmoradgoli M, Martínez E, Vegesna R, Kim H, Torres-Garcia W, et al. Inferring tumour purity and stromal and immune cell admixture from expression data. *Nat Commun.* (2013) 4:2612. doi: 10.1038/ncomms3612
47. Peng Y, Yu B, Qin H, Xue L, Liang Y, Quan ZJP. EMT-related gene expression is positively correlated with immunity and may be derived from stromal cells in osteosarcoma. *PeerJ.* (2020) 8:e8489. doi: 10.7717/peerj.8489
48. Wang Q, Hu B, Hu X, Kim H, Squatrito M, Scarpace L, et al. Tumor evolution of glioma-intrinsic gene expression subtypes associates with immunological changes in the microenvironment. *Cancer Cell.* (2018) 33:152. doi: 10.1016/j.ccell.2017.12.012
49. Zhang C, Cheng W, Ren X, Wang Z, Liu X, Li G, et al. Tumor purity as an underlying key factor in glioma. *Clin Cancer Res.* (2017) 23:6279–91. doi: 10.1158/1078-0432.Ccr-16-2598
50. Ye L, Zhang T, Kang Z, Guo G, Sun Y, Lin K, et al. Tumor-infiltrating immune cells act as a marker for prognosis in colorectal cancer. *Front Immunol.* (2019) 10:2368. doi: 10.3389/fimmu.2019.02368
51. Lim SY, Yuzhalin AE, Gordon-Weeks AN, Muschel RJ. Tumor-infiltrating monocytes/macrophages promote tumor invasion and migration by upregulating S100A8 and S100A9 expression in cancer cells. *Oncogene.* (2016) 35:5735–45. doi: 10.1038/onc.2016.107
52. Gielen PR, Schulte BM, Kers-Rebel ED, Verrijp K, Bossman SA, Ter Laan M, et al. Elevated levels of polymorphonuclear myeloid-derived suppressor cells in

patients with glioblastoma highly express S100A8/9 and arginase and suppress T cell function. *Neuro Oncol.* (2016) 18:1253–64. doi: 10.1093/neuonc/now034
53. Henke E, Nandigama R, Ergun S. Extracellular matrix in the tumor microenvironment and its impact on cancer therapy. *Front Mol Biosci.* (2019) 6:160. doi: 10.3389/fmolb.2019.00160
54. Prasad S, Gaedicke S, Machein M, Mittler G, Braun F, Hettich M, et al. Effective eradication of glioblastoma stem cells by local application of an AC133/CD133-specific T-cell-engaging antibody and CD8 T cells. *Cancer Res.* (2015) 75:2166–76. doi: 10.1158/0008-5472.CAN-14-2415
55. Chen PY, Wu CY, Fang JH, Chen HC, Feng LY, Huang CY, et al. Functional change of effector tumor-infiltrating CCR5(+)CD38(+)HLA-DR(+)CD8(+) T cells in glioma microenvironment. *Front Immunol.* (2019) 10:2395. doi: 10.3389/fimmu.2019.02395
56. Han S, Zhang C, Li Q, Dong J, Liu Y, Huang Y, et al. Tumour-infiltrating CD4(+) and CD8(+) lymphocytes as predictors of clinical outcome in glioma. *Br J Cancer.* (2014) 110:2560–8. doi: 10.1038/bjc.2014.162
57. Lu J, Li H, Chen Z, Fan L, Feng S, Cai X, et al. Identification of 3 subpopulations of tumor-infiltrating immune cells for malignant transformation of low-grade glioma. *Cancer Cell Int.* (2019) 19:265. doi: 10.1186/s12935-019-0972-1
58. Peng X. Advances in biomarkers of cerebral small vessel disease. *J Neurorestoratol.* (2019) 7:171–83. doi: 10.26599/jnr.2019.9040021
59. Chen Q, Cai J, Wang Q, Wang Y, Liu M, Yang J, et al. Long noncoding RNA NEAT1, regulated by the EGFR pathway, contributes to glioblastoma progression through the WNT/β-catenin pathway by scaffolding EZH2. *Clin Cancer Res.* (2018) 24:684–95. doi: 10.1158/1078-0432.Ccr-17-0605
60. Majmundar AJ, Wong WJ, Simon MC. Hypoxia-inducible factors and the response to hypoxic stress. *Mol Cell.* (2010) 40:294–309. doi: 10.1016/j.molcel.2010.09.022
61. Sullivan NJ, Sasser AK, Axel AE, Vesuna F, Raman V, Ramirez N, et al. Interleukin-6 induces an epithelial-mesenchymal transition phenotype in human breast cancer cells. *Oncogene.* (2009) 28:2940–7. doi: 10.1038/onc.2009.180
62. Jung HY, Fattet L, Yang J. Molecular pathways: linking tumor microenvironment to epithelial-mesenchymal transition in metastasis. *Clin Cancer Res.* (2015) 21:962–8. doi: 10.1158/1078-0432.CCR-13-3173
63. Lin L, Wang G, Ming J, Meng X, Han B, Sun B, et al. Analysis of expression and prognostic significance of vimentin and the response to temozolomide in glioma patients. *Tumour Biol.* (2016) 37:15333–9. doi: 10.1007/s13277-016-5462-7
64. Fazi B, Proserpio C, Galardi S, Annesi F, Cola M, Mangiola A, et al. The expression of the chemokine CXCL14 correlates with several aggressive aspects of glioblastoma and promotes key properties of glioblastoma cells. *Int J Mol Sci.* (2019) 20:2496. doi: 10.3390/ijms20102496
65. Clark K, Vendt B, Smith K, Freymann J, Kirby J, Koppel P, et al. The Cancer Imaging Archive (TCIA): maintaining and operating a public information repository. *J Digital Imag.* (2013) 26:1045–57. doi: 10.1007/s10278-013-9622-7
66. Deng Z, Yu H, Wang N, Alafate W, Wang J, Wang T, et al. Impact of preoperative Karnofsky Performance Scale (KPS) and American Society of Anesthesiologists (ASA) scores on perioperative complications in patients with recurrent glioma undergoing repeated operation. *J Neurorestoratol.* (2019) 7:143–52. doi: 10.26599/jnr.2019.9040015
67. Rios Velazquez E, Meier R, Dunn WD, Jr., Alexander B, Wiest R, et al. Fully automatic GBM segmentation in the TCGA-GBM dataset: prognosis and correlation with VASARI features. *Sci Rep.* (2015) 5:16822. doi: 10.1038/srep16822
68. Ashburner J, Friston KJ. Nonlinear spatial normalization using basis functions. *Human Brain Mapp.* (1999) 7:254–66.
69. Winder K, Linker RA, Seifert F, Wang R, Lee DH, Engelhorn T, et al. Cerebral lesion correlates of sympathetic cardiovascular activation in multiple sclerosis. *Human Brain Mapp.* (2019) 40:5083–93. doi: 10.1002/hbm.24759
70. Timmerman LA, Grego-Bessa J, Raya A, Bertrán E, Pérez-Pomares JM, Díez J, et al. Notch promotes epithelial-mesenchymal transition during cardiac development and oncogenic transformation. *Genes Dev.* (2004) 18:99–115. doi: 10.1101/gad.276304
71. Cai J, Chen Q, Cui Y, Dong J, Chen M, Wu P, et al. Immune heterogeneity and clinicopathologic characterization of IGFBP2 in 2447 glioma samples. *Oncoimmunology.* (2018) 7:e1426516. doi: 10.1080/2162402x.2018.1426516
72. Subramanian A, Tamayo P, Mootha VK, Mukherjee S, Ebert BL, Gillette MA, et al. Gene set enrichment analysis: a knowledge-based approach for interpreting genome-wide expression profiles. *Proc Natl Acad Sci USA.* (2005) 102:15545–50. doi: 10.1073/pnas.0506580102
73. Zhou H, Vallières M, Bai HX, Su C, Tang H, Oldridge D, et al. MRI features predict survival and molecular markers in diffuse lower-grade gliomas. *Neuro-Oncology.* (2017) 19:862–70. doi: 10.1093/neuonc/now256

Conflict of Interest: The authors declare that the research was conducted in the absence of any commercial or financial relationships that could be construed as a potential conflict of interest.

frontiers in Oncology

ORIGINAL RESEARCH
published: 15 April 2021
doi: 10.3389/fonc.2021.625220

Three-Dimensional Radiomics Features From Multi-Parameter MRI Combined With Clinical Characteristics Predict Postoperative Cerebral Edema Exacerbation in Patients With Meningioma

Bing Xiao[1†], Yanghua Fan[2†], Zhe Zhang[1], Zilong Tan[1], Huan Yang[1], Wei Tu[1], Lei Wu[1], Xiaoli Shen[1], Hua Guo[1], Zhen Wu[2] and Xingen Zhu[1*]*

[1] Department of Neurosurgery, Second Affiliated Hospital of Nanchang University, Nanchang, China, [2] Department of Neurosurgery, Beijing Tiantan Hospital, Capital Medical University, Beijing, China

OPEN ACCESS

Edited by:
Xuejun Li,
Central South University,
China

Reviewed by:
Alissa A. Thomas,
University of Vermont,
United States
Jinsong Wu,
Fudan University,
China

***Correspondence:**
Xingen Zhu
zxg2008vip@163.com
Zhen Wu
wz_ttyy@163.com

[†]These authors have contributed equally to this work

Specialty section:
This article was submitted to Neuro-Oncology and Neurosurgical Oncology, a section of the journal Frontiers in Oncology

Received: 02 November 2020
Accepted: 29 March 2021
Published: 15 April 2021

Citation:
Xiao B, Fan Y, Zhang Z, Tan Z, Yang H, Tu W, Wu L, Shen X, Guo H, Wu Z and Zhu X (2021) Three-Dimensional Radiomics Features From Multi-Parameter MRI Combined With Clinical Characteristics Predict Postoperative Cerebral Edema Exacerbation in Patients With Meningioma. Front. Oncol. 11:625220. doi: 10.3389/fonc.2021.625220

Background: Postoperative cerebral edema is common in patients with meningioma. It is of great clinical significance to predict the postoperative cerebral edema exacerbation (CEE) for the development of individual treatment programs in patients with meningioma.

Objective: To evaluate the value of three-dimensional radiomics Features from Multi-Parameter MRI in predicting the postoperative CEE in patients with meningioma.

Methods: A total of 136 meningioma patients with complete clinical and radiological data were collected for this retrospective study, and they were randomly divided into primary and validation cohorts. Three-dimensional radiomics features were extracted from multisequence MR images, and then screened through Wilcoxon rank sum test, elastic net and recursive feature elimination algorithms. A radiomics signature was established based support vector machine method. By combining clinical with the radiomics signature, a clin-radiomics combined model was constructed for individual CEE prediction.

Results: Three significance radiomics features were selected to construct a radiomics signature, with areas under the curves (AUCs) of 0.86 and 0.800 in the primary and validation cohorts, respectively. Two clinical characteristics (peritumoral edema and tumor size) and radiomics signature were determined to establish the clin-radiomics combined model, with an AUC of 0.91 in the primary cohort and 0.83 in the validation cohort. The clin-radiomics combined model showed good discrimination, calibration, and clinically useful for postoperative CEE prediction.

Conclusions: By integrating clinical characteristics with radiomics signature, the clin-radiomics combined model could assist in postoperative CEE prediction before surgery, and provide a basis for surgical treatment decisions in patients with meningioma.

Keywords: radiomics, meningioma, cerebral edema exacerbation, machine learning, MRI

INTRODUCTION

Meningioma is the most common intracranial tumor. Most meningiomas occur in the intracranial region, and more than 90% of meningiomas show benign growth (1). The incidence of meningiomas is 2:1 for females: males, the peak age is 45 years old, and it is rare for children, many asymptomatic meningiomas are incidental findings. At present, surgery is the first-line treatment, most of them have good prognosis (2), peritumoral edema is a common concomitant symptom of meningioma, up to 60-67.4% (3), easily complicated by cerebral edema postoperatively. Brain edema can be generally divided into cytotoxic brain edema and vasogenic brain edema. Meningioma edema is mainly angiogenic. For patients without peritumoral edema before operation, severe brain edema occurs after operation. Brain edema near the functional area is aggravated after operation, which seriously affects the prognosis of patients and prolongs the hospitalization time of patients. Peritumoral edema is a leading cause of morbidity and mortality in patients with brain tumors (4). Uncontrolled cerebral edema may result in refractory intracranial hypertension (RICH), and also leads to severe neurological deficits and potentially fatal herniation (5, 6). In a retrospective study, they evaluated the clinical and surgical records of 376 consecutive patients who underwent microsurgical removal of intracranial meningiomas between January 1995 and January 2001. 13 patients (3.5%) who met the following criteria were included for further analysis: CT scan or MR imaging showed increased extensive brain swelling with neurological deterioration after operation, which required further treatment intervention, such as artificial ventilation, endotracheal intubation or decompressive craniectomy for several days, however, not all of the edema worsened to the extent of the need to perform further treatment intervention, and most of them can get through the edema by strengthening dehydration (7). Therefore, it is very important to establish relevant models to predict the postoperative cerebral edema exacerbation (CEE) in patients with meningioma, also known as aggravation of postoperative edema (7, 8), closely observe the changes of patient's condition, regularly review the head CT, strengthen the rational use of dehydration drugs, glucocorticoids, and even remove bone flap, so as to formulate the corresponding treatment plan.

Radiomics is a new machine learning method, which can extract data reflecting important biological tissue characteristics from medical image information (9). Compared with the traditional methods, the data mining of radiomics has two unique advantages (10). First of all, it allows semi-automatic or automatic extraction of imaging features and provides rich data related to qualitative analysis. Secondly, by identifying different sub regions and defining the spatial complexity of the disease, high-dimensional imaging information can reveal the heterogeneity within a region.

Recent studies have shown that radiomics has broad application prospects in early screening, accurate diagnosis, grading and staging, molecular marker prediction, treatment and prognosis of central nervous system diseases, and is helpful to formulate individualized treatment strategies (11–13). Therefore, in this retrospective study, we aimed to develop a radiomics model based on the minimal radiomic feature set of MR images to predict the aggravation of brain edema after meningioma surgery.

MATERIALS AND METHODS

Patients

A total of 136 patients with meningioma from the Second Affiliated Hospital of Nanchang University were included in our study. The inclusion criteria were as follows: 1) meningioma patients who underwent initial tumor resection surgery from 2017 to 2019 at the Second Affiliated Hospital of Nanchang University; 2) available information of postoperative edema; 3) available preoperative brain MRI examination; 4) complete clinical data; and 5) meningioma confirmed by postoperative pathological analysis.

The Ethical Review Committee of the Second Affiliated Hospital of Nanchang University approved the study design and protocol. All included patients were randomized to the primary cohort (n=90) and validation cohort (n=46). The primary cohort was used for model construction, while the validation cohort was used for model internal validation.

Clinical Characteristics

Eight preoperative clinical features from these patients were artificially collected: gender, age, peritumoral edema (negative or positive), tumor size (<2cm, 2-5cm or >5cm), tumor location (parasinoidal, facies convexa, skull base or others), hypertension (negative or positive), diabetes (negative or positive), and epilepsy (negative or positive).

One postoperative clinical feature CEE was artificially collected, CEE was defined as CEE can be defined if it meets any of the following criteria (8): 1) New sheet or finger brain edema occurs after operation, and the maximum diameter of edema is not less than 2cm; 2) If there is no peritumoral edema before operation, flaky, finger shaped or annular brain edema occurs after operation, and the maximum diameter of the tumor cavity in the same layer of the tumor or operation area is not less than 2 cm before operation or on the first day after operation. 3, if there is peritumoral edema before operation, the maximum

diameter of lamellar, finger like or annular brain edema after operation is not less than 2 cm compared with the maximum diameter of brain edema on the same plane before operation or on the first day after operation.

Brain MRI Sequence and Regions of Interest Delineating

A flowchart of this study is shown in **Figure 1**. All patients underwent brain T2-weighted imaging (T2WI) and contrast-enhanced T1WI (CET1) MR imaging before surgery. The acquisition parameters of T2WI sequence were as follows: repetition time/echo time of 3640/98 ms, acquisition matrix of 320 × 224, slice thickness of 5 mm. Meanwhile, the acquisition parameters of T1WI sequence were as follows: repetition time/echo time of 2070/26 ms, flip angle of 90°, acquisition matrix of 320 × 256, slice thickness of 5 mm. CET1 was carried out the T1WI sequence parameters after rapid injection of a gadolinium-DTPA contrast agent. T2WI and contrast-enhanced T1WI in the in axial plane were utilized, and all DICOM format images were collected based on the picture archiving and communication system of the Second Affiliated Hospital of Nanchang University.

A neuroradiologist with 9 years of experience in meningioma diagnosis was responsible for mapping the three-dimensional regions of interest (ROIs) of tumors on the MRI images using ITK-SNAP software (University of Pennsylvania, www.itk snap.org). Then another neuroradiologist with 15 years of experience manually confirmed the findings. Any disagreement between the two neuroradiologists was resolved through a neuroradiologist with 31 years of experience.

Radiomics Feature Extraction

Then, quantitative radiomics features were extracted from these ROIs using PyRadiomics (https://github.com/Radiomics/pyradiomics) (14). Each sequence can extract a total of 1,562 features, and these features were normalized to a value of 0 to 1 and classified into four categories (15): shape and size features (n = 14), first-order features (n = 180), textural features (n = 680), and wavelet features (n = 688).

The four types offeatures were described as follows (16, 17): first-order statistics describe the distribution of voxel intensities within the brain MRI image through commonly used and basic metrics; the three-dimensional size and shape features were independent from the gray level intensity distribution in the ROI, and were calculated on the non-derived image and mask; the textural features describing patterns or the spatial distribution of voxel intensities, which were calculated from respectively gray level co-occurrence (GLCM) and gray level run-length (GLRLM) texture matrices; Wavelet transform effectively decouples textural information by decomposing the original image, in a similar manner as Fourier analysis, in low –and high-frequencies.

Radiomics Features Selection and Radiomics Signature Construction

Due to the large number and high complexity of the radiomics features, we needed to perform a selection process to reduce overfitting (18). The selection method was conducted as previously described (15) to prioritize the features. In short, univariate analysis by Wilcoxon rank sum test was used to identify the differential radiomics features between patients with postoperative CEE and non-CEE. In addition, elastic net algorithm (19) was used to select the most informative features. Elastic net is a method combining least absolute shrinkage and selection operator (LASSO) and ridge regression. LASSO (20) is a commonly used high-dimensional data analysis method that can improve the prediction accuracy and interpretation ability. Finally, a recursive feature elimination (RFE) algorithm through five-fold cross-validation was used to identity the finally radiomics features.

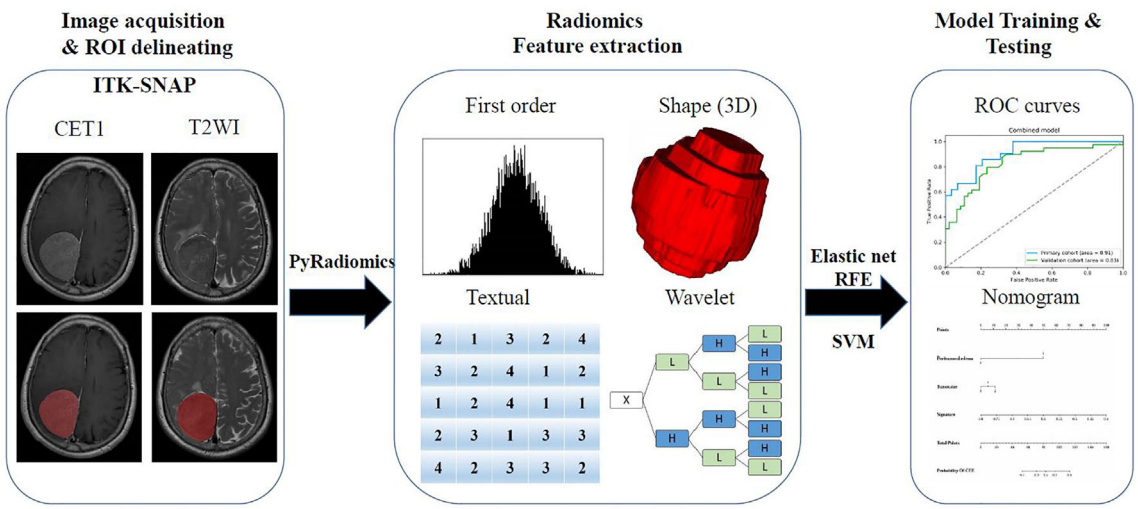

FIGURE 1 | The flow chart of the present study. (I) Brain axial contrast-enhanced T1WI (CET1) T2-weighted imaging (T2WI) and MR images acquisition; Regions of interest (ROI) segmentation by ITK-SNAP software. (II) Four categories radiomics features extracted by PyRadiomics algorithm. (III) Radiomics Feature selection by elastic net and RFE algorithm, and model training and testing.

A radiomics signature was established based on the radiomics features selected from the primary cohort through the support vector machine (SVM) method. At the same time, differences in the signature distribution between soft and firm tumors were compared between the two cohorts using a violin plot. A receiver operating characteristic (ROC) (21) curve was drawn to display the predictive value of the radiomics signature.

Construction and Validation of Clinical and Clin-Radiomics Combined Model

Multivariable logistic regression analysis was applied to construct a clinical model based on all included clinical features. Then, to establish a more comprehensive and accurate model for predicting the postoperative CEE, a clin-radiomics combined model was constructed by combining the most valuable clinical features with the radiomics signature. Akaike information criterion (AIC) (22) were used to screen the most valuable clinical features. And the usage and structure of the combined model was presented as a nomogram. ROC curve analyses and area under the ROC curve (AUC) were performed to evaluate the discriminative efficacy of the clinical and clin-radiomics combined model in both the primary and validation cohorts.

Calibration Curve Analysis and Decision Curve Analysis

Calibration curves and the Hosmer–Lemeshow test were used to assess the similarity between the predicted and observed postoperative CEE (23). Decision curve analysis was performed to evaluate the clinical application of the clin-radiomics combined model by quantifying the net benefits at different threshold probabilities (24).

Statistical Analysis

A two-sided *P*-value of <0.05 was deemed to be statistically significant. The statistical software R (version 3.4.1, R Foundation for Statistical Computing, Vienna, Austria) was used to perform the statistical analysis. The calibration plot was analyzed with the 'hdnom' packages. The decision curve analysis was conducted by the function 'dca.R'.

RESULTS

Clinical Characteristics

In total, 207 patients with meningioma underwent neurosurgery at the Second Affiliated Hospital of Nanchang University from 2017 to 2019. After screening, 71 patients were excluded due to unavailable preoperative MRI data, excessive preoperative information loss or lack of postoperative information, or both. Ultimately, 136 patients with meningioma were identified and included in the study. The mean age at diagnosis was 54.169 ± 11.765 years, with a male-to-female ratio of 2.9:1 (101/35). Of the 136 patients, 45(33.1%) had a peritumoral edema. Postoperative CEE was present in 60 (44.1%) patients and non-CEE was present in 76 (55.9%) patients. All included clinical characteristics are summarized in **Table 1**.

All patients were randomly divided into a primary cohort (n=90) and a validation cohort (n=46). There was no significant interclass difference in terms of gender, age, peritumoral edema, tumor size, tumor location, hypertension, diabetes, epilepsy, and postoperative CEE between the primary cohort and the validation cohort (**Table 1**, P=0.086–0.741). The results justify the use of the two datasets for training and testing.

Correlation Between Postoperative CEE and Clinical Characteristics

As shown in **Table 2**, peritumoral edema, tumor size, and location showed significant relationships with postoperative CEE (P = 0.000–0.001). The results demonstrated that patients who had larger tumor size, peritumoral edema, parasinoidal and skull base tumor were more likely to have postoperative CEE. Conversely, we found no significant differences in gender, age, hypertension, diabetes, and epilepsy between the postoperative CEE and non-CEE groups (P = 0.076–0.810).

As shown in **Table 3**, univariate analysis was used to determine the independent clinical risk variables for postoperative CEE in the primary cohort and the validation cohort, respectively. Similar to the previous results, in the primary cohort, we found a significant association between postoperative CEE and peritumoral edema (P = 0.000), tumor size (P = 0.000), and location (P = 0.018). In the validation cohort, peritumoral edema (P = 0.021) and location (P = 0.038) tended to be associated with postoperative CEE.

Radiomics Feature Selection and Radiomics Signature Construction

We extracted 3,124 radiomics features from one patient in two sequences. First, 1962 radiomics features were selected by Wilcoxon rank-sum test. Then, we use elastic net algorithm to determine 45 informative features. Finally, through the screening by RFE algorithm with 5-fold cross validation, 3 features that gave the best performance were selected as the final features for subsequent use. Two features were selected from the CET1 images, and one features from the T2WI images. The three selected radiomics features had significant differences in postoperative CEE and non-CEE groups (**Figure 2**, **Table 4**).

All 3 selected features were then entered into an SVM to build a radiomics signature. The violin plot showed significant differences in the distribution of the radiomics signature between postoperative CEE and non-CEE groups in both primary and validation cohorts (P<0.01; **Figure 3**). The radiomics signature showed favorable discrimination in predicting the postoperative CEE with AUC values of 0.86 (95% confidence interval [CI], 0.833–0.881) and 0.800(0.771-0.828) in the primary and validation cohorts, respectively (**Figure 4A**).

Performance of Clinical and Clin-Radiomics Combined Model

The 8 available features in the primary cohort were used to build clinical model based on multivariable logistic regression analysis. We then verified the performance of these models in the

TABLE 1 | Patients' characteristics of primary and validation cohorts.

Characteristics	Whole cohort (n=136)	Primary cohort (n=90)	Validation cohort (n=46)	P-value
Gender				
Male	101 (74.3%)	70 (77.8%)	31 (67.4%)	0.19
Female	35 (25.7%)	20 (22.2%)	15 (32.6%)	
Age (year)	54.169 ± 11.765	53.578 ± 11.237	55.236 ± 12.786	0.414
Peritumoral edema				
Negative	91 (66.9%)	62 (68.9%)	29 (63.0%)	0.493
Positive	45 (33.1%)	28 (31.1%)	17 (37.0%)	
Tumor size				
<2cm	18 (13.2%)	11 (12.2%)	7 (15.2%)	0.444
2-5cm	95 (69.9%)	66 (73.3%)	29 (63.1%)	
>5cm	23 (16.9%)	13 (14.5%)	10 (21.7%)	
Location				
Parasinoidal	37 (27.2%)	23 (25.6%)	14 (30.4%)	0.741
Facies convexa	28 (20.6%)	19 (21.1%)	9 (19.6%)	
Skull base	24 (17.6%)	18 (20.0%)	6 (13.0%)	
Others	47 (34.6%)	30 (33.3%)	17 (37.0%)	
Hypertension				
Negative	113 (83.1%)	74 (82.2%)	39 (84.8%)	0.706
Positive	23 (16.9%)	16 (17.8%)	7 (15.2%)	
Diabetes				
Negative	132 (97.1%)	86 (95.6%)	46 (100%)	0.147
Positive	4 (2.9%)	4 (4.4%)	0 (0%)	
Epilepsy				
Negative	134 (98.5%)	89 (98.9%)	45 (97.8%)	0.626
Positive	2 (1.5%)	1 (1.1%)	1 (2.2%)	
Cerebral edema exacerbation				
Negative	76 (55.9%)	55 (61.1%)	21 (45.7%)	0.086
Positive	60 (44.1%)	35 (38.9%)	25 (54.3%)	

Categorical variables were presented as the number (percentage). Continuous variables consistent with a normal distribution were presented as mean ± standard deviation, otherwise the median and quartile are used. Chi-Square or Fisher Exact tests, as appropriate, were used to compare the differences in categorical variables, while the independent sample t-test was used to compare the differences in continuous variables.

TABLE 2 | Correlation between cerebral edema exacerbation and clinical characteristics of patients with meningioma in all patients.

Characteristics	All Patients (n=136)	Non-CEE (n=76)	CEE (n=60)	P-value
Gender				
Male	101 (74.3%)	59 (77.6%)	42 (70.0%)	0.312
Female	35 (25.7%)	17 (22.4%)	18 (30.0%)	
Age (year)	54.169 ± 11.765	55.066 ± 10.765	53.033 ± 12.926	0.319
Peritumoral edema				
Negative	91 (66.9%)	66 (86.8%)	25 (41.7%)	0.000
Positive	45 (33.1%)	10 (13.2%)	35 (58.3%)	
Tumor size				
<2cm	18 (13.2%)	16 (21.1%)	2 (3.3%)	0.000
2-5cm	95 (69.9%)	56 (73.7%)	39 (65.0%)	
>5cm	23 (16.9%)	4 (5.2%)	19 (32.7%)	
Location				
Parasinoidal	37 (27.2%)	16 (21.1%)	21 (35.0%)	0.001
Facies convexa	28 (20.6%)	16 (21.1%)	12 (20.0%)	
Skull base	24 (17.6%)	8 (10.5%)	16 (26.7%)	
Others	47 (34.6%)	36 (47.3%)	11 (18.3%)	
Hypertension				
Negative	113 (83.1%)	67 (88.2%)	46 (76.7%)	0.076
Positive	23 (16.9%)	9 (11.8%)	14 (23.3%)	
Diabetes				
Negative	132(97.1%)	74 (97.4%)	58 (96.7%)	0.810
Positive	4 (2.9%)	2 (2.6%)	2 (3.3%)	
Epilepsy				
Negative	134 (98.5%)	76 (100%)	58 (96.7%)	0.109
Positive	2 (1.5%)	0 (0%)	2 (3.3%)	

CEE, Cerebral edema exacerbation.

Categorical variables were presented as the number (percentage). Continuous variables consistent with a normal distribution were presented as mean ± standard deviation, otherwise the median and quartile are used. Chi-Square or Fisher Exact tests, as appropriate, were used to compare the differences in categorical variables, while the independent sample t-test was used to compare the differences in continuous variables.

TABLE 3 | Correlation between cerebral edema exacerbation and clinical characteristics of patients with meningioma in the primary cohort and validation cohort.

Characteristics	Primary cohort (n=90)		P-value	Validation cohort(n=46)		P-value
	Non-CEE	CEE		Non-CEE	CEE	
No.	55	35		21	25	
Gender						
Male	44 (80.0%)	26 (74.3%)	0.525	15 (71.4%)	16 (64.0%)	0.592
Female	11 (20.0%)	9 (25.7%)	6 (28.6%)	9 (36.0%)		
Age (year)	53.473 ± 10.706	53.743 ± 12.183	0.912	59.240 ± 9.990	52.040 ± 14.096	0.056
Peritumoral edema						
Negative	49 (89.1%)	13 (37.1%)	0.000	17(81.0%)	12 (48.0%)	0.021
Positive	6 (10.9%)	22 (62.9%)	4 (19.0%)	13(52.0%)		
Tumor size						
<2cm	11 (20.0%)	0 (0%)	0.000	5 (23.8%)	2 (8.0%)	0.100
2-5cm	42 (76.4%)	24 (68.6%)	14 (66.7%)	15 (60.0%)		
>5cm	2 (3.6%)	11 (31.4%)	2 (9.5%)	8 (32.0%)		
Location						
Parasinoidal	11 (20.0%)	12 (34.3%)	0.018	5 (23.8%)	9 (36.0%)	0.038
Facies convexa	11 (20.0%)	8 (22.8%)	5 (23.8%)	4 (16.0%)		
Skull base	8 (14.5%)	10 (28.6%)	0 (0%)	6 (24.0%)		
Others	25 (45.5%)	5 (14.3%)	11 (52.4%)	6 (24.0%)		
Hypertension						
Negative	48 (87.3%)	26 (74.3%)	0.116	19 (90.5%)	20 (80.0%)	0.324
Positive	7 (12.7%)	9 (25.7%)	2 (9.5%)	5 (20.0%)		
Diabetes						
Negative	53 (96.4%)	33 (94.3%)	0.641	21 (100%)	25 (100%)	a*
Positive	2 (3.6%)	2 (5.7%)	0 (0%)	0 (0%)		
Epilepsy						
Negative	55 (100%)	34 (97.1%)	0.207	21 (100%)	24(96.0%)	0.354
Positive	0 (0%)	1 (2.9%)	0 (0%)	1 (4.0%)		

CEE, Cerebral edema exacerbation. a means no comparative significance.*

Categorical variables were presented as the number (percentage). Continuous variables consistent with a normal distribution were presented as mean ± standard deviation, otherwise the median and quartile are used. Chi-Square or Fisher Exact tests, as appropriate, were used to compare the differences in categorical variables, while the independent sample t-test was used to compare the differences in continuous variables.

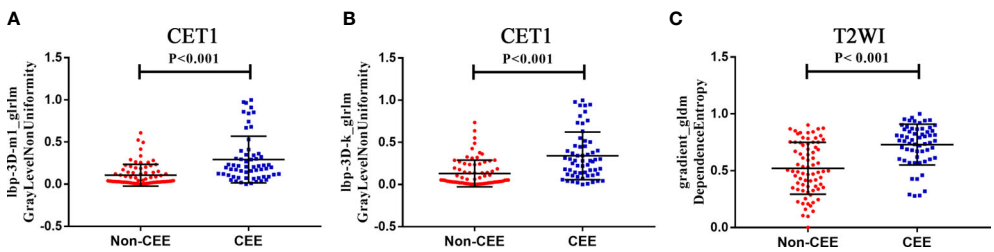

FIGURE 2 | The selected three radiomics features showed significant differences between the postoperative CEE and non-CEE groups. **(A)** Texture feature 'lbp-3D-m1_glrlm_GrayLevelNonUniformity' in contrast-enhanced T1-weighted imaging sequence; **(B)** Texture feature 'lbp-3D-k_glrlm_GrayLevelNonUniformity' in contrast-enhanced T1-weighted imaging sequence; **(C)** Texture feature 'gradient_gldm_DependenceEntropy' in T2-weighted imaging sequence.

validation cohort. As showed in **Figure 4B**, the AUCs were 0.85 (95% CI, 0.828-0.757) and 0.79 (95% CI, 0.757-0.815) in the primary and validation cohorts, respectively.

In addition, after screening by AIC, two clinical characteristics (including peritumoral edema and tumor size) and radiomics signature were determined to establish the clin-radiomics combined model, yielded an AUC of 0.91 (95% CI, 0.893-926) in the primary cohort and 0.83 (95% CI, 0.808-0.858) in the validation cohort (**Figure 4C**). The predictive accuracy of the clin-radiomics combined model was 0.800 (0.775-0.824) in the primary cohort and 0.744 (0.718-0.770) in the validation cohort. The detailed predictive indicators of the three models are shown in **Table 5**. As showed in **Figure 5**, The clin-radiomics combined model is presented as a nomogram.

TABLE 4 | The detail information of three selected radiomic features.

Sequence	Feature name	Feature type	Non-CEE	CEE	P value
CET1	lbp-3D-m1_glrlm_GrayLevelNonUniformity	Texture	0.03975 (0.0235-0.151)	0.2025 0.0938-0.3483)	<0.001
CET1	lbp-3D-k_glrlm_GrayLevelNonUniformity	Texture	0.05305 (0.0212-0.2258)	0.2820 (0.1215-0.4578)	<0.001
T2WI	gradient_gldm_DependenceEntropy	Texture	0.4970 (0.3500-0.7443)	0.7640 (0.6150-0.8648)	<0.001

CEE, Cerebral edema exacerbation; T2WI, T2-weighted imaging; CE-T1, contrast-enhanced T1-weighted imaging.

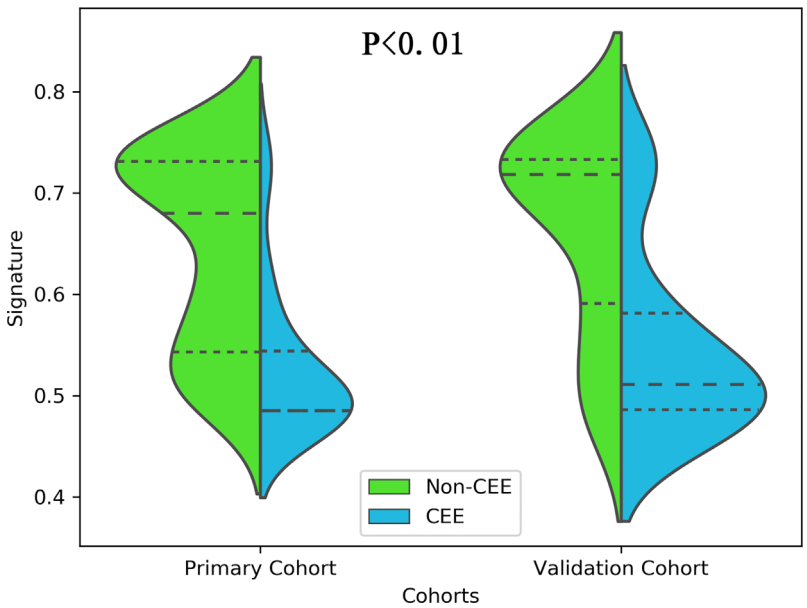

FIGURE 3 | The distribution of the radiomics signature between postoperative CEE and non-CEE groups was compared by violin plot in the primary and validation cohorts.

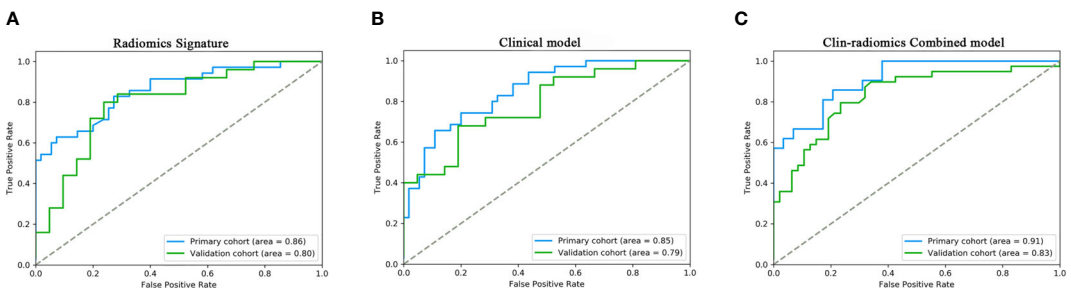

FIGURE 4 | ROC curves of the radiomics signature, clinical model, and the clin-radiomics combined model in the primary and validation cohorts. The performances of these models were assessed using the AUC value. **(A)** Radiomics signature. **(B)** Clinical model. **(C)** Clin-radiomics combined model.

Calibration and Clinical Usefulness Analysis

The calibration curve analysis and Hosmer-Lemeshow test for clin-radiomics combined model demonstrated good agreement between observations and predictions in both the primary (P=0.95; **Figure 6A**) and validation cohorts (P=0.57; **Figure 6B**).

The decision curve analysis for the clin-radiomics combined model is shown in **Figure 7**. The results showed that the clin-radiomics combined model performed a higher net benefit than both schemes, with a threshold probability of >0% for the primary cohort (**Figure 7A**) and a threshold probability of >13% for the validation cohort (**Figure 7B**). The results indicating that the clin-radiomics combined model were clinically useful.

TABLE 5 | Performance of radiomics signature, clinical model and combined model.

Model	Performance	AUC	ACC	SE	SP	PPV	NPV
Radiomic	Primary cohort	0.86 (0.833-0.881)	0.7 (0.672-0.727)	0.857 (0.822-0.891)	0.6 (0.561-0.638)	0.577 (0.537-0.617)	0.868 (0.836-0.899)
Signature	Validation cohort	0.800 (0.771-0.828)	0.761 (0.734-0.787)	0.84 (0.809-0.871)	0.667 (0.623-0.709)	0.75 (0.714-0.784)	0.778 (0.738-0.818)
Clinical	Primary cohort	0.85 (0.828-0.757)	0.778 (0.751-0.804)	0.600 (0.552-0.650)	0.891 (0.866-0.915)	0.778 (0.732-0.823)	0.778 (0.747-0.810)
model	Validation cohort	0.79 (0.757-0.815)	0.630 (0.600-0.660)	0.480 (0.438-0.520)	0.810 (0.772-0.845)	0.750 (0.703-0.780)	0.567 (0.529-0.604)
Combined	Primary cohort	0.91 (0.893-926)	0.800 (0.775-0.824)	0.667 (0.621-0.710)	0.897 (0.872-0.921)	0.824 (0.782-0.864)	0.788 (0.757-0.818)
model	Validation cohort	0.83 (0.808-0.858)	0.744 (0.718-0.770)	0.615 (0.572-0.659)	0.851 (0.822-0.880)	0.774 (0.733-0.816)	0.727 (0.693-0.761)

AUC, area under curve; ACC, accuracy; SN, sensitivity; SP, specificity; PPV, positive predict value; NPV, negative predictive value.

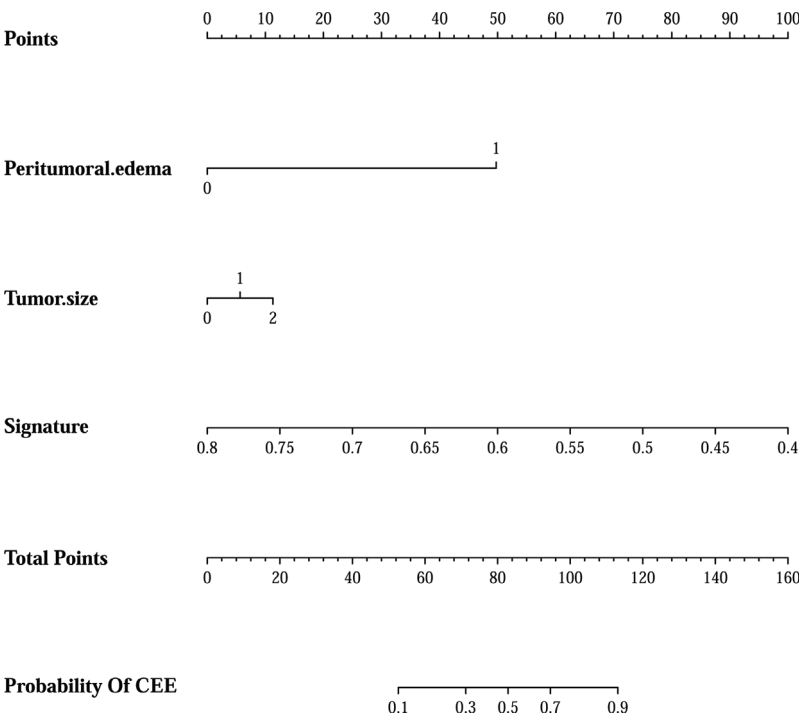

FIGURE 5 | The clin-radiomics combined model is presented as a nomogram, which incorporated patients' peritumoral edema, tumor size, and radiomics signature. The value of peritumoral edema, tumor size, and radiomics signature is located on corresponding lines 2-4, respectively. Draw a vertical line to the first line (point axis) to get the corresponding score. The total scores obtained for three included features are reflected in line 5 (total point axis), and the possibility of postoperative CEE has been determined in the last line.

DISCUSSION

Meningioma is a benign tumor originating from meningeal cells. It has the characteristics of high incidence rate, wide invasion area and high local recurrence rate. It seriously threatens people's health and lives. It has attracted widespread attention in clinic (25). However, many patients have postoperative brain edema and severe life threatening. Therefore, it is particularly important to predict postoperative edema of meningioma. At present, most of the studies are about peritumoral edema of meningiomas before operation, and the mechanism is not completely clear. It may be related to the tumor itself factors, location, volume, pathological type (26), blood-brain barrier damage (27), endocrine activity and so on. However, there are few studies on the aggravation of postoperative brain edema. The edema of meningioma was mainly vascular origin, and the edema fluid was generated in tumor tissue. The formation mechanism of angiogenic brain edema is that the increase of capillary permeability leads to the infiltration of edema fluid and edema protein into peripheral brain tissue (28).Therefore, some scholars have shown that the aggravation of brain edema after surgery may be due to the further destruction of the structure adjacent to the blood-brain barrier, increased permeability, a large amount of water seeps from the capillary and accumulates in the extracellular space of nerve cells. It is undeniable that surgical injury is indeed one of the factors for aggravating brain edema (29).Some studies have also shown that brain edema after meningioma surgery is caused by the relief of tumor compression. When the compression is relieved, the blood-brain barrier is affected, which is easy to induce vasospasm and further aggravate the edema (30). Studies have shown that there is a significant correlation between the expression of vascular

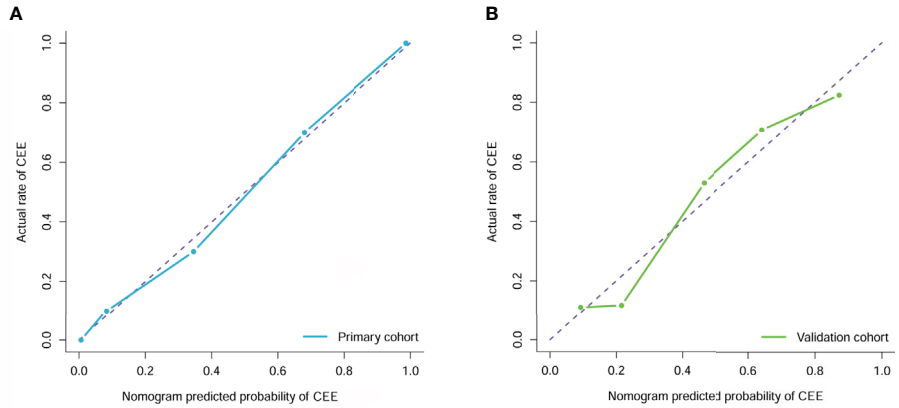

FIGURE 6 | Calibration curve analysis for the clin-radiomics combined model in the primary **(A)** and validation **(B)** cohorts. Calibration curves depict the calibration of each model in terms of the agreement between the predicted and actual probability of the postoperative CEE probability. The Y axis represents the actual rate. The X axis represents the predicted probability. The diagonal purple line represents perfect prediction by an ideal model. The blue (primary cohort) and green (validation cohort) lines represent the performance of the clin-radiomics combined model, of which a closer fit to the diagonal purple line represents a better prediction.

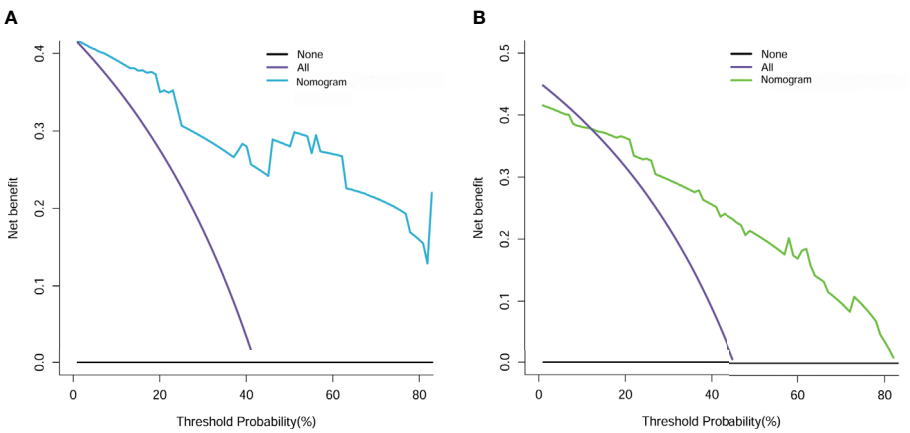

FIGURE 7 | Decision curve analysis for clin-radiomics combined model in the primary **(A)** and validation **(B)** cohorts. The Y axis measures the net benefit. The blue (primary cohort) and green (validation cohort) lines represent the clin-radiomics combined model. The purple line represents the assumption that the postoperative CEE is highly expressed in all patients. The black line represents the assumption that no patients had a postoperative CEE.

endothelial factor (31) and aquaporin-4 (32), which may be the factors of aggravating brain edema after surgery in patients with meningioma.

Radiomics is a new research field, which mainly through the extraction, processing and quantitative analysis of high-throughput data to explore the relationship with clinical value information (33). As described in our previous study and review (12), the radiomics process will first convert the radiographic images into the mineable data, which has involved 4 steps, namely, (a) image acquisition as well as reconstruction, (b) segmentation or labeling of the region of interest (ROI), (c) feature extraction as well as quantification, and (d) statistical analysis, establishment of the predictive and prognostic models. It has many applications in the central nervous system, such as differential diagnosis (34–37) and classification (15, 17), prediction of molecular characteristics (38, 39), therapeutic response and progress of central nervous system diseases (40, 41). These studies have shown that radiomics can be used to identify differences in treatment response, progression, and prognosis between patients with different CNS diseases, thus emphasizing that radiomics can be used as a new low-cost tool to improve treatment decisions for CNS diseases. Thus, we aim to develop an efficient and widely applicable preoperative radiomics model based on T2 and CET1 MRI images for predicting postoperative CEE in meningioma.

In the current study, Wilcoxon rank sum test, elastic net and RFE algorithm were sequentially utilized to reduce redundant features and select the most appropriate features for the

construction of a radiomics signature. It is crucial to exclude irrelevant features, because these features may obscure important information and affect the performance of the prediction model (42). First, after the Wilcoxon rank sum test, we conducted a preliminary screening and got 1962 radiomics features. Then, 45 radiomics features were further obtained through the elastic net algorithm, and a feasible number that balances insufficient fitting and over fitting is obtained. Finally, using the RFE algorithm to select 3 features, a prediction model was constructed, and balanced performance was achieved in both the primary and validation cohorts.

Next, a radiomics signature and a clin-radiomics combined model that combined the radiomics signature and clinical features were constructed to predict the postoperative CEE of meningioma. The clin-radiomics combined model demonstrated a stable and reliable performance, reaching an AUC of 0.91 (95% CI, 0.893-926) and 0.83 (95% CI, 0.808-0.858), and an accuracy of 0.800 (0.775-0.824) and 0.744 (0.718-0.770) in the primary and validation cohorts, respectively. Good discrimination and good calibration were observed with the clin-radiomics combined model. The performance of the clin-radiomics combined model constructed is significantly higher than that of the clinical model, so the use of the clin-radiomics combined model is more accurate and more effective in predicting the postoperative brain edema and assisting clinical decision-making. These results indicated the reliability of the radiomics approach to non-invasively predict postoperative CEE in patients with meningioma.

This study has some limitations. First, this is a single-center retrospective study. Second, although internal patients were used to validate the model, the number of patients we included was small. Thus, more patients from multiple centers and prospective studies are necessary to verify the effectiveness and robustness of this clin-radiomics combined model. Finally, the standard of CEE adopted by us is as mentioned above, but different CEE standards will lead to different results.

CONCLUSION

In conclusion, this retrospective study demonstrated that multiparametric MRI-based radiomics analysis is a promising approach for postoperative CEE prediction in patients with meningioma. It can serve as an effective noninvasive approach to predict postoperative CEE and determine individualized therapeutic schemes for patients with meningioma.

DATA AVAILABILITY STATEMENT

The raw data supporting the conclusions of this article will be made available by the authors, without undue reservation.

ETHICS STATEMENT

The Ethical Review Committee of the Second Affiliated Hospital of Nanchang University approved the study design and protocol.

AUTHOR CONTRIBUTIONS

All authors contributed to the article and approved the submitted version. All authors analyzed and interpreted the data. BX and YF revised the manuscript for important intellectual content and contributed equally. ZW and XZ take final responsibility for this article.

FUNDING

The present study was supported by Jiangxi provincial department of education natural science foundation youth project (grant no. GJJ180153), Science and technology plan of Jiangxi provincial health commission (grant no. 20201063).

REFERENCES

1. Claus EB, Bondy ML, Schildkraut JM, Wiemels JL, Wrensch M, Black PM. Epidemiology of intracranial meningioma. *Neurosurgery* (2005) 57(6):088–95. discussion -95. doi: 10.1227/01.neu.0000188281.91351.b9
2. Hasseleid BF, Meling TR, Ronning P, Scheie D, Helseth E. Surgery for convexity meningioma: Simpson Grade I resection as the goal: clinical article. *J Neurosurg* (2012) 117(6):999–1006. doi: 10.3171/2012.9.JNS12294
3. Gawlitza M, Fiedler E, Schob S, Hoffmann KT, Surov A. Peritumoral Brain Edema in Meningiomas Depends on Aquaporin-4 Expression and Not on Tumor Grade, Tumor Volume, Cell Count, or Ki-67 Labeling Index. *Mol Imaging Biol* (2017) 19(2):298–304. doi: 10.1007/s11307-016-1000-7
4. Berhouma M, Jacquesson T, Jouanneau E, Cotton F. Pathogenesis of peritumoral edema in intracranial meningiomas. *Neurosurg Rev* (2019) 42(1):59–71. doi: 10.1007/s10143-017-0897-x
5. Galani V, Lampri E, Varouktsi A, Alexiou G, Mitselou A, Kyritsis AP. Genetic and epigenetic alterations in meningiomas. *Clin Neurol Neurosurg* (2017) 158:119–25. doi: 10.1016/j.clineuro.2017.05.002
6. Palaniandy K, Haspani MSM, Zain NRM. Prediction of Histological Grade and Completeness of Resection of Intracranial Meningiomas: Role of Peritumoural Brain Edema. *Malays J Med Sci* (2017) 24(3):33–43. doi: 10.21315/mjms2017.24.3.5
7. Asgari S, Bassiouni H, Hunold A, Klassen D, Stolke D, Sandalcioglu IE. Extensive brain swelling with neurological deterioration after intracranial meningioma surgery - venous complication or 'unspecific' increase in tissue permeability. *Zentralbl Neurochir* (2008) 69(1):22–9. doi: 10.1055/s-2007-992136
8. Zhao Q, Li S, Tang Y, Zhao C, Xie M, Li Z. Related factors of aggravated cerebral edema after meningioma surgery. *J Regional Anat Operative Surg* (2019) 28(01):55–9. doi: 10.11659/jjssx.10E018066
9. Lambin P, Leijenaar RTH, Deist TM, Peerlings J, de Jong EEC, van Timmeren J, et al. Radiomics: the bridge between medical imaging and personalized medicine. *Nat Rev Clin Oncol* (2017) 14(12):749–62. doi: 10.1038/nrclinonc.2017.141
10. Park JE, Kim HS. Radiomics as a Quantitative Imaging Biomarker: Practical Considerations and the Current Standpoint in Neuro-oncologic Studies. *Nucl Med Mol Imaging* (2018) 52(2):99–108. doi: 10.1007/s13139-017-0512-7
11. Chaddad A, Kucharczyk MJ, Daniel P, Sabri S, Jean-Claude BJ, Niazi T, et al. Radiomics in Glioblastoma: Current Status and Challenges Facing Clinical Implementation. *Front Oncol* (2019) 9:374. doi: 10.3389/fonc.2019.00374
12. Fan Y, Feng M, Wang R. Application of Radiomics in Central Nervous System Diseases: a Systematic literature review. *Clin Neurol Neurosurg* (2019) 187:105565. doi: 10.1016/j.clineuro.2019.105565

13. Lu CF, Hsu FT, Hsieh KL, Kao YJ, Cheng SJ, Hsu JB, et al. Machine Learning-Based Radiomics for Molecular Subtyping of Gliomas. *Clin Cancer Res* (2018) 24(18):4429–36. doi: 10.1158/1078-0432.CCR-17-3445
14. van Griethuysen JJM, Fedorov A, Parmar C, Hosny A, Aucoin N, Narayan V, et al. Computational Radiomics System to Decode the Radiographic Phenotype. *Cancer Res* (2017) 77(21):e104–e7. doi: 10.1158/0008-5472.CAN-17-0339
15. Fan Y, Hua M, Mou A, Wu M, Liu X, Bao X, et al. Preoperative Noninvasive Radiomics Approach Predicts Tumor Consistency in Patients With Acromegaly: Development and Multicenter Prospective Validation. *Front Endocrinol (Lausanne)* (2019) 10:403. doi: 10.3389/fendo.2019.00403
16. Aerts HJ, Velazquez ER, Leijenaar RT, Parmar C, Grossmann P, Carvalho S, et al. Decoding tumour phenotype by noninvasive imaging using a quantitative radiomics approach. *Nat Commun* (2014) 5:4006. doi: 10.1038/ncomms5644
17. Fan Y, Chai Y, Li K, Fang H, Mou A, Feng S, et al. Non-invasive and real-time proliferative activity estimation based on a quantitative radiomics approach for patients with acromegaly: a multicenter study. *J Endocrinol Invest* (2020) 43(6):755–65. doi: 10.1007/s40618-019-01159-7
18. Wang Q, Li Q, Mi R, Ye H, Zhang H, Chen B, et al. Radiomics Nomogram Building From Multiparametric MRI to Predict Grade in Patients With Glioma: A Cohort Study. *J Magn Reson Imaging* (2019) 49(3):825–33. doi: 10.1002/jmri.26265
19. Qu J, Shen C, Qin J, Wang Z, Liu Z, Guo J, et al. The MR radiomic signature can predict preoperative lymph node metastasis in patients with esophageal cancer. *Eur Radiol* (2019) 29(2):906–14. doi: 10.1007/s00330-018-5583-z
20. Zinn PO, Singh SK, Kotrotsou A, Hassan I, Thomas G, Luedi MM, et al. A Coclinical Radiogenomic Validation Study: Conserved Magnetic Resonance Radiomic Appearance of Periostin-Expressing Glioblastoma in Patients and Xenograft Models. *Clin Cancer Res* (2018) 24(24):6288–99. doi: 10.1158/1078-0432.CCR-17-3420
21. Erturk SM. Receiver operating characteristic analysis. *AJR Am J Roentgenol* (2011) 197(4):W784. author reply W5. doi: 10.2214/AJR.11.6484
22. Pan W. Akaike's information criterion in generalized estimating equations. *Biometrics* (2001) 57(1):120–5. doi: 10.1111/j.0006-341X.2001.00120.x
23. Kramer AA, Zimmerman JE. Assessing the calibration of mortality benchmarks in critical care: The Hosmer-Lemeshow test revisited. *Crit Care Med* (2007) 35(9):2052–6. doi: 10.1097/01.CCM.0000275267.64078.B0
24. Vickers AJ, Cronin AM, Elkin EB, Gonen M. Extensions to decision curve analysis, a novel method for evaluating diagnostic tests, prediction models and molecular markers. *BMC Med Inform Decis Mak* (2008) 8:53. doi: 10.1186/1472-6947-8-53
25. Stepien K, Ostrowski RP, Matyja E. Hyperbaric oxygen as an adjunctive therapy in treatment of malignancies, including brain tumours. *Med Oncol* (2016) 33(9):101. doi: 10.1007/s12032-016-0814-0
26. Go KG, Wilmink JT, Molenaar WM. Peritumoral brain edema associated with meningiomas. *Neurosurgery* (1988) 23(2):175–9. doi: 10.1227/00006123-198808000-00008
27. Bitzer M, Topka H, Morgalla M, Friese S, Wockel L, Voigt K. Tumor-related venous obstruction and development of peritumoral brain edema in meningiomas. *Neurosurgery* (1998) 42(4):730–7. doi: 10.1097/00006123-199804000-00029
28. Klatzo I. Presidental address. Neuropathological aspects of brain edema. *J Neuropathol Exp Neurol* (1967) 26(1):1–14. doi: 10.1097/00005072-196701000-00001
29. Treggiari MM, Schutz N, Yanez ND, Romand JA. Role of intracranial pressure values and patterns in predicting outcome in traumatic brain injury: a systematic review. *Neurocrit Care* (2007) 6(2):104–12. doi: 10.1007/s12028-007-0012-1
30. Tao C, Wang J, Zhang Y, Qi S, Liu F, You C. Predictors of Acute Vertebrobasilar Vasospasm following Tumor Resection in the Foramen Magnum Region. *PloS One* (2016) 11(9):e0163908. doi: 10.1371/journal.pone.0163908
31. Clement T, Rodriguez-Grande B, Badaut J. Aquaporins in brain edema. *J Neurosci Res* (2020) 98(1):9–18. doi: 10.1002/jnr.24354
32. Schob S, Surov A, Wienke A, Meyer HJ, Spielmann RP, Fiedler E. Correlation Between Aquaporin 4 Expression and Different DWI Parameters in Grade I Meningioma. *Mol Imaging Biol* (2017) 19(1):138–42. doi: 10.1007/s11307-016-0978-1
33. Kermany DS, Goldbaum M, Cai W, Valentim CCS, Liang H, Baxter SL, et al. Identifying Medical Diagnoses and Treatable Diseases by Image-Based Deep Learning. *Cell* (2018) 172(5):1122–31 e9. doi: 10.1016/j.cell.2018.02.010
34. Kang D, Park JE, Kim YH, Kim JH, Oh JY, Kim J, et al. Diffusion radiomics as a diagnostic model for atypical manifestation of primary central nervous system lymphoma: development and multicenter external validation. *Neuro Oncol* (2018) 20(9):1251–61. doi: 10.1093/neuonc/noy021
35. Artzi M, Bressler I, Ben Bashat D. Differentiation between glioblastoma, brain metastasis and subtypes using radiomics analysis. *J Magn Reson Imaging* (2019) 50(2):519–28. doi: 10.1002/jmri.26643
36. Qian Z, Li Y, Wang Y, Li L, Li R, Wang K, et al. Differentiation of glioblastoma from solitary brain metastases using radiomic machine-learning classifiers. *Cancer Lett* (2019) 451:128–35. doi: 10.1016/j.canlet.2019.02.054
37. Kim JY, Park JE, Jo Y, Shim WH, Nam SJ, Kim JH, et al. Incorporating diffusion- and perfusion-weighted MRI into a radiomics model improves diagnostic performance for pseudoprogression in glioblastoma patients. *Neuro Oncol* (2019) 21(3):404–14. doi: 10.1093/neuonc/noy133
38. Zhou H, Vallieres M, Bai HX, Su C, Tang H, Oldridge D, et al. MRI features predict survival and molecular markers in diffuse lower-grade gliomas. *Neuro Oncol* (2017) 19(6):862–70. doi: 10.1093/neuonc/now256
39. Xi YB, Guo F, Xu ZL, Li C, Wei W, Tian P, et al. Radiomics signature: A potential biomarker for the prediction of MGMT promoter methylation in glioblastoma. *J Magn Reson Imaging* (2018) 47(5):1380–7. doi: 10.1002/jmri.25860
40. Zhou M, Scott J, Chaudhury B, Hall L, Goldgof D, Yeom KW, et al. Radiomics in Brain Tumor: Image Assessment, Quantitative Feature Descriptors, and Machine-Learning Approaches. *AJNR Am J Neuroradiol* (2018) 39(2):208–16. doi: 10.3174/ajnr.A5391
41. Fan Y, Jiang S, Hua M, Feng S, Feng M, Wang R. Machine Learning-Based Radiomics Predicts Radiotherapeutic Response in Patients With Acromegaly. *Front Endocrinol (Lausanne)* (2019) 10:588. doi: 10.3389/fendo.2019.00588
42. Niu J, Zhang S, Ma S, Diao J, Zhou W, Tian J, et al. Preoperative prediction of cavernous sinus invasion by pituitary adenomas using a radiomics method based on magnetic resonance images. *Eur Radiol* (2019) 29(3):1625–34. doi: 10.1007/s00330-018-5725-3

Conflict of Interest: The authors declare that the research was conducted in the absence of any commercial or financial relationships that could be construed as a potential conflict of interest.

frontiers in Neurology

ORIGINAL RESEARCH
published: 14 May 2021
doi: 10.3389/fneur.2021.636235

Pre-operative MRI Radiomics for the Prediction of Progression and Recurrence in Meningiomas

Ching-Chung Ko[1,2†], Yang Zhang[3†], Jeon-Hor Chen[3,4], Kai-Ting Chang[3], Tai-Yuan Chen[1,5], Sher-Wei Lim[6,7], Te-Chang Wu[1,5,8] and Min-Ying Su[3]*

[1] Department of Medical Imaging, Chi-Mei Medical Center, Tainan, Taiwan, [2] Department of Health and Nutrition, Chia Nan University of Pharmacy and Science, Tainan, Taiwan, [3] Department of Radiological Sciences, University of California, Irvine, Irvine, CA, United States, [4] Department of Radiology, E-DA Hospital, I-Shou University, Kaohsiung, Taiwan, [5] Graduate Institute of Medical Sciences, Chang Jung Christian University, Tainan, Taiwan, [6] Department of Neurosurgery, Chi-Mei Medical Center, Chiali, Tainan, Taiwan, [7] Department of Nursing, Min-Hwei College of Health Care Management, Tainan, Taiwan, [8] Department of Biomedical Imaging and Radiological Sciences, National Yang-Ming University, Taipei, Taiwan

OPEN ACCESS

Edited by:
Xuejun Li,
Central South University, China

Reviewed by:
Alissa A. Thomas,
University of Vermont, United States
Maria Caffo,
University of Messina, Italy

***Correspondence:**
Ching-Chung Ko
kocc0729@gmail.com

†These authors have contributed equally to this work

Specialty section:
This article was submitted to Neuro-Oncology and Neurosurgical Oncology, a section of the journal Frontiers in Neurology

Received: *01 December 2020*
Accepted: *29 March 2021*
Published: *14 May 2021*

Citation:
Ko C-C, Zhang Y, Chen J-H, Chang K-T, Chen T-Y, Lim S-W, Wu T-C and Su M-Y (2021) Pre-operative MRI Radiomics for the Prediction of Progression and Recurrence in Meningiomas. Front. Neurol. 12:636235. doi: 10.3389/fneur.2021.636235

Objectives: A subset of meningiomas may show progression/recurrence (P/R) after surgical resection. This study applied pre-operative MR radiomics based on support vector machine (SVM) to predict P/R in meningiomas.

Methods: From January 2007 to January 2018, 128 patients with pathologically confirmed WHO grade I meningiomas were included. Only patients who had undergone pre-operative MRIs and post-operative follow-up MRIs for more than 1 year were studied. Pre-operative T2WI and contrast-enhanced T1WI were analyzed. On each set of images, 32 first-order features and 75 textural features were extracted. The SVM classifier was utilized to evaluate the significance of extracted features, and the most significant four features were selected to calculate SVM score for each patient.

Results: Gross total resection (Simpson grades I–III) was performed in 93 (93/128, 72.7%) patients, and 19 (19/128, 14.8%) patients had P/R after surgery. Subtotal tumor resection, bone invasion, low apparent diffusion coefficient (ADC) value, and high SVM score were more frequently encountered in the P/R group ($p < 0.05$). In multivariate Cox hazards analysis, bone invasion, ADC value, and SVM score were high-risk factors for P/R ($p < 0.05$) with hazard ratios of 7.31, 4.67, and 8.13, respectively. Using the SVM score, an AUC of 0.80 with optimal cutoff value of 0.224 was obtained for predicting P/R. Patients with higher SVM scores were associated with shorter progression-free survival ($p = 0.003$).

Conclusions: Our preliminary results showed that pre-operative MR radiomic features may have the potential to offer valuable information in treatment planning for meningiomas.

Keywords: magnetic resonance imaging, radiomics, support vector machine, meningioma, progression, recurrence

INTRODUCTION

Meningiomas are the most frequently diagnosed primary brain tumors (1). Although most meningiomas are classified as grade I benign tumors according to the 2016 WHO classification system (2), a subset of these tumors may show early progression/recurrence (P/R) after surgical resection (3–5). Furthermore, the rate of P/R is especially high in cases in which Simpson grade I resection is difficult to achieve, such as for parasagittal and skull base meningiomas (6). Conventional MR imaging findings such as tumor size, bone invasion, and parasagittal location have all been identified as important imaging parameters related to P/R in meningiomas (5, 7). However, most data are presented in qualitative and subjective terms, and interreader inconsistencies may occur during data interpretation.

Radiomics is a new approach in the diagnosis, treatment planning, and prediction of prognosis in brain tumors (8–10). It works by extracting a large number of quantitative characteristics from a medical image and then analyses these features by means of a series of machine learning algorithms (11). Although the radiomics approach for the evaluation of meningiomas pertaining to tumor grades and histological subtypes had recently been reported (12–15), models for predicting clinical outcomes in overall meningiomas are still rare (10, 16). Among the machine learning techniques, several studies had reported that support vector machine (SVM) classifiers offer excellent results in the classification and segmentation in brain tumors (17–22). The purpose of this study is to investigate the role of quantitative radiomics approach based on automatically segmented tumor and SVM classification for the prediction of P/R in meningiomas.

MATERIALS AND METHODS

Ethics Statement

This study was approved by our Institutional Review Board (IRB no.: 10902-009). Written consent was waived because the retrospective nature of this study meant that the healthcare of the included subjects was not affected. Personal information of all included patients was anonymized and de-identified before analyses were carried out.

Patient Selection

The inclusion criteria were patients diagnosed with WHO grade I meningiomas by means of pathological confirmation. All the included patients must have undergone pre-operative brain MRI, post-operative follow-up brain MRIs for more than 1 year, and at least one MRI performed at 3 to 6 months after surgery. Patients diagnosed with neurofibromatosis ($N = 3$) were excluded. From January 2007 to January 2018, a total of 128 patients (43 men and 85 women with a median age of 57.5 years) diagnosed with WHO grade I meningiomas were included according to the abovementioned criteria. No known history of pre-operative intracranial radiation was documented in any of the included subjects. The mean follow-up time was 64.2 months (ranging from 14 to 149 months). A total of 19 (19/128, 14.8%) patients were found to have P/R, and the mean time to P/R was 33.3 months (ranging from 8 to 92 months). Based on anatomic location, the tumors were classified into four subgroups: convexity, parasagittal and parafalcine (PSPF), skull base, and intraventricular meningiomas. Skull base meningiomas included tumors arising from the anterior fossa/olfactory groove, spheno-orbital region, temporal floor, sellar/cavernous sinus, and posterior fossa (23). The extent of tumor resection was determined by a review of pre-operative brain MRI and the first time post-operative MRI (3–6 months after surgery) by a neuroradiologist (C.C.K.) and a neurosurgeon (S.W.L.). Simpson grade I–III resections (considered gross total resection, GTR) were performed in 93 patients, and Simpson grade IV–V resections (considered subtotal tumor resection, STR) were performed in 35 patients. Post-operative adjuvant radiotherapy (RT) was provided for patients who underwent STR in our institution. A total of 35 patients received post-operative adjuvant RT. Post-operative adjuvant RT was carried out *via* stereotactic radiosurgery (SRS) ($N = 28$, median dose of 25 Gy, ranging from 18 to 30 Gy; median fraction of 5, ranging from 3 to 5 fractions) or fractionated stereotactic intensity-modulated radiotherapy (IMRT) ($N = 7$, dose ranging from 55 to 60 Gy with 30 to 33 fractions) by linear accelerators. Detailed information of post-operative RT protocols is provided in Supplementary File 1 in **Supplementary Material**.

Determination of Progression/Recurrence

P/R was evaluated by two experienced neuroradiologists (C.C.K., 7 years of work experience, and T.Y.C., 19 years of work experience) by comparing the post-operative brain MRI findings between the 3–6 months and more than 1 year follow-up. Both readers were blinded to the clinical information of the studied patients. In equivocal cases, final agreement was arrived at by consensus. P/R was defined as recurrence of tumor in Simpson grade I–III resections (GTR) or increasing residual tumor size in Simpson grade IV–V resections (STR) on contrast-enhanced T1WI. In cases of STR, the threshold of P/R was defined as a 10% increase in tumor volume in comparison with post-operative brain MRIs (10). Interobserver reliability in determining P/R with intraclass correlation coefficient (ICC) of 0.8 was obtained. For patients who received post-operative adjuvant RT, P/R was differentiated from post-irradiation effects (pseudoprogression) based on progressive tumor growth, not transient increase in tumor volume (24).

Imaging Acquisition

Pre-operative brain MRI images were acquired using a 1.5-T (Siemens, MAGNETOM Avanto, $n = 53$, or GE Healthcare, Signa HDxt, $n = 58$) or a 3-T (GE Healthcare, Discovery MR750) ($n = 17$) MR scanner, equipped with eight-channel head coils in each machine. Scanning protocols were as follows: axial and sagittal spin echo T1-weighted imaging (T1WI), fast spin-echo T2-weighted imaging (T2WI), axial fluid attenuated inversion recovery (FLAIR), axial gradient recalled echo (GRE) T2*-weighted imaging, axial diffusion-weighted imaging (DWI), and contrast-enhanced (CE) T1WI in axial and coronal sections. Detailed MR imaging parameters can be found in Supplementary File 2 in **Supplementary Material**.

Tumor Segmentation

T2WI and CE T1WI were known to be associated with histopathology and tumor grades in meningiomas (8, 25), and the two sequences (slice thickness/spacing, 5 mm/5 mm) were consistently acquired in all subjects. Thus, they were selected for radiomics analysis in this study. **Figure 1** shows the flowchart of the analysis process. For each lesion, the operator placed an initial rectangle region of interest (ROI) on axial CE T1WI exhibiting the maximal tumor diameter, locating the approximate location and also deciding the initial and final slices containing the lesion. The fuzzy c-mean (FCM) clustering-based algorithm was developed to calculate the outline of the ROI on each imaging slice (26). In cases of under- or oversegmentation, manual correction by inclusion of more tumor tissue or exclusion of unnecessary normal tissue was performed. After segmentation and correction, the ROIs gleaned from all imaging slices containing the lesion were combined to obtain the 3D information of the whole lesion. The 3D connected component labeling was applied for removing scattered voxels not connecting to the main lesion. The hole-filling algorithm was then applied to include all voxels contained within the main ROI that had been labeled as nonlesion. The final 3D tumor mask was mapped to the axial T2WI to determine the tumor ROI on corresponding imaging slices using affine transformation and linear interpolation by FMRIB's Linear Image Registration Tool (FLIRT) (27).

Texture Feature Extraction and Selection

Within the segmented tumor on axial CE T1W images and T2W images, 107 imaging features, consisting of 32 first-order features and 75 textural features, were extracted on each modality (**Figure 1**). Therefore, a total of 214 descriptor features were obtained for each case. In order to evaluate the importance of these features in differentiating P/R, the sequential feature selection process was implemented *via* constructing multiple SVM classifiers (28). Using this method, we selected imaging features with high importance. In this process, SVM with Gaussian kernel was used as the objective function (29, 30). Ten-fold cross-validation was applied to test the model performance (31). In each iteration, the training process was repeated 1,000 times to explore the robustness of each imaging feature. After each iteration, the feature which contributed to the best performance was added into the candidate set. When the addition of features no longer improves the performance, the selection process was terminated and a final set containing the optimal features was obtained. The termination criterion for the objective function was determined at 10^{-6}. This procedure was implemented in MATLAB 2018b. The most significant four features selected by the SVM model for the prediction of P/R were T1 gray-level co-occurrence matrix (GLCM) cluster shade, T1 gray-level size zone matrix (GLSZM) gray-level non-uniformity, T2 GLCM cluster prominence, and T2 GLCM cluster shade. The SVM score for each patient was calculated using the following equation based on the selected features.

$$f(x) = \sum_{n=1}^{N} w_n y_n G(x_n, x) + b$$

where x is the input features and N is the length of the support vector. w_n is the parameter and b is the bias. y_n and x_n are the entries of the supporting vector. $G(x_n, x)$ is the Gaussian kernel function that indicates the dot product in the predictor space between x and the support vectors. Herein,

$$G(x_n, x) = e^{-\|x_n - x\|^2}$$

Measurement of Apparent Diffusion Coefficient Value

For comparison with the radiomics model in the prediction of P/R in meningiomas, apparent diffusion coefficient (ADC) values (b = 1,000 s/mm^2) on DWI were measured manually by two experienced neuroradiologists (C.C.K. and T.Y.C.) as

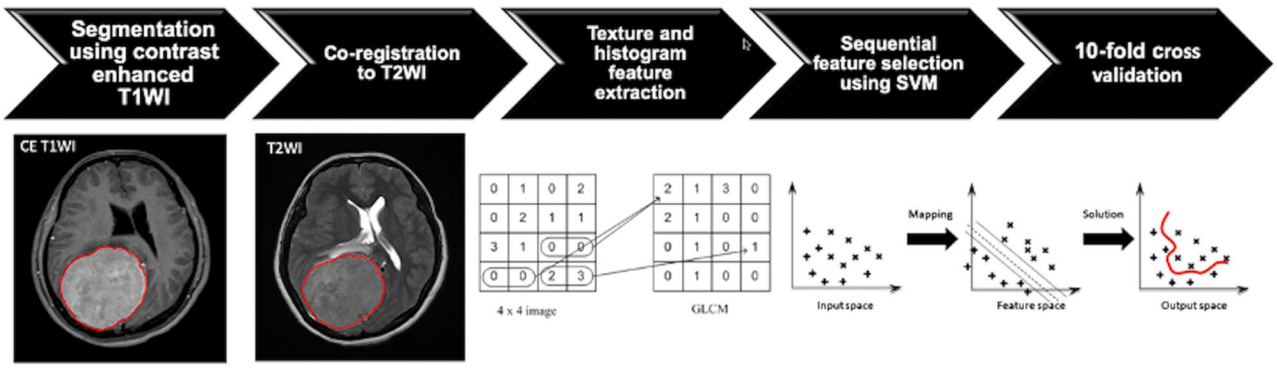

FIGURE 1 | Flowchart indicating the process of analysis for the prediction of progression/recurrence (P/R) in meningiomas. The tumor is first segmented based on contrast-enhanced (CE) T1-weighted image (T1WI), and the region of interest (ROI) of the tumor is then mapped onto the T2-weighted image (T2WI). On each set of the two sequences, a total of 32 first-order features and 75 textural features are extracted, and a total of 214 parameters for each case are collected to develop the classification model. The most important four features are selected by means of the sequential feature selection and support vector machine (SVM) classifiers to calculate SVM score. The 10-fold cross-validation method is applied to test the model performance.

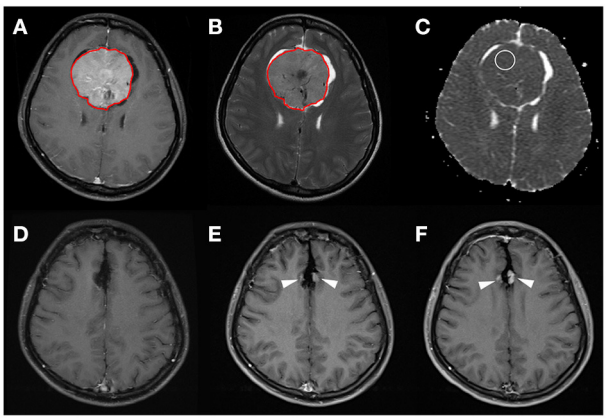

FIGURE 2 | A 31-year-old woman with pathologically proven parafalcine meningioma (WHO grade I). **(A)** Axial CE T1WI showing an enhancing parafalcine tumor (red outline) at the frontal region. The tumor (red outline) is segmented on axial CE T1WI **(A)** and then mapped onto axial T2WI **(B)**. The SVM score based on the four selected radiomic features is 0.831. **(C)** The measured ADC value (circular ROI) is 0.805 × 10^{-3} mm^2/s (b = 1,000 s/mm^2). **(D)** Gross total tumor resection is performed. **(E,F)** Progressive recurrence of tumor (arrowheads) was observed in 36 months **(E)** and 60 months **(F)** after surgery.

in previously published works (7, 29). The circular ROI (area ranging from 35 to 78 mm^2) was placed in a homogeneous area of the tumor to avoid volume averaging with calcification, necrosis, and cystic regions that might influence ADC values (**Figure 2**) (7, 32, 33). Due to the almost perfect reproducibility in the interobserver reliability, the subsequent statistical evaluation of ADC values was performed using the mean value calculated from both interpreters.

Statistical Analysis

Statistical analyses were performed using statistical package SPSS (V.24.0, IBM, Chicago, IL, USA). For the evaluation of the clinical parameters and conventional MRI findings, chi-square (or Fisher's exact test) and Mann–Whitney U tests were performed for categorical and continuous data, respectively. The area under the receiver operating characteristic curve (ROC) curve (AUC) was calculated for SVM scores and ADC values to obtain the optimal cutoff values. Kaplan–Meier analysis was used to evaluate progression-free survival (PFS), and the log-rank test was used to assess significance. Cox hazard regression model with univariate and multivariate analyses was performed to determine independent predictors of P/R. Variables with a $p < 0.05$ in univariate analysis were brought forward to the multivariate analysis. For multivariate analysis and all other statistical analyses, $p < 0.05$ was considered statistically significant.

RESULTS

Clinical Data and Conventional MRI Findings

The clinical data and conventional MRI findings of the included 128 meningiomas are summarized in **Table 1**. Nineteen (19/128, 14.8%) patients were diagnosed with P/R. Statistically significant differences ($p < 0.05$) were observed in the extent of resection, adjacent bone invasion, ADC value, and SVM score between P/R and non-P/R groups (**Table 1**) (**Figures 2**, **3**). In multivariate Cox hazards analysis (**Table 2**), adjacent bone invasion, low ADC value, and high SVM score were high-risk factors for P/R ($p < 0.05$) with hazard ratios of 7.31, 4.67, and 8.13.

TABLE 1 | Clinical data and conventional MRI findings of meningiomas with and without progression/recurrence (P/R).

	P/R	Non-P/R	*p*-value
Number of patients	19	109	
Sex			0.057
Male	10 (52.6%)	33 (30.3%)	
Female	9 (47.4%)	76 (69.7%)	
Age (years)	55 (49.5, 60.5)	59 (52, 66)	0.289
Histological subtypes			0.748
Meningothelial (syncytial)	17 (89.5%)	87 (79.8%)	
Transitional (mixed)	2 (10.5%)	12 (11%)	
Fibroblastic (fibrous)	0	7 (6.4%)	
Angiomatous	0	2 (1.8%)	
Psammomatous	0	1 (0.9%)	
Simpson grade resection			0.007*
Grades I, II, and III (gross total resection, GTR)	9 (47.4%)	84 (77.1%)	
Grade IV and V (subtotal resection, STR)	10 (52.6%)	25 (22.9%)	
Post-operative adjuvant RT			0.118
Yes	8 (42.1%)	27 (24.8%)	
No	11 (57.9%)	82 (75.2%)	
Location			0.296
Convexity	4 (21.1%)	30 (27.5%)	
Parasagittal and parafalcine	11 (57.9%)	43 (39.4%)	
Skull base	3 (15.8%)	34 (31.2%)	
Intraventricular	1 (5.3%)	2 (1.8%)	
Peritumoral edema	9 (47.4%)	59 (54.1%)	0.586
Calcification	3 (15.8%)	38 (34.9%)	0.100
Heterogeneous enhancement	7 (36.8%)	46 (42.2%)	0.662
Cystic change or necrosis	3 (15.8%)	19 (17.4%)	1.000
Dural tail sign	11 (57.9%)	65 (59.6%)	0.887
Adjacent bone invasion	8 (42.1%)	7 (6.4%)	<0.001*
Reactive hyperostosis	5 (26.3%)	27 (24.8%)	1.000
Multiplicity	3 (15.8%)	5 (4.6%)	0.096
Maximal diameter (cm)	5.12 (4.22, 6.03)	4.43 (4.09, 4.76)	0.118
Tumor volume (cm^3)	59.19 (30.35, 88.02)	44.07 (34.96, 53.17)	0.294
ADC value (×10^{-3} mm^2/s)	0.785 (0.725, 0.845)	0.865 (0.78, 0.95)	0.002*
SVM score	0.787 (0.543, 1.032)	0.272 (0.080, 0.464)	<0.001*
Follow-up time (months)	72 (40, 104)	57 (35.2, 78.8)	0.437

Continuous variables were presented as median and interquartile range (IQR).
**Statistical difference ($p < 0.05$).*

Radiomics Approach for the Prediction of P/R

The most significant four imagining features selected by the SVM model for the prediction of P/R were T1 GLCM cluster shade, T1 GLSZM gray-level non-uniformity, T2 GLCM cluster prominence, and T2 GLCM cluster shade. The reproducibility of ROI-based radiomics feature was good, and the ICCs of the four imaging features were 0.92, 0.78, 0.82, and 0.94, respectively.

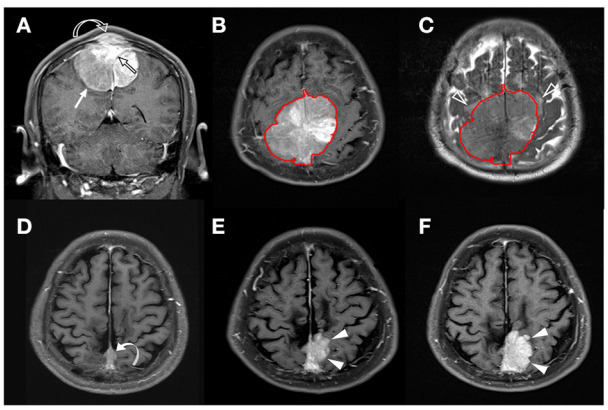

FIGURE 3 | A 58-year-old man with pathologically proven parasagittal meningioma (WHO grade I). **(A)** Coronal CE T1WI shows an enhancing tumor mass (white arrow) in the midline parasagittal region with invasion into the superior sagittal sinus (SSS) (open black arrow) and adjacent skull bone (open curved arrow). **(B,C)** The tumor (red outline) is segmented on the axial CE T1WI **(B)** and then mapped onto the axial T2WI **(C)**. Mild peritumoral edema (white open arrowheads) is noted on T2WI **(C)**. The calculated SVM score based on the four selected radiomic features is 0.337. **(D)** Subtotal tumor resection is performed to preserve the SSS; residual tumor (curved arrow) is noted in the posterior SSS. **(E,F)** Progressive recurrence of tumor (white arrowheads) was observed in 37 months **(E)** and 56 months **(F)** after surgery.

For the prediction of P/R, AUCs of 0.80 and 0.73 with optimal cutoff values of 0.224 and 0.825 $\times$ 10^{-3} mm^2/s were obtained in SVM score and ADC value, respectively (**Figure 4**). Furthermore, improved performance in predictive model was observed after combining SVM score and ADC value, with AUC of 0.88 (**Figure 4**). When tumor progression trends were compared, patients with adjacent bone invasion, high SVM score (more than the cutoff value of 0.224), and low ADC value (lower than the cutoff value of 0.825 $\times$ 10^{-3} mm^2/s) were found to exhibit shorter PSF ($p < 0.05$) (**Figure 5**).

DISCUSSION

In this study, an SVM-based radiomics model was built for the prediction of P/R in meningiomas. A total of 214 first-order and textural features were extracted from CE T1WI and T2WI, and the four most significant features were selected by the SVM algorithm to calculate the personalized SVM score. In multivariate Cox hazards and Kaplan–Meier survival analyses, adjacent bone invasion, low ADC value, and high SVM score were high-risk factors of P/R in meningiomas. For the prediction of P/R in meningiomas, the SVM score-based predictive model is superior to the model based on the ADC value measured manually.

Although 90% of meningiomas are WHO grade I benign tumors, about 21% of these tumors may recur in 5 years after surgical resection (3, 4). Radiomics plays significant roles in

TABLE 2 | Cox proportional hazards analysis for P/R.

	Univariate analysis		Multivariate analysis	
	HR (95% CI) for P/R	***p***	**HR (95% CI) for P/R**	***p***
Sex (fraction male)	2.559 (0.952, 6.879)	0.063		
Age (years)	0.986 (0.950, 1.024)	0.476		
STR	3.733 (1.366, 10.201)	0.010*	2.567 (0.746, 8.834)	0.135
Post-operative adjuvant RT	0.453 (0.165, 1.242)	0.124		
Parasagittal and parafalcine	2.110 (0.785, 5.671)	0.139		
Peritumoral edema	0.763 (0.287, 2.024)	0.587		
Calcification	0.350 (0.096, 1.278)	0.112		
Heterogeneous enhancement	0.642 (0.152, 2.721)	0.548		
Cystic change or necrosis	0.888 (0.235, 3.354)	0.861		
Dural tail sign	0.931 (0.347, 2.499)	0.887		
Adjacent bone invasion	10.597 (3.224, 34.831)	<0.001*	7.314 (1.830, 29.239)	0.005*
Reactive hyperostosis	1.085 (0.358, 3.291)	0.886		
Multiplicity	3.900 (0.849, 17.922)	0.080		
Maximal diameter (cm)	1.228 (0.947, 1.591)	0.121		
Tumor volume (cm^3)	1.005 (0.997, 1.014)	0.227		
ADC <0.825 $\times$ 10^{-3} mm^2/s (cutoff value)	5.752 (1.895, 17.458)	0.002*	4.667 (1.335, 16.319)	0.016*
SVM score >0.224 (cutoff value)	14.400 (1.855, 111.760)	0.011*	8.129 (0.978, 67.569)	0.048*

**Statistical difference ($p < 0.05$).*

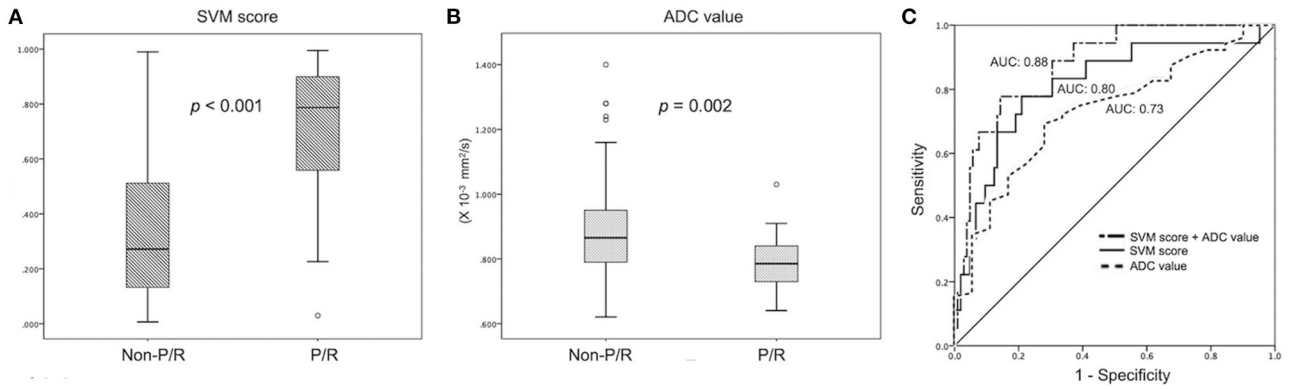

FIGURE 4 | Statistically significant differences ($p < 0.05$) (Mann–Whitney *U* test) are observed in the box plot of **(A)** SVM score and **(B)** ADC value to differentiate between patients with and without P/R. **(C)** Receiver operating characteristic (ROC) curves of SVM score and ADC value for the prediction of P/R in meningiomas, with optimal cutoff value of 0.224 and AUC of 0.825 $\times$ 10^{-3} mm^2/s, respectively. The AUCs of SVM score, ADC value, and combination of SVM and ADC in the prediction of P/R are 0.80, 0.73, and 0.88, respectively.

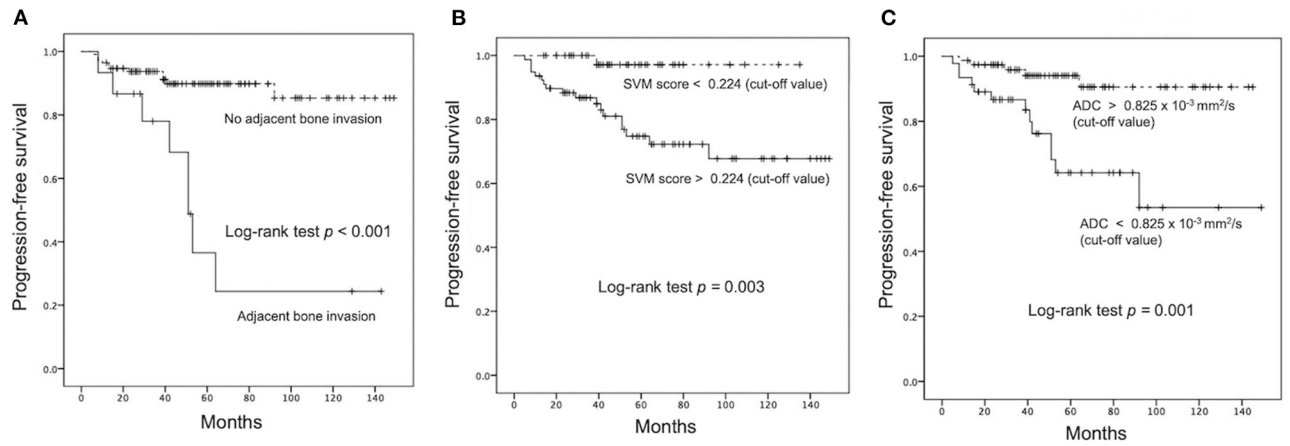

FIGURE 5 | Kaplan–Meier survival curves of **(A)** adjacent bone invasion, **(B)** SVM score, and **(C)** ADC value for the prediction of P/R in meningiomas. All three parameters showed significant difference ($p < 0.05$) (log-rank test) in overall trend of progression-free survival.

the analysis of meningioma characteristics both quantitatively and objectively. Zhu et al. (12) and Chen et al. (34) performed radiomics-based machine learning for pre-operative grading in meningiomas, with AUC of 0.81 and accuracy of 75.6%. Park et al. (8) used the radiomics feature-based machine learning classifiers on conventional and diffusion tensor imaging to predict the grade and histological subtype in meningiomas, with accuracy of 89.7% and AUC of 0.86. Morin et al. (16) integrated radiologic and radiomic features to predict meningioma grade, local failure, and overall survival with AUCs of 0.75 to 0.78. The clinical application of SVM or radiomics score is a new concept. A personalized SVM score could be calculated based on selected radiomic features (35–37). Xu et al. (35) used SVM score to predict pre-operative lymph node metastasis in intrahepatic cholangiocarcinoma, with AUC of 0.87. Fan et al. (38) used SVM-based radiomics score to predict radiotherapeutic response in acromegaly, with AUC of 0.96. Liu et al. (36) reported excellent performance in SVM score to predict treatment response in advanced rectal cancer, with AUC of 0.98. Zhang et al. (10) first applied radiomics to evaluate recurrence in skull base meningiomas, with accuracy of 90%. These studies suggest that SVM score based on radiomics might be a useful tool in predicting recurrences in meningiomas, but rare reports regarding this concept have been published.

Recently, research of computer-extracted radiomic imaging features has become a new field in medical imaging. However, the reproducibility and robustness of the selected imaging features need to be extensively studied before their applications in clinical practice. Factors influencing the robustness of the radiomics approach are modality dependent. However, only few studies have investigated the robustness in MR radiomics (39–42). How different imaging sequences and parameters will affect the reproducibility of radiomic features is still unclear. A recent phantom study showed that obvious differences exist

among different MRI sequences in the number of robust and reproducible features (43). However, more than 30% (15 of 45) of the features still showed excellent robustness across all different MR sequences and demonstrate excellent reproducibility. It was supposed that these 15 features can be applied reliably for the design of radiomic models in clinical studies. Among these features, the shape-related feature was noted to be the most robust and reproducible. Only robust and reproducible T1W and T2W radiomic features were suggested to build a radiomics-based model (43). However, it was also true that the effect of operator-dependent bias can be reduced in radiomic features through fully automatic image segmentation as in our study (43).

Lower ADC values have been reported to be associated with a higher rate of recurrence in meningiomas (7). However, subjective ROI placement with various methods for ADC measurement may result in varying results (44). Susceptibility artifact caused by intratumoral calcifications, necrosis, and cystic changes within meningiomas may also interfere with obtaining optimal ADC values (45). The extent of surgical resection is the most important determining factor in the rate of recurrence in meningiomas (46). Nanda et al. (47) reported that the overall recurrence rates of WHO grade I meningiomas in Simpson resection grades I, II, III, and IV are 5, 22, 31, and 35%, respectively. Recurrence rates of 9.7% in the GTR group and 28.6% in the STR group are observed in our study. Although post-operative adjuvant RT improves tumor control status in high-grade meningiomas (48), no standard protocol could be reliably adopted regarding adjuvant RT for benign meningiomas, and clinical practices among different institutions are varied (49). Whether post-operative adjuvant RT will be beneficial for benign meningiomas is still unclear because it increases the risk of complications such as symptomatic peritumoral edema, cranial nerve deficits, and other neurologic deficits (50). Pre-operative radiomics-based prediction for P/R, thus, offers additional information for determining the treatment strategies in meningiomas. For patients with high risks of P/R, aggressive tumor resection in primary surgery combined with post-operative adjuvant RT should be considered. In contrast, the aim of surgery would be the relief of clinical symptoms for other patients to avoid post-operative neurological deficits. Although adjuvant RT may affect the independent predictive value for P/R in our study, no statistically significant difference was observed between the P/R and non-P/R groups.

This study still had several limitations. Selection bias existed due to its retrospective nature. All images are acquired from a single institution, and there is a lack of external validation. Future testing with multi-institutional data and varying imaging protocols is necessary to determine whether the trained predictive classifier is generalizable. The extent of tumor resection and adjuvant RT may affect the independent predictive performance in radiomics analysis although this limitation always exists in studies focusing on this topic due to variations in treatment protocol (6, 7, 10, 32). Because the sample size of P/R is relatively small, only a few imaging features can be selected to build the classification model in order to avoid overfitting. When more cases become available, other machine learning algorithms such as the fully automated convolutional neural network could be implemented. Finally, there is a lack of complete histopathologic findings such as Ki-67 (MIB-1), nuclear atypia, and genomic signature for correlation in this retrospective study.

CONCLUSIONS

Our preliminary study revealed that SVM score based on pre-operative MR radiomic features was a useful tool for the prediction of P/R in meningiomas. Although this was a single institution study, the imaging features extracted based on automatic segmentation and imaging registration were quantitative and objective. Pre-operative MRI radiomics and SVM score, thus, may have the potential to offer valuable information for the planning of treatments in meningiomas, such as the extent of tumor resection, implementation of post-operative adjuvant RT, and the time interval of imaging follow-up. Nevertheless, this method still needs to be validated in a larger-scale study in the future.

DATA AVAILABILITY STATEMENT

The raw data supporting the conclusions of this article will be made available by the authors, without undue reservation.

ETHICS STATEMENT

The studies involving human participants were reviewed and approved by Institutional Review Board of the Chi Mei Medical Center (IRB no.: 10902-009). Written informed consent for participation was not required for this study in accordance with the national legislation and the institutional requirements.

AUTHOR CONTRIBUTIONS

C-CK and J-HC: conceived and designed the experiments. C-CK and YZ: performed the experiments. C-CK, YZ, J-HC, K-TC, T-YC, and S-WL: analyzed the data. T-YC and T-CW: contributed reagents, materials, and analysis tools. C-CK, YZ, and J-HC: wrote the paper. J-HC and M-YS: critically revised the article. All authors contributed to the article and approved the submitted version.

FUNDING

This work was supported by the Chi Mei Medical Center/Chia Nan University of Pharmacy and Science, Tainan, Taiwan. The funders had no role in the study design, data collection and analysis, decision to publish, or preparation of the manuscript.

SUPPLEMENTARY MATERIAL

The Supplementary Material for this article can be found online at: https://www.frontiersin.org/articles/10.3389/fneur.2021.636235/full#supplementary-material

REFERENCES

1. Wiemels J, Wrensch M, Claus EB. Epidemiology and etiology of meningioma. *J Neuro Oncol.* (2010) 99:307–14. doi: 10.1007/s11060-010-0386-3
2. Louis DN, Perry A, Reifenberger G, von Deimling A, Figarella-Branger D, Cavenee WK, et al. The 2016 world health organization classification of tumors of the central nervous system: a summary. *Acta Neuropathol.* (2016) 131:803–20. doi: 10.1007/s00401-016-1545-1
3. Maillo A, Orfao A, Espinosa AB, Sayagues JM, Merino M, Sousa P, et al. Early recurrences in histologically benign/grade i meningiomas are associated with large tumors and coexistence of monosomy 14 and del(1p36) in the ancestral tumor cell clone. *Neuro Oncol.* (2007) 9:438–6. doi: 10.1215/15228517-2007-026
4. Perry A, Stafford SL, Scheithauer BW, Suman VJ, Lohse CM. Meningioma grading: an analysis of histologic parameters. *Am J Surg Pathol.* (1997) 21:1455–65. doi: 10.1097/00000478-199712000-00008
5. Ildan F, Erman T, Gocer AI, Tuna M, Bagdatoglu H, Cetinalp E, et al. Predicting the probability of meningioma recurrence in the preoperative and early postoperative period: a multivariate analysis in the midterm follow-up. *Skull Base.* (2007) 17:157–71. doi: 10.1055/s-2007-970554
6. Savardekar AR, Patra DP, Bir S, Thakur JD, Mohammed N, Bollam P, et al. Differential tumor progression patterns in skull base versus non-Skull base meningiomas: a Critical analysis from a long-Term follow-Up study and review of literature. *World Neurosurg.* (2018) 112:e74–83. doi: 10.1016/j.wneu.2017.12.035
7. Ko CC, Lim SW, Chen TY, Chen JH, Li CF, Shiue YL. Prediction of progression in skull base meningiomas: additional benefits of apparent diffusion coefficient value. *J Neuro Oncol.* (2018) 138:63–71. doi: 10.1007/s11060-018-2769-9
8. Park YW, Oh J, You SC, Han K, Ahn SS, Choi YS, et al. Radiomics and machine learning may accurately predict the grade and histological subtype in meningiomas using conventional and diffusion tensor imaging. *Eur Radiol.* (2019) 29:4068–76. doi: 10.1007/s00330-018-5830-3
9. Koçak B, Durmaz E, Ateş E, Kiliçkesmez Ö. Radiomics with artificial intelligence: a practical guide for beginners. *Diagn Interv Radiol.* (2019) 25:485–95. doi: 10.5152/dir.2019.19321
10. Zhang Y, Chen JH, Chen TY, Lim SW, Wu TC, Kuo YT, et al. Radiomics approach for prediction of recurrence in skull base meningiomas. *Neuroradiology.* (2019) 61:1355–64. doi: 10.1007/s00234-019-02259-0
11. Aerts HJ, Velazquez ER, Leijenaar RT, Parmar C, Grossmann P, Carvalho S, et al. Decoding tumour phenotype by noninvasive imaging using a quantitative radiomics approach. *Nat Commun.* (2014) 5:4006. doi: 10.1038/ncomms5644
12. Zhu Y, Man C, Gong L, Dong D, Yu X, Wang S, et al. A deep learning radiomics model for preoperative grading in meningioma. *Eur J Radiol.* (2019) 116:128–34. doi: 10.1016/j.ejrad.2019.04.022
13. Hamerla G, Meyer HJ, Schob S, Ginat DT, Altman A, Lim T, et al. Comparison of machine learning classifiers for differentiation of grade 1 from higher gradings in meningioma: a multicenter radiomics study. *Magn Reson Imaging.* (2019) 63:244–9. doi: 10.1016/j.mri.2019.08.011
14. Kalasauskas D, Kronfeld A, Renovanz M, Kurz E, Leukel P, Krenzlin H, et al. Identification of high-Risk atypical meningiomas according to semantic and radiomic features. *Cancers.* (2020) 12:2942. doi: 10.3390/cancers12102942
15. Fioravanzo A, Caffo M, Di Bonaventura R, Gardiman MP, Ghimenton C, Ius T, et al. A risk score based on 5 clinico-pathological variables predicts recurrence of atypical meningiomas. *J Neuropathol Exp Neurol.* (2020) 79:500–7. doi: 10.1093/jnen/nlaa018
16. Morin O, Chen WC, Nassiri F, Susko M, Magill ST, Vasudevan HN, et al. Integrated models incorporating radiologic and radiomic features predict meningioma grade, local failure, and overall survival. *Neurooncol Adv.* (2019) 1:vdz011. doi: 10.1093/noajnl/vdz011
17. Hari Babu N, Salankar SS, Bora VR, editors. MRI brain cancer classification using Support Vector Machine. In: *2014 IEEE Students' Conference on Electrical, Electronics and Computer Science.* Bhopal (2014).
18. Ansari MA, Mehrotra R, Agrawal R. Detection and classification of brain tumor in mRI images using wavelet transform and support vector machine. *J Interdiscipl Math.* (2020) 23:955–66. doi: 10.1080/09720502.2020.1723921
19. Agar NYR, Malcolm JG, Mohan V, Yang HW, Johnson MD, Tannenbaum A, et al. Imaging of meningioma progression by matrix-assisted laser desorption ionization time-of-flight mass spectrometry. *Anal Chem.* (2010) 82:2621–5. doi: 10.1021/ac100113w
20. Hale AT, Stonko DP, Wang L, Strother MK, Chambless LB. Machine learning analyses can differentiate meningioma grade by features on magnetic resonance imaging. *Neurosurg Focus.* (2018) 45:E4. doi: 10.3171/2018.8.FOCUS18191
21. Bauer S, Nolte L-P, Reyes M, editors. Fully automatic segmentation of brain tumor images using support vector machine classification in combination with hierarchical conditional random field regularization. In: *Medical Image Computing and Computer-Assisted Intervention – MICCAI 2011; 2011 2011//.* Berlin, Heidelberg: Springer Berlin Heidelberg (2011). doi: 10.1007/978-3-642-23626-6_44
22. Lee C-H, Schmidt M, Murtha A, Bistritz A, Sander J, Greiner R. Segmenting brain tumors with conditional random fields and support vector machines. In: Liu Y, Jiang T, Zhang C, editors. *Computer Vision for Biomedical Image Applications*. Berlin, Heidelberg: Springer Berlin Heidelberg (2005) 469–478. doi: 10.1007/11569541_47
23. Goto T, Ohata K. Surgical resectability of skull base meningiomas. *Neurol Med Chir.* (2016) 56:372–8. doi: 10.2176/nmc.ra.2015-0354
24. Walker AJ, Ruzevick J, Malayeri AA, Rigamonti D, Lim M, Redmond KJ, et al. Postradiation imaging changes in the cNS: how can we differentiate between treatment effect and disease progression? *Future Oncol.* (2014) 10:1277–97. doi: 10.2217/fon.13.271
25. Speckter H, Bido J, Hernandez G, Rivera D, Suazo L, Valenzuela S, et al. Pretreatment texture analysis of routine mR images and shape analysis of the diffusion tensor for prediction of volumetric response after radiosurgery for meningioma. *J Neurosurg.* (2018) 129:31–7. doi: 10.3171/2018.7.GKS181327
26. Nasrabadi NM. Pattern recognition and machine learning. *J Electron Imaging.* (2007) 16:049901. doi: 10.1117/1.2819119
27. Jenkinson M, Bannister P, Brady M, Smith S. Improved optimization for the robust and accurate linear registration and motion correction of brain images. *Neuroimage.* (2002) 17:825–41. doi: 10.1006/nimg.2002.1132
28. Guyon I, Elisseeff A. An introduction to variable and feature selection. *J Mach Learn Res.* (2003) 3:1157–82. doi: 10.1162/153244303322753616
29. Drucker H, Burges CJ, Kaufman L, Smola AJ, Vapnik V, editors. Support vector regression machines. *Adv Neural Inf Process Syst.* (1997) 28:779–784.
30. Tong S, Chang E, editors. Support vector machine active learning for image retrieval. In: *Proceedings of the Ninth ACM International Conference on Multimedia.* Ottawa, ON (2001). doi: 10.1145/500141.500159
31. Hastie T, Tibshirani R, Friedman J. *The Elements of Statistical Learning: Data Mining, Inference, and Prediction, Second Edition*. New York, NY: Springer (2009).
32. Hwang WL, Marciscano AE, Niemierko A, Kim DW, Stemmer-Rachamimov AO, Curry WT, et al. Imaging and extent of surgical resection predict risk of meningioma recurrence better than wHO histopathological grade. *Neuro Oncol.* (2016) 18:863–72. doi: 10.1093/neuonc/nov285
33. Ko CC, Chen TY, Lim SW, Kuo YT, Wu TC, Chen JH. Prediction of recurrence in parasagittal and parafalcine meningiomas: added value of diffusion-weighted magnetic resonance imaging. *World Neurosurg.* (2019) 124:e470–9. doi: 10.1016/j.wneu.2018.12.117
34. Chen C, Guo X, Wang J, Guo W, Ma X, Xu J. The diagnostic value of radiomics-based machine learning in predicting the grade of meningiomas using conventional magnetic resonance imaging: a preliminary study. *Front Oncol.* (2019) 9:1338. doi: 10.3389/fonc.2019.01338
35. Xu L, Yang P, Liang W, Liu W, Wang W, Luo C, et al. A radiomics approach based on support vector machine using mR images for preoperative lymph node status evaluation in intrahepatic cholangiocarcinoma. *Theranostics.* (2019) 9:5374–85. doi: 10.7150/thno.34149
36. Liu Z, Zhang XY, Shi YJ, Wang L, Zhu HT, Tang Z, et al. Radiomics analysis for evaluation of pathological complete response to neoadjuvant chemoradiotherapy in locally advanced rectal cancer. *Clin Cancer Res.* (2017) 23:7253–62. doi: 10.1158/1078-0432.CCR-17-1038
37. Park JE, Kim HS, Jo Y, Yoo RE, Choi SH, Nam SJ, et al. Radiomics prognostication model in glioblastoma using diffusion- and perfusion-weighted mRI. *Sci Rep.* (2020) 10:4250. doi: 10.1038/s41598-020-61178-w

38. Fan Y, Jiang S, Hua M, Feng S, Feng M, Wang R. Machine learning-based radiomics predicts radiotherapeutic response in patients with acromegaly. *Front Endocrinol.* (2019) 10:588. doi: 10.3389/fendo.2019.00588
39. Mayerhoefer ME, Szomolanyi P, Jirak D, Berg A, Materka A, Dirisamer A, et al. Effects of magnetic resonance image interpolation on the results of texture-based pattern classification: a phantom study. *Invest Radiol.* (2009) 44:405–11. doi: 10.1097/RLI.0b013e3181a50a66
40. Collewet G, Strzelecki M, Mariette F. Influence of mRI acquisition protocols and image intensity normalization methods on texture classification. *Magn Reson Imaging.* (2004) 22:81–91. doi: 10.1016/j.mri.2003.09.001
41. Park JE, Kim HS. Radiomics as a quantitative imaging biomarker: practical considerations and the current standpoint in neuro-oncologic studies. *Nucl Med Mol Imaging.* (2018) 52:99–108. doi: 10.1007/s13139-017-0512-7
42. Saha A, Harowicz MR, Mazurowski MA. Breast cancer mRI radiomics: an overview of algorithmic features and impact of inter-reader variability in annotating tumors. *Med Phys.* (2018) 45:3076–85. doi: 10.1002/mp.12925
43. Baeßler B, Weiss K, Pinto Dos Santos D. Robustness and reproducibility of radiomics in magnetic resonance imaging: a phantom study. *Invest Radiol.* (2019) 54:221–8. doi: 10.1097/RLI.0000000000000530
44. Ahn SJ, Shin HJ, Chang JH, Lee SK. Differentiation between primary cerebral lymphoma and glioblastoma using the apparent diffusion coefficient: comparison of three different rOI methods. *PLoS ONE.* (2014) 9:e112948. doi: 10.1371/journal.pone.0112948
45. Schweser F, Deistung A, Lehr BW, Reichenbach JR. Differentiation between diamagnetic and paramagnetic cerebral lesions based on magnetic susceptibility mapping. *Med Phys.* (2010) 37:5165–78. doi: 10.1118/1.3481505
46. Mansouri A, Klironomos G, Taslimi S, Kilian A, Gentili F, Khan OH, et al. Surgically resected skull base meningiomas demonstrate a divergent postoperative recurrence pattern compared with non-skull base meningiomas. *J Neurosurg.* (2016) 125:431–40. doi: 10.3171/2015.7.JNS15546
47. Nanda A, Bir SC, Maiti TK, Konar SK, Missios S, Guthikonda B. Relevance of simpson grading system and recurrence-free survival after surgery for world health organization grade i meningioma. *J Neurosurg.* (2017) 126:201–11. doi: 10.3171/2016.1.JNS151842
48. Kaur G, Sayegh ET, Larson A, Bloch O, Madden M, Sun MZ, et al. Adjuvant radiotherapy for atypical and malignant meningiomas: a systematic review. *Neuro Oncol.* (2014) 16:628–36. doi: 10.1093/neuonc/nou025
49. Maclean J, Fersht N, Short S. Controversies in radiotherapy for meningioma. *Clin Oncol.* (2014) 26:51–64. doi: 10.1016/j.clon.2013.10.001
50. Conti A, Pontoriero A, Siddi F, Iati G, Cardali S, Angileri FF, et al. Post-treatment edema after meningioma radiosurgery is a predictable complication. *Cureus.* (2016) 8:e605. doi: 10.7759/cureus.605

Conflict of Interest: The authors declare that the research was conducted in the absence of any commercial or financial relationships that could be construed as a potential conflict of interest.

frontiers in Oncology

ORIGINAL RESEARCH
published: 06 July 2021
doi: 10.3389/fonc.2021.616740

Preoperative Radiomics Analysis of 1p/19q Status in WHO Grade II Gliomas

Ziwen Fan[1†], Zhiyan Sun[2†], Shengyu Fang[2], Yiming Li[1], Xing Liu[3], Yucha Liang[1], Yukun Liu[1], Chunyao Zhou[1], Qiang Zhu[1], Hong Zhang[1], Tianshi Li[1], Shaowu Li[4], Tao Jiang[1,2], Yinyan Wang[1,2] and Lei Wang[1*]*

[1] Department of Neurosurgery, Beijing Tiantan Hospital, Capital Medical University, Beijing, China, [2] Beijing Neurosurgical Institute, Capital Medical University, Beijing, China, [3] Department of Pathology, Beijing Tiantan Hospital, Capital Medical University, Beijing, China, [4] Department of Neuroradiology, Beijing Tiantan Hospital, Capital Medical University, Beijing, China

OPEN ACCESS

Edited by:
Harrison Bai,
Brown University, United States

Reviewed by:
Xuezhi Zhou,
Xidian University, China
Sung Soo Ahn,
Yonsei University Health System, South Korea

***Correspondence:**
Lei Wang
wanglei_tiantan@163.com
Yinyan Wang
tiantanyinyan@126.com

[†]These authors have contributed equally to this work

Specialty section:
This article was submitted to Neuro-Oncology and Neurosurgical Oncology, a section of the journal Frontiers in Oncology

Received: 13 October 2020
Accepted: 17 June 2021
Published: 06 July 2021

Citation:
Fan Z, Sun Z, Fang S, Li Y, Liu X, Liang Y, Liu Y, Zhou C, Zhu Q, Zhang H, Li T, Li S, Jiang T, Wang Y and Wang L (2021) Preoperative Radiomics Analysis of 1p/19q Status in WHO Grade II Gliomas. Front. Oncol. 11:616740. doi: 10.3389/fonc.2021.616740

Purpose: The present study aimed to preoperatively predict the status of 1p/19q based on radiomics analysis in patients with World Health Organization (WHO) grade II gliomas.

Methods: This retrospective study enrolled 157 patients with WHO grade II gliomas (76 patients with astrocytomas with mutant IDH, 16 patients with astrocytomas with wild-type IDH, and 65 patients with oligodendrogliomas with mutant IDH and 1p/19q codeletion). Radiomic features were extracted from magnetic resonance images, including T1-weighted, T2-weighted, and contrast T1-weighted images. Elastic net and support vector machines with radial basis function kernel were applied in nested 10-fold cross-validation loops to predict the 1p/19q status. Receiver operating characteristic analysis and precision-recall analysis were used to evaluate the model performance. Student's *t*-tests were then used to compare the posterior probabilities of 1p/19q co-deletion prediction in the group with different 1p/19q status.

Results: Six valuable radiomic features, along with age, were selected with the nested 10-fold cross-validation loops. Five features showed significant difference in patients with different 1p/19q status. The area under curve and accuracy of the predictive model were 0.8079 (95% confidence interval, 0.733–0.8755) and 0.758 (0.6879–0.8217), respectively, and the F1-score of the precision-recall curve achieved 0.6667 (0.5201–0.7705). The posterior probabilities in the 1p/19q co-deletion group were significantly different from the non-deletion group.

Conclusion: Combined radiomics analysis and machine learning showed potential clinical utility in the preoperative prediction of 1p/19q status, which can aid in making customized neurosurgery plans and glioma management strategies before postoperative pathology.

Keywords: radiomics, 1p/19q co-deletion, low grade glioma, nested cross-validation, machine learning

INTRODUCTION

Molecular pathology is valuable for determining strategies for treating gliomas and for predicting the prognostic outcome (1). Patients without chromosome 1p/19q co-deletions showed poor overall and progression-free survival (2, 3). Neurosurgeons intended to protect the fundamental functions for patients whose eloquent cortices or white matter were invaded by gliomas, especially gliomas with 1p/19q co-deletions (4, 5). Although the association between prognosis and extent of tumor resection in gliomas with 1p/19q co-deletion remains controversial, some studies have indicated that gross total resection showed better prognosis than that in subtotal resection (6, 7). Nevertheless, other studies have shown no significant difference (8, 9). Undoubtedly, the prediction of the 1p/19q status before performing neurosurgery can aid in making customized neurosurgery plans and glioma management.

Radiomics is a novel practice for detecting the intrinsic imaging features of tumors (10–12). By using radiomics analysis (1), which converts sparse magnetic resonance imaging (MRI) data into big data, we can acquire a large amount of imaging information that is otherwise invisible to the naked eye in multiple dimensions (13–15). Moreover, machine learning is a prevalent artificial intelligent measurement to make classifications. The status of some well-known biomarkers has been accurately predicted in glioma patients, such as *IDH* mutations (16), *ATRX* mutations (17), p53 status (18), and the expression index of Ki-67 (19). However, an accurate and effective method for the preoperative prediction of 1p/19q co-deletion is lacking.

Consequently, in the current study, we retrospectively enrolled patients with low-grade glioma [grade II in pathological criteria of the World Health Organization (WHO, 2016)] (1). By using radiomics analysis, we acquired relevant neuroimaging features and then built a predictive model for 1p/19q status through a machine learning method.

MATERIALS AND METHODS

Patients

In this retrospective study, we collected the clinical data and biological information regarding the gliomas from the Chinese Glioma Genome Atlas (CGGA, http://www.cgga.org.cn/) database (from June 2014 to June 2019; **Figure 1**). A total of 157 patients formed a consecutive series following the selection criteria: (a) older than 18 years; (b) histopathological diagnosis of primary World Health Organization (WHO) II gliomas; (c) no preoperative treatment or biopsy; and (d) available preoperative contrast-enhancement T1-weighted images (CE-T1WI), T1WI, and T2-weighted images (T2WI). The tumor subtypes of WHO grade II gliomas were identified according to the WHO 2016 classification (20). The information of IDH mutations was acquired from the CGGA database, and the details of the measurements can be found in the **Supplementary Materials**.

Imaging Acquisition and Tumor Segmentation

MRI scans were performed using a Trio 3.0-T scanner (Siemens, Erlangen, Germany) to obtain the MR images and typically included axial T1WI (TE, 15 ms; TR, 450 ms; slice thickness, 5 mm), T2WI (TE, 110 ms; TR 5800 ms; slice thickness, 5 mm), and CE scans using 0.1 mM/kg gadopentetate dimeglumine (Ga-DTPA injection, Beilu Pharma, Beijing, China) (TE, 15 ms; TR, 450 ms; slice thickness, 5 mm), with field of view 240 × 188 mm^2. The tumor masks were manually segmented on T2WI by two experienced neurosurgeons (ZF and SF >5 years of experience in diagnosis) using MRIcro software (http://www.mccauslandcenter.sc.edu/mricro/), and a third senior neuroradiologist (SL, >20 years of experience) reevaluated the tumor masks and made the final decision when discrepancies were >5%.

Fluorescence In Situ Hybridization of 1p/19q Co-Deletion

The 4-μm formalin-fixed paraffin-embedded tissue sections, which were obtained from neurosurgical operations, were deparaffinized, permeabilized, and hybridized. Dual-color fluorescence was performed using Vysis (Illinois, USA) of 1p36/1q25 and 19q13/19p13 according to the standardized procedure (21) and evaluated in at least 200 non-overlapping nuclei with intact morphology. We defined >25% of nuclei showing DNA loss as having chromosome loss. Co-deletion of 1p/19q was defined as loss of both 1p and 19q in tumor cells; 1p/19q non-codeletion included tumors with maintenance in 1p or 19q.

Extraction of Radiomic Signatures

All the sequences of the MRIs and ROIs for each patient were resliced to high-resolution (1.0-mm isotropic) images using MATLAB, and the T1WI and CE-T1WI were then registered to the T2WI using the SPM8 software (http://www.fil.ion.ucl.ac.uk/spm/software/spm8). The z-score transformations were used to normalize the brain MRI signal intensity values into standardized intensity ranges. These procedures helped avoid bias from heterogeneity and sequences. Thereafter, the radiomic features were extracted from the tumor masks based on different types of MRI sequences using an automated approach in MATLAB (details shown in **Supplementary Material**) (22). A total of 431 radiomic features were included for each sequence. The feature groups included 14 first-order statistics (pertaining to the distribution of signal intensity of images, Group 1), eight shape- and size-based features (Group 2), 33 textural features (pertaining to intratumoral heterogeneity, Group 3), and 376 wavelet features that were derived from group 1 and group 3 features *via* wavelet decomposition (using directional low-pass and high-pass filtering; the original features were decomposed into eight decompositions, group 4).

Feature Selection Method: Elastic Net

Elastic net (E-net), which linearly combined the penalty terms of the least absolute shrinkage and selection operator and ridge methods, was used to select features. This method minimized the

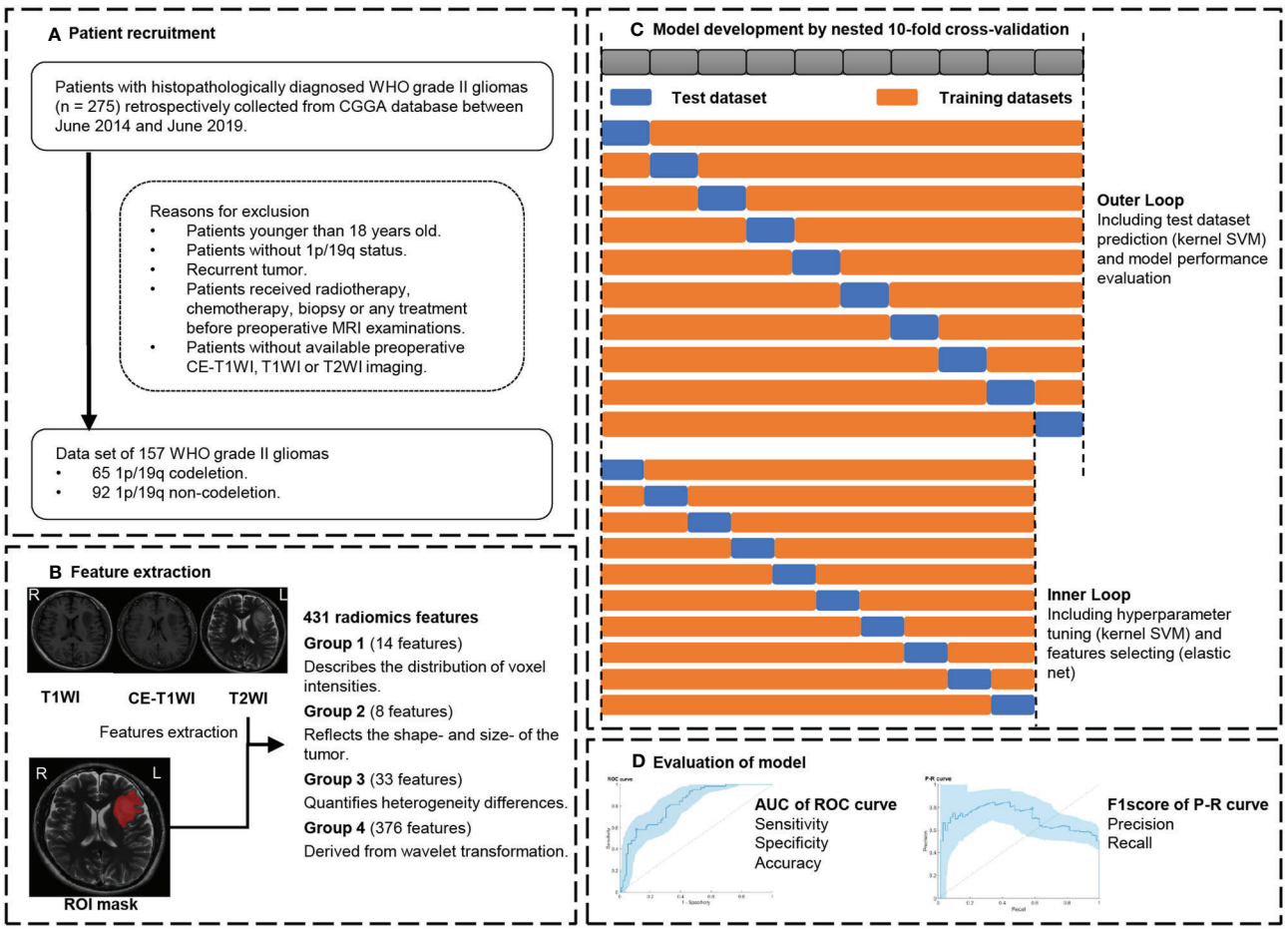

FIGURE 1 | Workflow. **(A)** Patient recruitment strategy. **(B)** 431 features were extracted from region of interest (ROI) on each magnetic resonance imaging (MRI) sequence. **(C)** To compute a 10 × 10-fold nested cross-validation scheme, data were split into 9 training sets and a test set in the outer loop. The inner loop included hyperparameter tuning and features selection in the training datasets. After feature selection, the model with optimal parameters was used for prediction in the test set. This procedure developed 10 different models with specific sets of features and hyperparameters. **(D)** receiver operating characteristic (ROC) analysis and precision and recall (P-R) analysis were used for model performance evaluation. CGGA, Chinese Glioma Genome Atlas database; CE-T1WI, contrast-enhanced T1-weighted imaging; T2WI, T2-weighted imaging; AUC, area under the curve.

residual sum of squares of the estimated errors plus the penalty term to select a model with the best trade-off between fit and complexity (23, 24). E-net was trained in the training set with tuning parameter α (0–1, step 0.1) and λ using 10-fold cross-validation, which followed the criterion of minimum standard deviation. Features with non-zero coefficients were finally selected from the model with optimal values of α and λ.

Model Development: Kernel Support Vector Machine

A support vector machine (SVM) was used to develop the predictive 1p/19q co-deletion model. SVM is one of the most widely used machine learning algorithms. This classifier is based on Gaussian or Radial Basis Function kernel, which deals with non-linearity and higher dimensions and is aimed to find the best hyperplane that separates two groups of data points having a clear gap as wide as possible (25–29). The optimization attempts to minimize the loss of 10-fold cross-validation by varying the parameters, including box constraint and kernel scale parameter. The algorithms of E-net and kernel SVM were adopted from the MATLAB toolbox provided by the Statistics and Machine Learning Toolbox.

Cross-Validation Strategy

The 1p/19q co-deletion status for WHO grade II gliomas was predicted using radiomic features while also considering age and gender as predictors. Nested cross-validation (CV) was considered as the gold standard method when an independent validation set was lacking. The nested CV makes full use of information without leaking and double dipping (30). To thoroughly assess the classifiers' performance, a 10 × 10-fold nested CV scheme (**Figure 1**) was used in this study. Data were split into 10 sets; nine sets were used for training, whereas one non-overlapped set was used for testing, in each outer loop.

Feature selection and model optimization of hyperparameter tuning were trained in each outer loop with an additional 10-fold CV, which was called the inner loop. After the feature selection and model optimization, we evaluated the model performance in the test set with the optimal model in each outer loop. This procedure was repeated 10 times and formed the outer loops of the nested CV. Finally, we built 10 different optimal models.

Statistical Analysis

We used MATLAB 2019b (MathWorks, Natick, MA, USA) for data processing. The paired classification models, based on radiomic signatures, which underwent z-score transformation, were evaluated by receiver operating characteristic (ROC) analysis and precision-recall (P-R) analysis. We computed the area under the curve (AUC), accuracy, sensitivity [also known as true-positive rate (TPR) or recall)], specificity [also known as 1 − false-positive rate (1 − FPR)] from the ROC analysis, and precision, recall, and F1-score from the P-R analysis. The 95% confidence interval (CI) of performance was evaluated by the bootstrap method (1000 times sampling). We used point-biserial-correlation to compute the r and p values between the posterior probabilities of the 1p/19q co-deletion predicted by the SVM model and the true labels (31). To compare the posterior probability (transformed from the decision value of each model) of the kernel SVM model between the 1p/19q co-deletion and non-codeletion groups, a t-test was used, and a 1p/19q co-deletion was considered as 1 and non-codeletion as 0. A p-value < 0.05 was considered statistically significant.

TABLE 1 | Baseline demographics and clinical characteristics of patients.

Variable	Value
Number of Patients	157
Sex, %	
Male	84 (53.5%)
Female	73 (46.5%)
Age (years)*	41.6 ± 10.4
Pathology classification, %	
Diffuse astrocytoma, IDH-mutant	76 (48.4%)
Diffuse astrocytoma, IDH-wildtype	16 (10.2%)
Oligodendroglioma, IDH-mutant, and 1p/19q codeletion	65 (41.4%)
Tumor volume (cm^3)*	59.87 ± 52.74

*Data are mean ± standard deviation.
IDH, isocitrate dehydrogenase; NOS, not otherwise specified.

RESULTS

Clinical Characteristics

The clinical and pathological characteristics of all 157 patients are summarized in **Table 1**. Of the 157 enrolled patients with WHO grade II gliomas, 73 (46.5%) were women and the ages of patients ranged from 20 to 68 years (mean ± standard deviation, 41.6 ± 10.4 years). There were 76 (48.4%) patients with astrocytomas with mutant IDH, 16 (10.2%) patients with astrocytoma with wild-type IDH, and 65 (41.4%) patients with oligodendrogliomas with mutant IDH and 1p/19q codeletion. The mean ± standard deviation of tumor volume was 59.87 ± 52.74 cm^3.

Radiomic Features Selection

A total of 431 radiomic features were extracted from each sequence, and a total of 1,293 radiomic features grouped by age and gender were screened by the E-net in the nested cross-validation. The number of selected signatures ranged from 11 to 103. Features that were selected in all of the 10 loops were considered to be the most valuable features. Six valuable radiomic features and age were selected in each outer loop (**Table 2**). Most of the radiomic features were textual (group 3) with wavelet transformed features (group 4) such as Informational Measure of Correlation_2, Long Run High Gray Level Emphasis_2, Long Run High Gray Level Emphasis_1, Short Run Low Gray Level Emphasis_1, Low Gray Level Run Emphasis_1, and Cluster Tendency. Only Skewness_1 extracted from CE-T1WI belonged to the wavelet transformation of first-order statistics (Group 1) features. We compared the value of age and z-scored value of six selected radiomic features between 1p/19q co-deletion and non-codeletion groups. The results showed that all the features except age (p = 0.2366) and CE-T1WI_Group 4_Cluster Tendency_6 (p = 0.7415) in the 1p/19q co-deletion group were significantly different ($p < 0.05$) from those in the 1p/19q non-codeletion groups.

Model Performances

The AUC of the SVM models with features selected by E-net in the nested CV was 0.8079 (95% CI, 0.733–0.8755) (**Figure 2**). The accuracy, sensitivity, specificity, precision, and F1-score of the prediction model were 0.758 (0.6879–0.8217), 0.5846 (0.4328–0.68), 0.8804 (0.8025–0.9359), 0.7755 (0.6515–0.8889), and 0.6667 (0.5201–0.7705), respectively. The range of box

TABLE 2 | Selected valuable features.

Feature name	Selected times	p*
Age	10	0.2366
T2WI_Group 4_Informational Measure of Correlation_2	10	**0.0004**
T2WI_Group 3_Long Run High Gray Level Emphasis_2	10	**0.0319**
T2WI_Group 4_Long Run High Gray Level Emphasis_1	10	**<0.0001**
T1WI_Group 4_Short Run Low Gray Level Emphasis_1	10	**<0.0001**
T1WI_Group 4_Low Gray Level Run Emphasis_1	10	**<0.0001**
CE-T1WI_Group 4_Skewness_1	10	**<0.0001**
CE-T1WI_Group 4_Cluster Tendency_6	10	0.7415

*p-value of comparison between 1p/19q co-deletion and non-codeletion groups using unpaired t-test, the p-value < 0.05 were bolded.

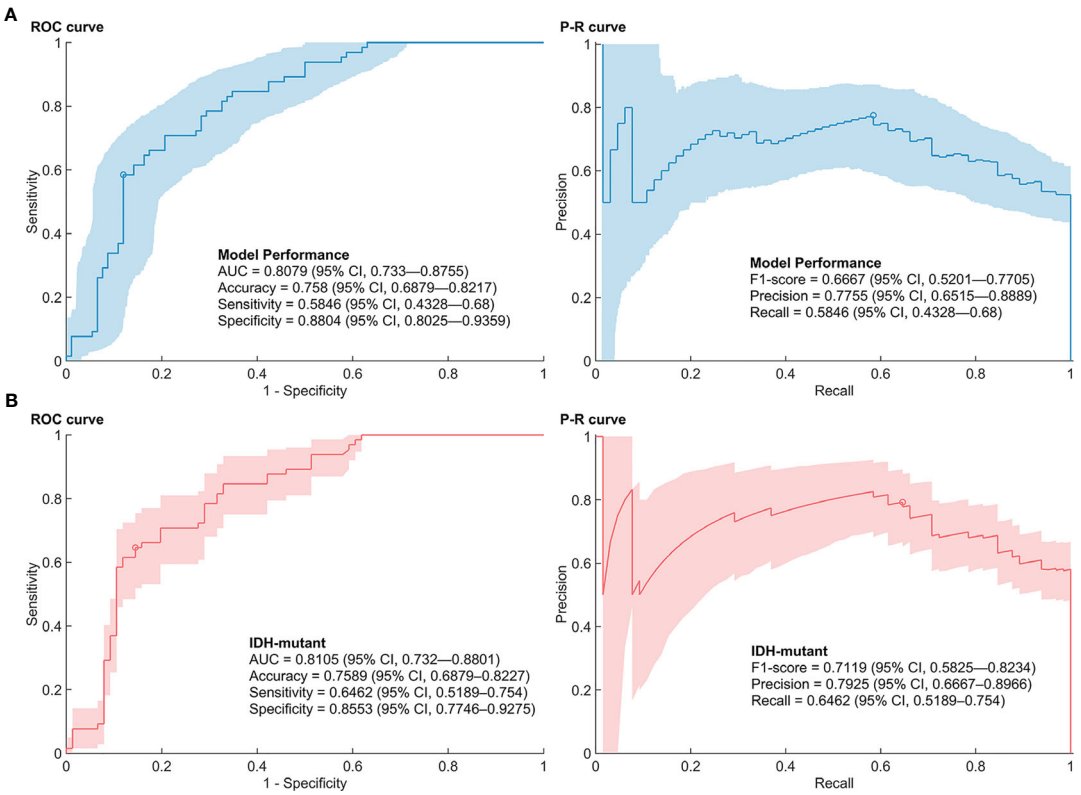

FIGURE 2 | Performance of 1p/19q co-deletion predictive models. **(A)** Receiver operating characteristic (ROC) curve and precision-recall (P-R) curve of the predictive models in low-grade gliomas. **(B)** ROC curve and P-R curve of the predictive models in low-grade gliomas with mutant IDH.

constraint and kernel scale parameters of SVM classifiers in the nested CV were 2.1544–1000 and 10–215.4435, respectively. The hyperparameters and performances of models in each outer loop are summarized in **Supplementary Table S1**. The misclassified number of patients in the patients with wild-type IDH was 4/16. We further performed the 1p/19q predictive models in patients with mutant IDH. The predictive models reached an AUC, accuracy, sensitivity/recall, specificity, precision and F1-score of 0.8105 (0.732—0.8801), 0.7589 (0.6879—0.8227), 0.6462 (0.5189—0.754), 0.8553 (0.7746—0.9275), 0.7925 (0.6667—0.8966) and 0.7119 (0.5825—0.8234).

The p and r values of the point-biserial-correlation were < 0.001 and 0.52, respectively. Moreover, the p value of t tests for comparison of posterior probabilities of groups, which was computed by the 1p/19q predictive model, for different 1p/19q status was < 0.001. The results indicated that these radiomic features could distinguish and predict the 1p/19q status of patients (**Figure 3**).

DISCUSSION

Patients with gliomas without 1p/19q co-deletions have poor prognostic survival outcomes (32, 33). Previous findings showed similar survival outcomes for patients with 1p/19q co-deletions who underwent subtotal resection. This information prevents damage to the eloquent cortices through total resection, which could potentially cause functional deficits (paralysis, aphasia, etc.) (8). Considering this, the prediction of 1p/19q co-deletion before surgery is useful in determining neurosurgery strategies. In this study, we built a machine learning model to preoperatively predict the status of 1p/19q co-deletion using radiomics analysis.

The predictive models of lower-grade gliomas (including WHO grade II and III gliomas) based on 1p/19q status and radiomics analysis can be clinically useful. Zhou et al. extracted textural features from preoperative MRIs of 165 patients of The Cancer Imaging Archive (TCIA) data set to develop a logistic regression model that achieves an AUC of 0.78 in predicting 1p/19q status of lower-grade gliomas (34). Further studies by this group showed a lower AUC of 0.72 of 1p/19q status prediction (random forest model) in all grade gliomas with an *IDH* mutation (35). Another study using nested LOOCV Xg-boost model exhibited a higher AUC (0.83 ± 0.03) in lower-grade gliomas (36), which may owe to the nested cross-validation. Considering information leakage of the validation group in the holdout method for CV and the small sample size, nested CV was considered the "gold standard" for building a predictive model (30). Previous studies developed a deep learning model including the features extracted from MRI, positron emission tomography,

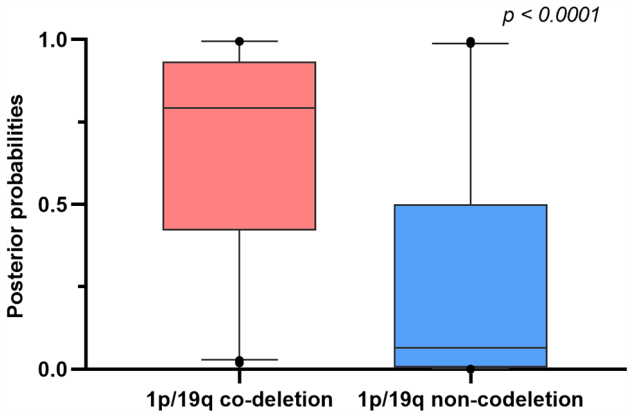

FIGURE 3 | Boxplots comparing differences of posterior probabilities between 1p/19q co-deletion and non-codeletion groups.

and computed tomography (CT), which showed an overall accuracy of 75.1% in the prediction of 1p/19q status in lower-grade gliomas (37). Since the predictive performance of these models was restrained by the small sample size, data augmentation was introduced to enlarge the size of the training set. Based on Cycle Generative Adversarial Network, multi-stream convolutional autoencoder and feature fusion are proposed for the prediction of 1p/19q co-deletion, which displayed an accuracy of 78.41% in low-grade gliomas (38). After adding 30-fold augmented data, another study improved the accuracy of the convolutional neural networks model from 78.3% to 87.7% (39). However, it ignored the global information of tumors since only three MRI slices were used.

Although the prediction of 1p/19q status can achieve good outcomes among patients with lower-grade gliomas (40), building an effective predictive model for low-grade gliomas, which only contain WHO grade II gliomas, is complicated primarily because of the limited sample size. However, the radiomic features of low-grade gliomas are different from those in WHO grade III in conventional MRI sequences (41, 42). To avoid bias caused by the differences of radiomic features in different WHO grades, our study developed a radiomic-based SVM model to predict 1p/19q co-deletions in WHO grade II gliomas. Although the sample size was limited, it allowed the results to be more consistent. Our model showed a similar performance to the machine-learning and deep-learning models mentioned above, with an overall AUC of 0.8079 and an accuracy of 0.758 (34, 35, 38, 39). We specifically analyzed the predictive model in the subgroup analysis of gliomas with mutant IDH, which excluded the influence of gliomas with wild-type IDH, and found a similar performance value. We further compared the predictive probabilities for patients with 1p/19q co-deletion and non-codeletion, and the result exhibited a significant difference. These results indicated that radiomics analysis combined with machine learning can potentially predict 1p/19q mutation in WHO grade II gliomas.

We extracted six valuable radiomic signatures from each outer loop for our predictive model. Gliomas with 1p/19q co-deletion showed a lower homogeneity than those without (43). Our findings confirmed that a lower Informational Measure of correlation in T2WI is exhibited in patients with 1p/19q co-deletion, which shows a positive correlation with homogeneity degrees (44). Moreover, cluster tendency is another feature used to reveal the degree of homogeneity, which represents the measure of the groupings of voxels with similar gray-level values. Our results showed that patients with 1p/19q co-deletion had a lower Cluster Tendency than those patients without. This finding indicated that the degree of homogeneity in an oligodendroglioma is lower compared with an astrocytoma (45). Besides, features belonging to Gray Level Run Length are often applied to distinguish malignant and benign brain tumors (46). In our model, these features (Long Run High Gray Level Emphasis and Short Run Low Gray Level) were crucial for predicting the status of 1p/19q co-deletion due to the difference in prognostic outcomes between oligodendroglioma and astrocytoma (1, 3). Furthermore, skewness, which was significantly different in patients with or without 1p/19q co-deletion, was a classical feature used in distinguishing brain tumors and in the differentiation of glioblastomas and primary central neuro-lymphoma (8, 47, 48).

There are several limitations to the present study. First, our model was generated using retrospectively collected data. Although we performed nested CV to minimize the potential bias, the lack of an external validation data set limited the generalizability of our models. In addition, since our small sample size limited the efficacy of our model, we plan to develop a model based on a larger population combined with independent external validation. Furthermore, we would like to develop a multi-model radiological data-based classifiers in the future, which would include T2-FLAIR, diffusion-weighted imaging, and CT (49–53).

In conclusion, we developed a nested cross-validation machine learning model with efficacy and robust performance, which displayed an AUC of 0.8079 and an accuracy of 0.758. Our results revealed the potential clinical utility of radiomics analysis in the preoperative prediction of 1p/19q status, which can aid in

preoperative genomic marker prediction and making customized neurosurgery plans and glioma management before postoperative pathology.

DATA AVAILABILITY STATEMENT

The raw data supporting the conclusions of this article will be made available by the authors, without undue reservation.

ETHICS STATEMENT

The studies involving human participants were reviewed and approved by IRB of Beijing Tiantan Hospital. The patients/participants provided their written informed consent to participate in this study.

AUTHOR CONTRIBUTIONS

Study conception and design: YW and LW. Acquisition of data: XL, YCL, YKL, CZ, QZ, TL, and HZ. Analysis and interpretation of data: ZS, ZF, SF, YL, and YW. Drafting of manuscript: ZF and ZS, Critical revision: YW and LW. All authors contributed to the article and approved the submitted version.

FUNDING

This study was supported by grants from the National Natural Science Foundation of China (grant 82072786), the Beijing Municipal Natural Science Foundation (7202021), and Capital's Funds for Health Improvement and Research (CFH 2018-2-1072).

ACKNOWLEDGMENTS

The authors would like to acknowledge the support of Zitong Zhao.

SUPPLEMENTARY MATERIAL

The Supplementary Material for this article can be found online at: https://www.frontiersin.org/articles/10.3389/fonc.2021.616740/full#supplementary-material

REFERENCES

1. Louis DN, Perry A, Reifenberger G, von Deimling A, Figarella-Branger D, Cavenee WK, et al. The 2016 World Health Organization Classification of Tumors of the Central Nervous System: A Summary. *Acta Neuropathol* (2016) 131(6):803–20. doi: 10.1007/s00401-016-1545-1
2. Kawaguchi T, Sonoda Y, Shibahara I, Saito R, Kanamori M, Kumabe T, et al. Impact of Gross Total Resection in Patients With WHO Grade III Glioma Harboring the IDH 1/2 Mutation Without the 1p/19q Co-Deletion. *J Neurooncol* (2016) 129(3):505–14. doi: 10.1007/s11060-016-2201-2
3. Jiang T, Mao Y, Ma W, Mao Q, You Y, Yang X, et al. CGCG Clinical Practice Guidelines for the Management of Adult Diffuse Gliomas. *Cancer Lett* (2016) 375(2):263–73. doi: 10.1016/j.canlet.2016.01.024
4. Cordier D, Goze C, Schadelin S, Rigau V, Mariani L, Duffau H. A Better Surgical Resectability of WHO Grade II Gliomas Is Independent of Favorable Molecular Markers. *J Neurooncol* (2015) 121(1):185–93. doi: 10.1007/s11060-014-1623-y
5. Xia L, Fang C, Chen G, Sun C. Relationship Between the Extent of Resection and the Survival of Patients With Low-Grade Gliomas: A Systematic Review and Meta-Analysis. *BMC Cancer* (2018) 18(1):48. doi: 10.1186/s12885-017-3909-x
6. Wijnenga M, French P, Dubbink H, Dinjens W, Atmodimedjo P, Kros J, et al. The Impact of Surgery in Molecularly Defined Low-Grade Glioma: An Integrated Clinical, Radiological, and Molecular Analysis. *Neuro Oncol* (2018) 20(1):103–12. doi: 10.1093/neuonc/nox176
7. Kinslow C, Garton A, Rae A, Marcus L, Adams C, McKhann G, et al. Extent of Resection and Survival for Oligodendroglioma: A U.S. Population-Based Study. *J Neurooncol* (2019) 144(3):591–601. doi: 10.1007/s11060-019-03261-5
8. Ding X, Wang Z, Chen D, Wang Y, Zhao Z, Sun C, et al. The Prognostic Value of Maximal Surgical Resection is Attenuated in Oligodendroglioma Subgroups of Adult Diffuse Glioma: A Multicenter Retrospective Study. *J Neurooncol* (2018) 140(3):591–603. doi: 10.1007/s11060-018-2985-3
9. Harary M, Kavouridis V, Torre M, Zaidi H, Chukwueke U, Reardon D, et al. Predictors and Early Survival Outcomes of Maximal Resection in WHO Grade II 1p/19q-Codeleted Oligodendrogliomas. *Neuro Oncol* (2020) 22 (3):369–80. doi: 10.1093/neuonc/noz168
10. Wang Y, Wei W, Liu Z, Liang Y, Liu X, Li Y, et al. Predicting the Type of Tumor-Related Epilepsy in Patients With Low-Grade Gliomas: A Radiomics Study. *Front Oncol* (2020) 10:235. doi: 10.3389/fonc.2020.00235
11. Lambin P, Rios-Velazquez E, Leijenaar R, Carvalho S, van Stiphout RG, Granton P, et al. Radiomics: Extracting More Information From Medical Images Using Advanced Feature Analysis. *Eur J Cancer* (2012) 48(4):441–6. doi: 10.1016/j.ejca.2011.11.036
12. Kumar V, Gu Y, Basu S, Berglund A, Eschrich SA, Schabath MB, et al. Radiomics: The Process and the Challenges. *Magn Reson Imaging* (2012) 30 (9):1234–48. doi: 10.1016/j.mri.2012.06.010
13. Qian Z, Li Y, Sun Z, Fan X, Xu K, Wang K, et al. Radiogenomics of Lower-Grade Gliomas: A Radiomic Signature as a Biological Surrogate for Survival Prediction. *Aging* (2018) 10(10):2884–99. doi: 10.18632/aging.101594
14. Liu X, Li Y, Sun Z, Li S, Wang K, Fan X, et al. Molecular Profiles of Tumor Contrast Enhancement: A Radiogenomic Analysis in Anaplastic Gliomas. *Cancer Med* (2018) 7(9):4273–83. doi: 10.1002/cam4.1672
15. Liu X, Li Y, Qian Z, Sun Z, Xu K, Wang K, et al. A Radiomic Signature as a non-Invasive Predictor of Progression-Free Survival in Patients With Lower-Grade Gliomas. *NeuroImage Clin* (2018) 20:1070–7. doi: 10.1016/j.nicl.2018.10.014
16. Liu X, Li Y, Li S, Fan X, Sun Z, Yang Z, et al. IDH Mutation-Specific Radiomic Signature in Lower-Grade Gliomas. *Aging* (2019) 11(2):673–96. doi: 10.18632/aging.101769
17. Li Y, Liu X, Qian Z, Sun Z, Xu K, Wang K, et al. Genotype Prediction of ATRX Mutation in Lower-Grade Gliomas Using an MRI Radiomics Signature. *Eur Radiol* (2018) 28(7):2960–8. doi: 10.1007/s00330-017-5267-0
18. Li Y, Qian Z, Xu K, Wang K, Fan X, Li S, et al. MRI Features Predict p53 Status in Lower-Grade Gliomas Via a Machine-Learning Approach. *NeuroImage Clin* (2018) 17:306–11. doi: 10.1016/j.nicl.2017.10.030
19. Li Y, Qian Z, Xu K, Wang K, Fan X, Li S, et al. Radiomic Features Predict Ki-67 Expression Level and Survival in Lower Grade Gliomas. *J Neurooncol* (2017) 135(2):317–24. doi: 10.1007/s11060-017-2576-8
20. Wen PY, Huse JT. 2016 World Health Organization Classification of Central Nervous System Tumors. *Continuum (Minneap Minn)* (2017) 23(6, Neuro-oncology):1531–47. doi: 10.1212/CON.0000000000000536

21. Wang K, Wang Y, Fan X, Li Y, Liu X, Wang J, et al. Regional Specificity of 1p/19q Co-Deletion Combined With Radiological Features for Predicting the Survival Outcomes of Anaplastic Oligodendroglial Tumor Patients. *J Neurooncol* (2018) 136(3):523–31. doi: 10.1007/s11060-017-2673-8
22. Aerts HJ, Velazquez ER, Leijenaar RT, Parmar C, Grossmann P, Carvalho S, et al. Decoding Tumour Phenotype by Noninvasive Imaging Using a Quantitative Radiomics Approach. *Nat Commun* (2014) 5:4006. doi: 10.1038/ncomms5644
23. Friedman J, Hastie T, Tibshirani R. Regularization Paths for Generalized Linear Models Via Coordinate Descent. *J Stat Softw* (2010) 33(1):1–22. doi: 10.18637/jss.v033.i01
24. Zou H, Hastie T. Regularization and Variable Selection Via the Elastic Net. *J R Stat Soc Ser B (Stat Methodol)* (2005) 67(2):301–20. doi: 10.1111/j.1467-9868.2005.00503.x
25. Hastie T, Tibshirani R, Friedman J. *The Elements of Statistical Learning*. New York: Spriner (2008).
26. Cristianini N, Shawe-Taylor J. An Introduction to Support Vector Machines and Other Kernel-Based Learning Methods. Cambridge, England: Cambridge University Press (2000). doi: 10.1017/CBO9780511801389
27. Schölkopf B, Smola AJ, Bach F. Learning With Kernels: Support Vector Machines, Regularization, Optimization, and Beyond. Cambridge, MA, London, England: MIT press (2002). doi: 10.1109/tnn.2005.848998
28. Fan R-E, Chen P-H, Lin C-J. Working Set Selection Using Second Order Information for Training Support Vector Machines. *J Mach Learn Res* (2005) 6(Dec):1889–918. doi: 10.1007/s11042-014-2292-8
29. Kecman V, Huang T-M, Vogt M. Iterative Single Data Algorithm for Training Kernel Machines From Huge Data Sets: Theory and Performance. Support Vector Machines: Theory and Applications. Berlin, Germany: Springer (2005) p. 255–74. doi: 10.1007/10984697_12
30. Varoquaux G, Raamana P, Engemann D, Hoyos-Idrobo A, Schwartz Y, Thirion B. Assessing and Tuning Brain Decoders: Cross-Validation, Caveats, and Guidelines. *NeuroImage* (2017) 145:166–79. doi: 10.1016/j.neuroimage.2016.10.038
31. De Cáceres M, Legendre P. Associations Between Species and Groups of Sites: Indices and Statistical Inference. *Ecology* (2009) 90(12):3566–74. doi: 10.1890/08-1823.1
32. Tom M, Varra V, Leyrer C, Park D, Chao S, Yu J, et al. Risk Factors for Progression Among Low-Grade Gliomas After Gross Total Resection and Initial Observation in the Molecular Era. *Int J Radiat Oncol Biol Phys* (2019) 104(5):1099–105. doi: 10.1016/j.ijrobp.2019.04.010
33. Brat D, Verhaak R, Aldape K, Yung W, Salama S, Cooper L, et al. Comprehensive, Integrative Genomic Analysis of Diffuse Lower-Grade Gliomas. *N Engl J Med* (2015) 372(26):2481–98. doi: 10.1056/NEJMoa1402121
34. Zhou H, Vallieres M, Bai HX, Su C, Tang H, Oldridge D, et al. MRI Features Predict Survival and Molecular Markers in Diffuse Lower-Grade Gliomas. *Neuro Oncol* (2017) 19(6):862–70. doi: 10.1093/neuonc/now256
35. Zhou H, Chang K, Bai HX, Xiao B, Su C, Bi WL, et al. Machine Learning Reveals Multimodal MRI Patterns Predictive of Isocitrate Dehydrogenase and 1p/19q Status in Diffuse Low- and High-Grade Gliomas. *J Neurooncol* (2019) 142(2):299–307. doi: 10.1007/s11060-019-03096-0
36. Shboul Z, Chen J M, Iftekharuddin K. Prediction of Molecular Mutations in Diffuse Low-Grade Gliomas Using MR Imaging Features. *Sci Rep* (2020) 10 (1):3711. doi: 10.1038/s41598-020-60550-0
37. Matsui Y, Maruyama T, Nitta M, Saito T, Tsuzuki S, Tamura M, et al. Prediction of Lower-Grade Glioma Molecular Subtypes Using Deep Learning. *J Neurooncol* (2020) 146(2):321–7. doi: 10.1007/s11060-019-03376-9
38. Ali M, Gu I, Berger M, Pallud J, Southwell D, Widhalm G, et al. Domain Mapping and Deep Learning From Multiple MRI Clinical Datasets for Prediction of Molecular Subtypes in Low Grade Gliomas. *Brain Sci* (2020) 10(7):463. doi: 10.3390/brainsci10070463
39. Akkus Z, Ali I, Sedlář J, Agrawal J, Parney I, Giannini C, et al. Predicting Deletion of Chromosomal Arms 1p/19q in Low-Grade Gliomas From MR Images Using Machine Intelligence. *J Digit Imaging* (2017) 30(4):469–76. doi: 10.1007/s10278-017-9984-3
40. Lu C, Hsu F, Hsieh K, Kao Y, Cheng S, Hsu J, et al. Machine Learning-Based Radiomics for Molecular Subtyping of Gliomas. *Clin Cancer Res* (2018) 24 (18):4429–36. doi: 10.1158/1078-0432.CCR-17-3445
41. Zhao S, Feng X, Hu Y, Han Y, Tian Q, Sun Y, et al. Better Efficacy in Differentiating WHO Grade II From III Oligodendrogliomas With Machine-Learning Than Radiologist's Reading From Conventional T1 Contrast-Enhanced and Fluid Attenuated Inversion Recovery Images. *BMC Neurol* (2020) 20(1):48. doi: 10.1186/s12883-020-1613-y
42. Tian Q, Yan L, Zhang X, Zhang X, Hu Y, Han Y, et al. Radiomics Strategy for Glioma Grading Using Texture Features From Multiparametric MRI. *J Magn Reson Imaging* (2018) 48(6):1518–28. doi: 10.1002/jmri.26010
43. Bahrami N, Hartman SJ, Chang YH, Delfanti R, White NS, Karunamuni R, et al. Molecular Classification of Patients With Grade II/III Glioma Using Quantitative MRI Characteristics. *J Neurooncol* (2018) 139(3):633–42. doi: 10.1007/s11060-018-2908-3
44. Ekert K, Hinterleitner C, Baumgartner K, Fritz J, Horger M. Extended Texture Analysis of Non-Enhanced Whole-Body MRI Image Data for Response Assessment in Multiple Myeloma Patients Undergoing Systemic Therapy. *Cancers (Basel)* (2020) 12(3):761. doi: 10.3390/cancers12030761
45. Sun Z, Li Y, Wang Y, Fan X, Xu K, Wang K, et al. Radiogenomic Analysis of Vascular Endothelial Growth Factor in Patients With Diffuse Gliomas. *Cancer Imaging* (2019) 19(1):68. doi: 10.1186/s40644-019-0256-y
46. Wady SH, Yousif RZ, Hasan HR. A Novel Intelligent System for Brain Tumor Diagnosis Based on a Composite Neutrosophic-Slantlet Transform Domain for Statistical Texture Feature Extraction. *BioMed Res Int* (2020) 2020:8125392. doi: 10.1155/2020/8125392
47. Baek HJ, Kim HS, Kim N, Choi YJ, Kim YJ. Percent Change of Perfusion Skewness and Kurtosis: A Potential Imaging Biomarker for Early Treatment Response in Patients With Newly Diagnosed Glioblastomas. *Radiology* (2012) 264(3):834–43. doi: 10.1148/radiol.12112120
48. Bisdas S, Shen H, Thust S, Katsaros V, Stranjalis G, Boskos C, et al. Texture Analysis- and Support Vector Machine-Assisted Diffusional Kurtosis Imaging may Allow In Vivo Gliomas Grading and IDH-mutation Status Prediction: A Preliminary Study. *Sci Rep* (2018) 8(1):6108. doi: 10.1038/s41598-018-24438-4
49. Haubold J, Demircioglu A, Gratz M, Glas M, Wrede K, Sure U, et al. Non-Invasive Tumor Decoding and Phenotyping of Cerebral Gliomas Utilizing Multiparametric F-FET PET-MRI and MR Fingerprinting. *Eur J Nucl Med Mol Imaging* (2020) 47(6):1435–45. doi: 10.1007/s00259-019-04602-2
50. Diamandis E, Gabriel C, Würtemberger U, Guggenberger K, Urbach H, Staszewski O, et al. MR-Spectroscopic Imaging of Glial Tumors in the Spotlight of the 2016 WHO Classification. *J Neurooncol* (2018) 139(2):431–40. doi: 10.1007/s11060-018-2881-x
51. Latysheva A, Emblem K, Brandal P, Vik-Mo E, Pahnke J, Røysland K, et al. Dynamic Susceptibility Contrast and Diffusion MR Imaging Identify Oligodendroglioma as Defined by the 2016 WHO Classification for Brain Tumors: Histogram Analysis Approach. *Neuroradiology* (2019) 61(5):545–55. doi: 10.1007/s00234-019-02173-5
52. Lee M, Park J, Jo Y, Park S, Kim S, Kim H. Advanced Imaging Parameters Improve the Prediction of Diffuse Lower-Grade Gliomas Subtype, IDH Mutant With No 1p19q Codeletion: Added Value to the T2/FLAIR Mismatch Sign. *Eur Radiol* (2020) 30(2):844–54. doi: 10.1007/s00330-019-06395-2
53. Broen M, Smits M, Wijnenga M, Dubbink H, Anten M, Schijns O, et al. The T2-FLAIR Mismatch Sign as an Imaging Marker for non-Enhancing IDH-Mutant, 1p/19q-Intact Lower-Grade Glioma: A Validation Study. *Neuro Oncol* (2018) 20(10):1393–9. doi: 10.1093/neuonc/noy048

Conflict of Interest: The authors declare that the research was conducted in the absence of any commercial or financial relationships that could be construed as a potential conflict of interest.

The handling editor HB declared a past co-authorship with one of the authors YW.

frontiers in Oncology

ORIGINAL RESEARCH
published: 18 August 2021
doi: 10.3389/fonc.2021.665891

Deep Learning With Data Enhancement for the Differentiation of Solitary and Multiple Cerebral Glioblastoma, Lymphoma, and Tumefactive Demyelinating Lesion

Yu Zhang[1,2†], Kewei Liang[2,3,4†], Jiaqi He[2,5], He Ma[4], Hongyan Chen[1], Fei Zheng[1], Lingling Zhang[1], Xinsheng Wang[6], Xibo Ma[2,3*] and Xuzhu Chen[1*]*

[1] Department of Radiology, Beijing Tiantan Hospital, Capital Medical University, Beijing, China, [2] CBSR&NLPR, Institute of Automation, Chinese Academy of Sciences, Beijing, China, [3] School of Artificial Intelligence, University of Chinese Academy of Sciences, Beijing, China, [4] College of Medicine and Biological Information Engineering, Northeastern University, Shenyang, China, [5] Dalian Medical University, School of Stomatology, Dalian, China, [6] School of Information Science and Engineering, Harbin Institute of Technology at Weihai, Weihai, China

Objectives: To explore the MRI-based differential diagnosis of deep learning with data enhancement for cerebral glioblastoma (GBM), primary central nervous system lymphoma (PCNSL), and tumefactive demyelinating lesion (TDL).

Materials and Methods: This retrospective study analyzed the MRI data of 261 patients with pathologically diagnosed solitary and multiple cerebral GBM (n = 97), PCNSL (n = 92), and TDL (n = 72). The 3D segmentation model was trained to capture the lesion. Different enhancement data were generated by changing the pixel ratio of the lesion and non-lesion areas. The 3D classification network was trained by using the enhancement data. The accuracy, sensitivity, specificity, and area under the curve (AUC) were used to assess the value of different enhancement data on the discrimination performance. These results were then compared with the neuroradiologists' diagnoses.

Results: The diagnostic performance fluctuated with the ratio of lesion to non-lesion area changed. The diagnostic performance was best when the ratio was 1.5. The AUCs of GBM, PCNSL, and TDL were 1.00 (95% confidence interval [CI]: 1.000–1.000), 0.96 (95% CI: 0.923–1.000), and 0.954 (95% CI: 0.904–1.000), respectively.

Conclusions: Deep learning with data enhancement is useful for the accurate identification of GBM, PCNSL, and TDL, and its diagnostic performance is better than that of the neuroradiologists.

Keywords: glioblastoma, lymphoma, tumefactive demyelination, differential diagnosis, deep learning

OPEN ACCESS

Edited by:
Xuejun Li,
Central South University, China

Reviewed by:
Xavier Ayrignac,
Université de Montpellier, France
Xinhua Wei,
Guangzhou First People's Hospital, China

***Correspondence:**
Xinsheng Wang
xswang@hit.edu.cn
Xibo Ma
xibo.ma@ia.ac.cn
Xuzhu Chen
radiology888@aliyun.com

†These authors have contributed equally to this work

Specialty section:
This article was submitted to Neuro-Oncology and Neurosurgical Oncology, a section of the journal Frontiers in Oncology

Received: *09 February 2021*
Accepted: *29 July 2021*
Published: *18 August 2021*

Citation:
Zhang Y, Liang K, He J, Ma H, Chen H, Zheng F, Zhang L, Wang X, Ma X and Chen X (2021) Deep Learning With Data Enhancement for the Differentiation of Solitary and Multiple Cerebral Glioblastoma, Lymphoma, and Tumefactive Demyelinating Lesion. Front. Oncol. 11:665891. doi: 10.3389/fonc.2021.665891

INTRODUCTION

Cerebral glioblastoma (GBM), primary central nervous system lymphoma (PCNSL), and tumefactive demyelinating lesion (TDL) are distinct neurological lesions with respect to their pathology, treatment, and prognosis. GBM and PCNSL are both malignant primary intracranial tumors in adults (1, 2). The conventional management strategies are surgical resection followed by radiochemotherapy for GBM, and chemotherapy for PCNSL, respectively. The clinical onsets of the two kinds of neoplasms are not specific and closely related to the extent and location of lesions (3). TDL is an inflammatory disease characterized by varied neurodegenerative clinical manifestations, such as movement disorder and vision impairment (4). Hormone therapy is effective for TDL, and the clinical course is more favorable than brain malignancy.

All these three kinds of lesions can be either solitary or multiple (5–7). The conventional MRI findings of these three kinds of lesions are overlapping. As solitary lesions, they usually present as enhanced masses with peripheral edema. As multiple lesions, they present as scattered and enhanced masses in the brain. The open-ring enhancement in TDL may be an important sign that distinguishes it from other tumors (8). This typical radiological finding, however, is not frequent, resulting in a difficult diagnosis.

The similar routine MRI findings represent a challenge for the differential diagnosis. Given the conventional radiology characteristics, some advanced MRI modalities have been used for the differentiation of three lesions. A systematic review showed that the dynamic susceptibility contrast-enhanced image (DSC) and arterial spin labeling (ASL) had the potential to discriminate PCNSL from GBM (9). Another study reported that diffusion-weighted imaging (DWI) could be a useful diagnostic tool to differentiate among PCNSL, GBM, and inflammatory demyelination pseudotumor (10). Moreover, MRS had been a valuable approach to distinguish the mimicked pathologies (11).

However, these advanced MR modalities mainly focused only on the enhanced component of the lesion. Radiomics-based analysis, on the other hand, can explore the whole lesion including the enhanced and non-enhanced components. Recently, different radiomics have been developed to better understand cerebral entities. For example, the deep learning approach has been used for the differential diagnosis or grading in meningioma (12–14).

Thus far, both the advanced MR modalities and radiomics analysis have been used for the differentiation of the three lesions; however, these have only focused on the solitary form of the three lesions. All three lesion types can be multiple (4, 15). Moreover, most radiomics analysis have only considered machine learning algorithms with small datasets (10, 16). Thus, we collected more data and attempted to identify the three types of lesions by using MRI-based deep learning with data enhancement algorithm, with simultaneous focus on single and multiple lesions.

MATERIALS AND METHODS

Ethics Statement

This study is retrospective in nature. It was approved by the ethics committee of Beijing Tiantan Hospital. The need for patient informed consent was waived.

Subjects

Our study recruited 97, 92, and 72 patients with GBM, PCNSL, and TDL, between January 2005 and December 2019. Of these subjects, 97 patients with GBM, 76 patients with PCNSL, and 52 patients with TDL were from a single medical institute. The remaining 16 patients with PCNSL and 20 patients with TDL were from another medical institute. All patients with GBM and PCNSL were confirmed by pathology. Among 72 patients with TDL, 52 were diagnosed based on the definition of TDL: demyelinating lesions (2 cm or greater) or lesions between 0.5 and 2 cm with possible mass effect that can be mistaken for tumor-like space-occupying lesions and have a characteristic radiographic appearance (17). With analysis of medical records and clinical and MRI characteristics, 20 were pathologically confirmed owing to the diagnostic uncertainty.

The inclusion criteria were as follows: (1) GBM and PCNSL confirmed by pathology, respectively; (2) TDL diagnosed by pathology or the corresponding criteria (17); (3) available cerebral MRI before diagnosis. The exclusion criteria were as follows: (1) patient age <18 years; (2) missing clinical information; (3) receipt of hormone therapy before undergoing MRI; (4) no data on enhanced MRI; (5) lesions not in the cerebral parenchyma; and (6) MR images with obvious artifact. The enrollment process is presented in **Supplementary File 1**. Each type of entity was composed of solitary or multiple lesions.

MRI Acquisition and Lesions Segmentation

The MRI acquisition protocols were composed of pre- and post-enhanced T1-weighted (CE-T1) images. The contrast media type, venous injection dose, and acquisition parameters for CE-T1 are given in **Supplementary File 2**.

All MR images in the form of digital imaging and communications in medicine (DICOM) were input to the ITK-SNAP (version 3.4.0, www.itk-snap.org). The regions of interest (ROIs) of these three types of lesions were manually delineated on axial CE-T1 by a neuroradiologist using ITK-SNAP.

Before the ROI segmentation, two blinded neuroradiologists with 10 years of experience independently diagnosed these three types of diseases for 130 randomly selected cases out of the 261 cases. Each neuroradiologist had access to the full DICOM images from different MRI scanners. The number of accurately diagnosed cases by the two senior neuroradiologists were divided by that of all diagnosed cases. The result was determined to calculate the diagnostic performance.

Statistical Analysis

All continuous and categorical variables were expressed as the mean ± standard deviation and the number (percentage),

respectively. One-way analysis of variance (ANOVA) and Pearson's chi-square tests were used to compare the group differences with regard to patient age, sex ratio, and number of multiple lesions by SPSS (version 23.0, IBM Corporation, Armonk, NY, USA). A $p < 0.05$ was considered to indicate statistical significance. The receiver operating characteristic (ROC) curve obtained from the pROC (version 1.16.2) of R (version 4.0.2) was used to show the area under the curve (AUC), accuracy, specificity, and sensitivity under different thresholds to evaluate the performance of the classification model.

Algorithm Implementation

Most of the algorithms were implemented by Python 3.7.4. The 261 subjects were randomly divided into a training set and a testing set. The training set included 67 cases of GBM, 65 cases of PCNSL, and 50 cases of TDL, and the testing set consisted of 30 cases of GBM, 27 cases of PCNSL, and 22 cases of TDL. All data were converted into a NIFTI format to adapt to a 3D network.

The diagnosis process is presented in **Figure 1**. It was divided into three stages and was not an end-to-end solution.

In the first stage, a 3D U-Net (18) was used to automatically predict the lesion area. First, MRI was cropped to reduce the consumption of computing resources, and then the data were normalized to reduce the interference of medical image caused by uneven light. The initial input network image size was reduced to 128 × 128 × 32 without affecting the segmentation performance. Second, the fixed-size image was entered into a convolution layer and four ResBlock downsampling modules to obtain different depth features. Third, the features obtained after the fourth downsampling were fused with the features obtained after the third downsampling module. The fused features were entered into the upsampling ResBlock module to obtain the upsampling features. By analogy, the image size was finally restored to 128 × 128 × 32. Finally, the number of channels were reduced to two after the image entered a convolution layer. The segmentation mask was obtained by argmax function, and the segmentation mask was restored to 512 × 512 × 24 by bilinear interpolation.

In the second stage, the segmented lesion area was combined with the original MR image to change the pixels of the lesion area by a certain multiple, and the pixels of the non-lesion area were unchanged. The following combination equation was used:

$$Mn = M + M \bullet n \bullet k$$

Where *M*n represents the enhanced data, M represents the original MR image, n represents the segmented mask, and k represents the enhancement coefficient. In this experiment, five k values were selected, namely, −0.5, 0, 0.5, 1, and 2, to explore the best model. The *M*n visualization for different k values is shown in **Figure 2**.

In the third stage, the enhanced data were preprocessed similar to the first stage. The Resnet18 (19) was trained and tested by the preprocessed images to identify GBM, PCNSL, and TDL.

In addition, identification using the lesion area was considered one of the comparative experiments. The mask segmented by the automatic segmentation network was multiplied with the original MR image so that the surrounding area of the original MR image was removed and only the lesion area was retained. Resnet18 was used for identification of the lesion area. The flow chart of a comparative experiment is shown in **Figure 3**.

The AUC, accuracy, sensitivity, and specificity were calculated according to the output of the classification network. When ROC curves were plotted, one disease was considered positive and the other two were considered negative.

RESULTS

Subjects' Clinical Characteristics

Patients with TDL were the youngest. Those with GBM had the highest ratio of solitary lesions (85.6%, 83/97) (**Table 1**).

Diagnostic Performance

The AUC (95% confidence interval [CI]), accuracy, sensitivity, specificity, and overall accuracy are presented in **Tables 2** and **3**. The ROC curves are shown in **Figure 4**. When k was 0.5, the diagnostic performance was the best, and the overall accuracy was 92.4%. The AUC (95% CI) of GBM, PCNSL, and TDL were 1.00 (1.000–1.000), 0.96 (0.923–1.000), and 0.95 (0.904–1.000), respectively. The selected radiomics features of GBM, PCNSL, and TDL at the optimal k value are shown in **Figure 5**. The overall diagnostic performances of the two neuroradiologists were 52.4%.

DISCUSSION

In our study, GBM and PCNSL were found more in male than female patients, while TDL was found more in female than male patients. This observation was in accordance with previous studies (7, 20). The mean age of patients with these three types of lesions was between 40 and 50 years in our subjects, consistent with some previous reports (7, 20, 21). Regarding the number of lesions, solitary GBM was found in 85.6% (83/97) patients, similar to that reported by Kapoor et al. (6). The ratio of multifocal PCNSL and TDL lesions was slightly higher than that of non-focal lesions, inconsistent with some previous reports (7, 22). This discrepancy may be due to the different case selection criteria among studies.

In this study, we aimed to simultaneously differentiate among three types of lesions. This is different from existing similar studies that only differentiated between two types of lesions. For example, GBM was differentiated from PCNSL by using different MRI modalities (23, 24), machine learning

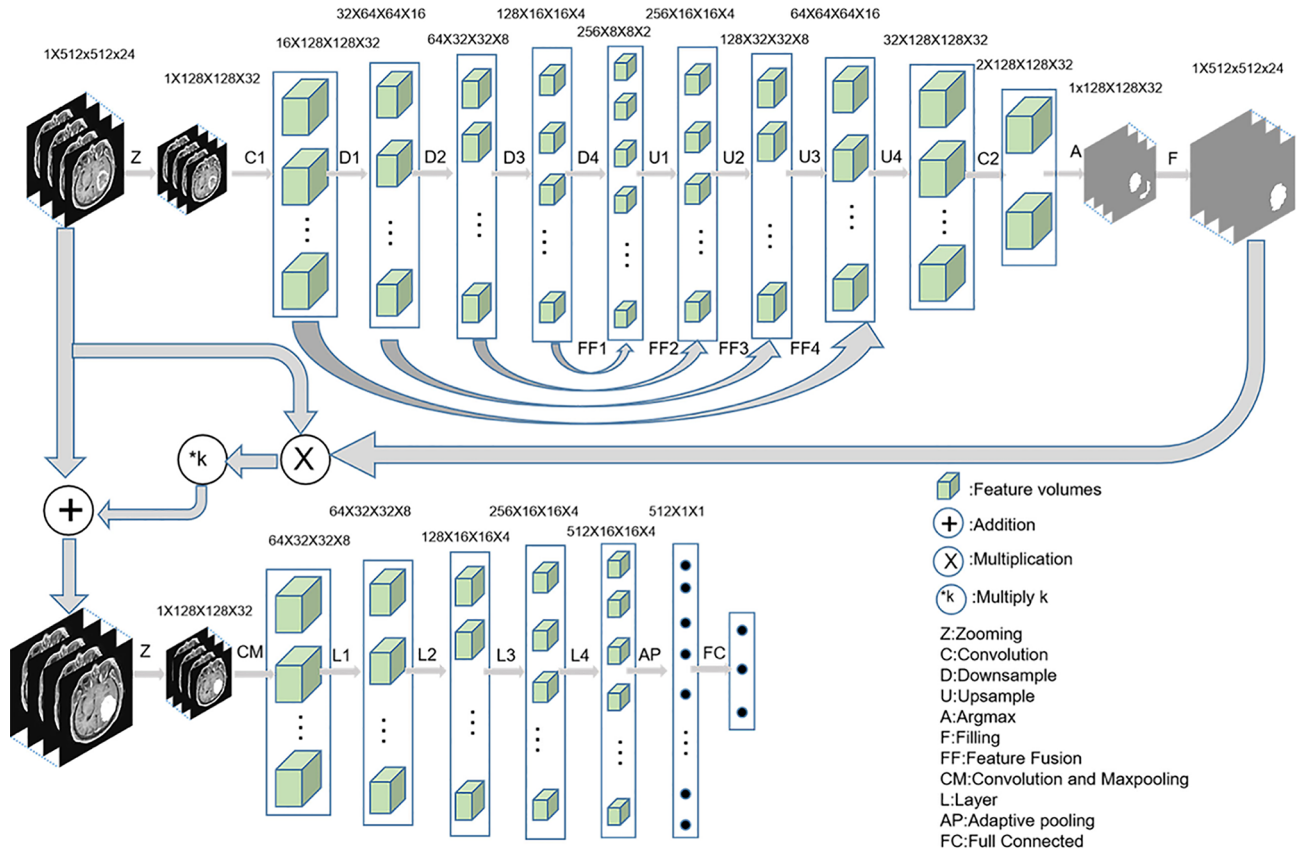

FIGURE 1 | The implementation process of three-stage algorithm based on deep learning with data enhancement. In the first stage, 3D u-net is used to capture the lesion area; in the second stage, enhanced data are generated; and in the third stage, 3D Resnet is used for diagnosis.

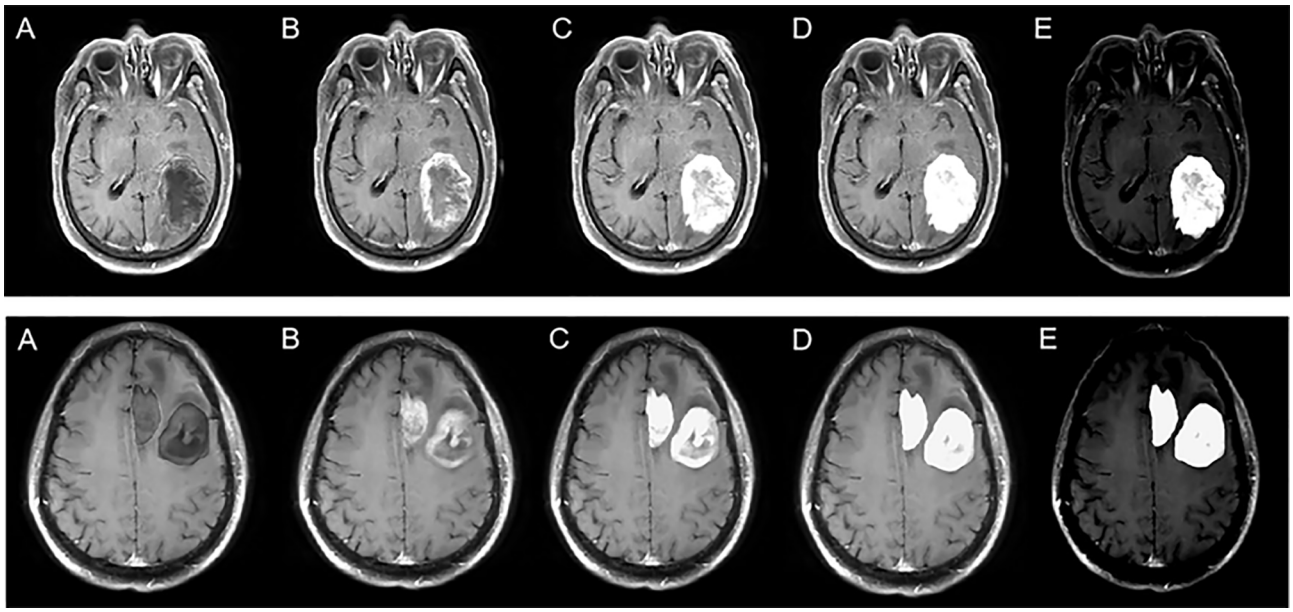

FIGURE 2 | Enhanced data with different k values. The top row represents solitary figures, and the bottom row represents multiple lesions. k is –0.5 **(A)**, 0 **(B)**, 0.5 **(C)**, 1 **(D)**, and 2 **(E)**.

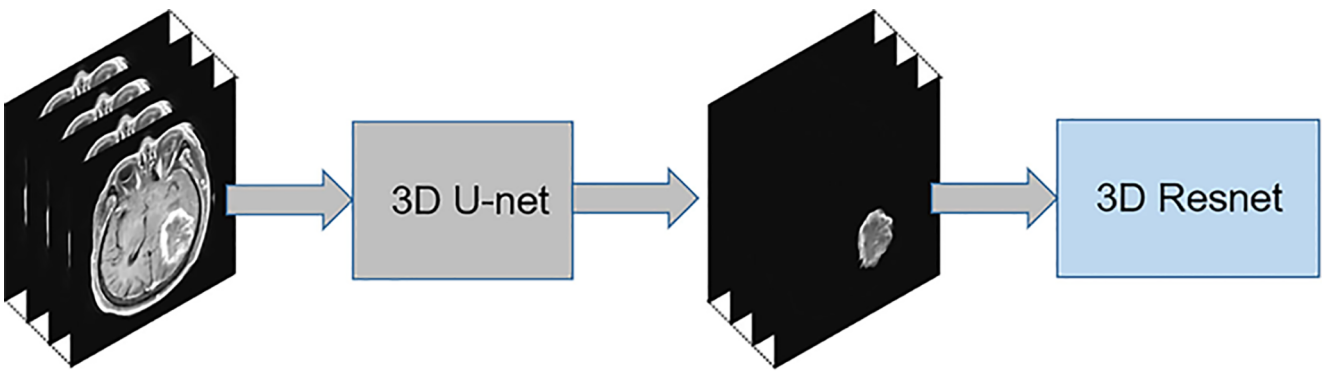

FIGURE 3 | The implementation process of the lesion area diagnosis algorithm.

TABLE 1 | Clinical characteristics of subjects.

	GBM	PCNSL	TDL	*p*
Number of subjects	97	92	72	
Age (years, mean ± SD)	54.61 ± 12.35	53.34 ± 12.57	41.33 ± 12.82	<0.001*
Sex				0.224
Male	56 (57.7%)	57 (62.0%)	35 (48.6%)	
Female	41 (42.3%)	35 (38.0%)	37 (51.4%)	
Number of lesions				<0.001*
Solitary	83 (85.6%)	45 (48.9%)	32 (44.4%)	
Multiple	14 (14.4%)	47 (51.1%)	40 (55.6%)	

**p < 0.05. GBM, cerebral glioblastoma; PCNSL, primary central nervous system lymphoma; TDL, tumefactive demyelinating lesion; SD, standard deviation.*

TABLE 2 | Diagnostic performance at different k values.

k	Overall accuracy	AUC (95% CI)			ACC			SEN			SPE		
		GBM	PCNSL	TDL	GBM	PCNSL	TDL	GBM	PCNSL	TDL	GBM	PCNSL	TDL
–0.5	0.81	1.00 (1.000–1.000)	0.86 (0.785–0.943)	0.83 (0.738–0.924)	1.00	0.81	0.81	1.00	0.82	0.55	1.00	0.81	0.91
0	0.86	1.00 (1.000–1.000)	0.92 (0.856–0.980)	0.90 (0.823–0.975)	1.00	0.86	0.86	1.00	0.82	0.73	1.00	0.88	0.91
0.5	0.92	1.00 (1.000–1.000)	0.96 (0.923–1.000)	0.95 (0.904–1.000)	1.00	0.92	0.92	1.00	0.85	0.91	1.00	0.96	0.93
1	0.91	1.00 (1.000–1.000)	0.95 (0.900–1.000)	0.92 (0.838–1.000)	1.00	0.91	0.91	1.00	0.85	0.86	1.00	0.94	0.93
2	0.92	1.00 (1.000–1.000)	0.96 (0.906–1.000)	0.92 (0.813–1.000)	1.00	0.92	0.92	1.00	0.85	0.91	1.00	0.96	0.93

AUC, area under the curve; ACC, accuracy; SEN, sensitivity; SPE, specificity; GBM, cerebral glioblastoma; PCNSL, primary central nervous system lymphoma; TDL, tumefactive demyelinating lesion.

TABLE 3 | Diagnostic performance of the model using the lesion area.

	AUC (95% CI)	ACC	SEN	SPE
GBM	1.00 (1.000–1.000)	1.00	1.00	1.00
PCNSL	0.94 (0.900–0.989)	0.84	0.70	0.90
TDL	0.94 (0.892–0.991)	0.84	0.77	0.86
Overall accuracy	0.84			

AUC, area under the curve; ACC, accuracy; SEN, sensitivity; SPE, specificity; GBM, cerebral glioblastoma; PCNSL, primary central nervous system lymphoma; TDL, tumefactive demyelinating lesion.

applications (25), and radiomics approach (26); GBM was differentiated from TDL by using methionine positron emission tomography (PET) (27); and PCNSL was differentiated from TDL by using different MRI modalities (28, 29). Moreover, these differential studies between two kinds of entities only focused on solitary lesion. Multiple PCNSL was differentiated from multifocal gliomas by using PET (30). However, the differentiation was also being performed between two types of lesions. To our knowledge, our study is the first to simultaneously differentiate the three entities with solitary and multifocal types by radiomics analysis.

Our study showed that a deep learning algorithm with data enhancement could accurately differentiate among solitary and multifocal GBM, PCNSL, and TDL. This method has two advantages. First, an automatic segmentation network was designed for the lesion region. The neural network can improve focus to the lesion area by enhancing it; this significantly improves the overall diagnostic performance of the neural network for GBM, PCNSL, and TDL. The performance of the model rises first and then falls with the increase in the ratio of lesion area to non-lesion area, and there is an optimal ratio. This means that both the focus area and the non-focus area contain information that can be used for diagnosis. When the ratio is appropriate, the neural network can maximize the information in the two areas for the identification of three lesions. Second, the data were transformed into 3D data, and 3D u-net and 3D Resnet were used for image segmentation and classification, respectively. 3D data have better diagnostic performance than 2D data and 2D networks. The consumption of computing resources is reduced by dividing the training into three stages.

Our study had several limitations. First, although we tried to minimize it, there may be some selection bias owing to the retrospective nature of the study. Second, our training process was not end-to-end, and while this saves computing resources, this makes it more challenging for non-professionals to use this diagnostic method. Although we tried to use the end-to-end network for training, the existing data could not support training several times larger than the existing model to achieve better diagnostic performance. Therefore, more data need to be collected to support end-to-end networks. Third, this experiment only studied the differentiation of three radiologically similar lesions; neuroradiologists may consider additional diseases when making a diagnosis. The existing supervised machine learning and deep learning methods can only diagnose the disease as one of the training set labels, and ignore other possible diseases. If the subject is not one of the training set labels, there is no possibility of being diagnosed correctly. Fourth, no external validation was performed. Last, only single-mode MRI data were used in this study. Inclusion of multimodal data will provide more diagnostic information and is one of the important ways to improve diagnostic performance. However, the single-model data reduce the difficulty of data collection, which makes our method more easily applicable to other diagnosis processes than other methods. Therefore, our method showed good performance in diagnostic accuracy and can provide a feasible reference for the identification of other diseases.

CONCLUSION

Deep learning with data enhancement is useful for the identification of GBM, PCNSL, and TDL, and its diagnostic performance is better than that of neuroradiologists.

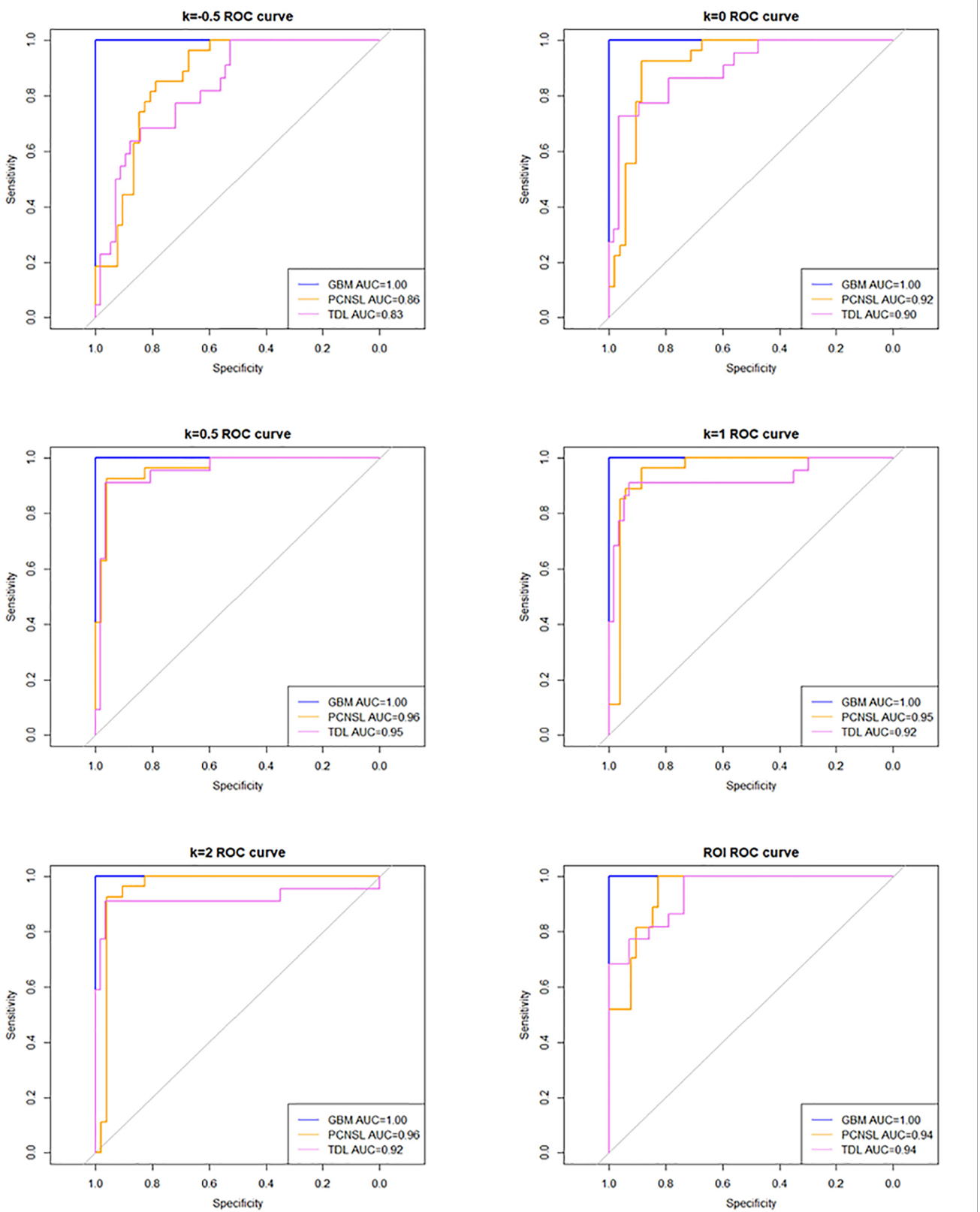

FIGURE 4 | Receiver operating characteristic (ROC) curve at different k values and region of interest (ROI).

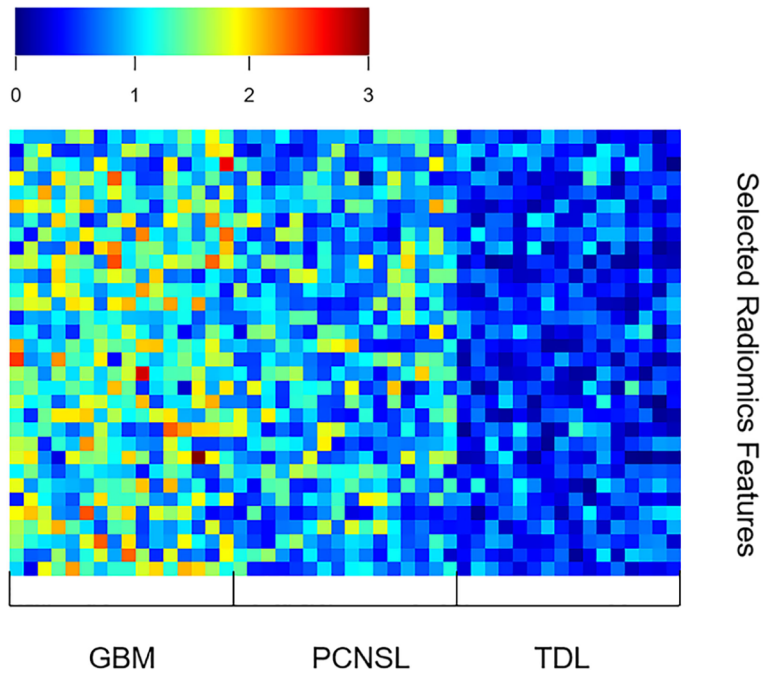

FIGURE 5 | The selected radiomics features of GBM, PCNSL, and TDL at the optimal k value.

DATA AVAILABILITY STATEMENT

The raw data supporting the conclusions of this article will be made available by the authors, without undue reservation.

ETHICS STATEMENT

The studies involving human participants were reviewed and approved by the Department of Radiology, Beijing Tiantan Hospital, Capital Medical University. Written informed consent for participation was not required for this study in accordance with the national legislation and the institutional requirements.

AUTHOR CONTRIBUTIONS

XC and XM designed the original research. YZ, KL, JH, HM, HC, FZ, and LZ conducted the research. KL analyzed the data. YZ and KL wrote the manuscript. XC, XM, and XW revised the paper. All authors contributed to the article and approved the submitted version.

FUNDING

This work is supported by the National Key Research and Development Program of China Grant under grant (Nos. 2018YFC0115604, 2016YFA0100900, 2016YFA0100902); the National Natural Science Foundation of China under grant (Nos. 81772005, 82090051, 81871442); Collaborative innovative major special project supported by Beijing Municipal Science & Technology Commission (Z19110 0006619088); the Youth Innovation Promotion Association CAS (Y201930); and Shandong Province Natural Science Foundation (ZR2020KF016).

SUPPLEMENTARY MATERIAL

The Supplementary Material for this article can be found online at: https://www.frontiersin.org/articles/10.3389/fonc.2021.665891/full#supplementary-material

REFERENCES

1. Linhares P, Carvalho B, Vaz R, Costa BM. Glioblastoma: Is There Any Blood Biomarker With True Clinical Relevance? *Int J Mol Sci* (2020) 21(16):5809. doi: 10.3390/ijms21165809
2. de Melo SM, Marta GN, Yan M, Cruz C, Moraes FY, Riera R. Management of Elderly Patients With Glioblastoma: Current Status With a Focus on the Post-Operative Radiation Therapy. *Ann Palliat Med* (2020) 9(5):3553–61. doi: 10.21037/apm-20-768
3. Grommes C, Rubenstein JL, DeAngelis LM, Ferreri AJM, Batchelor TT. Comprehensive Approach to Diagnosis and Treatment of Newly Diagnosed Primary CNS Lymphoma. *Neuro Oncol* (2019) 21(3):296–305. doi: 10.1093/neuonc/noy192
4. Sánchez P, Meca-Lallana V, Barbosa A, Manzanares R, Palmí I, Vivancos J. Tumefactive Demyelinating Lesions of 15 Patients: Clinico-Radiological Features, Management and Review of the Literature. *J Neurol Sci* (2017) 381:32–8. doi: 10.1016/j.jns.2017.08.005
5. Li Y, Zhang ZX, Huang GH, Xiang Y, Yang L, Pei YC. A Systematic Review of Multifocal and Multicentric Glioblastoma. *J Clin Neurosci* (2021) 83:71–6. doi: 10.1016/j.jocn.2020.11.025
6. Kapoor A, Mohindra S, Singla N, Sodhi HB, Chatterjee D, Gupta SK. Multiple Glioblastoma: A Diagnostic Challenge and Controversies in

Management. *Neurol India* (2015) 63(3):449–52. doi: 10.4103/0028-3886.158267
7. Partovi S, Karimi S, JK L, Esmaeili A, Tan J, Deangelis LM. Multimodality Imaging of Primary CNS Lymphoma in Immunocompetent Patients. *Br J Radiol* (2014) 87(1036):20130684. doi: 10.1259/bjr.20130684
8. Smirniotopoulos JG, Murphy FM, Rushing EJ, Rees JH, Schroeder JW. Patterns of Contrast Enhancement in the Brain and Meninges. *Radiographics* (2007) 27(2):525–51. doi: 10.1148/rg.272065155
9. Suh CH, Kim HS, Jung SC, Park JE, Choi CG, Kim SJ. MRI as a Diagnostic Biomarker for Differentiating Primary Central Nervous System Lymphoma From Glioblastoma: A Systematic Review and Meta-Analysis. *J Magn Reson Imaging* (2019) 50(2):560–72. doi: 10.1002/jmri.26602
10. Wen JB, Huang WY, Xu WX, Wu G, Geng DY, Yin B. Differentiating Primary Central Nervous System Lymphomas From Glioblastomas and Inflammatory Demyelinating Pseudotumor Using Relative Minimum Apparent Diffusion Coefficients. *J Comput Assist Tomogr* (2017) 41(6):904–9. doi: 10.1097/RCT.0000000000000636
11. Brandão LA, Castillo M. Adult Brain Tumors: Clinical Applications of Magnetic Resonance Spectroscopy. *Magn Reson Imaging Clin N Am* (2016) 24(4):781–809. doi: 10.1016/j.mric.2016.07.005
12. Gao Y, Xiao X, Han B, Li G, Ning X, Wang D, et al. Deep Learning Methodology for Differentiating Glioma Recurrence From Radiation Necrosis Using Multimodal Magnetic Resonance Imaging: Algorithm Development and Validation. *JMIR Med Inform* (2020) 8(11):e19805. doi: 10.2196/19805
13. Zhu Y, Man C, Gong L, Dong D, Yu X, Wang S, et al. A Deep Learning Radiomics Model for Preoperative Grading in Meningioma. *Eur J Radiol* (2019) 116:128–34. doi: 10.1016/j.ejrad.2019.04.022
14. Qian Z, Li Y, Wang Y, Li L, Li R, Wang K, et al. Differentiation of Glioblastoma From Solitary Brain Metastases Using Radiomic Machine-Learning Classifiers. *Cancer Lett* (2019) 451:128–35. doi: 10.1016/j.canlet.2019.02.054
15. Zali A, Shahzadi S, Mohammad-Mohammadi A, Taherzadeh K, Parsa K. Cerebral Lymphoma: Clinical and Radiological Findings in 90 Cases. *Arch Iran Med* (2007) 10(2):194–8. doi: 10.07102/AIM.0013
16. Kim DS, Na DG, Kim KH, Kim JH, Kim E, Yun BL, et al. Distinguishing Tumefactive Demyelinating Lesions From Glioma or Central Nervous System Lymphoma: Added Value of Unenhanced CT Compared With Conventional Contrast-Enhanced MR Imaging. *Radiology* (2009) 251(2):467–75. doi: 10.1148/radiol.2512072071
17. Brod SA, Lindsey JW, Nelson F. Tumefactive Demyelination: Clinical Outcomes, Lesion Evolution and Treatments. *Mult Scler J Exp Transl Clin* (2019) 5(2):2055217319855755. doi: 10.1177/2055217319855755
18. Milletari F, Navab N, Ahmadi S. V-Net: Fully Convolutional Neural Networks for Volumetric Medical Image Segmentation. In: *2016 Fourth International Conference on 3D Vision (3dv)*. Stanford, USA: IEEE (2016).
19. He K, Zhang X, Ren S, Sun J. Deep Residual Learning for Image Recognition. In: *2016 IEEE Conference on Computer Vision and Pattern Recognition (CVPR)*. Las Vegas, USA: IEEE (2016).
20. Suh CH, Kim HS, Jung SC, Choi CG, Kim SJ. MRI Findings in Tumefactive Demyelinating Lesions: A Systematic Review and Meta-Analysis. *AJNR Am J Neuroradiol* (2018) 39(9):1643–9. doi: 10.3174/ajnr.A5775
21. Kanderi T, Gupta V. Glioblastoma Multiforme. In: *StatPearls*. Treasure Island (FL): StatPearls Publishing (2020).
22. Lucchinetti CF, Gavrilova RH, Metz I, Parisi JE, Scheithauer BW, Weigand S, et al. Clinical and Radiographic Spectrum of Pathologically Confirmed Tumefactive Multiple Sclerosis. *Brain* (2008) 131(7):1759–75. doi: 10.1093/brain/awn098
23. Saini J, Kumar Gupta P, Awasthi A, Pandey CM, Singh A, Patir R, et al. Multiparametric Imaging-Based Differentiation of Lymphoma and Glioblastoma: Using T1-Perfusion, Diffusion, and Susceptibility-Weighted MRI. *Clin Radiol* (2018) 73(11):986.e7–15. doi: 10.1016/j.crad.2018.07.107
24. You SH, Yun TJ, Choi HJ, Yoo RE, Kang KM, Choi SH, et al. Differentiation Between Primary CNS Lymphoma and Glioblastoma: Qualitative and Quantitative Analysis Using Arterial Spin Labeling MR Imaging. *Eur Radiol* (2018) 28(9):3801–10. doi: 10.1007/s00330-018-5359-5
25. Nguyen AV, Blears EE, Ross E, Lall RR, Ortega-Barnett J. Machine Learning Applications for the Differentiation of Primary Central Nervous System Lymphoma From Glioblastoma on Imaging: A Systematic Review and Meta-Analysis. *Neurosurg Focus* (2018) 45(5):E5. doi: 10.3171/2018.8.FOCUS18325
26. Suh HB, Choi YS, Bae S, Ahn SS, Chang JH, Kang SG, et al. Primary Central Nervous System Lymphoma and Atypical Glioblastoma: Differentiation Using Radiomics Approach. *Eur Radiol* (2018) 28(9):3832–9. doi: 10.1007/s00330-018-5368-4
27. Yasuda S, Yano H, Kimura A, Suzui N, Nakayama N, Shinoda J, et al. Frontal Tumefactive Demyelinating Lesion Mimicking Glioblastoma Differentiated by Methionine Positron Emission Tomography. *World Neurosurg* (2018) 119:244–8. doi: 10.1016/j.wneu.2018.08.027
28. Mabray MC, Cohen BA, Villanueva-Meyer JE, Valles FE, Barajas RF, Rubenstein JL, et al. Performance of Apparent Diffusion Coefficient Values and Conventional MRI Features in Differentiating Tumefactive Demyelinating Lesions From Primary Brain Neoplasms. *AJR Am J Roentgenol* (2015) 205(5):1075–85. doi: 10.2214/AJR.14.13970
29. Lu SS, Kim SJ, Kim N, Kim HS, Choi CG, Lim YM. Histogram Analysis of Apparent Diffusion Coefficient Maps of Differentiating Primary CNS Lymphomas From Tumefactive Demyelinating Lesion. *AJR Am J Roentgenol* (2015) 204(4):827–34. doi: 10.2214/AJR.14.12677
30. Wang K, Zhao X, Chen Q, Fan D, Qiao Z, Lin S, et al. A New Diagnostic Marker for Differentiating Multicentric Gliomas From Multiple Intracranial Diffuse Large B-Cell Lymphomas on 18F-FDG PET Images. *Med (Baltimore)* (2017) 96(32):e7756. doi: 10.1097/MD.0000000000007756

Conflict of Interest: The authors declare that the research was conducted in the absence of any commercial or financial relationships that could be construed as a potential conflict of interest.

Frontiers in Oncology

Advances knowledge of carcinogenesis and tumor progression for better treatment and management

The third most-cited oncology journal, which highlights research in carcinogenesis and tumor progression, bridging the gap between basic research and applications to imrpove diagnosis, therapeutics and management strategies.

Discover the latest Research Topics

See more →

Frontiers

Avenue du Tribunal-Fédéral 34
1005 Lausanne, Switzerland
frontiersin.org

Contact us

+41 (0)21 510 17 00
frontiersin.org/about/contact